Synthesis and supporting of carbon dots onto titania, carbonized chitosan, silica spheres, hollow and solid carbon spheres for the removal of methyl orange from wastewater

By: Mkhari Orlette

Student number: 1901046

Supervisors: Dr. M.S. Maubane-Nkadimeng

Prof. N.J. Coville

Prof. E.N. Nxumalo

A thesis submitted to the faculty of Science at the University of the Witwatersrand, Johannesburg, in fulfillment of the requirements of the degree of

Doctor of Philosophy in Chemistry (Material Science)

2021

Declaration

I hereby declare that the work reported in this thesis is my own, unaided work submitted to the School of Chemistry, University of the Witwatersrand, Johannesburg. This work has not been previously included in a thesis or dissertation at any other institution for the same purpose or other qualifications.

04/03/2021

…….. ……

(Signature of candidate) Date

04/03/2021

…….. ……

(Supervisor) Date:

Dedications

This thesis is dedicated to my mother, Khubayi Emmelinah Mkhari, and my late father Madlayisani Jim Mkhari. I also dedicate this to my family (sisters, best friends, and my princesses): Tsakani, Ntavasi, Hakhensa, Shiluva, and Nyeleti Mkhari.

Ndzi khensa muvumbi wanga ndziri:

"Wena hosi, u mirisi wanga, ndzi nga ka ndzi nga pfumali nchumu. U ndzi fikisa emadyelweni ya rihlaza, undzi yisa ematini layo tenga. U hlayisa moya wa mina. U ndzi fambisa etindleleno leto lulama hikwalaho ka vito ra wena. Ni loko ndzi famba enkoveni wa xiyimo xo chavisa, andzi chavi nchumu xo biha, hikuva una mina. Undzi endlela nkhuvo valala vamina va langutile: u ndzi chela mafurha yo nun'hwela enhlokweni, ni ndzheko wa mina wa khapa. Ina vunene ni rhirhandzu ra wena swi ta ndzi sirhelela masiku hinkwawo yaku hanya ka mina, kutani ndzita ta tshama endlwini ya wena vutomi bya mina hinkwabyo."

Pisalema 23: 1-6

Acknowledgments

• I would like to acknowledge my supervisor, Dr. M.S Maubane-Nkadimeng for offering me the opportunity to work under her supervision. I will forever be grateful for your kindness and patience. Your everlasting guidance and suggestions have managed to make this project possible.

• A big thanks to Prof. N.J. Coville, your supervision, guidance, and scientific suggestions shaped my thesis and gave me hope. I will be forever grateful for your kindness, patience, and contribution throughout the project. I cannot express how grateful I am through wording; may God bless you with many more years to come so that other students can witness your wisdom and care.

• I acknowledge my co-supervisor, Prof. E.N. Nxumalo, you have been amazing throughout the project, and your scientific suggestions, guidance, and contributions have helped shape and give my writing direction. Thank you very much.

• I would like to express my warm hugs to my Wits buddy, M.Sc. Clinton Masemola may our friendship grow into family and partnership. Many thanks to Cdots/CNO's group, colleagues, and office mates for making the journey smooth. *Bra*. Themba Ntuli, Dr. Thomas Mongwe, Thapelo Mofokeng, Lerato Mokoloko, Alice Magubane, Dr. Pumza Mente, Dr. Victor Mashindi, Ludwe Sikeyi, and Thuli Buthelezi. I also acknowledge my friends from UNISA, Brian Chabalala, and Kgolofelo Malatjie.

• Amazing training and availability of characterization techniques from the Microscopy and Microanalysis Unit (MMU) at the University of the Witwatersrand. A very big thanks to all MMU staff.

• Catalysis and Materials group (CATMAT), thanks to everyone who shared their presentations, suggestions, and the wonderful meetings we had.

• Many thanks to Dr. Rudolph Erasmus (Raman, and Luminescence Laboratory, School of Physics, University of the Witwatersrand,). Petra Dinham, Technical Assistant, CHMT, Mokgaetji Angelina Monyai, Senior Environmental Technician, School of Chemistry, Mr. W. Jordaan of the National Metrology Institute of South Africa, Pretoria, and Rhandzu Rikhotso at the CSIR, Pretoria.

• I acknowledge the School of Chemistry and the Molecular Sciences Institute, and the University of the Witwatersrand at large, for granting me the opportunity and giving me access to your facilities.

• The National Research Foundation (NRF) and Department of Science and Innovation (DSI-NRF) Centre of Excellence in Strong Materials for funding and a travel grant award.

Publications, Presentations, and Awards

Publications

1. O. Mkhari, T.D. Ntuli, N.J. Coville, E.N. Nxumalo, M.S. Maubane-Nkadimeng. "*A comparison of fluorescent N-doped carbon dots supported on the surface of hollow and solid carbon spheres, and solid silica spheres.*" ***Diamond and Related Materials 118 (2021) 108500.***

2. T.D. Ntuli, T.H. Mongwe, L.L. Sikeyi, O. Mkhari, N.J. Coville, E.N. Nxumalo, M. S. Maubane-Nkadimeng. "*Removal of hexavalent chromium via an adsorption coupled reduction mechanism using olive oil derived carbon nano-onions*". ***Env Nano, Monitoring & Management 16 (2021) 100477.*** Contributions: Data curation, Formal analysis, Investigation.

3. O. Mkhari, T.D. Ntuli, L.L. Sikeyi, N.J. Coville, E.N. Nxumalo, M.S. Maubane-Nkadimeng. "*Microwave-assisted strategy for entrapping of carbon-dots made from glycerol and urea inside hollow carbon spheres*." ***To be submitted.***

4. O. Mkhari, T.D. Ntuli, K.I. Malatjie, L.L. Sikeyi, N.J. Coville, E.N. Nxumalo, M.S. Maubane-Nkadimeng. "*One-pot carbonization of chitosan into N-doped carbon-dots/chitosan nanocomposites for the adsorption of methyl orange from aqueous solution*." ***To be submitted.***

5. O. Mkhari, T.D. Ntuli, B.M Chabalala. L.L Sikeyi N.J. Coville, E.N. Nxumalo, M.S. Maubane-Nkadimeng. *"N-doped carbon dots decorated on the surface of TiO_2 for photocatalytic degradation of methyl orange from aqueous solution."* ***To be submitted.***

Presentations

• Poster presentation: *"Fluorescent properties of carbon dots supported on silica and hollow carbon spheres."* Microscopy Society of Southern Africa (MSSA) conference (2019), Cape Town (South Africa).

• Flash talk: *"Synthesis and loading of carbon dots inside/outside hollow carbon spheres."* 10^{th} Cross Faculty Postgraduate Symposium (2019), University of the Witwatersrand (Johannesburg).

• Poster presentation: *"Carbon dots supported on the surface of TiO_2, SiO_2, and HCSs for photocatalytic degradation of methyl orange."* IUPAC Post-Graduate Summer School on Green Chemistry (2019), Dar es Salaam, (Tanzania).

• Poster presentation: *Synthesis and loading of carbon dots inside and outside hollow carbon spheres: Application in photocatalysis."* 9th Cross faculty Postgraduate Symposium (2018), University of the Witwatersrand (Johannesburg).
• Poster presentation: "*Synthesis and loading of carbon dots inside and outside hollow carbon spheres: Application in photocatalysis"* South Africa Nanotechnology Initiative, SANi (2018), poster presentation, Durban (South Africa).

• Oral presentation: "*Hollow carbon spheres encapsulated with carbon dots for photocatalytic application."* Catalysis and Materials (CATMAT) group, School of Chemistry (2019), University of the Witwatersrand.

• Oral presentation: "*Synthesis, characterization, and incorporation of N-doped carbon dots on the surface of hollow and silica spheres."* Catalysis and Materials (CATMAT) group, School of Chemistry (2018), University of the Witwatersrand.

• Oral presentation: "*Synthesis of N-doped carbon dots from chitosan using autoclave reactor."* Catalysis and Materials (CATMAT) group, School of Chemistry (2017), University of the Witwatersrand.

Award

• Travel, training, and conference grant: Scholarship and fellowship holders. National research foundation (NRF), 2019. To attend the IUPAC Post-Graduate Summer School on Green Chemistry (2019), Dar es Salaam, (Tanzania).

Abbreviations

AC: Activated carbon

AOPs: Advanced Oxidation Processes

a.u: Arbitrary unit

BET: Brunauer-Emmett-Teller

ca: Approximately

Cdots or CDs: Carbon dots

Ch: Chitosan

CTAB: Cetyltrimethylammonium bromide

CVD: Chemical vapor deposition

FTIR: Fourier transforms infrared spectroscopy

FWHM: Full width at half maximum

H: Hours

HCSs: Hollow carbon spheres

HTC: Hydrothermal carbonization

I_D: Intensity of the D-band

I_G: Intensity of the G-band

ID/IG: The intensity ratio of D and G bands

MO: Methyl Orange

MW: Microwave

NCdots: Nitrogen-doped carbon dots

nm: Nanometres

PL: Photoluminescence

PLQY: Photoluminescence quantum yield

RF: Resorcinol-formaldehyde

SCSs: Solid carbon spheres

SEM: Scanning electron microscope

SSs: Silica spheres

TEM: Transmission Electron Microscopy

TEOS: Tetraethyl orthosilicate

TGA: Thermogravimetric analysis

TiO_2: Titanium dioxide

UV-Vis: Ultraviolet-Visible

VB: Valence Band

x-% loading = wt.%: Weight percentage

XPS: X-ray photoelectron spectroscopy

XRD: X-Ray diffraction

Abstract

Since the discovery of carbon dots (Cdots) in 2004, there has been an exponential increase in the number of research publications reporting on their synthesis, characterization, and potential applications. This is attributed to their excellent fluorescence properties which are central to potential applications in various scientific fields such as catalysis, nanomedicine, sensing and bioimaging, among others. However, issues pertaining to Cdots such as the origin of their fluorescent emissions, fluorescent quenching when in the solid-state, purification procedures (due to ultra-particle size ≤ 10 nm), and exploration of Cdots/support composites, among others still need to be addressed.

In this project, Cdots and nitrogen-doped Cdots (NCdots) derived from chitosan, glycerol, and urea were synthesized using a hydrothermal carbonization method in an autoclave (180 and 200 °C) and a microwave-assisted method (700 W). To obtain the NCdots in the solid-state, a systematic approach was established for the incorporation of the NCdots on the surface of a solid support such as silica spheres (SSs), hollow carbon spheres (HCSs), solid carbon spheres (SCSs), carbonized chitosan (CHIT-*x*h), and TiO_2 particles. A mixture of ethanol, water, and ammonia solution provided a medium for the good dispersion and incorporation of NCdots on the surface of the solid supports. The obtained NCdots were characterized using various techniques and were observed to have a typical size below 10 nm, spherical shapes, abundant functional groups, and enhanced fluorescent emission. The fluorescent emissions of the unsupported and supported Cdots were observed to be dependent on the excitation wavelength and exhibited a typical redshift as the wavelength was increased. In addition, the fluorescent emissions were influenced by the nature and interaction between NCdots and the support matrix. For example, the photoluminescence quantum yield (PLQY) of bare NCdots derived from chitosan was 34 %, while the supported NCdots PLQY values were dependent on the support with values in the order SSs (35.3 %) > HCSs (13 %) > SCSs (7.5 %) at 20 wt. % loading.

In addition, a “ship in a bottle” approach was used to contain the Cdots and NCdots nanoparticles derived from glycerol and urea inside the hollow cavity of HCSs via a microwave-assisted method. The solvatochromism of the encapsulated Cdots and NCdots revealed solvent-dependent characteristics when dispersed in water, hexane, and acetone. This suggests that the

surface functional groups of Cdots and NCdots are the prominent constituents responsible for fluorescent emission and interacted with the solvent via hydrogen bonding and/or dipole-dipole interactions, resulting in the tuning of the fluorescent emissions.

The composite materials consisting of NCdots, carbonized chitosan (CHIT-*x*h), and TiO_2 were explored for potential application in wastewater treatment via adsorption and photodegradation processes. For this, NCdots/CHIT-*x*h and NCdots/TiO_2 nanocomposites were prepared and used for the adsorption and photodegradation of methyl orange (MO) in an aqueous solution, respectively. These composites exhibited high MO adsorption and photodegradation efficiency which was attributed to the presence of NCdots on their surfaces. For example, the incorporation of 10 wt. % NCdots on the surface of TiO_2 was an optimum concentration that exhibited higher MO photodegradation efficiency compared to pristine TiO_2. This was attributed to photosensitization (photo-induced electron transfer process) and a synergetic effect between TiO_2 and NCdots. In both the adsorption and photodegradation studies, the MO removal/degradation efficiency was dependant on the initial pH, the concentration of the solution, and catalyst dosage. These composites have demonstrated a potential for application in the removal of MO from wastewater via adsorption and photodegradation processes.

Table of contents

Contents

List of figures

List of tables

Chapter 1: Introductory chapter

1. Synopsis

The images below show how poor handling of chemical processes in textile industries result in poor disposal mechanisms. This result in higher concentration of dyes in the environment and poses a challenge to the ecosystem. Safety and strict regulations are essential to monitor the dyeing processes and its disposal mechanisms.

Water treatments: photocatalysis/adsorption

Due to the colorful nature of dye solutions, water treatment processes such as photocatalysis and adsorption, among others have been used to remove/break-down dyes from wastewater. Although these processes have not gained a significant commercial value, they form a core as a potential mechanism for the treatment of dyes from wastewater. Hence, there is a need for the advancement of these processes through scientific research and sufficient documentation is ideal.

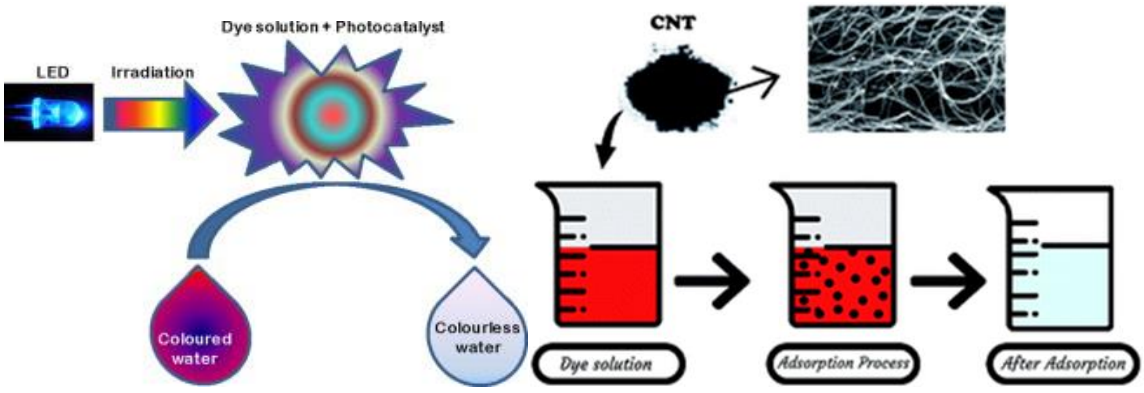

It is mostly said that “water is life”, the truth is “clean and drinkable water is life” and the bar for providing clean water to every household is a prerequisite. The image below signifies how clean and drinkable water puts a smile on a person. Thus, this project is aimed at reflecting on how strategies such as adsorption and photocatalysis can be used to remedy dye contaminants from wastewater.

 [1,2,3,4,5]

1.1 Introduction

Clean water and drinkable water is essential for the well-being of humans, animals, and a sustainable ecosystem.[6,7] The shortage of water due to poor rainfall and mismanagement of water on a global scale can cause social, economic, and environmental problems.[6,8,9] In 2015, the world health organization reported that approximately 663 million people lack access to clean drinking water in various parts of the world.[10] Globally, a significant number of people succumb to death and disability-adjusted life years due to lack of clean water access and poor sanitation infrastructure each year.[11] South Africa is considered one of the water-stressed countries with uneven distribution of water among racial groups and also between urban and rural communities.[12,13] To avoid water-related deaths and sickness, adequate amounts of clean water should be provided to humans for consumption, cooking, personal and household hygienic needs.[14,15] With only 1 % of freshwater available as groundwater for human use, it is of great concern that water contamination by agricultural activities, industries, human effluents, and other human activities is on the rise and a need for alternative water resources is in demand.[16] In addition, the world population is expected to be around 10 billion between the years 2035 and 2040, and this calls for adequate and sustainable methods to deal with the already existing water crisis.[7]

Among the toxic chemicals that are released from textile industries, dyes are one of the major concerns due to their hazardous nature and a threat to the ecosystem.[17-18] Annually, about 700 000 tons of dyes containing several organic compounds are produced from textile industries, of which 1-20 % in the world are released as effluents and end in wastewater or the environment.[19,20] The classification of dyes takes into consideration their method of application, colour, and structure. For example, azo, nitro, anthraquinone, nitroso, and indigoid dyes are classified based on the chromospheres present in the dye. Of these dyes, azo dyes are the major class that constitutes between 60-70% of all dyes in the textile industry.[21,22] Due to their chemical stability and lightfast properties, they are mainly used as coloring agents in the textile, leather, and paper industries.[23] However, an estimate of 50 % of the azo dyes are not strongly bound to their substrates, and as a result, these dyes are discharged as effluents that end up in the environment and contaminate water.[23] Dye stability causes slow biodegradability which leads to difficulties in degrading the dyes using the current conventional water purification methods.[24] As a result, dyes became common pollutants in water and are usually found in small and undesirable amounts which are highly visible in the water.[25] This in turn causes serious health problems for aquatic animals and humans because they are non-biodegradable, toxic, and can accumulate into water streams and affect water quality.[18] Their toxicity can result from the original dyes and/or its metabolites that are generated when the dye is broken down. Aromatic amines released by the transformation of azo dyes by either dermal or systematic bacterial biotransformation can be absorbed by the skin and can cause mutagenic and carcinogenic effects. In addition, aromatic amines can generate reactive hydroxylamine intermediates which can damage DNA and proteins depending on the metabolic activation of the amino group that it contains.[21] Metabolites such as aryl-amines and free radicals can also be generated and easily be integrated into the food chain.[26] In addition, the colorful nature of dyes can prevent sunlight penetration and oxygen dissolution in water affecting photosynthesis processes for aquatic species.[24] These pose a threat not only to humans but to most mammals and the ecosystem at large.[26,27]

Methyl orange (MO) as our model dye falls under the classification of an azo dye and it is one of the dyes that gets discharged into water streams from various industries. It is water-soluble and mainly found and discharged from textile, food, pharmaceutical, printing, and paper manufacturing industries.[28] As an azo-dye, MO contributes significantly as an organic contaminant in the environment. It has many undesirable drawbacks and affects the ecosystem even at low concentrations due to its undesirable visibility.[29,30] Its chemical structure is shown in figure 1.1 Its carcinogenic and mutagenic effects can result either from its original form or

from its metabolites such as 2-*N, N*-dimethyl aniline diazine, 4-hydroxy-[methanol methyl]-amino azobenzene, *N*-methyl aniline, and [4-hydroxy diazinyl]-3-hydroxy benzene sulphonate. Hence its complete mineralization is essential before its disposal.[31]

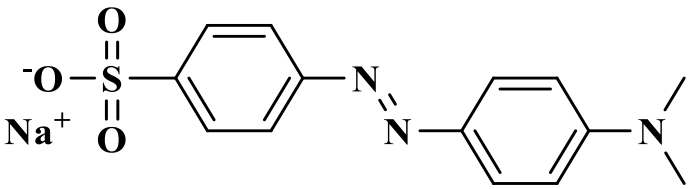

Figure 1. 1 Chemical structure of methyl orange.

1.2 Problem statement

In an attempt to mitigate the removal of contaminants from water, various methods such as oxidation, reduction, bioremediation, reverse osmosis, electrochemical treatment, coagulation, lime softening, precipitation, membrane filtration, ion exchange, and adsorption have been explored.[32,33,34] Although most of these methods are effective for the removal of dyes from wastewater, there are several drawbacks still to be addressed in their use. These range from upscaling cost-effectiveness, selectivity, sludge generation (secondary waste generation), process complexity, and the long time required for use in the removal operation.[35,36] As such, effective and efficient methods to deal with water contamination from industries and human activities need to be addressed urgently.

Adsorption processes have been used for centuries to separate substances of one phase by which an adsorbate accumulates on the surface of the adsorbent. The adsorption method is superior to other wastewater treatment techniques owing to its simplicity of design and operation, insensitive to toxic chemicals, and does not generate undesirable by-products. However, factors such as generation of secondary pollutants, selectivity, regeneration of the adsorbent have been encountered. For example, activated carbons (ACs) have been widely used for adsorption or removal of various types of emerging compounds, however, drawbacks such as cost, and regeneration limit their use.[37] Hence, an adsorbent that occurs naturally, is cheap, easy to regenerate, and can adsorb emerging pollutants is essential. Another superior method that is used for the removal of toxic compounds in wastewater is the advanced oxidation process (AOPs) such as photocatalysis.

Photocatalytic degradation has emerged as one of the effective solutions to remedy the environmental concerns resulting from the presence of organics, including dyes, that contaminate water.[20,38] Photocatalysis is defined as the use of light energy together with a photocatalyst, which absorbs an energy package that is equal to or higher than its band structure to speed up a chemical reaction.[39,40] In the past several years, titanium dioxide (TiO_2) has been the most used catalyst (photo-catalyst) for breaking down toxic organic molecules from wastewater.[41] Compared to other photocatalysts such as ZnO, WO_3, CdS, SnO_2, and SiO_2, TiO_2 has shown the greatest potential as a photocatalyst for breaking down organic contaminants. The outstanding advantages of TiO_2 as a photocatalyst are demonstrated by its properties such as its indirect smaller bandgap (3.2 eV), chemical stability, high reactivity, porosity, natural abundance, low cost, low toxicity, high surface areas, and broad absorption spectrum with high absorption coefficients.[42,43] However, the use of TiO_2 and its constituents as photocatalysts have several drawbacks ranging from, (i) an inability to utilize enough of the solar spectrum energy (only can use of up to 5 % of the solar spectrum), (ii) fast electron-hole pair recombination, (iii) agglomeration of the TiO_2 nanoparticles and (v) its recovery for reuse which limits its potential application for photodegradation processes.[44,45] To counteract the drawbacks faced by TiO_2 photocatalysts, metal and metal oxides such as Sc, Gd, Ho, Ce, Fe, Al, Ga, In, Pb, SnO_2, Bi, B, Si, and Ge have been used to improve its photocatalytic activity.[25] Furthermore, non-metal dopants such as C, N, and S have been used to improve the photocatalytic activity of TiO_2, i.e. N is known to increase the catalyst activity toward visible light, and changes the TiO_2 hardness, refraction index, elastic modulus, and electronic conductivity.

On the other hand, C as a dopant can narrow the bandgap, increase the surface area, and introduce new electronic states (C 2p) close to the valence band (VB) of TiO_2 (O 2p).[25] Carbon materials such as carbon nanotubes [46,47], single-walled carbon nanotubes [48], graphene [49], carbon nanotube-modified-Ag-TiO_2 [50], granular activated carbon [51], and other carbon allotropes have been used to modify TiO_2. A catalyst composite consisting of multiwall carbon nanotubes (MWCNTs) and TiO_2 prepared via reflux was used for MO degradation by Saleh et al. After 100 min, the MWCNT/TiO_2 composite reached 93 % degradation while TiO_2 alone gave 65 % degradation. The increase in MO degradation was attributed to the synergetic effects whereby the MWCNTs acted as an adsorption trap of the dye, which enhanced the photocatalytic degradation activity.[52] Zhang et al. demonstrated the use of a TiO_2-supported activated carbon (TiO_2/AC) composite under microwave irradiation for use in the photodegradation of MO. It was concluded that supporting TiO_2 on AC (under microwave irradiation) exhibits several

advantages such as higher degradation, no residual intermediates, and complete mineralization of MO.

Although doping or addition of carbon co-sorbents improves the photocatalytic activity of the TiO_2, drawbacks such as thermal instability, partial active sites blockage, visible light utilization, and faster recombination of photogenerated electron-hole pairs have been encountered.[25] In addition, the availability of carbon sources (e.g. AC), complex synthesis procedures, use of hazardous chemicals (strong acids), and cost-effectiveness limit their large-scale implementation. Hence, a highly available source of carbon is needed, and the use of harsh chemicals should be avoided. In this study, the focus is given to the utilization of carbon dots (Cdots) to improve the photon absorption and photocatalytic activity of a TiO_2 photocatalyst, while avoiding the use of harsh chemicals and utilizing the abundant carbon source (chitosan, CHIT. In addition, we explore the multipurpose use of chitosan as an adsorbent and support.

1.3 Motivation

Among the family of nanostructured carbons, carbon dots (Cdots) have demonstrated several advantages and unique properties such as luminescence, inexpensive preparation, low toxicity, diverse intrinsic electronic and magnetic properties, chemical diversity, higher electron transfers, and biocompatibility.[53,54] The broadband light absorption of Cdots can be used to mitigate the light sensitivity of (or to sensitize) TiO_2, which can then improve its photocatalytic activity.[54,55] In addition, the surface functional groups (i.e. N, O,) and their small particle sizes of Cdots can be used for the adsorption of dyes from wastewater and/or as electron traps to enhance the photocatalytic activity of TiO_2. Several reports have described the use of Cdots as a carbon co-sorbent to enhance the photocatalytic properties of TiO_2 toward dyes and organic degradation.[54,56,57] These was attributed to a (i) synergetic effect between Cdots and the photocatalyst, (ii) Cdots PL up-conversion of lower energy to higher energy photons which can be utilized by TiO_2, (iii) photo-induced electron transfer from Cdots to TiO_2, and (iv) good adsorption affinity of dyes by Cdots, which resulted in increased photocatalytic activity.

Although Cdots have demonstrated outstanding properties, their drawbacks such as an effective purification method, agglomeration in their solid-state, and the origin of its fluorescent properties are still not fully understood.[58] Cdots supported on various surfaces have been investigated and this approach can be used to mitigate the above-mentioned drawbacks. It was noted that supporting Cdots can improve properties such as adsorption, surface area, light

capture, electron transfer, and can introduce new functional groups that influence the Cdot/support interactions.[59] Several studies have shown that supporting Cdots on various solid supports such as silica, carbon nanotubes, cytopore, polymers (e.g. PVA), solid and hollow carbon materials can improve properties such as adsorption, fluorescence, and many other properties as compared to the unsupported Cdots.[60,61]

This supporting material could be used in various applications such as adsorption and imaging, photocatalysis, sensing, and many others.[62] Hence, the use of supports as an approach to improve the properties of Cdots and the support has formed a central motivation to this study. Therefore, the basis of this study is to support Cdots (synthesized from chitosan, glycerol, and urea) on various supports for use in adsorption, photocatalysis and to demonstrate how the support can influence the fluorescent properties of the Cdots. The supports that will be used in this project are silica spheres, TiO_2, solid and hollow carbon spheres, and carbonized chitosan.[63,64] These supports have received consideration because of their unique structures and functional behaviour such as their high specific area, low specific density, large controllable inner pore volume, good conductivity and good mechanical strength, easy functionalization, and good biocompatibility.[63,65,66] We can hypothesize that supporting Cdots on the above-mentioned solid support will modify and hopefully improve the fluorescent, adsorption, and photocatalytic properties of the Cdots/support composites.

1.4 Aim and objectives of the study

The aim of the study is: To synthesize, modify and investigate the feasibility and applicability of carbon dots supported on silica spheres, solid and hollow carbon spheres, anatase TiO_2, and carbonized chitosan for enhancing the optical and adsorption properties of the composite materials for application in photodegradation and the adsorption of methyl orange in an aqueous medium.

Objectives of the study are to:

i. Synthesize and characterize nitrogen functionalized Cdots derived from chitosan, glycerol, and urea using hydrothermal carbonization and microwave-assisted methods.

ii. Synthesize silica spheres (SSs), hollow carbon spheres (HCSs), solid carbon spheres (SCSs), carbonized chitosan (CHIT-*x*h), and TiO_2 particles and use them to support NCdots.

iii. Investigate the effect of solid support and solvents on the optical properties of NCdots supported on the surface of SSs, SCS, HCS, CHIT-*x*h and TiO_2.

iv. Investigate and monitor the effect of NCdots on the surface of Ch and TiO_2 particles toward the adsorption and photocatalytic degradation of methyl orange in an aqueous medium, respectively.

v. Study and evaluate the effect of the initial dye concentration, pH of the solution, time, and catalyst dosage toward the removal of methyl orange from aqueous medium via adsorption and photo-degradation using NCdots/CHIT-*x*h and NCdots/TiO_2 composites.

1.5 Arrangement of the thesis

The thesis consists of seven chapters, the first two chapters contain an introduction and a literature review, respectively. Four main chapters present the work done in this project with each chapter containing a background, methodology, results, and discussions section, followed by a summary. The last chapter, which is chapter 7 consists of the overall summary of the project, recommendations, and future perspectives derived from the research. Thereafter, the appendix of the main chapters is given which is followed by references used in the entire project.

C**hapter 1:** This chapter highlights the research background, problem statement, justification, and aims and objectives of the study.

Chapter 2: Here, an insightful literature review that relates to the project is given. The chapter highlights the challenges related to water contamination, with particular emphasis on azo dyes. This expands to heterogeneous photocatalysis and adsorption processes as a means for reducing dyes from wastewater. Thereafter, a review on carbon-based nanomaterials and their fascinating characteristic properties is summarized with emphasis given to the newly discovered carbon-based nanomaterial called carbon dots and their composite materials.

Chapter 3: This chapter presents the study on the synthesis of nitrogen-containing Cdots, using chitosan as both nitrogen and carbon source, via a hydrothermal method. Due to the hygroscopic nature of Cdots, a systematic strategy to incorporate the NCdots on the surface of solid supports such as SSs, HCSs, SCSs is presented. Furthermore, the fluorescence emission of the obtained solid-state NCdots/support composites was explored.

Chapter 4: In this chapter, a microwave-assisted method is used to synthesize Cdots and NCdots inside hollow carbon spheres. The "ship-in-a-bottle" approach is used to diffuse small carbon molecules of glycerol and urea inside HCSs and use them to synthesize Cdots and NCdots inside HCSs cavities. Glycerol serves as a carbon source while urea provides both carbon and nitrogen groups. Thereafter, the solvatochromism of the Cdots@HCSs and NCdots@HCSs composites using three different solvents was explored.

Chapter 5: Here, the hydrothermal method is used to convert chitosan into a carbonized hydrochar consisting of NCdots and carbonized chitosan. The well-structured NCdots/carbonized-chitosan composite is realized and stabilized for use in the adsorption of methyl orange from an aqueous medium. The optimum conditions for methyl orange removal are explored using the batch adsorption method.

Chapter 6: In this chapter, a study on the destruction of methyl orange using a NCdots/TiO_2 composite under visible light is investigated. The nitrogen-doped Cdots derived from chitosan are aimed at the photosensitization of TiO_2 to induce its photocatalytic activity. Various amounts of the nitrogen-doped Cdots were incorporated on the surface of the photocatalyst.

Chapter 7: Here, the outcome of the thesis, its detailed conclusions, a summary, and finally the recommendations and the future perspectives are highlighted. Thereafter, appendix and references used in the project are given.

Chapter 2: Literature review

2.1 Water shortage

Globally, the shortage of freshwater has demonstrated a huge impact on social and economic developments and other activities, especially in developing countries.[9,15] With an estimate of about 10 billion people expected in the world in the next two decades, access to uncontaminated and clean water is expected to rise.[7] The United Nations Millenium Development Goals (MDGs) has stipulated that the number of people without sustainable water supply will be reduced by half by the year 2015.[15] This stipulation was not achieved since many people live without a sustainable water supply, hence it is essential to implement new strategies to improve the supply of clean and uncontaminated water, especially to disadvantaged or developing countries.[15] For example, during the COVID-19 pandemic (figure 2.1), in South Africa, Ximausa village outside of Giyani in the province of Limpopo under Mopani district experienced a significant water crisis in which people were forced to share water with cattle and other animals from the river streams.[67] The desperate plea for water from Ximausa residents reached ministerial level after families were left to dig at a dry riverbed, defying nationwide lockdown regulations. The supply of clean and uncontaminated water needs to be addressed both locally and internationally.

Figure 2.1 Ximausa residents in Limpopo left to dig in a dry riverbed for water. (Eyewitness News, COVID-19): https://ewn.co.za/2020/04/17/covid-19-ximausa-residents-in-limpopo-left-to-dig-in-dry-riverbed-for-water.[68]

With only 3 % water available as fresh water and only 1% of freshwater available as surface water (river and lakes) for daily use, water contamination should be minimized or completely avoided.[69] Water contaminations from traces of heavy metals and toxic organics from various industries, pharmaceuticals, and personal care products is on the rise. Although these contaminants have drawn significant attention due to their potential environmental and health impact, little is being done to address their disposal mechanisms.[70] Dyes have become one of the most prominent contaminants found in water streams and the environment. So far, scientific research remains central in providing a means to explore issues surrounding the removal of toxic contaminants from water streams and the environment, which also provide a basis for disposal regulations.

2.2 Water contamination by dyes

Dyes and dyestuffs are a class of colorants and soluble pigments that are used in dyeing/textile industries to colour objects by using physical or chemical methods. The dyes waste is exponentially on the rise as a major water contaminant.[71] Studies have shown that an increase in the organic compounds from textile dyes and other industrial dyestuffs pose an environmental concern.[72,19] It is estimated that about 70, 000 tons of dyes are produced every year for use in industries such as textiles, cosmetics, paper, leather, pharmaceuticals, and nutrition.[72,19] In textile industries, 1-20 % of the dye is lost during the dyeing process and ends up in the environment and water streams. This has led to undesirable trace concentrations of dyes that are sometimes visible in the water streams and environment. They also pose a serious concern to both humans, aquatic animals since exposure to dyes can negatively affect the ecosystem.[20,25]

The effluents from textile industries pose a big concern to many countries, including South Africa.[73] Of all the synthetic dyes such as direct dyes, processing dyes, and reactive dyes that are used in textile dyeing processes, azoic dyes constitute about 65 % of the total synthetic dyes produced every year.[24,17] Structurally, azo dyes consist of a nitrogen-to-nitrogen double bond (N=N) with two side moieties of/or two aromatic groups such as benzene and naphthalene rings. Some of the azo dye structures, viz. methyl orange, acid orange 7, methyl red, disperse red 1,

amaranth, chrysoidine, amido black, and tartrazine are shown in figure 2.2.[24] Depending on the number of azo bonds present in the dye molecule/structure it can be classified as mono-azo, di-azo and tri-azo (table 2.2). Due to a low interaction between azo dyes and the substrate to be colored, about 50 % of a dye molecule is weakly bound to the substrate which usually gets discharged as an effluent after the dyeing processes.[23] As a result, azo dyes have become a common pollutant in water and are usually found in small and undesirable quantities.[25] Several reports have demonstrated that dyes are carcinogenic and mutagenic to humans or mammals.[18]

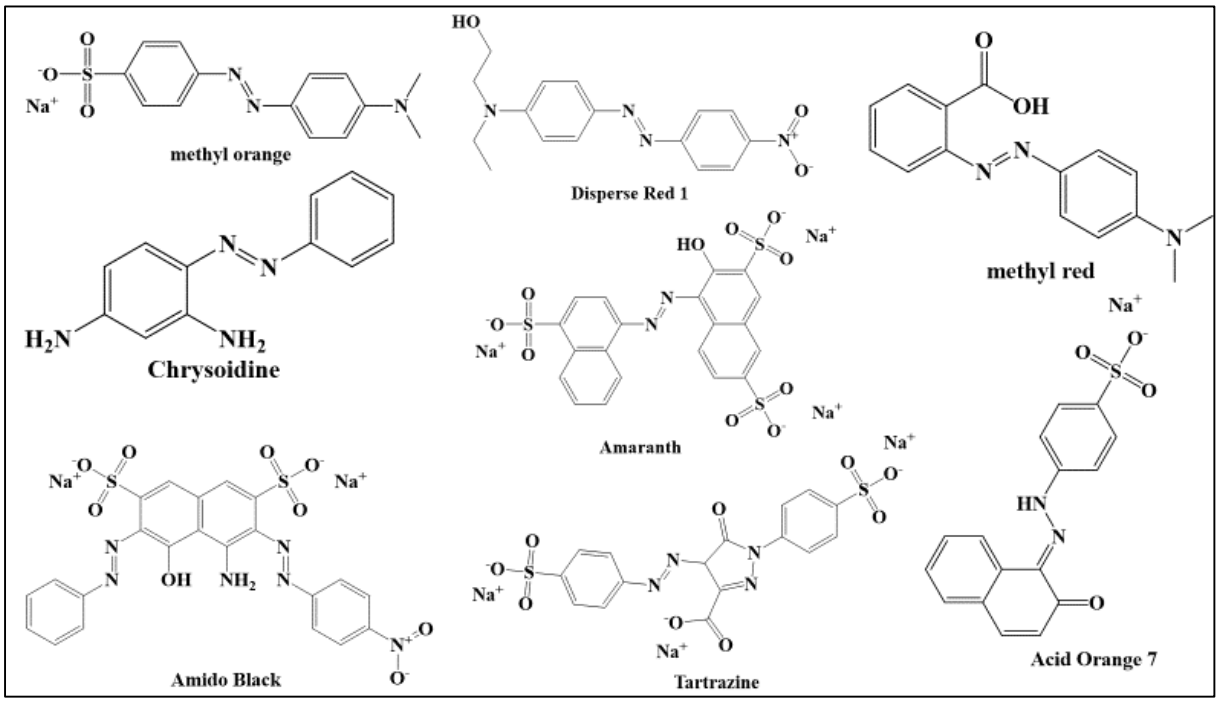

Figure 2.2 Structures of azo dyes; methyl orange, acid orange 7, methyl red, disperse red 1, amaranth, chrysoidine, amido black and tartrazine.[24]

Table 2.1 Classification of azo dyes depending on the number of bonds present within the dye structures.[71]

Class	Dye name	Dye structure
Mono-azo	Acid red 88	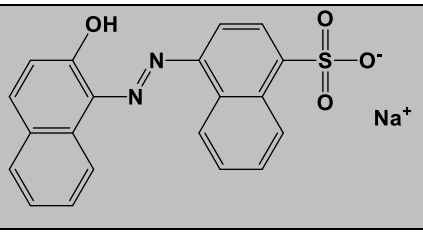

Di-azo	Acid black 1	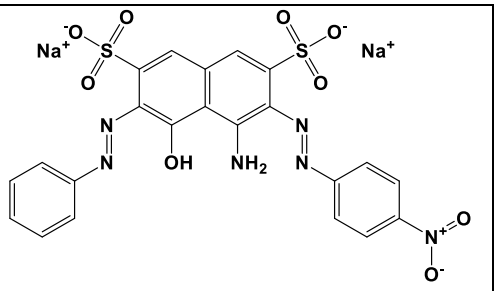
Tri-azo	Direct blue 71	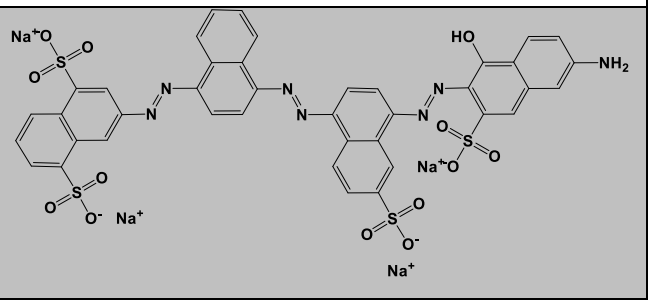

Their toxicity can result from the original dyes and/or their metabolites that are generated when the dye is broken down. Aromatic amines released by the transformation of azo dyes by either a dermal or systematic bacterial biotransformation can be absorbed by the skin leading to mutagenic and carcinogenic effects. These aromatic amines can generate reactive hydroxylamine intermediates which can damage DNA and proteins depending on the metabolic activation of the amino group it contains.[21] Metabolites such as aryl-amines and free radicals can be generated and can be accumulated in food chains.[26] The effect of this aromatic amine transformation, when in contact with sweat, saliva, or gastric juices, still needs to be addressed.[26,27] In addition, the colorful nature of dyes can prevent sunlight penetration and oxygen dissolution into the water which affects aquatic life.[24] Hence, there is an urgent need for an adequate method to deal with dye disposal, handling, and removal from water streams and the environment.

2.3 Water treatment strategies

Although regulations and laws exist for the control, disposal, and handling of chemical waste from industries, much waste still finds its way into the environment. Currently, the biological treatment of dyes is used to remove effluents from the dyeing industries, however, most of the dyes are not biodegradable.[17] This method and other water treatment strategies such as bioremediation, reverse osmosis, electrochemical treatment, coagulation, precipitation, membrane filtration, ion exchange, and oxidation are not sufficient to remove or to biologically degrade dyes completely due to factors such as dye stability, upscaling cost, generation of

secondary waste, among others.[22,] A mechanism or strategy that can effectively eliminate dyes and other chemical waste at low cost is essential and urgently needed.

Adsorption is one of the most feasible method for wastewater treatment due to factors such as simple to operate, non-selectivity toward water contaminants, easy recovery, cost-effective, and high efficiency, among others.[74] Its cost-effective emanates from abundant natural occuuring adsorbents such as leaves, seeds, clay minerals, fungi, fly ash, fibers, barks, and other biomass.[75] A good adsorbent should have a higher surface area, good stability, compatibility, higher adsorption capacity and should be easily accessible. Although adsorption is deemed as a feasible method for wastewater treatment, drawbacks such as generation of secondary pollutants, selectivity, and activation of adsorbent are encountered. In addition, pre-treatment methods such as extrusion, grinding, acid activation, thermal activation, hydrothermal treatment, among others are necessary for the adsorbent to be highly effective.[76]

Among these factors, operation parameters such as pH, contact time, adsorbent dosage, initial dye concentration, and experimental setup are crucial in adsorption processes.[77] The initial pH of the solution plays a crucial role in adsorption, for example, at acidic pH the surface of the adsorbent will be protonated and thus the surface will be positively charged and will be effective for adsorption of anionic dyes due to favored electrostatic attraction between positively charged surface groups of the adsorbent and anionic dye molecules.[78] The effect of contact time can be used to determine the adsorption kinetics and a shorter contact time reflects on the economic efficiency of the process, while optimum adsorbent dosage provides sufficient adsorption sites for dye molecules to adsorb. Initial dye concentration and experimental setup are very important, these factors can be used to reduce operation time and efficiency of the adsorption process.[79] Thus, investigation of optimum operation conditions is crucial for the adsorption process to be effective.

One of the promising ways to deal with organic contaminant removal is the advanced oxidation processes (AOPs). AOPs such as heterogeneous photocatalysis has been demonstrated to be very useful in the removal of dyes from aqueous solution due to their ability to generate highly reactive radicals which facilitate the destruction of toxic organic/dye pollutants into less harmful substances or preferably to their complete mineralization into the water, carbon dioxide and mineral acids.[20,25] TiO_2 (titania) is the most widely documented semiconductor used for

photo-induced processes. This is due to properties such as higher chemical and physical stability, optical and electronic stability, biocompatibility, and cost-effectiveness.[70]

Although anatase TiO_2 has shown an outstanding performance toward the degradation of a wide range of gaseous and liquid pollutants, its photocatalytic activity is limited because it requires UV light (about 5 % of solar energy) to be active as a photocatalyst. Other disadvantages such as fast electron-hole pair recombination rate and lower interfacial charge-transfer rate of the photogenerated carriers have been noticed.[25] These have led to many researchers working on stimulating the utilization of solar energy by TiO_2 by manipulating its bandgap and its sensitization to visible light. Which have been achieved by various synthetic strategies: novel starting materials, doping with hetero-atoms to keep the electron-hole separated, supporting TiO_2 on various surfaces, and forming composites with other materials. In addition, operating parameters such as the pH of the contaminant and catalyst solution, oxidizing agent, catalyst calcination temperature, dopant content, and catalyst loading have all been found to influence the photocatalytic degradation processes of dyes in wastewater.[72]

TiO_2 has been doped with metals such as Sc, Gd, Ho, and Ce to prolong the electron-hole pairs. Doping with a transition metal such as Fe, Co, Ni has been reported to improve the stability of the photogenerated electron-hole. While noble metal doping can increase reactive sites, it also can cause phase transformation from anatase to rutile and improve electron-hole pairs separation. Other metals such as Al, Ga, In, Pb, etc. can also improve the photocatalytic activity, e.g., doping with SnO_2 and Bi can increase the number of generated hydroxyl radicals and the narrow bandgap, respectively. While doping with metalloids such as B, Si, Ge, and As, can also improve photocatalytic activity, e.g., B was found to promote a phase transformation from brookite to anatase while it also retarded grain growth and caused a redshift absorption.

Furthermore, non-metal dopants such as C, N, and S also improve photocatalytic activity, e.g. N is known to increase the catalyst activity toward visible light, changes hardness, refractive index, elastic modulus, and electronic conductivity of TiO_2. Carbon as a dopant can narrow the bandgap, increase surface area, and introduce new states (C 2p) close to the VB of TiO_2 (O 2p). Although doping improves the photocatalytic activity of the TiO_2, drawbacks such as thermal stability, partial active sites blockage, visible light utilization, and faster recombination of photogenerated electron-hole pairs have been encountered. In this study, the focus is given to the utilization of carbon as a primary element to improve the light sensitivity and photocatalytic activity of an anatase TiO_2 photocatalyst. It is worth stating that the carbon will be used to form composites with TiO_2 (NCdots/TiO_2 composites) rather than to dope the TiO_2. To date, various

carbon materials such as carbon nanotubes, graphene, activated carbon, and other carbon derivatives have been used to stimulate TiO_2 sensitivity toward light capture, reduce electron-hole recombination, and for narrowing of its bandgap.[55] Therefore, the use of carbon-based materials as co-sorbent to improve photocatalytic properties of TiO_2 should be explored.

2.4 Background on carbon-based nanomaterials

Carbon is one of the most common and essential elements that have been explored and continue to be explored and applied in numerous scientific fields.[80] Carbon can form strong carbon-carbon bonds giving rise to various oligomers, polymers in numerous dimensions to having different structures.[81,82] The discovery of structured carbon materials can be traced to the ancient era, with graphite and diamond being the first allotropes of carbon to be discovered. These were later followed by the discovery of fullerene in 1985 by Kroto, Rice, and Smalley as a new allotrope of the carbon family.[83] Thereafter, a report of another carbon allotrope named carbon nanotubes (CNTs) was described by Sumio Iijima and co-workers in the early 1990s.[84]

Carbon as a nanomaterial has led the nanotechnology revolution. Different structures of the carbon materials (graphite, diamond, graphene, and CNTs) are shown in figure 2.3 and are described below. The highest *hierarchy* of all carbon materials is ‘‘graphite’’ which was given its name by Abraham Gottlob Werner in 1789, it consists of carbon atoms that are connected in the shape of hexagons into a huge flat network that are stacked on top of each other. The American scientist, Edward Acheson was the first scientist to produce graphite in 1896. Graphene, a single layer of a graphite sheet in a two-dimensional arrangement consists of sp^2 hybridized carbon atoms that are covalently bonded together to form a honeycomb flat structure. The structure was explored theoretically in 1947 with its exploitation started in 2004 after its synthesis at the University of Manchester by Geim and Novoselov.[85,86]

The other historically important carbon material is diamond. A diamond can be described as an interconnected amorphous carbon material (comprising of only sp^3 carbon atoms).[80] Since then, many other carbon structures such as carbon nanotubes (CNTs) which comprise of two classes known as single-walled carbon nanotubes (SWCNTs) and multi-walled carbon nanotubes (MWCNTs). In SWCNTs, a single layer of graphene sheet is rolled into a tube, while MWCNTs are formed by an array of single-wall carbon nanotubes which are concentrically placed inside each other.[87] Another important carbon material is the fullerenes (bulky-ball). This can be described as a carbon material that resembles a hollow sphere with various sizes and shapes similar to soccer ball.[85]

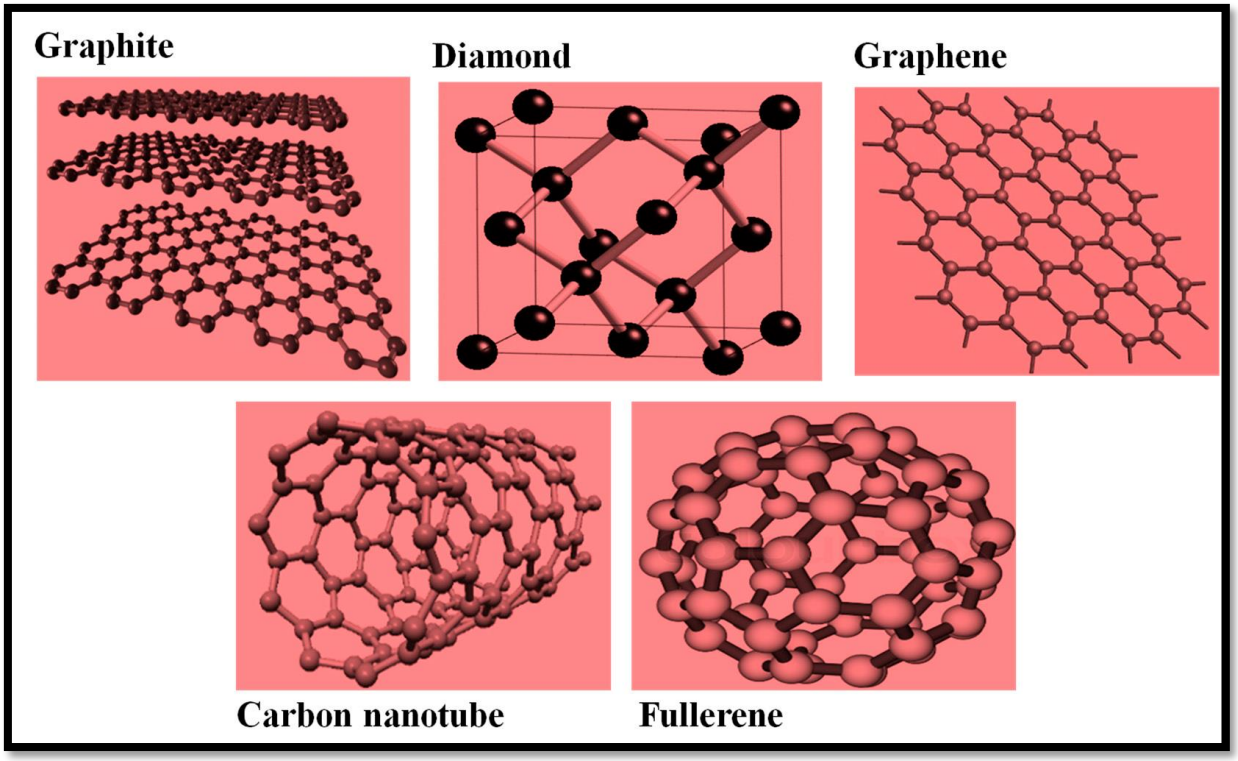

Figure 2.3 Structures of carbon-based nanomaterials or allotropes of carbon: graphite, diamond, graphene, carbon nanotube, and fullerene.[85]

These carbon nanomaterials (fullerenes, carbon nanotubes (CNTs), and graphite/graphene) have mesmerized both academic and industrial researchers. They play a significant role in the field of nanoscience and nanotechnology.[88] Their fascinating properties such as high surface area, mechanical stability, high electrical conductivity, and flexibility have led to their application as electrodes, catalysts, catalyst supports, adsorbents, and gas sensors.[89] With scientific endeavors shifting toward designing structured nanomaterials, it will be very beneficial to put more effort into designing, characterizing, and initializing the potential application of carbon-based nanomaterials. Due to the natural abundance of carbon sources its nanoscale exploration is investible and beneficial.

2.4.1 Quantum dots

‘‘There’s plenty of room at the bottom’’, these were famous words spoken by Nobel Laureate and quantum theorist, Richard Feynman at a talk given in 1959. In his talk, he introduced the concept of nanotechnology which later opened and created numerous advances and opportunities in science and technology. A nanomaterial can be defined as any material having a size below 100 nm in one of its dimensions. Importantly, the discovery of quantum dots at the

end of the 1970s played a major role in downscaling of structured nanomaterials. Quantum dots are materials (semiconductor particles) having a few nanometres in size with optical and electronic properties that differ from larger particles due to quantum effects. Various inorganic quantum dots such as CdSe, CdS, CdTe, PbS, and SiO_2 have been made to date.[90]

Of our interest, is the carbon dots or carbon quantum dots which can be defined as zero-dimensional (spherically shaped and having a size range below 10 nm) carbon-based nanomaterials, see figure 2.4. There are three kinds of carbon quantum dots and these can be grouped into polymer dots (primarily consisting of π-conjugated polymers),[91] graphene quantum dots[92] (primarily of one or few layers of graphene with lateral dimension being larger than their height), and lastly carbon nanodots or carbon dots which are sphere-like carbon nanomaterials.[93,94] Carbon dots are the main focus of this project and a reflection on their discovery, synthesis, drawbacks, and their fascinating properties with a possible potential application is outlined.

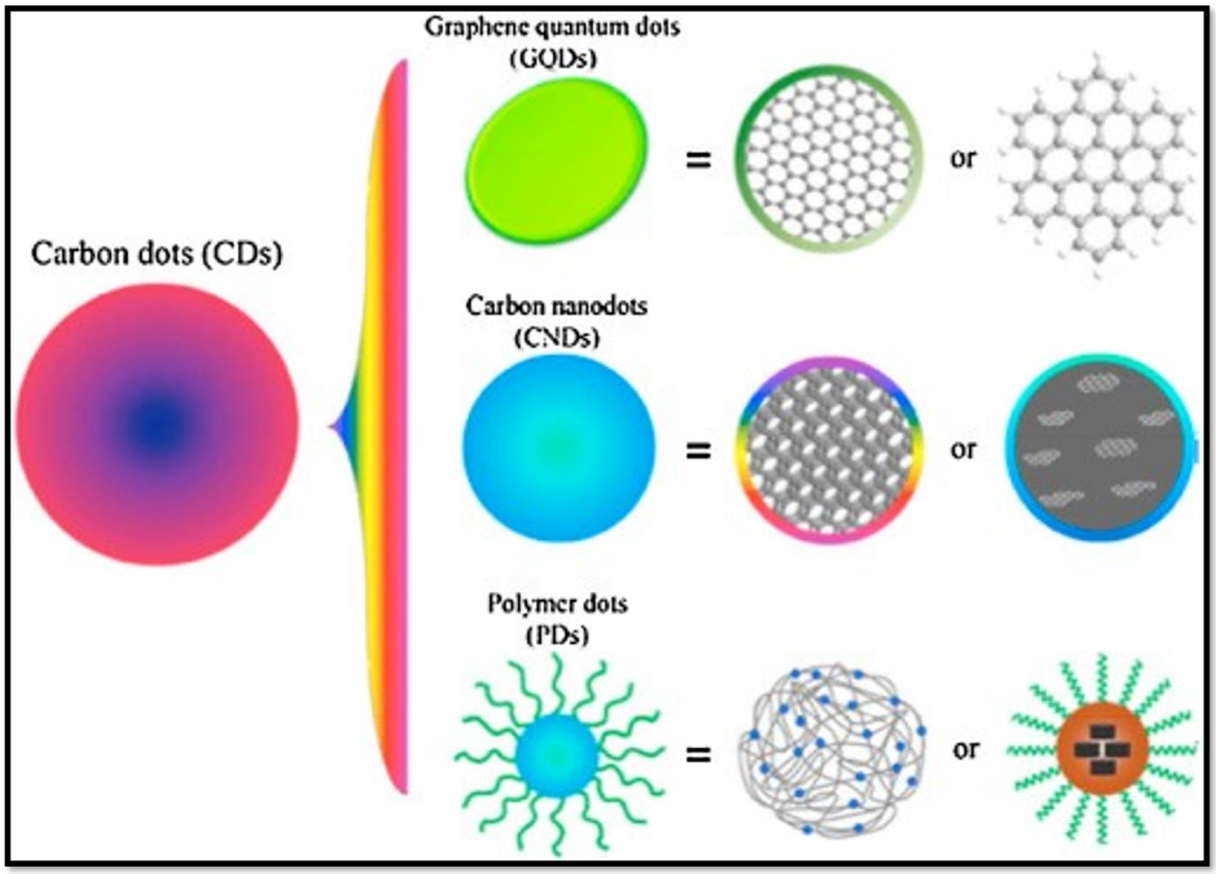

Figure 2.4 Types of carbon dots: graphene quantum dots, carbon nanodots, and polymer dots.[95]

2.4.2 Carbon dots

Carbon dots (Cdots) are one of the newly discovered structured carbon-based nanomaterials with zero dimension. Cdots are small carbon nanoparticles (diameter ≤ 10 nm)[96] with the particle surface functionalized by organic molecules or coated with polymers or other species.[97,98] Since their discovery, Cdots have drawn tremendous attention as a new member of the carbon nanomaterial family.[99] They were accidentally discovered by Xu et al. in 2004 during the synthesis of carbon nanotubes through electrophoresis.[100] They were first identified as carbon nanoparticles and later called Cdots, with similarities to the well-studied inorganic quantum dots and structurally related to graphene quantum dots. Recently, exponential growth in scientific articles published with Cdots has been experienced due to their fascinating properties and promising applications.[53]

Structurally, Cdots are presumed to be spherical carbon aggregates with carbon, oxygen, and hydrogen as main constituents, see figure 2.5 below.[53,101] The first discovered Cdots were found to have a composition of 53.93 % C, 2.56 % H, 1.20 % N, and 40.33 % O.[93] In comparison to traditional semiconductor quantum dots based on metallic elements such as CdS, CdSe, PbSe, and Ag_2S[102], Cdots have unique and advantageous properties such as water solubility[93] luminescence[53], inexpensive preparation, low toxicity, diverse intrinsic electronic and magnetic properties, chemical diversity, higher electron transfers, and biocompatibility which makes them attractive for many applications.[54,103]

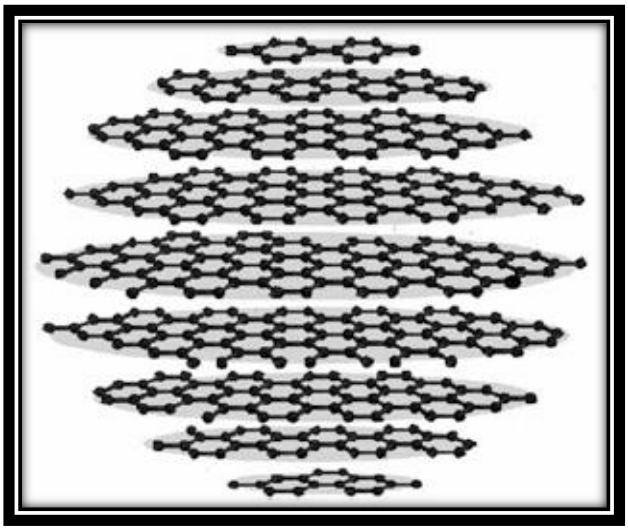

Figure 2.5 Structural feature of carbon dots.[53]

2.4.3 Synthesis of carbon dots

As shown in figure 2.6, general preparations of Cdots involve two synthesis strategies, namely: bottom-up and top-down approaches.[104] The bottom-up approach makes use of small organic components or carbon-containing compounds as the starting reagent for the synthesis of Cdots, usually by pyrolysis or carbonization methods, starting precursors such as chitosan, banana juice, citric acids, and glucose among others can be used.[56] The top-down approach uses larger carbon materials (i.e graphite and carbon nanotubes) as starting materials, which are then broken down into Cdots via chemical, physical or electrochemical means. The bottom-up approach is advantageous as compared to the top-down approach due to the low cost, fast, one-pot synthesis and ease of functionalization, and Cdots with well-defined shape and size are obtained.[96,98]

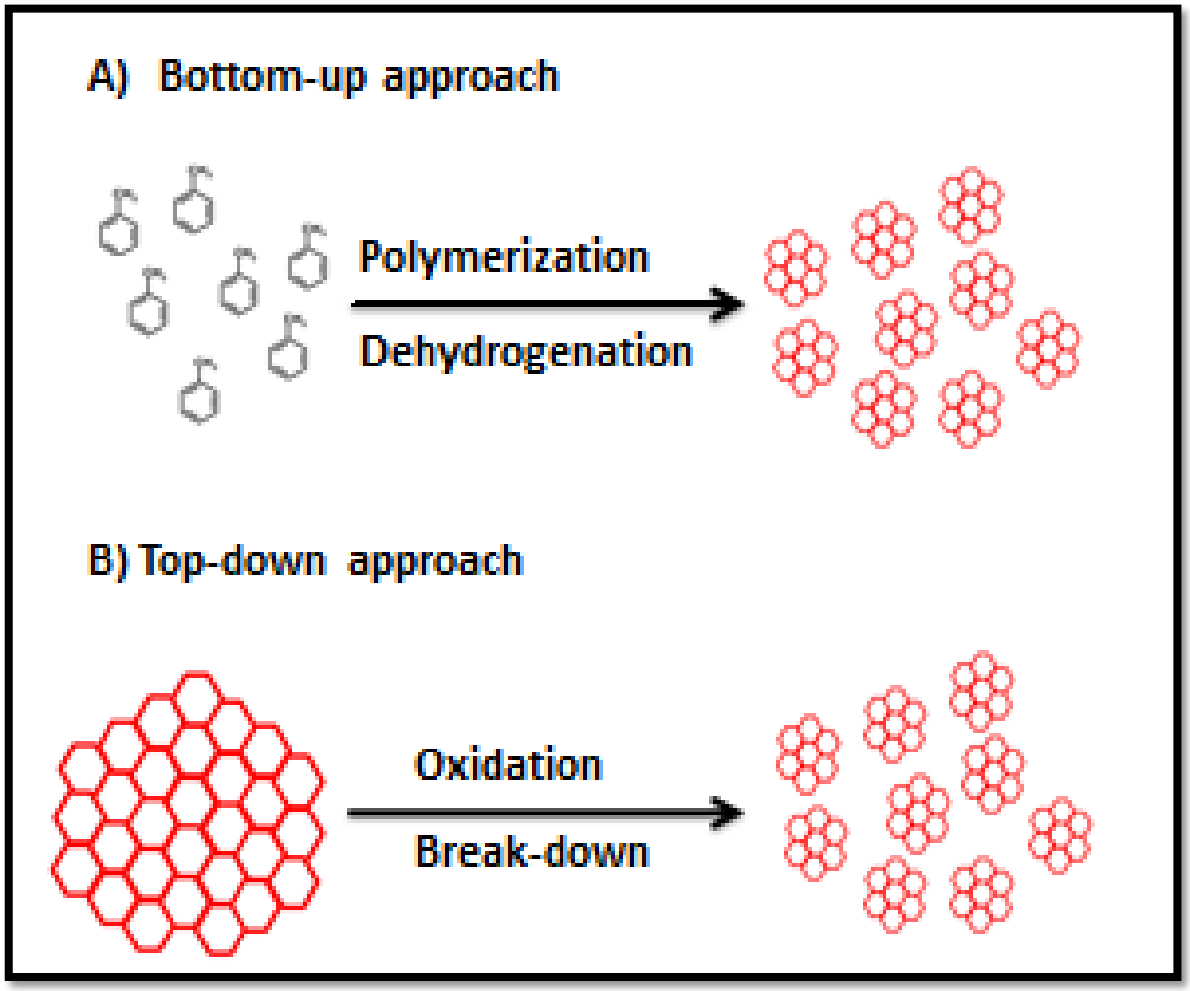

Figure 2.6 Two strategies for the synthesis of carbon dots (A) top-down and (B) bottom-up approach.

In the top-down strategy, methods such as laser ablation, arc discharge, electrochemical oxidation, ultrasonic treatment, and chemical oxidation are used for Cdots synthesis. While the bottom-up strategy makes use of methods such as pyrolysis, templating, as well as hydrothermal/solvothermal, and microwave-assisted methods. The hydrothermal method is preferred due to its simplicity, controlled reaction conditions, rapidity, and cost-effectiveness.[105] It makes use of organic solutions which are sealed and heated by increasing temperature in a hydrothermal reactor (i.e. autoclave reactor).[106] Cdots have been prepared from different carbon sources such as foodstuffs, biomass, protein, organic solvents, sugar, and carbon waste materials.[103,53,102]

Recent methodologies have been aimed at obtaining Cdots using simple methods and less toxic chemicals (green chemistry) that are environmentally friendly and cost-effective. For example, Liang *et al*. demonstrated a simple method for the synthesis of carbon quantum dots with high fluorescence and a quantum yield of 31.6 % using gelatin as the carbon source and water as a solvent.[102] Mehta *et al.* used *Saccharum officinarum juice* to synthesize Cdots and used them for the imaging of bacterias, however, their quantum yield was low, i.e 5.76%.[107] Some of the methods used for the synthesis of Cdots are summarized below.

2.4.3.1 Hydrothermal method

In the hydrothermal method, carbon precursor molecules are carbonized into well-structured Cdots under mild temperatures (100 °C to 240 °C) and at high pressure. Usually, carbon-based molecules are dispersed in water or a solvent and then sealed in a Teflon cup which is placed in an autoclave reactor. The autoclave reactor is hydrothermally treated (usually for hours) to allow the carbonization of carbon precursor molecules. The obtained mixture of Cdots and other carbon hydrochar (residuals) are separated using filtration methods and centrifugation. This can be followed by dialysis using a membrane with varying pore sizes. Hydrothermal methods have many advantages such as low cost, one-pot modification and/or passivation of Cdots, and the use of cheap apparatus. In addition, the hydrothermal method produces monosized and spherical Cdots with good reproducibility. Although this method is reliable, disadvantages such as temperature fluctuation and uncontrolled pressure can be experienced.

Its preference has led to several researchers using it for the synthesis of Cdots. For example, Sachdev and Gopinath synthesized carbon dots using hydrothermal synthesis at 240 ℃ for 4 h. The obtained carbon dots were self-passivated with various functional groups that exhibited

good photostability with good selectivity and sensitive Fe^{3+} probing capability.[105] Monodisoersed and spherical Cdots with intense fluorescent emissions were prepared using the hydrothermal method in an autoclave reactor at 200 ℃ for 5/12 h.[108,60] Moon et al. demonstrated a facile hydrothermal (225 ℃) procedure for the synthesis of graphitic carbon dots with good fluorescent properties, at low cost and possible upscaling without using harsh conditions for potential application in photovoltaics.[109] Among others, De,[110] Yang,[111] Huang,[112], and Mehta et al.[107] used the hydrothermal method for synthesis of Cdots from banana juice, honey, sucrose, and apple juice, respectively. The hydrothermal procedure used for Cdots synthesis was simple, scalable, green (water was used as a solvent, no harsh reagents), cheap, and Cdots with narrow size distributions with potential application in optoelectronics, sensing, and imaging. Therefore, the hydrothermal procedure is good for the synthesis of Cdots.

2.4.3.2 Microwave-assisted method

The microwave (MW) strategy is known to provide high energy for the decomposition of the chemical bonds of the precursor molecule. The precursor molecule is exposed to electromagnetic radiation in the microwave region. The MW method has advantages that range from short reaction times, mild conditions, low energy, and cost-effectiveness. For example, in only 6 minutes, Zhang and colleagues produced carbon dots from glycerin and PEG 1500 under microwave irradiation. The carbon dots were monodispersed having an average size of 5 nm and a typical excitation wavelength dependency nature.[59] In addition, the microwave-assisted method was used for the synthesis of carbon dots using citric acid and urea as starting reagents. This study was insightful as it identified the fundamental mechanism of action as well as components responsible for the fluorescent emissions.[113] However, it is not easy to control the microwave power which can result in poor reproducibility.

2.4.3.3 Chemical ablation

In this method, small carbon molecules are turned into carbonaceous materials by using strong oxidizing acids. The hydrothermal oxidation of nano-diamond with concentrated sulfuric acid, $NaNO_3$, and $KMnO_4$ was used for the synthesis of carbon dots with tunable photoluminescence properties. The obtained carbon dots were spherical with sizes ranging from 3-7 nm having abundant hydroxyl and carbonyl functional groups, and proven biocompatibility toward cells.[114] Although it produced carbon dots at a better scale, the use of strong oxidizing agents is a drawback and thus the method has received minimal attention as compared to the

hydrothermal treatment and microwave-assisted methods which are greener and use more eco-friendly chemicals.

2.4.3.4 Electrochemical method

This method breaks down bigger carbon structures such as carbon nanotubes, graphite rods, and graphene to Cdots through electrochemical cleavage. It has been reported to generate radicals from water molecules through an anodic oxidation reaction. The formed radicals then facilitate the breaking down or cleavage of the bigger carbon structures into Cdots. After it was reported by Zhang and co-workers, only a few reports have been published so far.[56]

2.4.3.5 Laser ablation

The laser ablation method makes use of a high-energy laser pulse that is directed into a solution containing the precursor molecule. The laser pulse irradiation generates high temperatures and pressures, which causes evaporation of the carbon into a plasma and the vapor is then crystallized into nanoparticles.[115] Reyes et al, varied the ablation laser wavelenght and time and at the laser of 355 nm ablation wavelength Cdots with size below 5 nm were obtained, with longer wavelength of 532 nm and 1064 nm resulting in large aggregates.[116] This method is fast and effective method for producing Cdots, however, a post-modification treatment is needed for the realization of PL emission when an ablation wavelength of 1064 nm is used.[117,118]

2.4.3.6 Template method

This method uses a template that allows the shape and size of the synthesized material to be controlled. This method has been intensively explored using mesoporous silicates or porous silica spheres as a template. The synthesis and size control of Cdots happens in the pores of the silica template and a nanocomposite is formed; thereafter the silica template can be etched away to obtain nanosized Cdots.[119,120] Carbon dots with green fluorescent emission under UV light illumination were embedded into a mesoporous silica oxide. Intriguingly, carbon dots were trapped inside the silica mesostructured which made it easy to obtain a solid-state silica/C-dots composite with good luminescent emission.[121]

2.4.4 Properties of carbon dots

Fluorescence emission: Carbon dots are important due to their photoluminescence emissions properties which exceed that of other organic and inorganic quantum/semiconductor nanodots.[57] The photostability, non-blinking photoluminescence, and huge spectral light adsorption give Cdots merit over other organic fluorescent materials. Figure 2.7 shows the typical emission photoluminescent spectra with quinone sulphate as a reference standard to calculate the quantum yield.[122] The PL quantum yield (QY) of bare Cdots is low (typically <10%) due to emissive traps on their surface. Therefore, a surface passivation layer is necessary to improve their brightness.[123] Interestingly, factors such as particle size and distribution, surface passivation, functional groups, synthesis method, and reagents used can influence the fluorescent emission in Cdots.[106] A typical characteristic of photoluminescence in Cdots is their excitation wavelength-dependency in which their emission profile is known to strongly depend on the energy package used for excitation of the Cdots. Handful studies have demonstrated the possibility of excitation-independent characteristics in Cdots, which relates to their homogeneous particle size distribution. Photoluminescent monitoring in Cdots presents a potential application in various fields such as drug/gene delivery, biological imaging, antibacterial and antioxidant activity, and sensing applications including PL sensors, electrochemiluminescence sensors, and electrochemical sensors, catalysis, and in water treatment.[123,124]

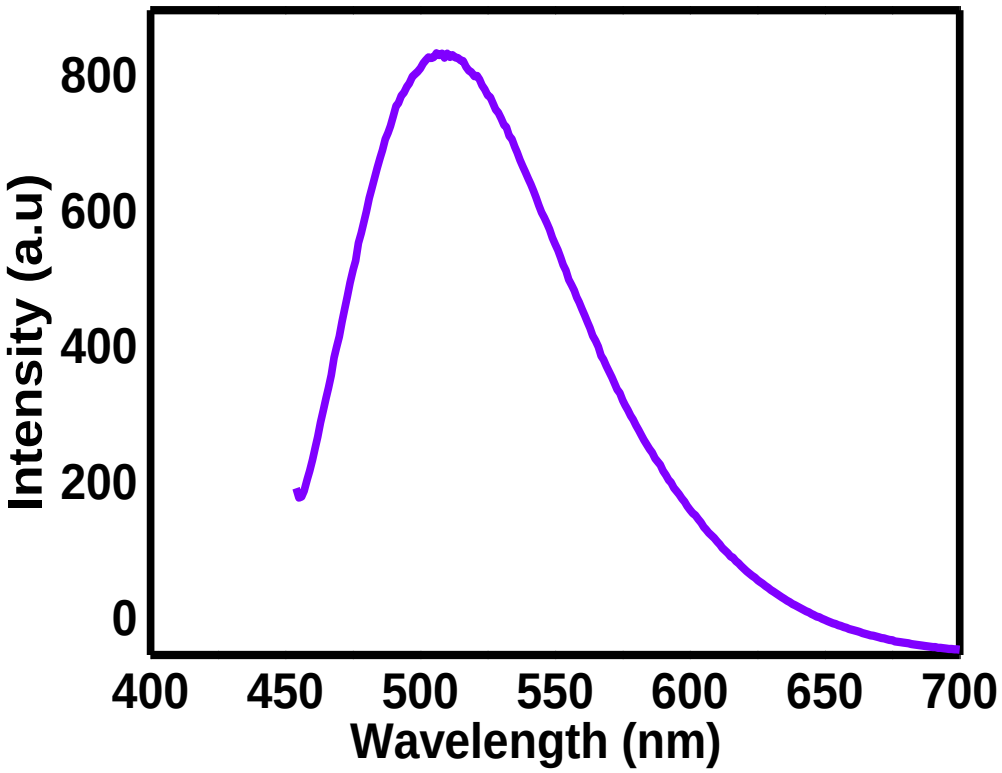

Figure 2.7 Typical photoluminescent spectra of Cdots.[125]

Biocompatibility: Cdots have been tested on various tissues, organs, and mice tumors for biological applications. The findings have shown that Cdots have played a significant role in the visualization and identification of healthy cells from tumor cells. Interestingly, the Cdots particles could be excreted via renal filtration which was monitored by a change in the fluorescent emission. The excretion of Cdots offers a promise for their application in biological systems since they do not accumulate in the body. To date, various tissues, cells, organs, and drug delivery studies have been conducted and have shown that Cdots are biocompatible with low to no toxic effects. Figure 2.8 shows the images of cells at two different excitation wavelengths, where the biocompatibility of carbon dots was demonstrated using cells that maintained their original morphology after 4 h exposure to 300 µg/L of Cdots.[114]

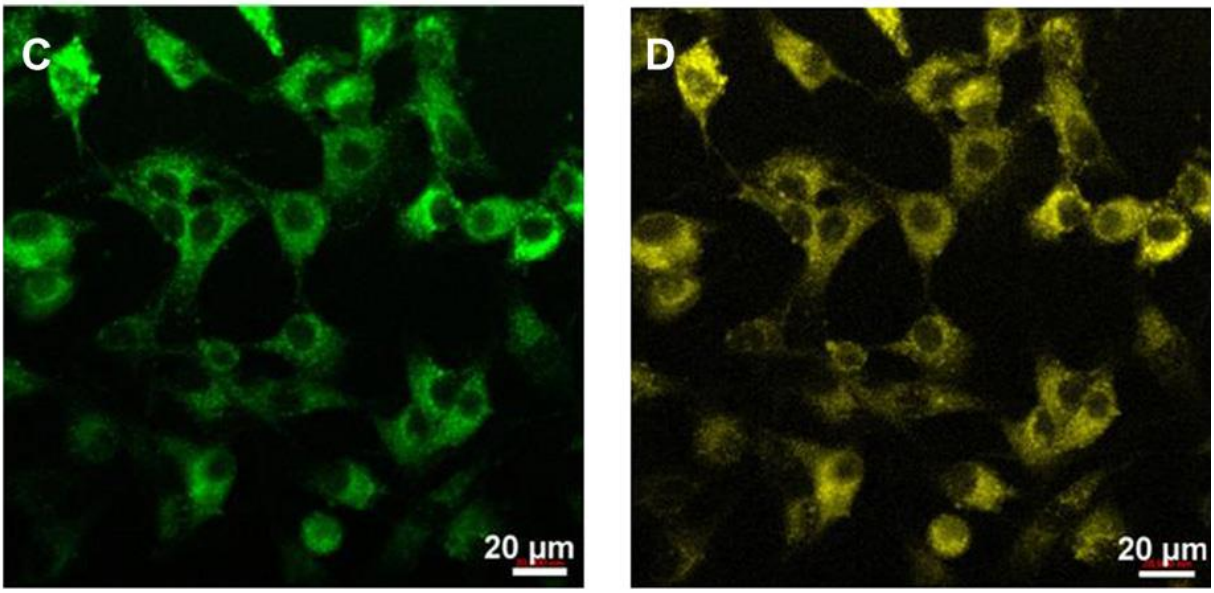

Figure 2.8 (a) and (b) CLSM images of cells imaged under, 405 nm, 458 nm excitations, respectively. Cells were incubated with 300 μg mL^{-1} of CDs for 4 h. the cell imaging demonstrated that CDs could be uptaken by cells and located in the cytoplasm. Adopted from Zang et al.[114]

Electrical properties: The electronic properties of Cdots are known to originate from the carbon core, functional groups, and hetero-atom dopants. Cdots were found to facilitate the oxygen reduction reaction which demonstrated the possibilities of Cdots being used in electron transfer reactions. This could open doors for Cdots application in fields such as electro-catalysis, sensing, and photocatalysis.[126]

***Availability source*:** Many carbon sources have been used to synthesize Cdots. These include natural carbons such as citric acid, food waste, humic acid, oils, milk, banana wastes, graphitic particles, chitosan, ascorbic acid, coffee, and dried leaf.[127,128] As a result, various Cdots having various functional groups and varying surface passivation such as carbonyl, carboxyl, nitrogen, and hydroxyl groups have been made. In addition to being made from cheap sources, carbon dots can be synthesized by many methods as mentioned and discussed above.

2.4.5 Application of carbon dots

Owing to the above-mentioned exotic properties such as good biocompatibility, fluorescent emission, and lower toxicity, carbon dots have been explored for potential applications in sensing devices, catalysis, solar energy, bioimaging, drug delivery, nanomedicine, optronic devices, and multi imaging.[53] Due to the exponential growth in Cdots research, it is without a

doubt that shortly many commercial and valuable Cdots devices will be available in the marketplace.

2.4.5.1 Sensor

Sensing equipment plays a major role in everyday life as sensors can detect and alert about disastrous situations before they happen. These devices continue to help the prevention of explosions, toxic chemical exposure, and criminal activities. The intense PL emission of Cdots has made them a potential candidate for sensing applications. As shown in figure 2.9, a captivating study by Siddique demonstrated how the PL intensity was reduced as the concentration of 2,4,6-trinitrophenol (TNT) was increased. Carbon dots exhibited selectivity and the best detection of TNT which is known to be very explosive. The study concluded that the abundant surface traps are responsible for the excitation dependant PL nature of carbon dots.[129] In another study by Li *et al.* nitrogen-rich carbon dots exhibited a good detection limit (23 μM) toward toxic Be^{2+} ions.[130] It has become apparent that the fluorescent emission of Cdots is promising for use in possible commercial valuable sensing devices.

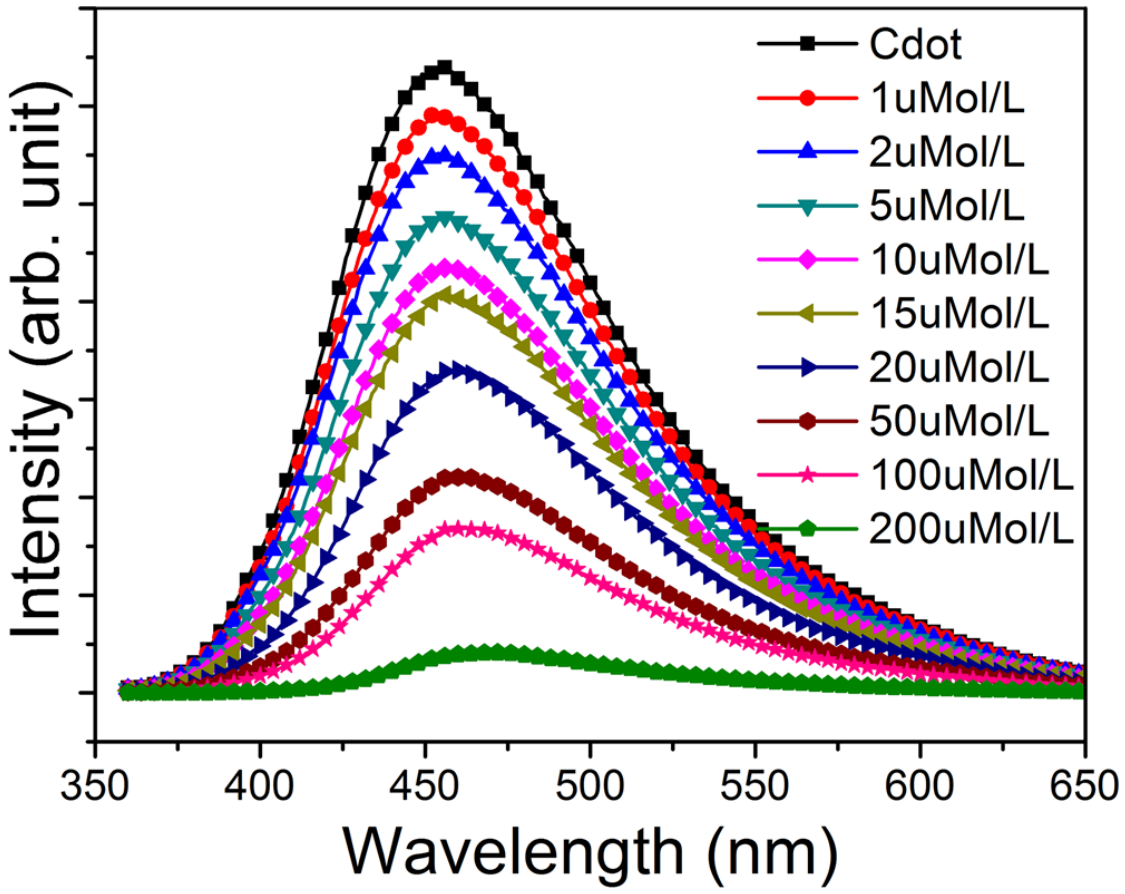

Figure 2.9 Variation of PL intensity profiles at various concentrations of TNP additions to the colloidal Cdots. Adopted from Siddique et al.[129]

2.4.5.2 Biosensor

Cdots are biofriendly and this has led to their exploration and application in various biomedical fields. They have been investigated as light emitters for biosensor applications. The research on biosensing has been extensively explored and investigated for the design approach, sensing mechanism, sensing probe optimization, and possibility of detecting various analytes such as glucose, nucleic acids, phosphate, and cellular copper.[104,122,131]

2.4.5.3 Bioimaging

In bioimaging, a microscopic technique is used for the visualization of living species such as tissues and cells. The higher PL emission of Cdots in the near-infrared (NIR) spectral region under NIR light excitation has opened doors for their in vivo application in biological labeling and imaging.[95] So far, injecting, imaging, and identifying healthy and tumor tissues or cells has been possible. Commonly, fluorescence microscopy, magnetic resonance microscopy, and

confocal laser scanning microscopy have been used to scrutinize tissues and cells that are injected with Cdots.[132] The study by Zang et al. demonstrated the use of Cdots in the imaging of peritoneal macrophages of mice. The peritoneal macrophages that contained Cdots had different colors under UV light while isolated peritoneal microphages without Cdots were colorless.[133] Carbon dots synthesized via hydrothermal carbonization were also proven to be good for biological imaging of Hela cells with low toxicity and good biocompatibility. At higher carbon dots concentration of 750 µg/mL, 78 % of Hela cells still were viable after 24 h incubation.[131]

2.4.5.4 Wastewater

Fluorescent probing: As mentioned before, Cdots fluorescent emission is the central property that led to their exploration and documentation. Their photoluminescence emission can be used for probing of various metals ions (mercury, chromium, iron, and copper) in wastewater by tracing the change in the PL emission intensities of PL quenching caused by metal ions.[103,134] The process is similar to sensing or probing in which an increase in metal ion concentration results in a reduction or quenching of the PL emission. Liu et al. used carbon dots synthesized from bamboo leaves to detect Cu^{2+} and from the study, they concluded that Cdots were good for selective and sensitive Cu^{2+} detection.[135] A lot more research is needed in this area, with more focus on selectivity since different metal ions (at higher concentrations) can have a similar effect on the intensity of fluorescent emissions in Cdots.

Membrane nanocomposites: A membrane can be defined as a barrier that allows some particles/molecules to pass through it while others are retained, an effect determined by the size, shape, and chemical nature of the particles/molecules. This strategy has been used for centuries in water sanitation where bigger particles were separated from water molecules using stones, sand, and membrane filters. In this millennium, membrane nanocomposites that can separate smaller particles such as microorganisms and metal ions are essential. The hydrophobicity, ultra-small particle size, and abundant functional groups on Cdots make them convenient for fabrication in various membranes. They exhibit good dispersion when fabricated in membranes that can increase water permeability by offering a shorter path length for water molecules.[134] Multi-walled carbon nanotube coated carbon dots filters exhibited good removal and inactivation of bacterial cells from aqueous solution. Coating with 0.2 mg carbon dots inhibited 94.21 % of the bacterial cells retained on the filter surface.[136] Although research in

Cdots/membrane nanocomposites is in the early stages, their ultra-small particle size could be useful in membrane technology.

Photocatalysis: For a photocatalyst to be active it needs an energy frequency that is equal to or above threshold frequency to move an electron from the valence band to the conduction band. The major drawback for a semiconductor is their fast recombination of generated electron/holes pairs which result in poor performance of the photocatalyst.[134] In addition, a photocatalyst like an anatase TiO_2 can only be activated by ~ 5 % of the solar spectrum. Cdots have been reported to utilize a wide range of solar spectrums and can reduce the recombination of electrons and holes due to good trapping and transferring of electrons.[126] As such, Cdots are good candidates for use as a carbon co-sorbent for improving photocatalytic activity owing to their electron donor and electron acceptor characteristics. Since their discovery, many studies have explored their photocatalytic activity and photosensitization mechanisms when supported on various photocatalysts.[55,137] This resulted in them being used in hydrogen evolution reaction, dye degradation, and normal light photocatalyst design.

Figure 2.10 shows the mechanism of action that can be used in photocatalysis design that involves Cdots, with TiO_2 used as an example here. Cdots absorb visible light with lower energy (i.e 500 - 1000 nm) which cannot be utilized or activate TiO_2. The energy absorbed by Cdots results in the excitation of electrons to higher energy levels which can later move to the ground state by emitting shorter wavelength light (300- 400 nm) through a phenomenon called up-conversion PL emission. The emitted energy can be utilized by a TiO_2 photocatalyst to form an electron/hole pair that in turn reacts with oxidants/reducers to produce active oxygen radicals, which facilitate the degradation of dyes. In addition, photo-induced electron transfers in which the excited electrons from Cdots are injected into the CB of TiO_2 are possible, which also improves the photocatalytic activity. Importantly, when Cdots are incorporated into the surface of the TiO_2 the relative position of the Cdots band edge permits the transfer of electrons from Cdots to the conduction band of TiO_2 thereby transferring to the production of radicals capable to attack the adsorbed pollutants. In addition, the Cdots/TiO2 composites exhibit charge separation, stabilization, and hindered recombination.[138] These mechanisms make Cdots a good candidate for photocatalyst design.[139]

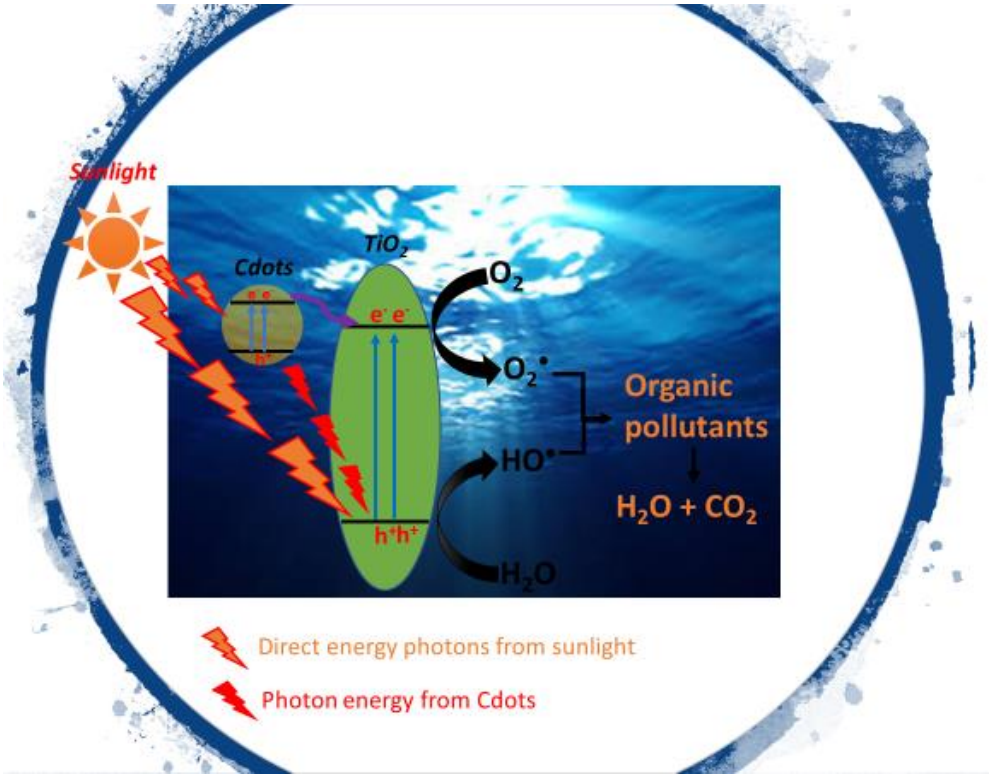

Figure 2.10 Possible photosensitization of TiO_2 using Cdots.[55,138]

Adsorption: Flocculation, oxidation, precipitation, and membrane separation are examples of the known conventional methods used for the removal of dyes from wastewater. The adsorption process is very effective in the removal of colored dyes from wastewater. Various adsorbents have been used for the removal of dyes from waster water, and among them activated carbon has demonstrated a good adsorption capacity. However, reactivation or recycling and the source of activated carbon can be a drawback that limits its application. The use of naturally occurring, abundant, and cost-effective carbon-based adsorbents has gained more attention. For example, chitosan is one of the highly available polysaccharides with a promising application as an adsorbent.

Although chitosan has shown potential for metal ions and dye removal from wastewater, in its pure form, the activity of chitosan for metal and dye removal is problematic due to the formation of a gel in aqueous media. It can also readily agglomerate which makes it lose its adsorption capacity. Furthermore, chitosan is less stable under harsh conditions and soluble at low pH, especially in organic acids, thus limiting its applicability as an adsorbent.[140,141] Processes such as cross-linking, grafting of new functionalities, and acetylation have been used to chemically modify chitosan to improve its absorption activity.[142]

Cdots derived from chitosan have been reported to have abundant functional groups such as amines, amides, carbonyl, and hydroxyl.[104] Which makes chitosan a good candidate for synthesis of Cdots and applying them in adsorption processes. In addition, the feasibility of tuning the surface chemistry of Cdots by using various heteroatoms such as nitrogen, sulfur, and oxygen offers a great potential for their application in adsorption studies. To date, Cdots have been used for the adsorption of organic and inorganic pollutants from wastewater using the adsorption method.[143,144] However, their ultra-small size and hygroscopicity limit them for potential as adsorbents. To mitigate this, a solid support matrix has been used to support Cdots, and the Cdots/support composite exhibited good adsorption capacity for use in wastewater.[134,145]

2.4.6 Shortcomings of carbon dots

Origin of PL emission: Regardless of their promising potential applications, Cdots research is still at an infant stage. The mechanism that leads to photoluminescence emissions and their mechanism of action when interacting with biological systems is still not yet understood. Some reports have shown that the mechanism of action for optical absorption and fluorescence emissions in Cdots does not originate from a bandgap, but instead is due to the π-plasmon and radiative recombination of the surface-confined electrons and holes, which is different from the way that semiconductor quantum dots operate.[126,146] To date, their excitation wavelength dependency in fluorescent emission has been proposed to be due to quantum confinement (particle size), surface states (functional groups), and the carbon core. Solvatochromism studies are promising for identifying the main components responsible for PL emission in Cdots. These methods explore the effect of solvent polarity on the emission of Cdots. So far, solvents with higher polarity have been observed to exhibit redshift emission and this was suggested to be due to hydrogen bonding and dipole-dipole interactions between surface states in Cdots and the solvent. More attention to the mechanism involved in PL emissions in Cdots is needed.

Purification steps: The drawbacks associated with Cdots are due to their **small size** (below 10 nm) which makes them difficult to work with, i.e., their small size has led to purification difficulties when working with Cdots in solution. This is because during their synthesis other residuals with various particle sizes and structures are formed and separating them is challenging. The purification of Cdots involves multi steps such as centrifugation, micro-filtration, and dialysis. While working with dialysis with membranes < 1000 Daltons should be avoided because it can result in the loss of Cdots. In addition, obtaining solid-state Cdots is

difficult because they absorb lots of moisture and mostly remain as a gel. Freeze-drying of the aqueous solution is one method used to obtain solid-state Cdots products.

Fluorescent quenching: Cdots are very hygroscopic and difficult to obtain in solid form. In their solid form, Cdots tend to agglomerate and result in compromised fluorescent properties as a result of the self-quenching effect or aggregate-induced PL quenching.

Functional groups decomposition: The abundant functional groups and surface passivation of Cdots have been reported to be responsible for PL emission and for reducing metal nanoparticles. However, these surface functional groups decompose at a temperature below 250 °C which can limit their applications at high-temperature catalysis or industrial applications.[125,147] It is worth stating that Cdots are stable under UV illumination.[146]

2.4.7 Mitigation of carbon dots shortcomings

2.4.7.1 Surface passivation, functionalization, and doping

Surface passivation: Polymeric materials have been used to passivate the surface of Cdots, and they form a thin insulating layer that protects the surface of the Cdots. The passivation inhibits the surface contamination of Cdots and maintains their functional properties under various environmental changes.[148] Passivation of Cdots using diamine-terminated oligomeric poly (ethylene glycol) resulted in strong photoluminescence emission under UV lamp illumination at 365 nm, with a quantum yield of 14.7 %.[149]

Functionalization**:** This process allows for the introduction of various groups, such as amines, carbonyl, and hydroxyl functionalities, which result in new surface states that can act as electron traps or adsorption sites which also induce fluorescent emission. The acid treatment approach was used to introduce functional groups such as carbonyl and carboxyl while a one-pot reaction of a carbon precursor with a nitrogenated precursor can be used to introduce nitrogen groups onto the Cdots surface.[96,149] Interestingly, the one-pot hydrothermal carbonization of precursors (e.g. chitosan) with functional groups such as hydroxyl and amine produces carbon dots with abundant functional groups.[104] These functional groups play a major role during applications in which they can act as adsorption sites, electron traps, PL emission moieties, and acts as reducing/oxidizing agents for the metal in catalysis.

Doping: Doping involves the introduction of impurities into a pure natural matrix or compound. Cdots have been doped with various heteroatoms such as N, O, B, and P, and the addition of

these elements have been found to induce electronic and optical properties.[150,131,151] Doping can be achieved via the one-pot synthesis or a post-modification method. In most cases, doped Cdots have been reported to have improved properties when compared to their undoped counterparts.

2.4.7.2 Solid supports and nanocomposite

Synthesis methods and starting reagents have also been central in mitigating some of the shortcomings associated with Cdots. As such, various methods and carbon precursors (some mentioned above) have been used for changing and improving Cdots properties. Supporting Cdots on a solid matrix has been an alternative way to prevent aggregate-induced quenching. In addition, this method simplifies the purification steps and improves properties such as adsorption, light capture, and electron transfer. The method also introduces various functional groups on the support and reduces agglomeration in the solid-state.[59] With increasing literature on Cdots/supports composites, their future applications and commercialization will result from its composite materials. However, the difference between the fluorescent emission of Cdots in the liquid and solid-state still is experienced and needs to be addressed. Some of the supports that have been used to support Cdotss are mentioned below.

Silica supports: The synthesis, supporting, entrapment, and encapsulation of Cdots on a silica matrix has received more attention as compared to other supports. The attention arose due to the advantageous properties associated with silica support, such as its structural morphology, large surface area, higher loading capacity (especially hollow mesoporous silica), and the ability to homogeneously disperse nanoparticles on the surface. In addition, Cdots supported on silica have been found to overcome aggregation-induced emission or self-quenching which enhances their PL emission and quantum yield.[152,153] Studies by Guo et al. demonstrated a simple approach of embedding of Cdots into a mesoporous silica matrix. The composite exhibited an excitation-independent blue emission which is not generic in Cdots as they mostly show an excitation-dependant nature.[108] The fluorescence of carbon dot supported on silica nanoparticles was used to probe the presence of copper and vanadium. In the presence of the Cdots/SiO_2 nanosensor, they exhibited outstanding fluorescent quenching effects due to a catalytic oxidation reaction. In addition, the composite exhibited good selectivity, high sensitivity, and a wide linear response range.[154,155] In another study, Cdots@SiO_2 composites exhibited excellent emission resistance under UV irradiation and the material remained photostable due to the silica coating which protected the Cdots from luminescent quenching.

Compared to commercial fluorescein sodium dye that was quenched after 65 minutes of UV illumination, the Cdots@silica composites PL emission was reduced by less than 20 %. Figure 2.11 below shows how the Cdots@SiO_2 composite was syntheized.[156]

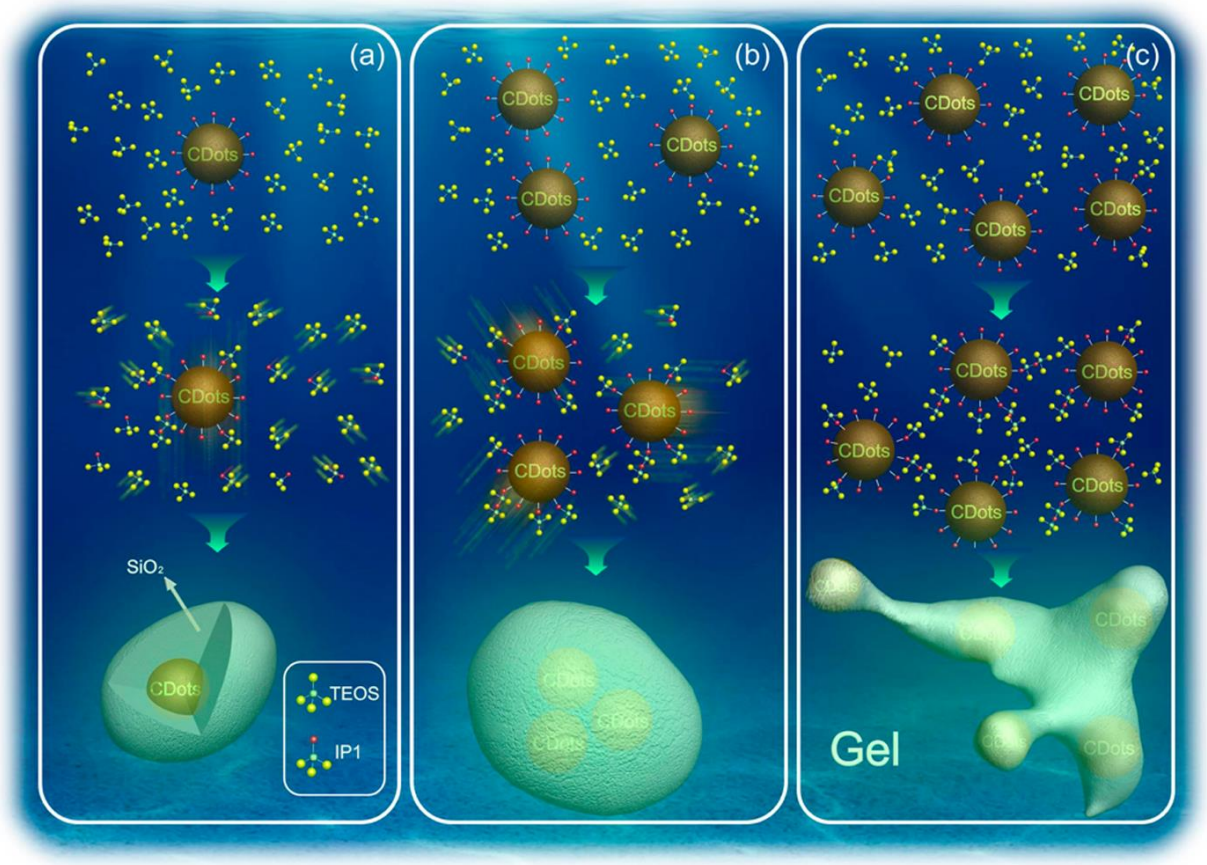

Figure 2.11 Schematics of the formation of a CDots@Silica composite Nanoparticles/Gel at (a) low, (b) medium, and (c) high concentration of CDots ethanol solutions. Adapted from Zhou et al.[156]

Carbon supports: Yanchun Deng and co-workers supported Cdots onto magnetite magnetic carbon nanotubes and used the composite for removal of carbamazepine from water or wastewater with an adsorption capacity of 65 mg/g. This was attributed to the introduction of abundant carboxyl groups from the Cdots and CNTs support.[144] Yi-Kun Li et al. immobilized Cdots on the microcarrier cytopore, and used the composite for the rapid adsorption of cadmium which reached adsorption equilibrium within a minute and a maximum adsorption capacity of 2420 µg/g with good selectivity.[60] Gogoi and Karak supported carbon dots on polyurethane and used the composite for the solar-driven production of hydrogen peroxide; the bandgap of the carbon dots facilitated the splitting of water and ethanol under solar irradiation. The composite was reported to be biodegradable using the *P. aeruginosa* organism.[157] The study by Qiao et al. paved a way for building and encapsulating carbon dots inside hollow carbon spheres.

Pioneering core-shell structures where carbon nanoparticles are entrapped inside a porous matrix is essential and simplifies the purification and reusability of caron dots.[158]

So far various hollow carbon spheres (HCSs) have been synthesized ranging from single-shell hollow carbon spheres, yolk-shell hollow carbon spheres, and multi-shell HCS's. HCS's or carbon capsules refer to ball-like carbon structures with pores and a hollow inside having sizes ranging from millimeter, micron, or even nanometre size and correspondingly thin shells. HCSs have received enormous consideration because of their unique structure and functional behavior such as higher specific area, low specific density, large controllable inner pore volume, good conductivity[63], and good mechanical strength.[61] With these fascinating properties, HCSs are promising candidates for a wide range of applications such as adsorption, catalysis, Li−S batteries, fuel cells, supercapacitor electrodes[63], delivery controlled release systems, chromatography, adsorption, microreactors, and energy storage and conversion.[159,160] HCSs have been used to support and encapsulate various metal nanoparticles.[161]

The encapsulation of various nanoparticles (metal nanoparticles) inside HCSs reduces the movement of the particles and minimizes collision, and as a result, the formation of aggregates of particles inside HCSs is reduced. Figure 2.12 shows how metal nanoparticles (or Cdots) can be entrapped inside HCSs, these can be done by (i) incorporation of metal nanoparticles/Cdots on the surface of silica spheres (acting at a template) to form nanoparticles/SSs composite, (ii) coating of a nanoparticle/SSs composite with a carbon source (e.g.., resorcinol and formaldehyde, RF) to form RF@nanoparticles/SSs, (iii) carbonization of the RF@nanoparticles/SSs which is later followed by removal of silica template to have Cdots@HCSs or metal-nanoparticles@HCSs composites. These steps favor the encapsulation of the nanoparticles inside HCSs support.

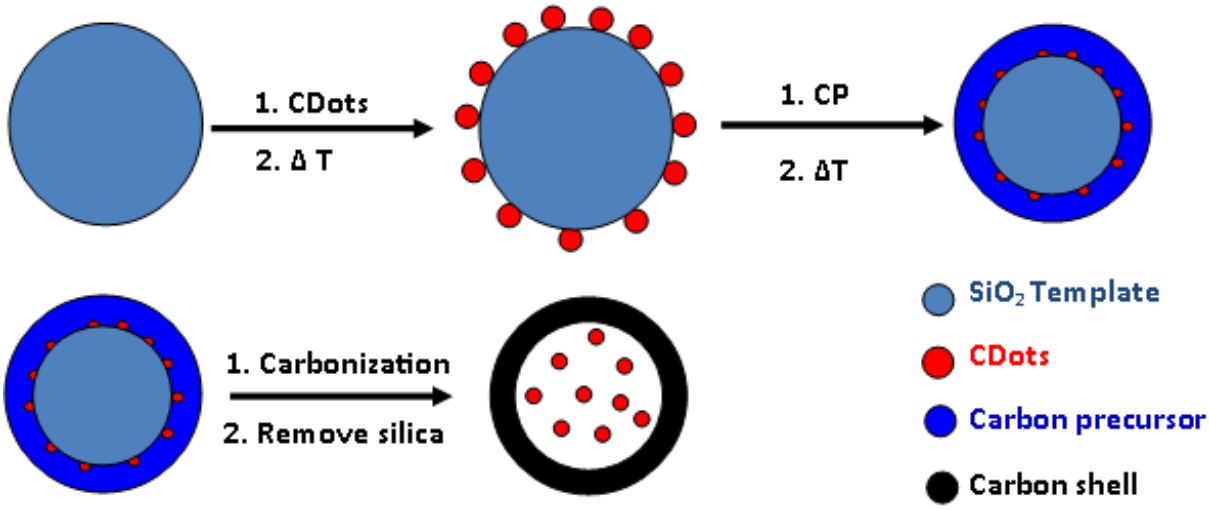

Figure 2.12 Possible methods for encapsulation of Cdots inside HCSs.

Cdots nanocomposites: The formation of Cdots nanocomposites with other functional materials has received scientific attention. The Cdots nanocomposites have advantages can have multi-functional properties. For example, Cdots/TiO_2 nanocomposites can use the light utilization characteristics from Cdots to activate the TiO_2 catalyst which in turn results in good synergetic enhanced photocatalytic conversion of an analyte to the desired product.[162] Zhang, synthesized Cdots coated with a metal (Au, Pt, Pd) and the luminescent Cdots served as a reducing agent for the metal nanoparticles.[163] Cdots supported on the surface of N-doped-TiO_2 nanorods improved the electrochemical performance when the complex was used as an anode material in sodium-ion batteries.[164] Table 2.3 shows some of the supports used to form solid-state Cdots/support composites.

Table 2. 2 Cdots/solid-support composites .

Support	**Cdots size**	**PLQY**	**Application or finding**	**Ref**
Silica	≤ 10 nm (19.2 wt %)	41 %	Fabricated on white LED prototypes	[156]
@chitosan/MOFs	≤ 10 nm	__	Optical bio-imaging/drug delivery	[165]
SiO_2-PEG	5.5 nm	32 %	Drug delivery	[119]
TiO_2	4.6 nm	__	Photocatalytic hydrogen evolution	[57]

MWCNT's	≤10 nm	__	Bacterial removal from water	[136]
HCSs	3 nm	__	Inkjet printing and sensitized solar cells	[166]
Cdots/porous carbon spheres	2-3 nm	__	Good for energy storage	[167]
Starch/g-CDs composite	≤10 nm	~50%	Enhanced PLQY	[168]
Cdots/Au or Ag	0.6 nm to 8.7 nm	__	Findings: Enhanced PL emissions	[169]
CD/polymer films	2.6 nm	~34%	Strong fluorescence emissions	[115]
Polymer-dots@Carbon core shell	~ 4 nm, polymer Cdots	8.6 %	Cu^{2+} adsorption	[158]

It has become apparent that supporting the Cdots on various solid support matrix can improve their properties and can open doors for their application in various fields.[145] Herein, various solid supports such as silica spheres, hollow and solid carbon spheres, TiO_2 particles, and carbonized chitosan will be used as supports for Cdots. The fluorescent properties of the Cdots/support composites will be investigated and the composites will be used for adsorption and photodegradation of MO from an aqueous solution.

Chapter 3

A comparison of fluorescent N-doped carbon dots supported on the surface of hollow and solid carbon spheres, and solid silica spheres

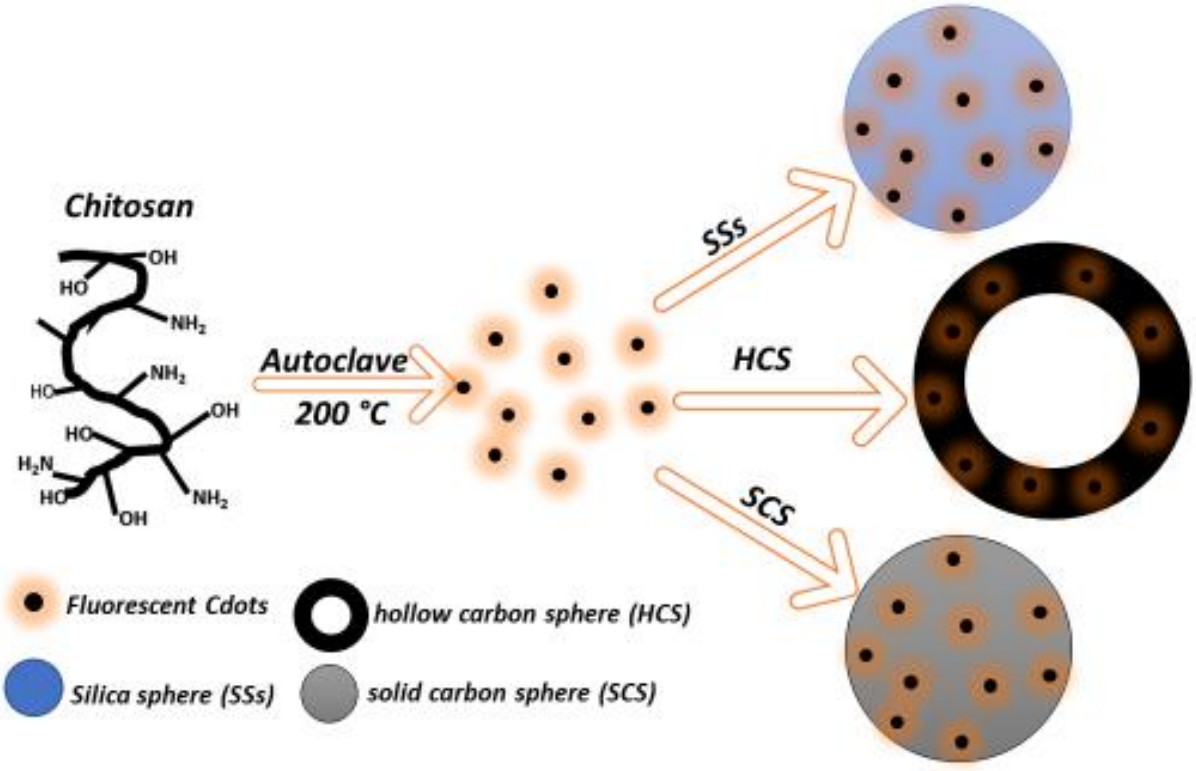

This chapter has been published in the "Diamond and Related Materials journal."

Citation: Mkhari, Orlette, et al. "A comparison of fluorescent N-doped carbon dots supported on the surface of hollow and solid carbon spheres, and solid silica spheres." Diamond and Related Materials (2021): 108500.

Abstract

Fluorescent carbon dots (Cdots) have attracted many researchers due to their strong optical photoluminescence (PL) properties; however, due to their small size, they agglomerate in the solid state which makes it difficult to remove them from the solution. To overcome these problems, Cdots can be deposited on a support, but to date, few systematic studies of Cdots-support systems have been reported, especially those on carbon supports. Herein, we report a systematic study of the effect of the use of nitrogen-doped carbon dots (NCdots) (5, 10, 15, and 20 wt. %) supported on the surface of hollow carbon spheres (HCSs), solid carbon spheres (SCSs), and silica spheres (SSs). The morphology of the NCdots and their composites (NCdots/SSs, NCdots/HCSs, and NCdots/SCSs) was studied by TEM, TGA, XRD, FTIR, UV-vis, XPS, CHNS, Raman, and PL techniques. FTIR, XPS, and CHNS revealed the existence of functional groups such as hydroxyl, carbonyl, and amines/amides, their chemical environment, and their compositions. The FTIR, XRD, and TGA data suggest different interactions of the NCdots with the supports. The PL quantum yield for bare NCdots was 34 % and this value decreased when loaded on the supports, in the order NCdots/SSs > NCdots/HCSs > NCdots/SCSs due to different interactions between the Cdots and the support.

Keywords: carbon dots; silica spheres; carbon spheres; photoluminescence; wavelength excitation-dependence.

3.1. Introduction

Carbon is the sixth most common element in the universe and one of the essential chemical elements required by living organisms.[85] It serves as a building block for all organic compounds and it plays a major role in nanoscience, materials science, and engineering.[85,80] To date, numerous carbon allotropes (for example, carbon nanotubes, graphene, graphite, amorphous carbon, and diamond) have been made and their nanostructures studied in detail.[89,170] This relates to the properties associated with carbon such as light absorption across the UV-visible region, variable surface area, and flexibility to form a range of different morphologies.[128]

Nanostructured carbons continue to reveal new allotropes and one of the most recently discovered is the carbon dot (Cdot), with a size $\leq$ 10 nm.[171,172] Cdots have interesting photoluminescence properties, diverse intrinsic electronic and magnetic properties, good electron transfer rates, and biocompatibility, all of which make them attractive for use in many

applications such as optoelectronic devices, biomedical imaging and catalysis.[173,174] Cdots have a spherical or near-spherical shape and are made by the layering of sp^2 graphene domains next to and on top of each other.[106] The Cdots surface can be passivated with O and H atoms and also importantly, sp^3 or sp^2 carbon atoms containing various functional groups.[175,176] Due to their limited size, their large number of structural defects and their abundant surface functional groups (containing typically O and N atoms) [177], they possess an electronic bandgap and a high electron transfer in the visible light region.[130] Their wide range of light absorption and efficient conversion of light energy into chemical energy makes them good candidates for accelerating photochemical reactions.[96]

Cdots have been prepared from many different carbon sources such as foodstuffs, biomass, proteins, small organic molecules, sugars and numerous waste materials.[178,58] Once made, there are difficulties with their use, due to their small size which leads to filtration issues when retrieving them from the solution. After removal from the solution, they can form carbonaceous aggregates that can lead to aggregation-induced luminescence quenching whereby their photoluminescence (PL) emissions are affected during applications.[109,58] The deteriorated photoluminescence spectrum can lead to poor quantum yields and an inadequate understanding of the origin of the photoluminescent properties of Cdots which can also result in poor spectral interpretations.[179]

One method to address the drawbacks associated with Cdots listed above is to support them on the surface of insoluble solids.[156,180,181] Cdots that have been supported on various surfaces have often been shown to have improved properties relative to their unsupported counterparts.[165,119] Furthermore, the addition of the Cdots to a surface can introduce functional groups to the support through the functional groups on the Cdots.[59] The synthesis of Cdots supported on silica spheres has received more attention as compared to other supports. The attention arose due to the advantageous properties that the silica support can provide, such as its structural morphology, large surface area, higher loading capacity (especially hollow mesoporous silica) and the ability to avoid interaction of supported Cdots particles. In addition, Cdots supported on silica supports have been found to have enhanced PL quantum yield.[152,153] In addition to silica supports, Cdots supported on the surface of N-doped TiO_2 nanorods have shown improved electrochemical performance when used as an anode material in sodium-ion batteries.[164] Thus, it is clear that supported Cdots show promise as a new type of reagent for

use in various chemical processes such as adsorption, energy storage and catalysis. Table S1 shows some of the supports that have been used to make Cdots/support materials.

Interestingly, although there are numerous examples of Cdots/carbon materials that have been reported, very few systematic studies have been performed using carbon as a support for the Cdots. Examples of the use of Cdots carbon materials include the use of multi-wall carbon nanotubes (MWCNTs) as supports.[60] Deng *et al.,* reported the synthesis of magnetic carbon nanotubes modified with Cdots and how the Cdots improved the removal of carbamazepine from wastewater.[144] Li *et al.,* made Cdots supported on cytopore and demonstrated the rapid adsorption of Cd using the Cdots/cytopore material.[60] Cdots have also been placed inside hollow carbon spheres.[166,61,158] In addition, Chen et al. have made PVA/Cdots and showed how their fluorescence properties were affected by the presence of the Cdots content.[62] Other examples of Cdots/carbon materials are given in Table S1.

However, to our knowledge, no systematic study has to date been undertaken to investigate the interaction of Cdots with carbon support surfaces. In this study, we have chosen to investigate the effect of hollow carbon spheres (HCSs) and solid carbon spheres (SCSs) as supports for the N-doped Cdots. HCSs can provide a thin carbon porous shell that provides a high surface area (and interesting porosity) and the ability to readily allow the detection of the Cdots by TEM.[166] We have also made solid silica spheres (SSs) that allows for a comparison of the effect of silica with carbon and also with the HCSs, on the properties of the supported Cdots. The composites have been studied by numerous techniques and the optical properties (PL emission) and the relative PL quantum yield (PLQY) of the Cdots/supports have been compared.

3.2. Experimental

3.2.1 Materials

Chitosan $(C_6H_{11}NO_4)_n$ with low molecular weight (50,000 Da) was purchased from Sigma Aldrich (75 - 85% deacetylated) and deionized water (resistivity > 18.2 MΩ cm $^{-1}$) was used as a solvent. Tetraethyl orthosilicate, (TEOS, 98%, Sigma Aldrich), ammonium hydroxide, (NH_4OH, 25%, Fluka) and ethanol, (EtOH, 96%, Merck) were used for the synthesis of the SSs. The SSs were coated with resorcinol (99%, Sigma Aldrich), formaldehyde (≥ 34.5 wt. %, Sigma Aldrich,) and hexadecyl trimethyl- ammonium bromide (CTAB; 98%, Aldrich). A 10%

hydrofluoric acid (HF; 48%, Associated Chemical Enterprise) solution in water was used for the etching reactions.

3.2.2 Cdots synthesis

The synthesis of the N-doped Cdots was carried out using a modified hydrothermal carbonization method adopted from a previous study.[131] Typically, chitosan (1 g) was dispersed in 50 mL deionized water and then sonicated for 30 min at a temperature of 40 °C. The sonicated mixture was transferred into a 50 mL Teflon cup that was placed inside an autoclave reactor. The synthesis was carried out at a temperature of 200 °C for 3 h after using a heating ramp of 2 °C/min, starting from room temperature (typically 25 °C).[162,175] After the reaction time, the sample was allowed to cool to room temperature, and then 200 mL of distilled water was added to fully disperse the product containing the NCdots. The resulting solution was filtered and centrifuged at 18 000 rpm for 20 min to further remove any insoluble black particles. The supernatant (NCdots) solution was further filtered using a 0.22 μm PVDF membrane to remove all unwanted residuals. The product was dried using a rotary evaporator at 60 °C, followed by drying at a temperature of 70 °C to obtain a solid NCdots product (~26 % yield).

3.2.3 Synthesis of silica spheres (SSs)

The SSs were synthesized from a mixture of ethanol, deionized H_2O, ammonia (25 %) and TEOS using a modification of literature procedures.[65,182] A solution of EtOH (390 mL), distilled water (50 mL) and NH_4OH (20 mL) was stirred vigorously for 15 min, then TEOS (50 mL) was added to the solution and the mixture was stirred for a further 24 h. After 24 h the solution was centrifuged at 18 000 rpm for 15 min followed by drying of the white silica sphere powder in an oven at a temperature of 100 °C overnight.

3.2.4 Synthesis of the hollow carbon spheres (HCSs)

HCSs were synthesized by using the above SSs as a sacrificial template.[183] Typically, two mixtures were prepared in two separate beakers. The first mixture contained SSs (1g), EtOH (100 mL), H_2O (75 mL), and NH_4OH (5 mL). The second mixture contained resorcinol (0.5 g), formaldehyde solution (4 mL), CTAB (2 g) and EtOH (150 mL). The mixtures were sonicated for 30 minutes and thereafter combined and stirred at room temperature for 24 h to form a resorcinol-formaldehyde (RF) coating around the SSs. The resulting dark red composite

(SSs@RF) was filtered and washed repeatedly with water and ethanol. This was followed by drying in an oven at 100 °C overnight. The SSs@RF was then carbonized inside a horizontal tube by heating under a nitrogen flow (50 mL/min) at 650 °C for 3 h. The sacrificial SSs template was etched out using 10 % HF for 6 h to form HCSs consisting of the same shape as the template. This was followed by drying the HCSs at 100 °C in an oven overnight.

3.2.5 Synthesis of the solid carbon spheres (SCSs)

Solid carbon spheres (SCSs) were synthesized using a modified method reported by Mutuma *et al.*[184] The synthesis of SCSs was done in a vertical CVD reactor fitted with a quartz tube (2.4 cm i.d. × 1.15 m length). Typically, Ar gas (99.99 % purity) at 550 sccm from a gas delivery line was allowed to pass through the quartz tube and flow through the bubbler as the reactor was heated to 1000 °C at 10 °C/min. Once the temperature of the furnace reached 1000 °C, acetylene (C_2H_2, 99.99 % purity) gas (25 sccm) from another delivery line was introduced to the reactor, and the reaction was allowed to proceed for 2 h and the SCSs product was collected in a 3 L round bottom flask. After 2 h, the product in the round bottom flask was purified by a Soxhlet extraction method where 200 mL toluene was heated at a temperature of 120 °C for 24 h. The product was dried on a paper towel and the SCSs sample was placed in an oven (80 °C, 6 h) for further drying.

3.2.6 Incorporation of NCdots onto the surface of SSs, HCSs and SCSs

The NCdots were loaded on the surface of the SSs, HCSs and SCSs using modified previous methods.[156,108] Typically, two solution mixtures were prepared in two different beakers. A desired amount of NCdots (5 %, 10 %, 15 % and 20 wt. %) were dispersed in a mixture of 20 ml water and 10 mL of ethanol under sonication for 15 min. In a second separate beaker, 100 mg of the support (SSs, HCSs and SCSs) was added to a mixture of NH_4OH (1 mL) and H_2O (10 mL) and the mixture was sonicated for 15 min. The two mixtures containing the support and NCdots were combined, sonicated for 15 min, and then stirred overnight at room temperature. This was followed by drying of the product in a rotary evaporator at 60 °C and then in an oven at 100 °C for 6 h.

3.2.7 Characterization techniques

Various techniques were used to investigate the optical, physical, and chemical properties of the synthesized materials. The characterization techniques used for the analysis of all synthesized materials in this project are listed below.

3.2.7.1 Transmission electron microscopy

Transmission electron microscopy (TEM) was used to probe the morphological properties (size, shape, diameter, and arrangement of particles) of the synthesized materials using an FEI Technai G^2 Spirit electron microscope operated at 120 kV. The synthesized samples were dispersed in water or ethanol, sonicated for 5 minutes and thereafter a drop of the solution was added to a carbon-coated copper grid which was allowed to dry at room temperature. Thereafter, the carbon-coated copper grid was taken for analysis using TEM. The obtained images during analysis were used to determine particle size using ImageJ software where more than 100 diameters of the particles were measured.

3.2.7.2 Scanning electron microscopy

Further morphological features of the synthesized materials were investigated using scanning electron microscopy (SEM). The samples were prepared by adding a small sample on a carbon tape which was attached to a solid holder. This was followed by coating the sample with 2 layers of Au and C to inhibit the conduction of the samples. Thereafter, a ZEISS SIGMA 03-09 FE-SEM at 20 kV was employed.

3.2.7.3 Fourier transform spectroscopy

The functional groups on the materials were recorded using Fourier Transform Infrared (FT-IR) spectroscopy in the range 4000 – 500 cm^{-1} (64 scans) on a Bruker Tensor 27 FT-IR spectrometer. No sample preparation was done before analysis. Before analysis, the instrument was cleaned with isopropyl alcohol solution and then a background check was scanned without any sample. This was followed by adding a small portion of solid samples to the sample holder for analysis, no sample preparation was done (no palletization).

3.2.7.4 X-ray photoelectron spectroscopy

The elemental composition and binding energies of the samples were determined using X-ray photoelectron spectroscopy (XPS). This was done using a Kratos Axis Ultra DLD XPS spectrometer equipped with both an Al (monochromatic) and dual Al/Mg anode and a charge neutralizer operated at 1486.7 Ev (working pressure of $<10^{-8}$ mBar). The samples were sent and analyzed at the National Metrology Institute of South Africa (NMISA), CSIR, Pretoria.

3.2.7.5 CHNS analysis

The Cdots chemical composition was further complimented with CHNS analysis. The percentage composition of carbon, hydrogen, and nitrogen was determined using a Carlo Erba EA 1108 organic elemental analyzer which makes use of approximately 10 mg of the samples combusted up to 1000 ℃.

3.2.7.5 X-ray diffraction

The purity and crystallinity (materials phase) of the bulk composition of the samples was determined using X-ray diffraction (XRD). This phase identification was done using a Bruker D2 phaser equipped with Cu-Kα radiation (λ = 1.5405 Å), an operating voltage of 30 kV and a current of 10 mA. The samples were crushed into a fine powder and then loaded into a zero-background sample holder and thereafter analyzed at the 2-theta range of 5 -90 °, with 0.026 ° steps.

3.2.7.6 Raman spectroscopy

The purity, vibrational modes, and I_D/I_G ratio of the sp^3 and sp^2 carbons were determined by Raman spectroscopy using a Jobin-Yvon T6400 micro-Raman spectrometer equipped Ar ion laser of 532 nm. The sample to be analyzed (ca. 5 mg) was placed on a glass slide and was kept flat using a spatula before analysis using a Brucker Senterra Laser Raman spectrometer.

3.2.7.7 Thermogravimetric analysis

The thermal stability of the synthesized materials was investigated by thermogravimetric analysis (TGA) using a Perkin Elmer TA TGA Q500. About 10 mg of each sample was placed in a ceramic pan and then placed in an analytic balance of TGA and heated up to a temperature

of 900 °C at a heating rate of 10 °C/min under air. The TGA data and derivative curves (DTA) were obtained simultaneously.

3.2.7.8 Brunauer-Emmet and Teller

The textural properties (surface area, pore-volume, pore diameter) were determined using Brunauer-Emmet and Teller (BET). A Micromeritics Tristar 300 instrument operated at 77 K was used and the samples were degassed at 150 ºC for 4 h under N_2 gas using a Micrometric Flow Prep 060 sample degasser before analysis. Samples were analyzed using either single and multi-point measurements.

3.2.7.9 Ultraviolet-visible spectroscopy

The absorption spectrophotometer was used to determine the absorption wavelength of samples and concentration of MO. Before analysis using an Analytik Jena SPECORD 50 the samples (*ca.* 2 mg) were dispersed in water and sonicated for 5 min. A background run was done using the water which was inside a cuvette.

3.2.7.10 Photoluminescence spectroscopy

The photoluminescence (PL) emissions of the samples were determined using a Varian Cary Eclipse EL04103870 fluorescence spectrophotometer at excitation wavelength varied between 300 to 600 nm. Here, *ca.* 2 mg of each sample was weighed and then dispersed in water using a sonicator for 5 min. Thereafter, a background effect was subtracted using water and the analyte solution inside a cuvette was analyzed at an angle of 5 slits.

3.3. Results

3.3.1 TEM analysis

By definition, Cdots have a diameter ≤ 10 nm. Figure 3.1 shows the TEM images of NCdots and NCdots/support composites. The corresponding particle size distribution of all the samples is given in figure S3.1. Figure 3.1 (a) shows the bare NCdots formed from chitosan having particle sizes ranging from 1 nm to 8.5 nm with the most dominant particles having sizes of 4.8 ± 0.94 nm. The particles were found to be quasi or nearly spherical and were homogeneously distributed with no agglomeration.[104] Figure 3.1 (b) shows the SSs formed by using a modified

Stober method which is based on the hydrolysis of silicon alkoxides that results in the formation of silica species with various shapes and sizes depending on the synthesis parameters used.[185] The SSs were spherically shaped with particle sizes ranging from 280 nm to 460 nm with an average size of 379 ± 38 nm. Figure 3.1 (c) shows the NCdots/SSs composite in which the NCdots have been supported on the surface of SSs and are seen to be well dispersed on the surface of SSs with no agglomeration. The particle sizes of the NCdots on the surface of SSs ranged from 3 nm to 10 nm having average diameters of 7.2 ± 0.99 nm.[119] The HCSs were found to have sizes ranging from 300 nm to 440 nm with average particle size of 380 ± 22 nm (Figure 3.1 d). Figure 3.1 (e) shows the NCdots/HCSs composites i.e., NCdots incorporated on the surface of HCSs. The NCdots were well distributed with minor agglomeration on the surface of spherical HCSs. The sizes of the NCdots on the surface of HCSs ranged from 3 nm to 8 nm with an average diameter of 5.1 ± 0.94 nm which is comparable to the diameter of the bare NCdots.

In figure 3.1 (f) and (g), the TEM images of SCSs and NCdots/SCSs composites are presented. The SCSs were observed to be spherically shaped with particle sizes ranging from 60 to 200 nm with an average diameter of 111 ± 27 nm.[184] The shape and size of SCSs were maintained after incorporation of NCdots on the surface with NCdots maintaining their sizes below 10 nm and having an average diameter of 3.79 ± 0.68 nm. The dispersion of the NCdots onto the support of the SSs, HCSs and SCSs can be attributed to the higher dispersion of NCdots in a mixture of ethanol and water. The addition of ammonia to the solution mixture also facilitated the incorporation and dispersion of NCdots into the surfaces of the support.[156] Furthermore, the dispersion of the NCdots particles onto the surface of the support is in accordance with Derjagin-Laundau-Verwey-Overbeek theory which propounded the instability of smaller particles in the presence of bigger particles, as such the smaller particles (NCdots) binds to the surface of the support (SSs, HCSs and SCSs) and avoid coagulation or agglomeration with each other.[186] In our case, minor agglomeration of NCdots was observed on the surface of HCSs and it was well dispersed on SSs and SCSs. This is likely to be due to the lower concentration of NCdots particles on the surface of the supports.[186]

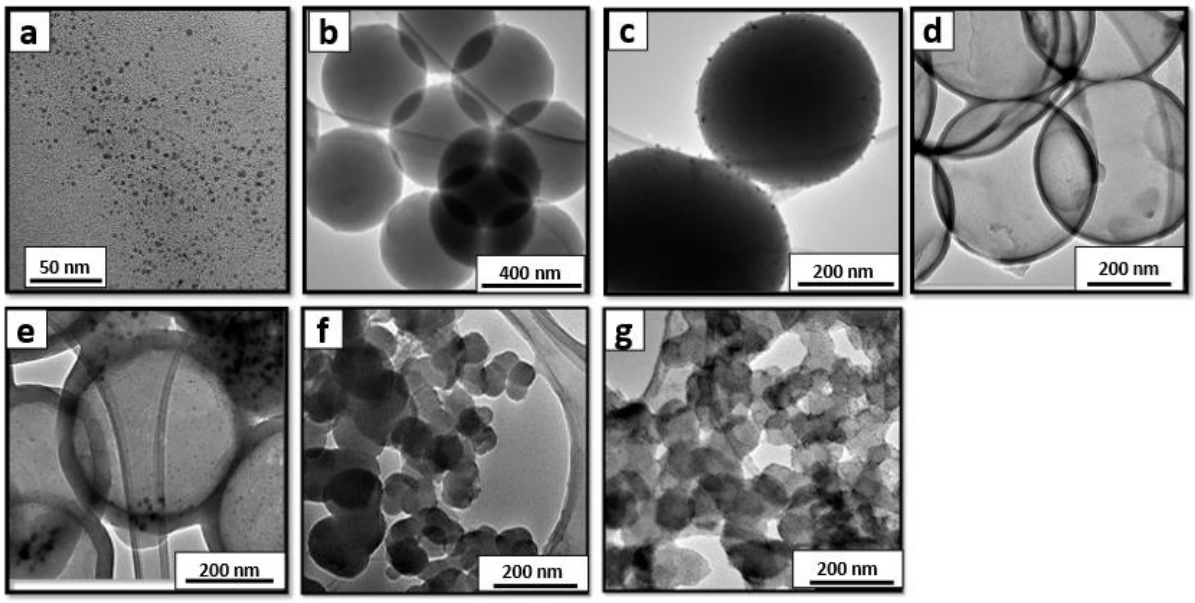

Figure 3.1 TEM images of (a) NCdots, (b) SSs and (c) NCdots/SSs, (d) HCSs and (e) NCdots/HCSs, (f) SCSs and (g) NCdots/SCSs composites at 20 % loading.

3.3.2 FTIR spectroscopy analysis

Fourier transform infra-red (FTIR) spectroscopy was used to determine the functional groups present in the materials. Figure 3.2 (a) shows the stretching and bending vibrations of NCdots, SSs and SSs incorporated NCdots composites (5- 20% incorporation).

NCdots: The as-synthesized NCdots were observed to have a broad peak between 3000-3661 cm^{-1} (centered at 3305 cm^{-1}) which corresponds to the overlap of N-H/O-H stretching vibrations, while the peaks at 2935/2880 cm^{-1} and 918/850 cm^{-1} are ascribed to the C-H stretching and bending vibrations, respectively.[104,102] The COO^-/C=O, C=C, N-H bending mode, C-C and/or C-O-C vibrational modes are observed at 1651/1583 cm^{-1}, 1408 cm^{-1}, 1325 cm^{-1} and 1035 cm^{-1}, respectively.[131,102] The chemical composition and bonding environments of the bare NCdots were also studied using XPS and CHNS (see Figure S2 and Table S3 in the supplementary).

NCdots/SSs: The bare SSs spheres have three peaks at 1069 cm^{-1} and 946/782 cm^{-1} which corresponds to Si-O-Si stretching and bending vibrations, respectively (Figure 2 a).[108,152] After the incorporation of the NCdots on the surface of SSs new peaks associated with NCdots were observed. The intensities of the peaks due to the incorporation of the NCdots onto the surface of the SSs increased with an increase in the NCdots loading, i.e., 20%NCdots/SSs > 15%NCdots/SSs >10%NCdots/SSs > 5%NCdots/SSs (Figure 3.2 b). A comparison of the FTIR

spectra of the 20%NCdots/SSs with the NCdots (and SSs) indicated that the ratio of peaks at ca 1600 cm^{-1} and those at ca 1400 cm^{-1} (I_{1400}/I_{1600}) increased after the addition of the NCdots to the SSs. Peaks that have been lost appear to be due to the COO^- and NH_2 absorptions. A small peak shift also occurred in the 1600 cm^{-1} suggesting some bonding interaction between the NCdots and the SSs support. The peak shift increased slightly as the NCdots loading was increased (5% = 1633 cm^{-1}, 10% and 15 % = 1638 cm^{-1} and 20 % = 1642 cm^{-1}) which further supports an interaction between NCdots and SSs.

NCdots/HCSs: As shown in Figure 3.2 (c), the HCSs have peaks at 1585 cm^{-1}, 1065 cm^{-1}, 796 cm^{-1} corresponding to aromatic rings, C-C and C-H vibrational modes, respectively. The typical peaks for C-H stretching vibrations were observed at 2840/2910 cm^{-1}.[187] Upon incorporation of the NCdots on the surface of HCSs only the HCSs spectrum is observed. Further, the OH/NH and COO^- region due to the NCdots does not grow in intensity with an increase in % NCdots, suggesting that these groups could interact with the HCS surface. The peak positions for NCdots before and after incorporation on the surface of and HCSs show insignificant shifts suggesting limited interaction of NCdots with the HCS surface (see table S3.2).

NCdots/SCSs: The NCdots were also incorporated on the surface of the SCSs with different loadings (5 % to 20 %) (figure 3.2 d). The functional groups detected for SCSs using FTIR were at 1195 cm^{-1}, 1110 cm^{-1}, 1047 cm^{-1}, and 887 cm^{-1}, corresponding C-O, C-C, C-H bending vibrations, respectively.[188] Upon incorporation of NCdots on the surface of SCSs, a slight increase in the peaks with increased NCdots loading is observed at 1455 cm^{-1}, 1195 cm^{-1}, 1047 cm^{-1} and 887 cm^{-1} corresponding to C=C, C-O, C-C/C-O-C and C-H bending vibrations. In summary, the IR data indicate an interaction between the SSs and the NCdots, but the small peaks observed when the NCdots are supported on carbon (HCSs and SCSs) do not allow for conclusions to be drawn on interactions with these supports.

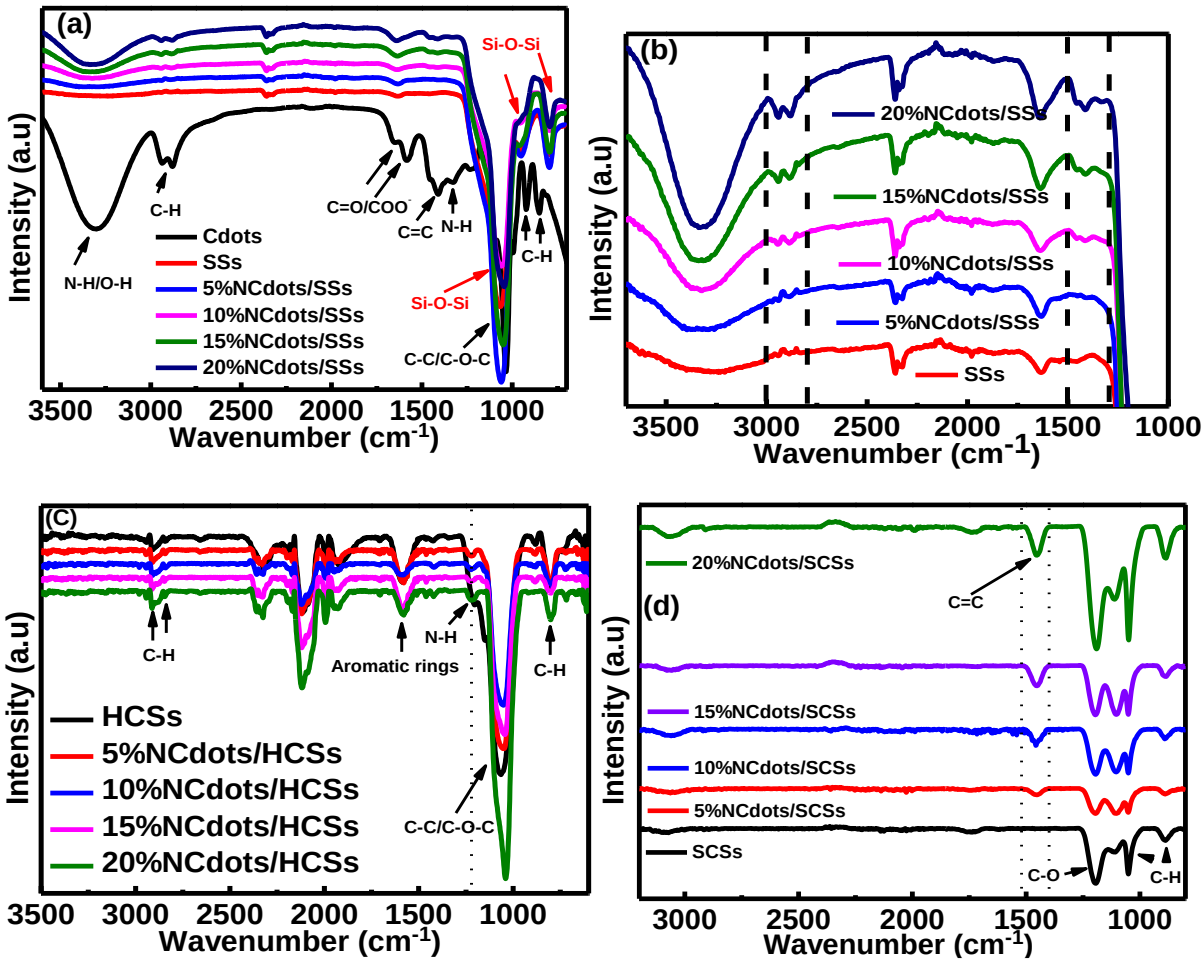

Figure 3.2 FTIR spectra of (a) NCdots and NCdots/SSs, (b) zoomed spectra of NCdots and NCdots/SSs, (c) HCSs and NCdots/HCSs and (d) SCSs and NCdots/SCSs composites.

3.3.3 XRD analysis

Figure 3.3 (a) shows the XRD reflections of chitosan and the NCdots. Chitosan has two reflection peaks at 10.5 and 19.8 ° which are assigned to the amorphous and crystalline carbon framework, respectively.[104] As shown in figure 3.3 (a), the NCdots have a broad reflection peak at 20.7 ° due to the presence of amorphous carbon which indicates that chitosan was fully carbonized.[104] The peak broadness is due to the highly disordered or amorphous carbon material, similar to the (200) planes of amorphous carbon.[129,104,110]

NCdots/SSs: Figure 3.3 (b) shows the XRD reflections of SSs and the NCdots/SSs composites. The broad reflection at 23.3 ° corresponds to the presence of amorphous SSs.[108] Upon incorporation of NCdots on the surface of the SSs the peak shifts slightly to lower 2θ values of

22.6 ° which is caused by the presence of the NCdots. The SSs spectrum overwhelms that of the NCdots so nothing more can be said about these composites.

NCdots/HCSs: Figure 3.3 (c) shows the reflections of the HCSs which have a broad amorphous carbon peak centered at 23 °.[189] After incorporation of NCdots on the surface of HCSs the peak has broadened due to the presence of the NCdots.

NCdots/SCSs: The XRD reflections of SCSs and the NCdots/SCSs composites can be observed in figure 3.3 (d). The SCSs have two reflections (25.2 ° and 43.9 °) which were ascribed to the graphitic planes (002) and (001), respectively.[188] After the incorporation of the NCdots on the surface of SCSs a new shoulder-like peak is observed at 20.8 ° for all composites which grew with NCdots loading. The peak position did not change when compared to the unsupported NCdots indicating no change in the size of the carbon domains.

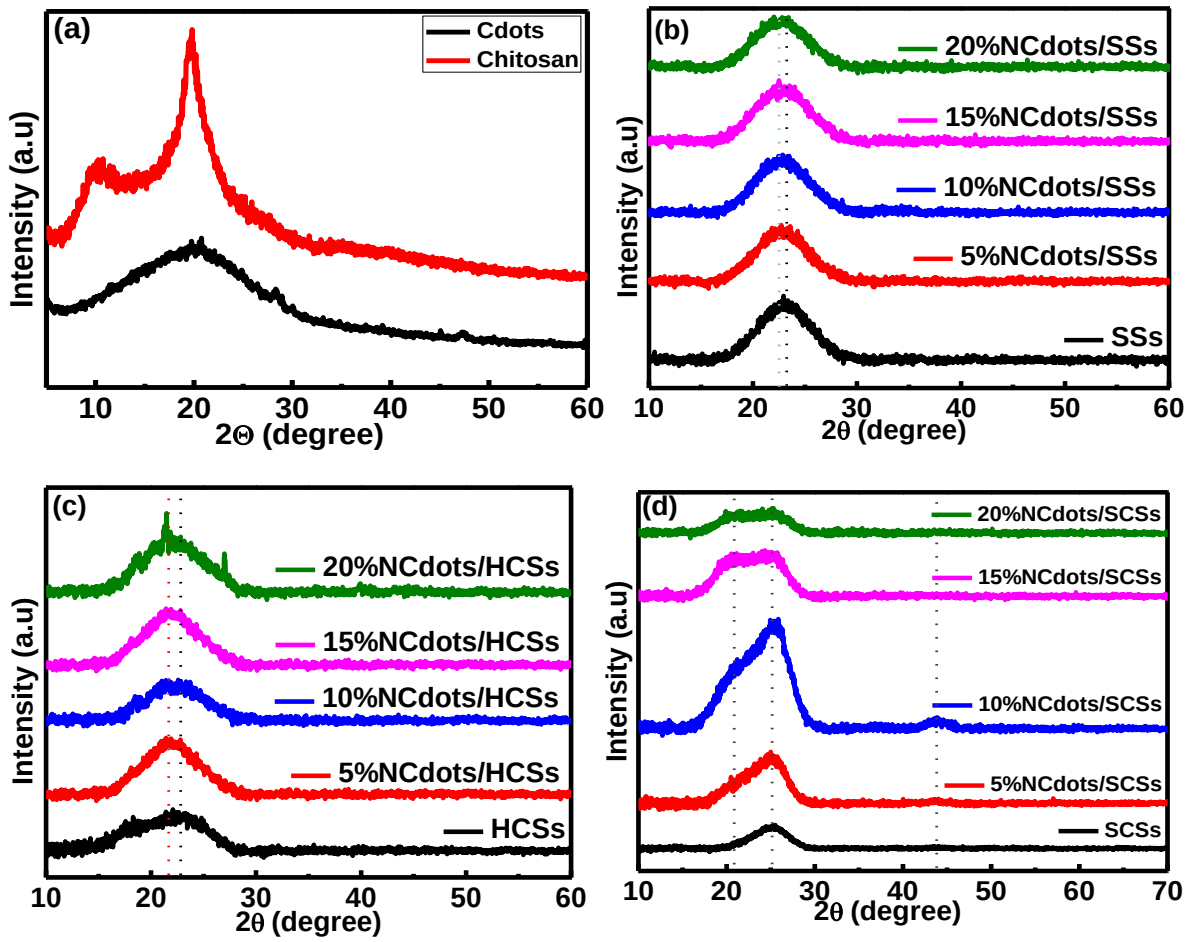

Figure 3.3 XRD reflections of (a) chitosan and NCdots, (b) SSs and NCdots/SSs composites, (c) HCSs and NCdots/HCSs composites and (d) SCSs and NCdots/SCSs composites.

3.3.4 TGA and DTA thermograms

The thermal stability of the new materials is illustrated by the TGA and DTA thermograms in figure 3.4. The thermal stability of NCdots was demonstrated by the TGA and DTA profiles which show two major weight loss steps (figure 3.4 (a)). The gradual decomposition and loss of mass observed at 230 °C (39.5 %) is due to the loss of functional groups such as hydroxyl, carboxylic, carbonyl, amines, and carbon dioxide; these functional groups were identified in the FTIR spectra. The second weight loss at 620 °C is ascribed to the decomposition of the carbon part of the NCdots (surface and core carbons).[190]

NCdots/SSs: The thermal stability of the SSs and the NCdots/SSs composites are shown in figure 3.4 (b). A 5 % weight loss for the SSs occurred up to 100 °C and is assigned to loss of moisture while the weight loss from 350 °C to 500 °C (~8 %) is attributed to structural rearrangement and/or loss of hydroxyl groups.[191] The TGA curves for the NCdots/SSs composites are shown in figure 3.4 (b). All composites show a weight loss of about 5 % that occurred up to 100 °C due to moisture on the surfaces. Two other decomposition steps were observed between 150 °C to 240 °C and 350 to 500 °C that is due to the loss of functional groups and carbon structures from the incorporated NCdots. The first decomposition step due to the loss of functional groups indicates a 4%, 6%, 8% and 15% weight loss for 5%NCdots/SSs, 10%NCdots/SSs, 15%NCdots/SSs and 20%NCdots/SSs composites, while the second decomposition peak caused by carbon structure decomposition has ~5% weight loss for all composites. In addition to TGA, DTA thermograms are plotted in figure 3.4 (c). All composites showed two peaks between 110 °C to 220 °C (centered at 167 °C, 172 °C, 181 °C and 182 °C for 5%, 10 %, 15 % and 20 % NCdots incorporation) and 240 °C to 400 °C (centered at ~330 °C) corresponding to the decomposition of functional groups and carbon structure of the NCdots, respectively. In all composites, as expected the intensity of both peaks increased as the amount of NCdots increased. Of note are (i) the lowered temperature of carbon decomposition and (ii) the change in the intensity ratio of the carbon peaks on the silica. This suggests an interaction between the silica and the carbon.

NCdots/HCSs: Figure 3.4 (d) and (e) show the TGA and DTA decomposition profiles of HCSs and NCdots/HCSs composites, respectively. The TGA curves for HCSs show one major weight loss between 345 °C to 665 °C centered at 540 °C which is allocated to the complete decomposition of the carbon structure (figure 3.4 d).[189] After incorporation of NCdots on the

surface of the HCSs to form NCdots/HCSs composites, two new peaks were observed between 120 °C to 240 °C and 260 °C to 380 °C which were ascribed to be due to loss of functional groups and the carbon structures associated with the NCdots. As seen in the DTA data (figure 3.4 e), the thermograms for decomposition of functional groups from NCdots, the 5% loaded material has peaks centered at 198 °C and 305 °C while the peaks are centered at 188 °C and 330 °C for 10 % to 20 % loaded material. The peaks for the carbon decomposition from HCSs were shifted to a lower temperature (510 °C) for the 5 % NCdots loading and a higher temperature (HCSs = 540 °C) for the 10% to 20 % material, it is clear that the thermal behavior of the NCdots is influenced by the HCS support and that the decomposition of the carbon onto the HCSs after removal of the functional groups from the HCSs leads to a more stable carbon at higher loading (10% to 20 %). This might be caused by kinks or rough surfaces present on HCS in which NCdots are trapped which results in an increased decomposition temperature.[192]

NCdots/SCSs: The TGA and DTA decomposition profiles of SCSs and NCdots/SCSs composites are shown in Figures 3.4 (f) and (g), respectively. The TGA curve for SCSs alone shows one peak with the DTA thermogram peak centered at 675 °C resulting from the carbon structure decomposition.[184] Upon incorporation of NCdots on the surface of SCSs new peaks were observed at various decomposition temperatures. In all the NCdots/SCSs composites, some moisture loss (2 % to 8%) loss is observed below 100 °C. Two peaks are also observed between 150 °C to 240 °C and 310 °C to 380 °C from the TGA curves which are ascribed to loss of surface functional groups, core functional groups and the carbon structure resulting from incorporated NCdots (figure 3.4 f). The 5% loaded sample shows a shift in the peak at 180 °C relative to the other samples. As shown in figure 3.4 (g), the DTA thermograms showed a significant peak shift toward lower temperature as the NCdots loading increased. The DTA peaks for SCSs is centred at 675 °C while for 5%NCdots/SCSs, 10%NCdots/SCSs, 15%NCdots/SCSs and 20%NCdots/SCSs composites are centred at 615 °C, 515 °C, 490 °C, 475 °C, respectively. The remarkable feature here is that the NCdots have reduced the carbon oxidation reaction. Interestingly, an increase in NCdots loading on the surface of the supports resulted in increased weight loss and peak intensities as observed by TGA and FTIR, respectively.

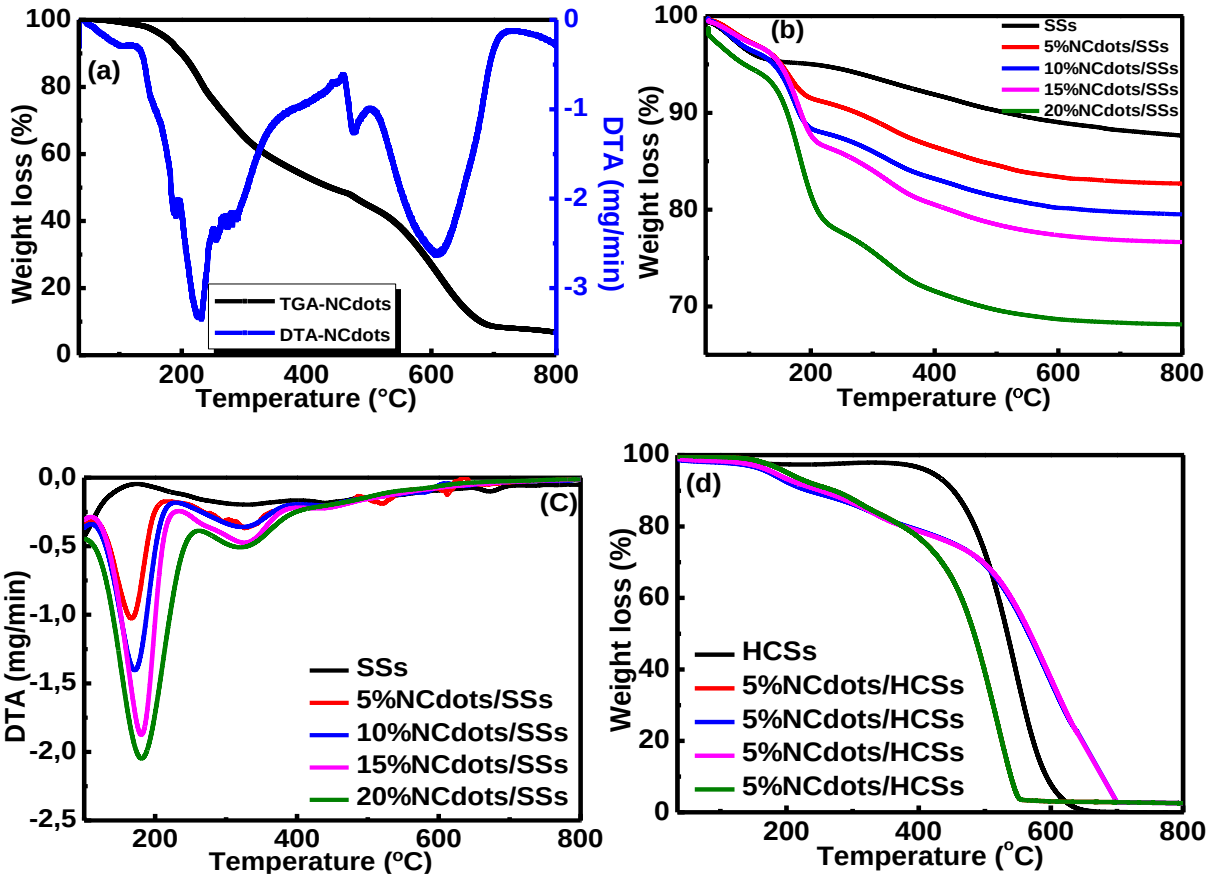
(a)
Weight loss (%)
DTA (mg/min)
Temperature (°C)
TGA-NCdots
DTA-NCdots
(b)
Weight loss (%)
Temperature (°C)
SSs
5%NCdots/SSs
10%NCdots/SSs
15%NCdots/SSs
20%NCdots/SSs
(C)
DTA (mg/min)
Temperature (°C)
SSs
5%NCdots/SSs
10%NCdots/SSs
15%NCdots/SSs
20%NCdots/SSs
(d)
Weight loss (%)
Temperature (°C)
HCSs
5%NCdots/HCSs
5%NCdots/HCSs
5%NCdots/HCSs
5%NCdots/HCSs

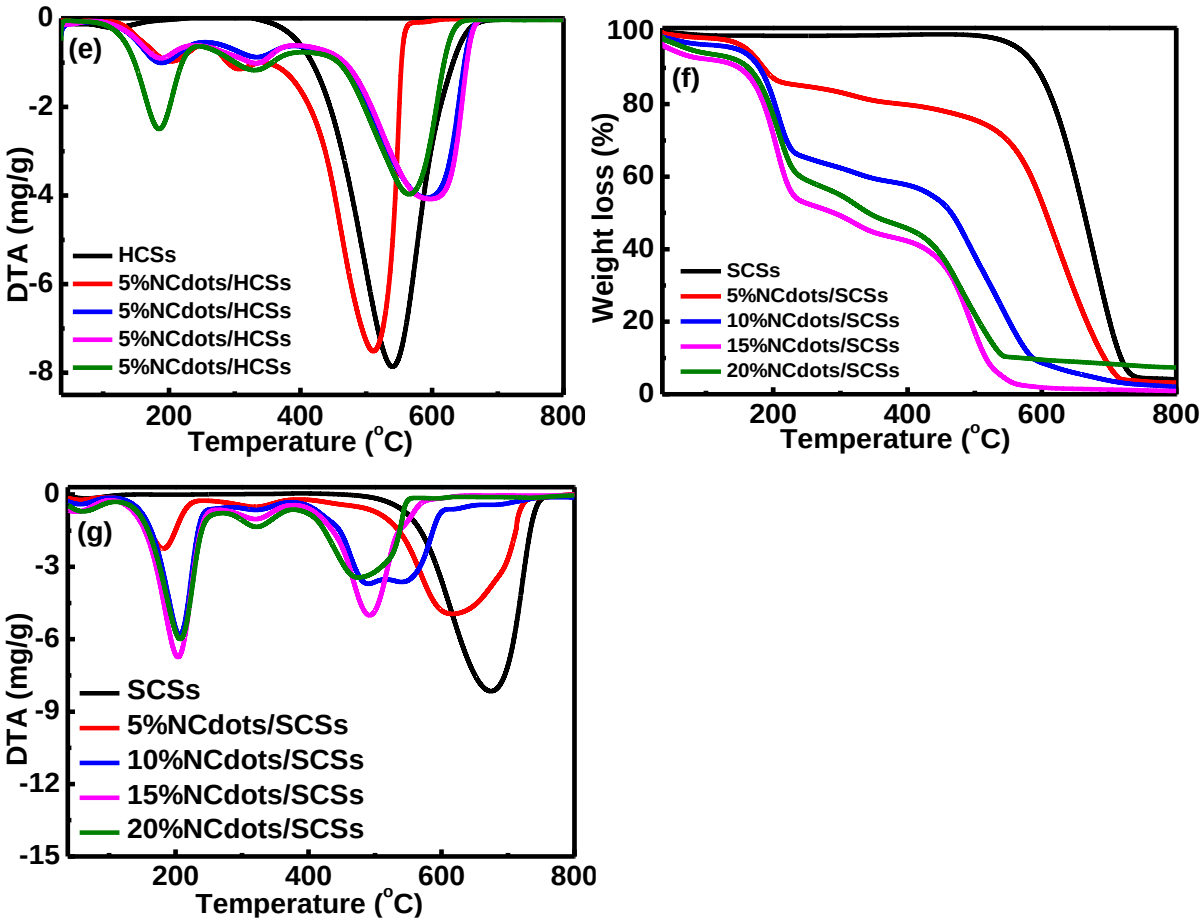

Figure 3.4 TGA curves and DTA thermograms of (a) NCdots, (b) TGA and (c) DTA of SSs and NCdots/SSs composites, (d) TGA and (e) DTA of HCSs and NCdots/HCSs composites, (f) TGA and (g) DTA of SCSc and NCdots/SCSs composite.

3.3.5 PL spectroscopy

The optical properties of the NCdots, NCdots/SSs, NCdots/HCSs and NCdots/SCSs composites were studied using PL spectroscopy. Figure 3.5 (a) and the insert shows the PL spectrum of NCdots probed at excitation wavelengths between 350 nm to 500 nm at 10 nm intervals.[193] The PL spectrum for all composites showed a typical red shift of the peak maximum as the excitation wavelength increased.[194,195] As shown in figure 3.5 (a), the maximum emission peak of the NCdots was observed at 510 nm with FWHM (full width at half maximum) of 101 nm when the excitation wavelength of 440 nm was used. Upon excitation with wavelengths from 350 nm to 440 nm an increase in peak intensity, a redshift, and an excitation-dependence of the NCdots is observed.[180] Thereafter, a decrease in peak intensity upon excitation with wavelengths above 450 nm to 500 nm is noted (insert). The excitation-dependent and redshift optical properties were similar to data reported in previous studies for bare Cdots.[104,169] Here the PL emissions

data are attributed to optical selection at different defects states, non-radiative recombination of excitons at defects sites and functional groups present in the NCdots.[195] [196,197]

The PL spectra of the differently loaded NCdots (5%-20 wt. %) on the different supports are shown in figure 3.5. Upon incorporation of the NCdots on the surface of the SSs, HCSs and SCSs, the maximum PL emissions (and FWHM) were observed at 448 nm (106 nm), 422 (101 nm) nm and 343 nm (75 nm) when the excitation wavelengths of 380 nm, 340 nm and 300 nm were used for the NCdots/SSs, NCdots/HCSs and NCdots/SCSs composites, respectively. Furthermore, when an excitation wavelength of 380 nm was used on NCdots, NCdots/SSs, NCdots/HCSs and NCdots/SCSs composites the PL emissions were observed at 472 nm, 450 nm, 445 nm and 440 nm, respectively. When using an excitation wavelength of 400 nm, the PL emissions were observed at 486 nm, 466 nm, 460 nm, and 462 nm for NCdots, NCdots/SSs, NCdots/HCSs and NCdots/SCSs, respectively. The interactions between NCdots and the support differ and have resulted in the different maximum PL emissions.

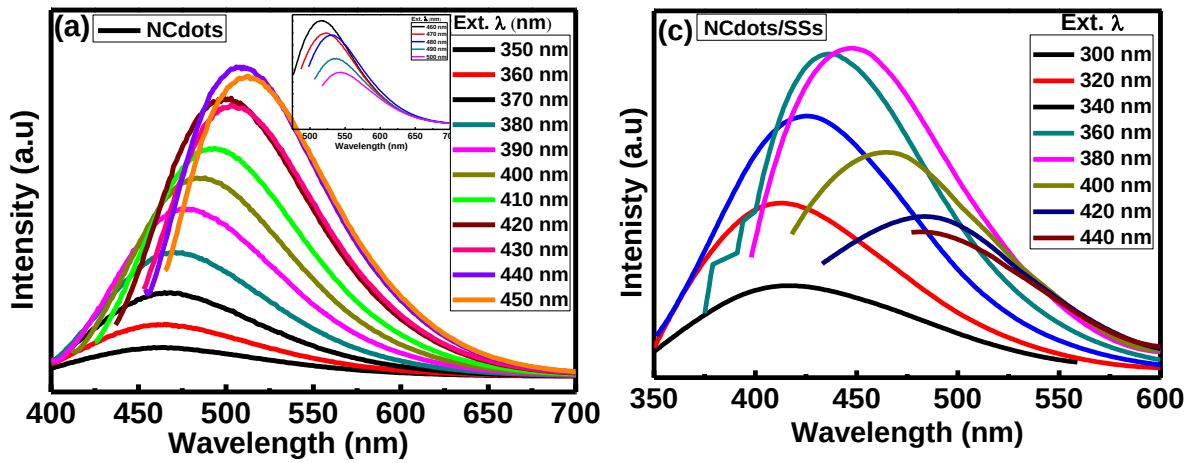

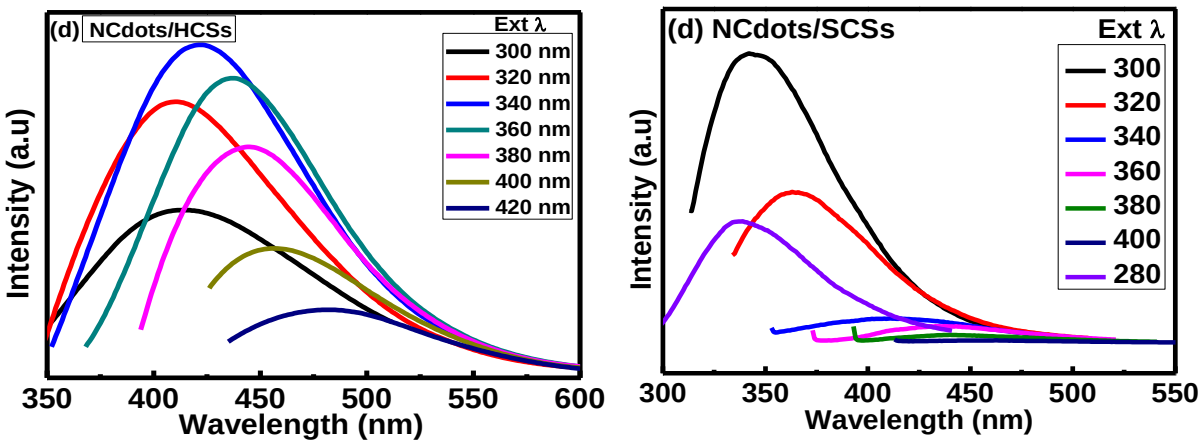

Figure 3.5 The PL spectrum of (a) NCdots and its insert, (b) SSs and NCdots/SSs composites, (c) HCSs and NCdots/HCSs composites and (d) SCSs and NCdots/SCSs composites at 20 % loading.

The real-time UV-vis of the NCdots, NCdots/SSs, NCdots/HSCs and NCdots/SCSs were observed using 365 nm lamp illumination. Figure 3.6 represents the images of the materials under natural and UV lamp illumination. All materials were glowing under UV lamp illumination and light blue emission was observed for bare NCdots and NCdots/SSs, while dark blue emission was observed for NCdots/HSCs and NCdots/SCSs.

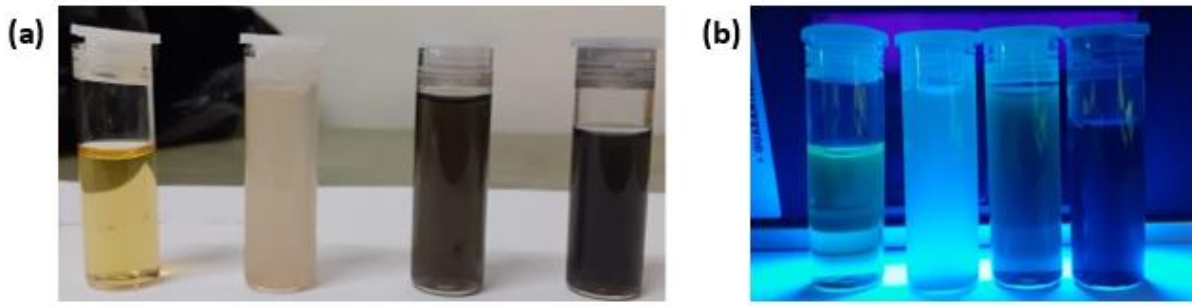

Figure 3.6 Image of materials taken under (a) natural light and (b) UV lamp illumination at 365 nm. Images from left to right are NCdots, NCdots/SSs, NCdots/HCSs and NCdots/SCSs.

The effect of the support on the PL emissions of the NCdots was further studied by observing the relative photoluminescent quantum yield (PLQY) using the PL excitation wavelength of 350 nm and absorbance data (Figure 3.7 and Table S3.4). The PLQY of the NCdots and the composites were determined by using quinine sulphate (QS) as reference (see table S3.5 for integrated PL emission intensities and absorbance data). The concentrations of the NCdots, NCdots/SSs composites, NCdots/HCSs composites, NCdots/SCSs composites and QS were similar to those used in a previous literature report.[166] As shown in Figure 3.7 (a), the PLQY of

the bare NCdots was calculated to be 34 % which is higher and comparable to earlier reported data.[166,104] The percentage PLQY for the 5%NCdots/SSs, 10%NCdots/SSs, 15%NCdots/SSs and 20%NCdots/SSs composites was calculated using equation S3.1 and S3.2 and was 15.4 %, 42 %, 33.7 % and 35.3 %, respectively. The PLQY for 5%NCdots/HCSs, 10%NCdots/HCSs, 15%NCdots/HCSs and 20%NCdots/HCSs composites was 5.1 %, 6 %, 7.8 % and 13 %, respectively, while the PLQY for 5%NCdots/SCSs, 10%NCdots/SCSs, 15%NCdots/SCSs and 20%NCdots/SCSs composites was calculated to be 2 %, 3.2 %, 4.6 % and 7.5 %, respectively. The PLQY when NCdots are supported on HCSs and SCSs are lower than that supported on SSs. A decrease in PLQY was also observed in a previous study when polymer NCdots were supported/entrapped on a carbon support.[158] The decrease in PLQY as a result of decrease in PL emission can be attributed to higher content of graphitic carbon on the support of the HCSs and SCSs. The core carbon of the HCSs and SCSs supports is likely to inhibit charge carrier recombination which greatly supress the radiative recombination of the NCdots. This is supported by the CHNS composition data whereby an increase in carbon content resulted in decreasing PL intensity. The carbon content for NCdots/SSs, NCdots/HCSs and NCdots/SCSs was 8.26 %, 52.14 % and 55.18 %, respectively. In addition, the higher PLQY and intense PL emission in bare NCdots is attributed to the higher content of nitrogen groups (6.95 %), (see table S3).

The differences in PL emissions when NCdots are supported on SSs, HSCs and SCSs are consistent with the synthesized NCdots having multistate (size, defects or functional groups and core carbon) that are responsible for the PL emissions.[108,198] In summary, the optical properties of NCdots are influenced by using different supports, as seen by the changes in the PL maximum emissions and PLQY of bare NCdots and NCdots supported onto SSs, HCSs and SCSs surfaces.[119,199]

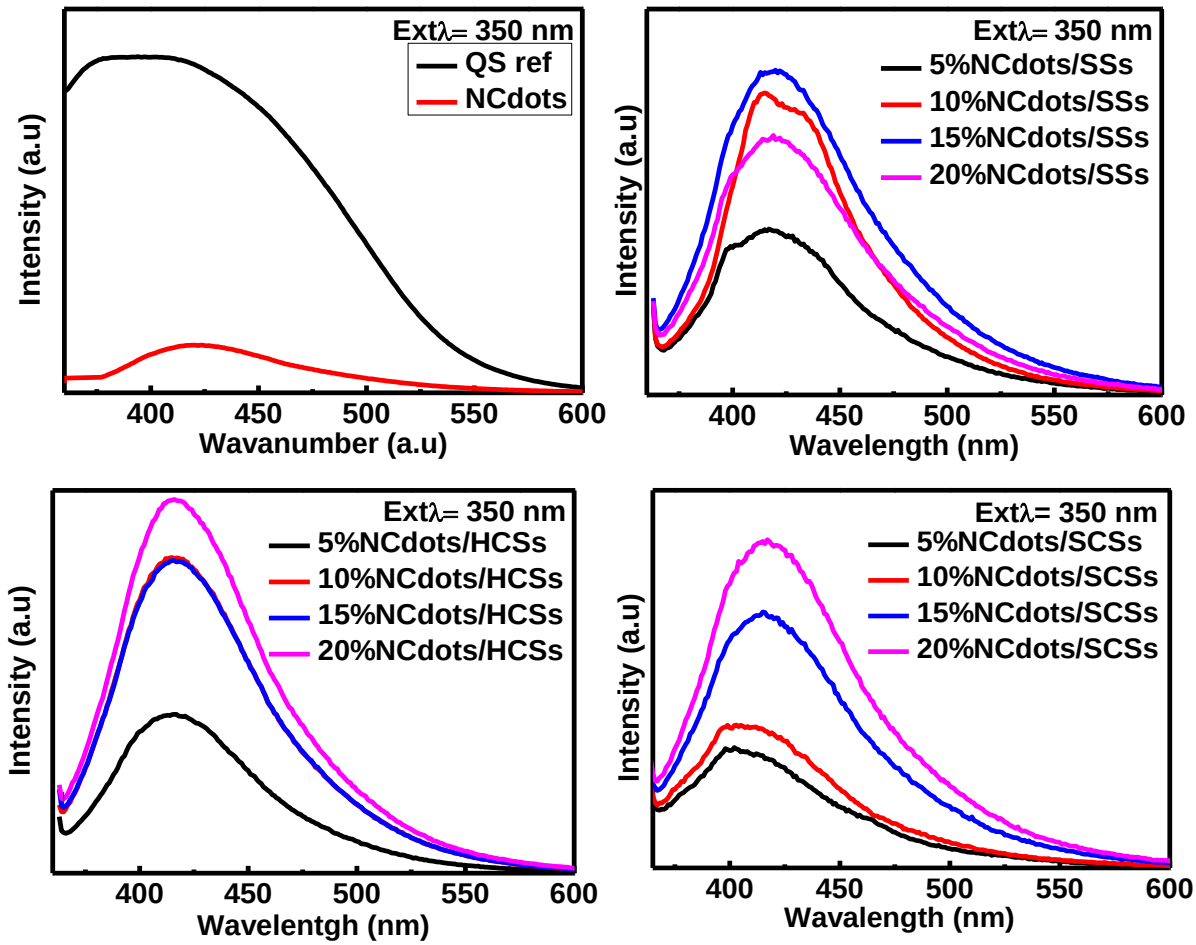

Figure 3.7 The PL spectrum taken at excitation wavelength of 350 nm (used for PLQY calculations), (a) NCdots and Quinine sulphate (QS reference), (b) NCdots/SSs composites, (c) NCdots/HCSs composites and (d) NCdots/SCSs composites.

The N-doped Cdots used in this study had the same size distribution implying that the PL changes would be only due to the support, surface-support interactions and support functional groups. Previous reports have demonstrated that the PL emissions of Cdots can also be changed by varying solvent pH and changing the solvent or water content.[165,169] A decrease in PL emission (lowered PLQY) has often been observed. For example, Cdots supported on metal-organic frameworks (MOFs) showed a decreased PLQY even though the Cdots maintained their shape and functional groups.[165] A study by Chowdhury *et al.*, demonstrated that the addition of metals to Cdots (Cdots/Au and Cdots/Ag) enhanced the Cdots PL emissions via the plasmonic effect.[169] In addition, the photoluminescence of Cdots was modified by varying the Cdots surface amino-groups density.[130] Thus the fluorescent properties of Cdots can be altered without changing the Cdots structure/shape and maintaining surface groups.

In the current study, TEM and XRD analysis, not unexpectedly, suggested little changes in the shape and size of the bare NCdots after being supported on both silica and carbon supports. The FTIR data are suggestive of interactions between the NCdots and the supports, especially as seen for the NCdots/SSs composites. TGA data showed remarkably different data for the NCdots on the three different supports. The NCdots-support interactions also led to significant changes in the photo-luminescent properties of the bare NCdots (maximum PL emissions and PLQY values) relative to the NCdots/support composites. The NCdots supported on SSs showed an enhanced PLQY as compared to carbon support which can be attributed to the Si-O(H) groups as suggested in previous studies. In addition, the silica supports have been reported to inhibit the self-quenching in Cdots.[200,201,202]

The changes in maximum PL emissions and the lower PLQY when NCdots are supported on HCSs and SCSs can be related to the NCdots functional groups, different interactions between NCdots and support or the existence of photoinduced electron transfer (PET) from Cdots to support.[203] PLQY of polymer NCdots supported on carbon support was lowered with no clear explanation being given.[158] While another explanation is drawn from a previous study of NCQDs/TiO_2 composites in which the lower PLQY was attributed to the injection of photogenerated electrons from Cdots to TiO_2.[162] It has been reported that the photoluminescence of Cdots can be quenched by electron acceptor or donor molecules in solution, with photoexcited Cdots being very good electron acceptor or donor.[204] In here, the lower PLQY when NCdots are supported on carbon supports (HCSs and SCSs) can be explained to be resulting from a possibility of photoinduced electron transfer from NCdots to carbon support (mainly caused by similar bandgap or the zig-zag of the surface or core carbon framework). This implies that the surface sites of the carbon support facilitate the trapping of the photoinduced electrons and holes from NCdots by acting as either electron acceptor or donor that lead to lower PL emission or reduced PLQY.[204,205] The PL emission intensity when NCdots are supported on a carbon support, is weaker due to the graphitic carbon of the supports which suppress the radiative recombination processes of the photoinduced electron/holes of the NCdots, as such the PLQY data indicates that the carbon support (HCSs and SCSs) are less effective than silica support at enhancing PLQY.[206]

The major drawback that limits the application of NCdots in solid-sate is their fluorescence self-quenching or aggregate-induced quenching.[202] This study has demonstrated a common and facile method for incorporation and well dispersion of the NCdots on the surface of SSs, HCSs

and SCSs. The NCdots/support nanocomposites demonstrated fluorescence emission properties and can be recommended for application in photonics, optoelectronics devices and photochemistry.[69]

3.5 Conclusions

In summary, nitrogen-doped carbon dots having a size below 10 nm have been synthesized by hydrothermal carbonization methods using chitosan as both carbon and nitrogen precursor. The study demonstrated a systematic method for the incorporation and distribution of NCdots on the surface of silica spheres, hollow carbon spheres and solid carbon spheres. The coagulation of NCdots on the surface of supports was suppressed by the mixture of ammonia, ethanol and water, and the lower concentration of NCdots facilitated the dispersion of the NCdots. The strong PL excitation dependence of bare and supported carbon dots was observed when different PL excitation wavelengths were used. The incorporation of the NCdots on the surface of silica spheres, hollow carbon spheres and solid carbon spheres was observed to influence the maximum PL emissions and the PLQY with the silica support being found to induce PLQY values than the carbon supports.

3.6. Supporting information: Appendix A

Chapter 4

Encapsulation of carbon dots prepared from glycerol and urea inside hollow carbon spheres

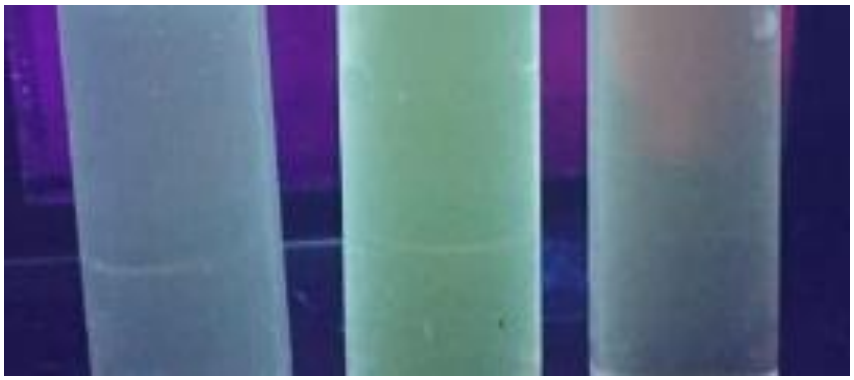

Abstract

The ultra particle size of carbon dots (≤ 10 nm) poses a challenge for their potential application due to the formation of aggregates when in solid-state, difficult to separate and re-use. Herein, we demonstrate a promising "ship-in-a-bottle" approach for the synthesis and encapsulation of carbon dots (Cdots) made from glycerol (GCdots) and nitrogen functionalized Cdots made from glycerol and urea (GUCdots) inside the hollow cavity of hollow carbon spheres (HCSs) via microwave-assisted technique. The properties of GCdots@HCSs and GUCdots@HCSs composites were investigated using TEM, Raman, FTIR, UV-vis, steady-state, time-resolved PL spectroscopy, and real-time illumination. The composites revealed an excitation-dependency nature under different PL excitation wavelengths and emitted at different wavelengths as compared to untrapped Cdots. A solvent-dependent nature or tunable PL emissions was observed when the composites were dispersed in water, acetone, and hexane. The shift in peak position was attributed to solvent polarity, hydrogen bonding, and dipole-dipole interactions between solvents and encapsulated Cdots surface states. Acetone treatment exhibited a higher bathochromic shift and induced peak intensities. Time-resolved spectroscopy revealed multi-decay steps and was best fitted to tri-exponential decay and the lifetime decays of the excited states in Cdots were greatly influenced by the HCSs support. The data showed that the surface states or functional groups of the encapsulated Cdots were the main components responsible for PL emissions.

Keywords: Carbon dots, "Ship-in-a-bottle", wavelength dependency, solvatochromism, solvent-dependent

4.1. Introduction

The superior optical properties in Cdots have attracted many researchers owing to their promising potential application in many scientific fields such as sensing, catalysis, nanomedicine, imaging, and/or probing of cells or metals.[205,207,208] However, their strong fluorescent emissions can be drastically reduced, quenched, or be tuned when Cdots state is changed from solution to solid due to resonance energy transfer or direct $\pi \rightarrow \pi$ interactions.[156,62] The quenching of their fluorescent emissions is a major concern that needs to be addressed for possible applications, especially in the fields that require solid-state photoluminescent emissions.[62] So far, major exploration of fluorescent properties has been done

using Cdots in a solution state which is not sufficient for their potential applications in fields such as photoelectronic devices and optronic sensors. In addition, Cdots are not easy to separate from solution due to their ultra-small size and they are highly hygroscopic, which questions their potential use and reusability in solid-state applications.[209,172]

To date, various supports structures such as starch, polymers, structured carbons and silica xerogel/nanoparticles have been used for the realization of fluorescent emissions of Cdots in their solid-state.[145,199] To this end, silica support matrix has been reported to exhibit good dispersion and induces fluorescent emissions in solid-state Cdots.[181] The enhancement of fluorescent emissions translates to better quantum yield (QY) and can open doors for the potential application of solid-state Cdots. However, the incorporation of Cdots on silica supports does not prevent the movement and collision of Cdots particles, especially those supported on the surfaces. As such, the Cdots particles tend to form aggregate which results in self-quenching of their fluorescent emissions. Other than silica supports, various carbon matrices such as carbon nitride,[210] carbon nanotubes, hollow carbon spheres, solid carbon spheres,[209] carbon polymers,[211,157] and biomass have been used to support Cdots and to obtain solid-state composites.[212,167,213] Supporting Cdots on carbon structures has been reported to reduce fluorescent emission which lowers photoluminescence quantum yield.[206] The main cause of reduced fluorescent emission or QY results from factors such as adsorption of photoinduced electrons, or inhibition of radiative recombination by the support due to graphitic carbon of the support.

Hollow carbon spheres (HCSs) emerged as one of the promising carbon support for minimizing the formation of aggregates of metal nanoparticles.[209] HCSs serve as an encapsulating or a caging matrix that confines molecules or metal nanoparticles in which migration or collision of particles is minimized.[209,158] One interesting advantage of encapsulating nanoparticles inside HCSs is that it serves as a nanoreactor and nanoparticles inside the cavity are not lost during application (easy recovery and reusability of the nanoparticles). Chen and co-workers demonstrated a one-step *in situ* method for synthesis of Cdots encapsulated inside HCS having higher QY (~34%) using fish scales and collagen as starting materials. The study offered a strategy for preparing fluorescent HCSs/Cdots composites at a scalable quantity.[166] Another study by Lou et al. demonstrated a method for encapsulation of carbon species inside carbon nitride hollow spheres, however, the luminescence emission intensity became weaker as more graphitic carbon content was increased.[206] One of the remarkable work in which polymer dots were encapsulated inside HCSs cavity was reported by Qiao and co-worker, polymer dots were

encapsulated inside HCSs cavity but the QY of entrapped Cdots were lowered as compared to untapped Cdots.[158] Additionally, drawbacks such as (i) ensuring that the nanoparticles are entrapped inside the shell, (ii) encapsulation of the desired loading inside the shell, and (iii) good distribution of the nanoparticles inside HCSs cavity has been experienced.[206]

The possibility of encapsulation of nanoparticles inside HCSs cavities has motivated this study. Hence, we conducted and demonstrated a promising and alternative method for encapsulation of Cdots inside HCSs cavities using the "ship-in-a-bottle" approach under microwave irradiation. For this, glycerol (GCdots) and the combination of glycerol and urea (GUCdots) were used as starting reagents for the synthesis of oxygen and nitrogen functionalized Cdots. As shown in fig 1, the encapsulation of Cdots was achieved by diffusing the glycerol and urea molecules into the hollow cavity of HCSs through its pores.

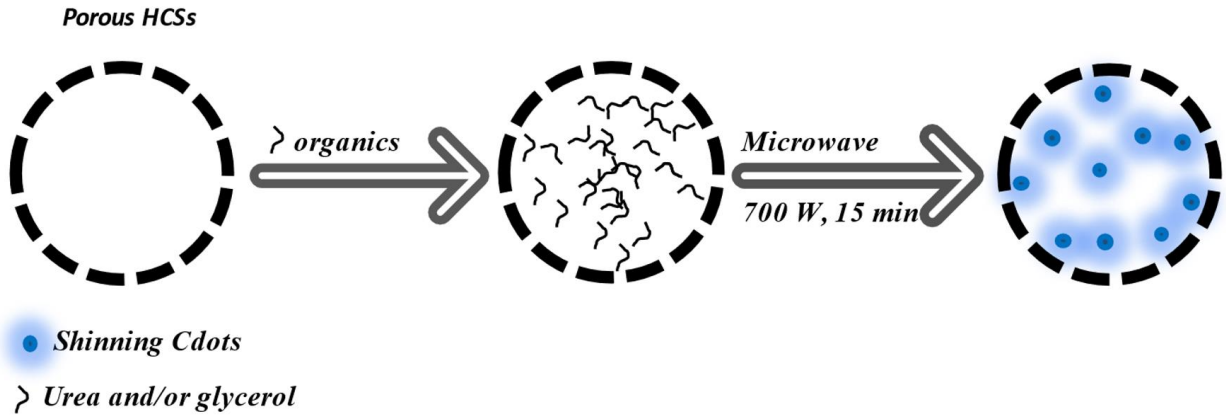

Figure 4.1 Schematic representation for the encapsulation of Cdots inside HCSs.

The optical properties of the obtained composites (GCdots@HCSs and GUCdots@HCSs) when dispersed in water, acetone and hexane were investigated using PL spectroscopy. Dispersion of Cdots in various solvents can be used as a post-modification method for tuning their optical properties and can be used to identify the major constituents responsible for their fluorescent emissions. For example, the shift in the absorption or emission in fluorescent materials arises from factors such as hydrogen bonding and dipole-dipole interactions between the fluorophores moieties and the solvent. The difference in dipole moments between the ground and excited state of the solvent and Cdots can result in stabilizing the excited state depending on the solvent polarity, which can change the energy gap between the highest occupied molecular orbital and lowest unoccupied molecular orbital. The change in the energy gap causes the PL emission to be redshifted to give different emission colors depending on the polarity of the solvent. Here, the solvatochromism study was carried out using water, acetone, and hexane as solvents to

study the effect of the solvents on the fluorescent emissions of the as-synthesized GCdots@HCSs and GUCdots@HCSs composites.

4.2. Experimental

4.2.1. Materials

Glycerol (99 % purity), urea (ACS reagent, 99.0-100.5 % purity), sodium hydroxide (NaOH, 98 % purity) were purchased from Sigma Aldrich. Tetraethyl orthosilicate, (TEOS, 98%, Sigma Aldrich), ammonium hydroxide, (NH_4OH, 25%, Fluka) and Ethanol, (EtOH, 96%, Merck) were used for the synthesis of the silica spheres (SSs). The SSs were coated with resorcinol (99%, Sigma Aldrich), formaldehyde (≥ 34.5 wt. %, Sigma Aldrich,) and hexadecyltrimethylammonium bromide (CTAB; 98%, Aldrich). A 10% hydrofluoric acid (HF; 48%, Associated Chemical Enterprise) solution in water was used for the etching of the silica template. In all reactions, deionized water (resistivity > 18.2 MΩ cm^{-1}) was used as a solvent. All chemicals were used without further purification.

4.2.2. Synthesis of silica spheres (SSs) and HCSs

Synthesis of SSs and HCS was achieved by following similar procedures in chapter 3, section 3.2, subsections 3.2.3 and 3.2.4, respectively.

4.2.3. Encapsulation of Cdots inside HCSs

The encapsulation of Cdots inside HCSs cavities was achieved by using a "ship-in-a-bottle'' approach using a microwave-assisted method for pyrolysis of glycerol and urea (see figure 4.1 for graphitic illustration). The approach used for synthesis and encapsulation of Cdots inside HCSs cavity was achieved by modifying methods established elsewhere.[158,214] Typically, glycerol (3 mL) or a mixture of glycerol and urea (0.5 g were dissolved in 20 mL of 0.1 M NaOH and sonicated for 30 min at 30 °C. Each solution was transferred into a centrifuge tube (50 mL capacity) containing 0.5 g HCSs dispersed in 10 mL water. This was followed by sonication for further 3 hours at 40 °C and stirring overnight to allow the infiltration of the precursor molecules into the cavity of HCSs. Thereafter, the mixture was transferred into microwave tubes (20 mL in each tube) and the synthesis of GCdots and GUCdots was done using a microwave reactor set at 700 W for approximately 15 minutes. The temperature inside the microwave tubes was between 180 °C to 190 °C and thereafter it was allowed to cool to

room temperature. This was followed by filling microwave tubes with a mixture of water/ethanol to disperse the GCdots@HCSs and GUCdots@HCSs composites. The composites were filtered and washed using water (1 L). The filtrate containing untrapped Cdots were microfiltered using a 0.22 µm PVDF membrane. The black powder consisting of the composites was dispersed in water and centrifuged 3 times at 18 000 rpm for 20 min until no Cdots were found at the supernatant matrix. This was to ensure that the remaining Cdots were encapsulated inside HCSs and not at the surface. Finally, the composites were dried at 80 °C for 6 h.

4.2.4. Characterization techniques

Characterization techniques that were used can be found in chapter 3, section 3.2, subsection 3.2.7.

4.3. Results and discussions

The essence of this study was to encapsulate Cdots made from glycerol and urea molecules inside HCSs. As shown in figure 4.1, the "ship-in-a-bottle" or a core-shell strategy relied on the porosity of HCSs to allow permeability of precursor molecules into the cavity of HCSs. The precursor molecules inside the HCSs are pyrolyzed using microwave irradiation to form Cdots. Due to diffusion limitation, not all precursor molecules diffuse into the cavity of the HCSs. Some of the precursor molecules remain outside and form Cdots outside the HCSs under microwave irradiation. The Cdots that are formed outside the hollow cavity are then washed with a mixture of ethanol/water and further centrifuged at 18 000 rpm until there are no Cdots on the supernatant matrix. The only Cdots remaining are those entrapped inside HCSs structure. The diffusion of the precursor molecules was possible via the 2.4 nm mesopores in HCSs, having a specific surface area of 254 m^2/g and pore volume of 0.16 cm^3/g.

4.3.1. TEM images

The microwave-assisted pyrolysis method is very fast and gives nanoparticles with homogeneous size distribution. The glycerol pyrolytic process using microwave processes is known to undergo dehydration, pyrolysis, and crosslinking with some oxygen surface functionalities. In addition, glycerol can also serve as a solvent for urea and allows dissolution without using any strong solvent or harsh synthetic procedure.[215]

The shape and size of the as-synthesized materials were obtained using TEM analysis. Figure 4.2 presents the TEM images of (a) HCSs, (b) GCdots@HCSs and (c) GUCdots@HCSs

composites. As shown in figure 4.2 (a), the HCSs have taken the spherical shape of the SSs template with diameter size ranging from 300 nm to 420 nm having an average diameter size of 366 ± 25 nm, see figure S4.1 for SSs image. Due to fewer and tiny GCdots and GUCdots particles encapsulated inside the HSCs structure, it was difficult to measure their particle size distribution. However, the particle size distribution of GCdots and GUCdots that were not trapped inside HCSs was calculated. The average diameter size of GCdots ranged from 1.5 nm to 5 nm with the most dominant size having a diameter of 3.2 ± 0.7 nm. While the GUCdots had a diameter size ranging from 0.5 nm to 4.5 nm having the most dominant average diameter size of 2.3 ± 0.5 nm. The GCdots and GUCdots were quasi-spherical in shape, with the combination of glycerol and urea resulting in the formation of smaller GUCdots, see Figures S4.1 and S4.2 for TEM images and particle size distribution, respectively.

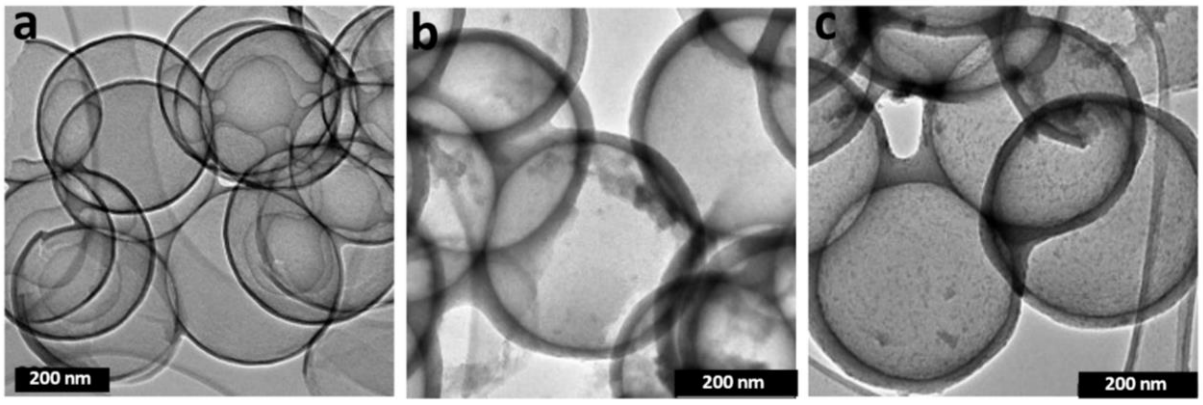

Figure 4.2 TEM images of (a) HCS, (b) GCdots@HCSs and (c) GUCdots@HCSs composites.

4.3.2. FTIR and Raman spectroscopy

The types of functional groups present on the as-synthesized GCdots@HCSs and GUCdots@HCSs composites were studied using FTIR. As shown in figure 4.3 (a), the typical vibrational bands of the HCSs are at 2921/2853, and 877 cm^{-1} and originate from C-H stretching and bending modes, respectively.[216] The vibrational band due to C=C was observed at 1568 cm^{-1}, while a broad vibrational band centered at 1157 cm^{-1} was ascribed to C-C vibrational mode.[217]

As shown in figure 4.3 (b), the GCdots@HCSs composite had new vibrational modes appearing at 3475 cm^{-1} and 3058 cm^{-1} due to O-H groups originating from the GCdots. The O-H peaks are likely to be from COOH and C-OH functionalities. While the combination of glycerol and urea (GUCdots@HCSs composite) resulted in stretching vibrational mode at 3330 cm^{-1} due to overlapping of O-H/N-H. In addition, the vibrations resulting from the incorporation of urea

are at 882 cm^{-1} and 813 cm^{-1} and are ascribed to amine and amide bending modes.[113] These vibrational modes confirm the combination of glycerol and urea which resulted in the formation of GUCdots inside HCSs cavities. The typical C-H stretching vibrations were observed at a vibrational frequency of 2930/2855 cm^{-1}. While the vibrations at 1577 cm^{-1}, 1397 cm^{-1}, 1311 cm^{-1} and can be ascribed to C=C, C-O, and C-H stretching and bending modes originating from the composites. In addition, the peaks due to C-O symmetric and asymmetric vibrational modes were observed at 1114 cm^{-1} and 1046 cm^{-1}, respectively.[215] In summary, encapsulation of GCdots and GUCdots inside HCSs resulted in a new and a shift in peak position in the composites, and functional groups such as hydroxyl, carbonyl, carboxyl, and amines/amides were depicted using FTIR. These functional groups can easily interact with solvents and can result in tuning or altering the PL emission of the composite, especially when they are the main constituent responsible for PL emissions within the composites.

Raman spectroscopy was used to depict the defects present in HCSs and the composites. As shown in figure 4.3 (b), the Raman spectrum of HCSs and the composites were observed to have two distinct peaks known to be from sp^3 disordered carbon and sp^2 carbon clusters.[64] The Raman peaks for HCSs at 1357 cm^{-1} and 1590 cm^{-1} were ascribed to be originating from disordered carbon (sp^3 defects) and ordered sp^2 carbon clusters. The vibrational frequencies of GCdots@HCSs and GUCdots@HCSs originating from the disordered/defect carbons shifted toward a lower frequency of 1339 cm^{-1} while insignificant shifts were observed in the sp^2 carbon clusters. This Raman shift of about 19 cm^{-1} toward lower frequencies can be ascribed to introduction of more defects or surface functional groups resulting from formation of GCdots and GUCdots, as observed using FTIR.

In addition, the GCdots@HCSs and GUCdots@HCSs composites were observed to have a decrease in I_G peak intensity while the I_D peaks broadened indicating the formation of more disordered or amorphous carbon structures. The I_D/I_G ratio of HCSs, GCdots@HCSs and GUCdots@HCSs composites were 1.82, 2.87 and 2.79 which further suggests the formation of more disordered and amorphous carbon structures.[64] The broadening of full width at half maximum (FWHM) of I_D peak and the reduction in both I_D and I_G peaks are in agreement with the FTIR data whereby new and abundant functional groups (defect states) were introduced when forming the composites, (see table S4.1).

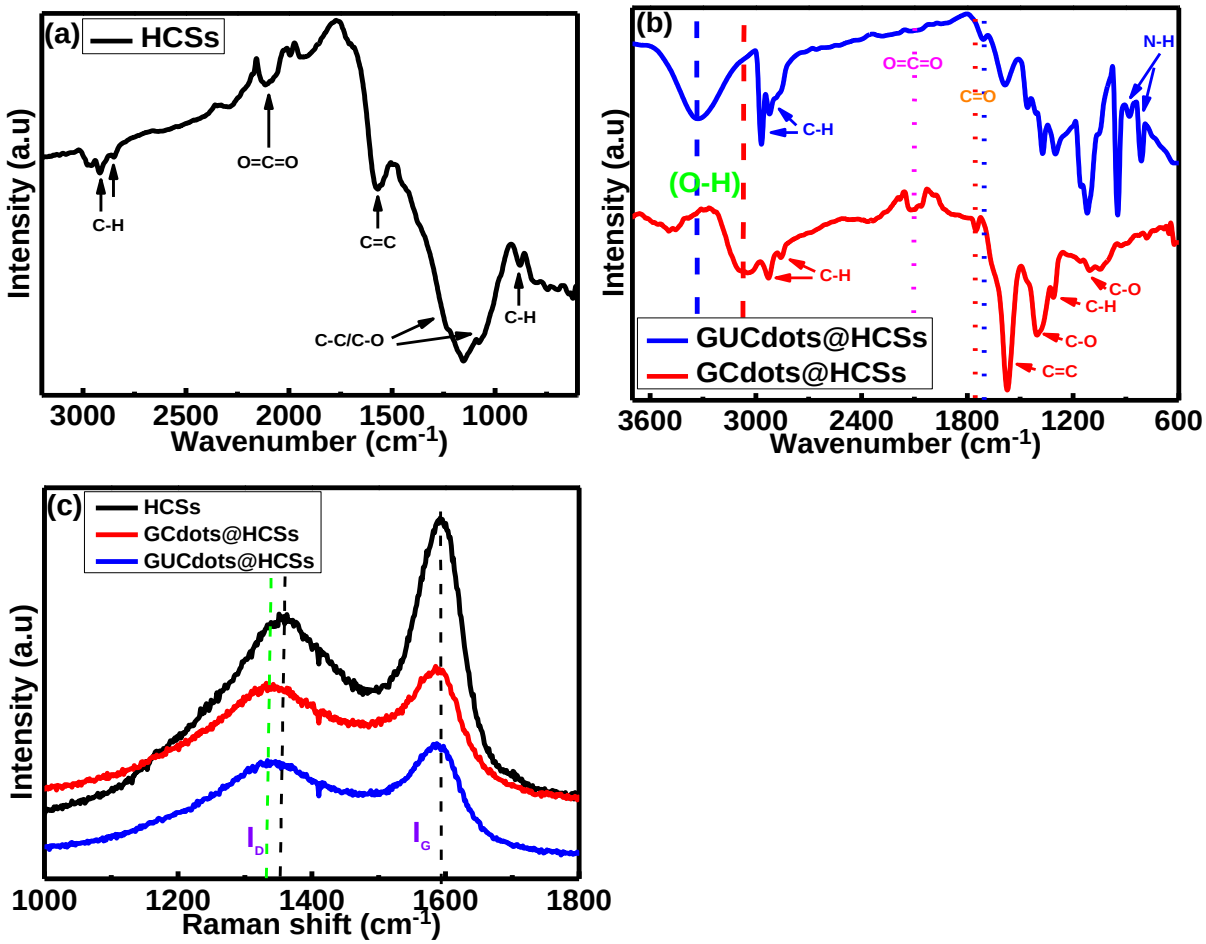

Figure 4.3 FTIR spectrum of (a) HCSs, (b) GCdots@HCSs and GUCdots@HCSs and (c) Raman spectrum of HCSs, GCdots@HCSs and GUCdots@HCSs.

4.3.3. Optical properties

4.3.3.1 UV-vis spectrophotometer

The optical properties of Cdots such as absorption and emission are very fascinating, mainly their PL emission which can originate from core carbon, surface states, quantum confinement effect, and molecular fluorophores. As shown in figure 4.4 (a) and (b), UV-vis spectroscopy was used to investigate the absorption properties of the Gcdots, GUCdots, GCdots@HCSs and GUCdots@HCSs composites. The bare GCdots have two adsorption bands at 208 nm and 264 nm. The weak absorption band at 208 can be attributed to the $\pi \rightarrow \pi^*$ electronic transitions of the core carbonaceous or the zigzag core carbon structure, while the broad absorption band at 264 nm can be attributed to $\pi \rightarrow \pi^*$ and $n \rightarrow \pi^*$ electronic transition from natural molecular states of the GCdots.[218,119] The absorption bands for GUCdots were observed at 205 nm, and two broad absorption humps at 266 nm and 315 nm which can be assigned to the carbonaceous

core and molecular states transitions as described above.[219,220] The existence of these electronic transitions suggests that functional groups such as carboxyl and nitrogen from urea/glycerol precursors were combined to form GUCdots. The typical weak absorption tail which extends toward a longer wavelength was also observed for all bare Cdots.[218]

The UV-vis absorption bands of HCSs, GCdots@HCSs and GUCdots@HCSs composites are presented in figure 4.4 (b). A typical absorption band due to core carbonaceous structure ascribed as $\pi \rightarrow \pi^*$ electronic transition was observed at 270 nm, 268 nm and 265 nm for HCSs, GCdots@HCSs and GUCdots@HCSs, respectively. The GUCdots@HCSs composite has a broad hump centered at 365 nm due to $n \rightarrow \pi^*$ transition which suggests the existence of a new state caused by nitrogen groups from urea. The $\pi \rightarrow \pi^*$ transition originates from the sp^2 (C=C) network carbogenic domains of carbon core while the $n \rightarrow \pi^*$ (C=O and C=N) results from trapping of excited-state energy by the surface states of composites.[221]

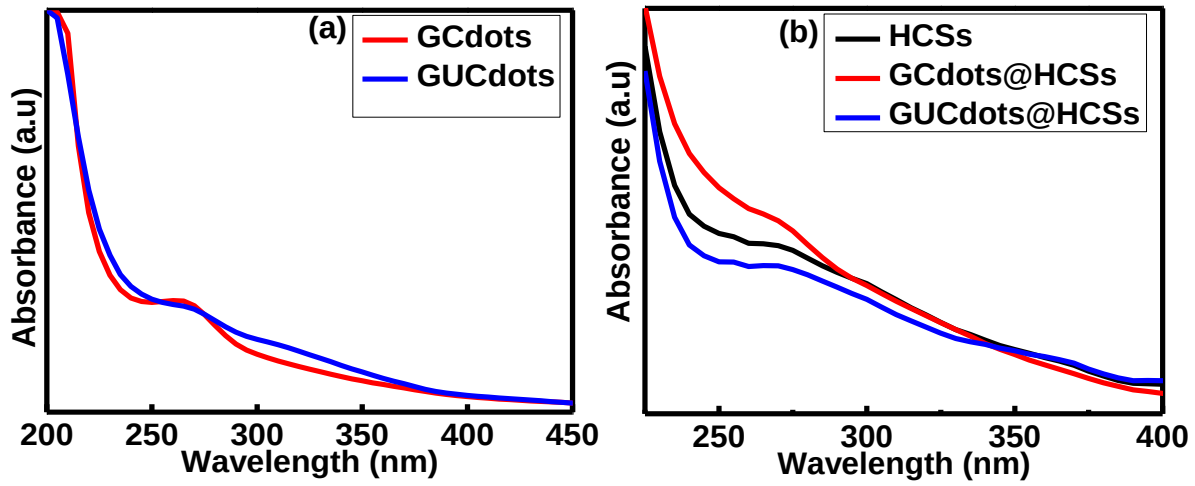

Figure 4.4 UV-vis absorbance spectrum of (a) GCdots and GUCdots (b) HCSs, GCdots@HCSs and GUCdots@HCSs composites.

4.3.3.2 Photoluminescence spectroscopy

The PL emissions in Cdots can either originate from surface functional groups, particles size, carbon core, among other factors.[222] Understanding the main constituent responsible for PL emissions in Cdots is vital. This can allow for employing Cdots in a field that will not suppress their superior optical properties. Recently, studies have investigated the effect of various solvents on the PL emission in Cdots. The solvatochromism studies can be used to tune the PL emissions and to identify the constituent responsible for PL emissions in Cdots.[223] In here, the PL emissions profiles were investigated using excitation wavelength at 300, 350 and 400 nm. In addition, three different solvents (water, acetone and hexane) were used to tune and for

identifying the component responsible for the PL emissions in Gcdots@HCSs and GUCdots@HCSs composites.

Figure 4.5 and 4.6 shows the PL spectrum of bare GCdots, GCdots@HCSs and GUCdots, GUCdots@HCSs, respectively. All samples (dispersed in water (w)) were observed to have a typical PL excitation wavelength-dependency nature which increases with an increase in excitation wavelength, see tables S4.2 and S4.3 for PL emission wavelengths.[119] This phenomenon is common in Cdots and can suggest optical heterogeneity which has specific luminescent centers with specific energy levels that photo-select light and emit it depending on the excitation wavelength used. It was also observed that peak intensity decreased as the excitation wavelength was increased from 300 nm to 450 nm. At the excitation wavelength of 300 nm, GCdots were observed to have a distinct peak and shoulder peak centered at 412 and 384 nm, while GUCdots had two prominent peaks at 365 and 395 nm. This suggests that the GCdots and GUCdots are comprised of multi-components (i.e. functional groups and particle size) responsible for PL emissions.[224] In addition, the introduction of N groups from urea was observed to cause the GUCdots to emit at different PL emissions. The emissions at a different wavelength in GUCdots suggest that the surface defects (functional groups) are likely to be prominent constituents responsible for PL emissions. The encapsulation of the GCdots and GUCdots resulted in a drastic reduction in the intensity of PL emission peaks. As it is known that PL emissions arise from charge recombination, the higher content of graphitic carbon from HCSs is likely to greatly suppress the radiative recombination of the Cdots excited state which results in weaker PL intensities.

The GCdots@HCSs and GUCdots@HCSs composites were further dispersed in acetone (a), and hexane (h). As shown in Figures 4.5 and 4.6, solvent-dependant PL emissions were observed from the composites. Dispersing the composites in water and hexane exhibited a mono-PL emission which emitted at a similar wavelength which might suggest similar interaction of the composites with the solvents. Interestingly, dispersing of the composites in acetone exhibited multi-PL emissions and the peaks were redshifted toward higher wavelengths as compared to other solvents. Furthermore, dispersion of the composites in acetone exhibited enhanced PL emission peaks which were more intense as compared to bare GCdots and GUCdots. The enhancement of peak intensities and the multi-PL emission suggests a strong interaction between acetone and the composites, see figure S4.6-7. Comparing the three solvents which were used to study the solvatochromism, it was noted that the solvent polarity played a significant role in tuning and enhancing the PL emission in the composites. Hence, the

higher polarity in acetone resulted in stronger (hydrogen bonding and dipole-dipole) interactions with the composites as compared to water and hexane.[225] In addition, the aprotic nature of acetone could have resulted in more hydrogen bonding and dipole-dipole interactions existing between acetone and Cdots which enhances specific surface states to strongly emit at a different wavelength. It was further observed that the GUCdots@HCSs composite had intense peaks as compared to the GCdots@HCSs composite. This can be related to the introduction of nitrogen groups in GUCdots@HCSs composite which is likely to have resulted in the enhancement of electron mobility within GUCdots.

In summary, dispersion of the composites in water (polar-protic), acetone (polar-aprotic), and in hexane (nonpolar-aprotic) resulted in tunning the PL emissions in GCdots and GUCdots. The tunning of PL emission could suggest that the surface states are the prominent components acting as fluorophores in GCdots and GUCdots. This is based on the theoretical assumption that a solvent can easily interact with surface state or functional groups via hydrogen bonding or dipole-dipole which can easily tune their fluorescent properties of the surface states than the core carbon structure. As a result, changing the solvent can be used as a post-modification method to tune the fluorescence emission in Cdots [224] Hence, treatment of Cdots with different solvents can be classified as a post-treatment method to optimize Cdots since the solvent-dependent nature of Cdots was observed.

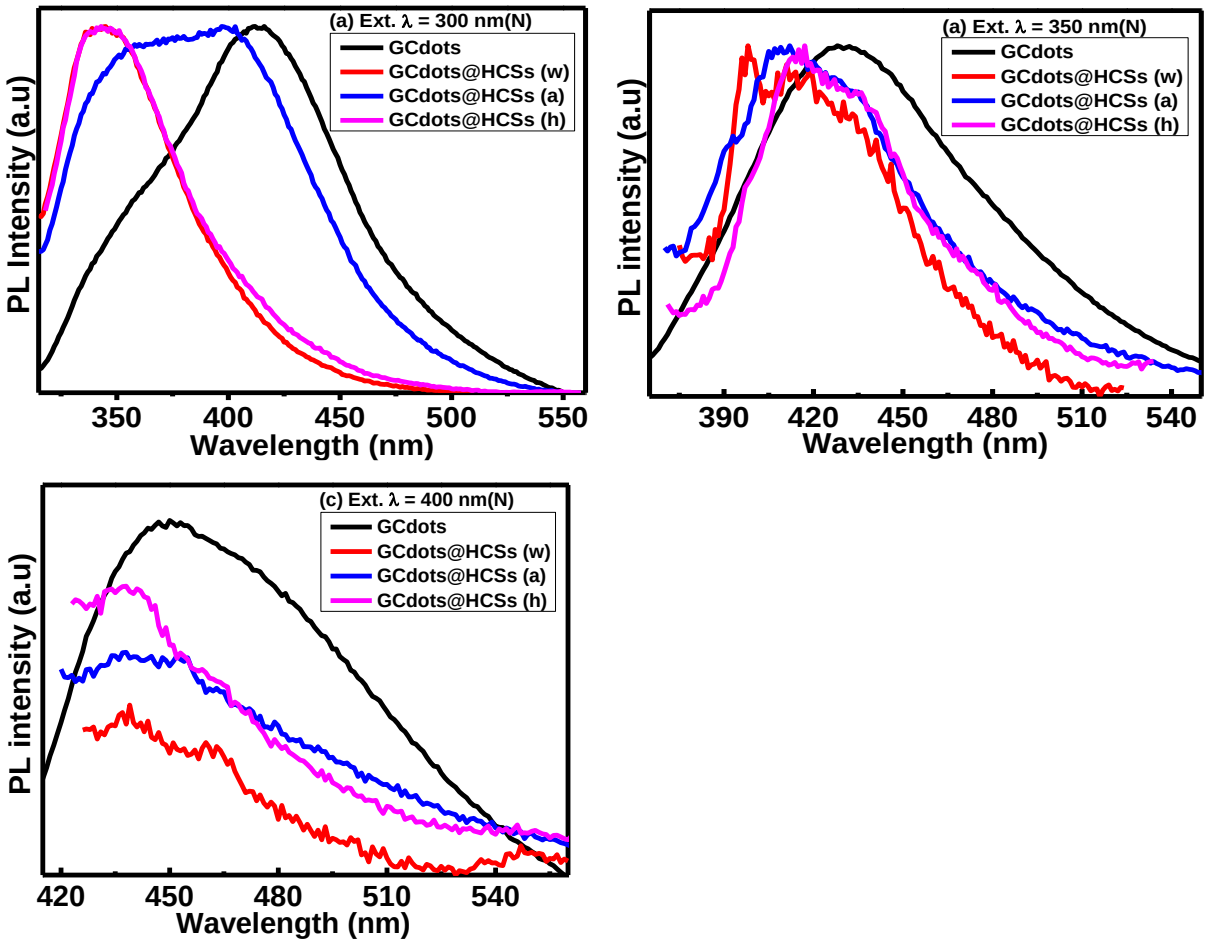

Figure 4.5 Normalized PL spectrum of GCdots and GCdots@HCSs composite excited with (a) 300 nm, (b) 350 nm, and 400 nm wavelength and dispersed in water, acetone and hexane. *Note, w = water, a = acetone and h = hexane solvent.

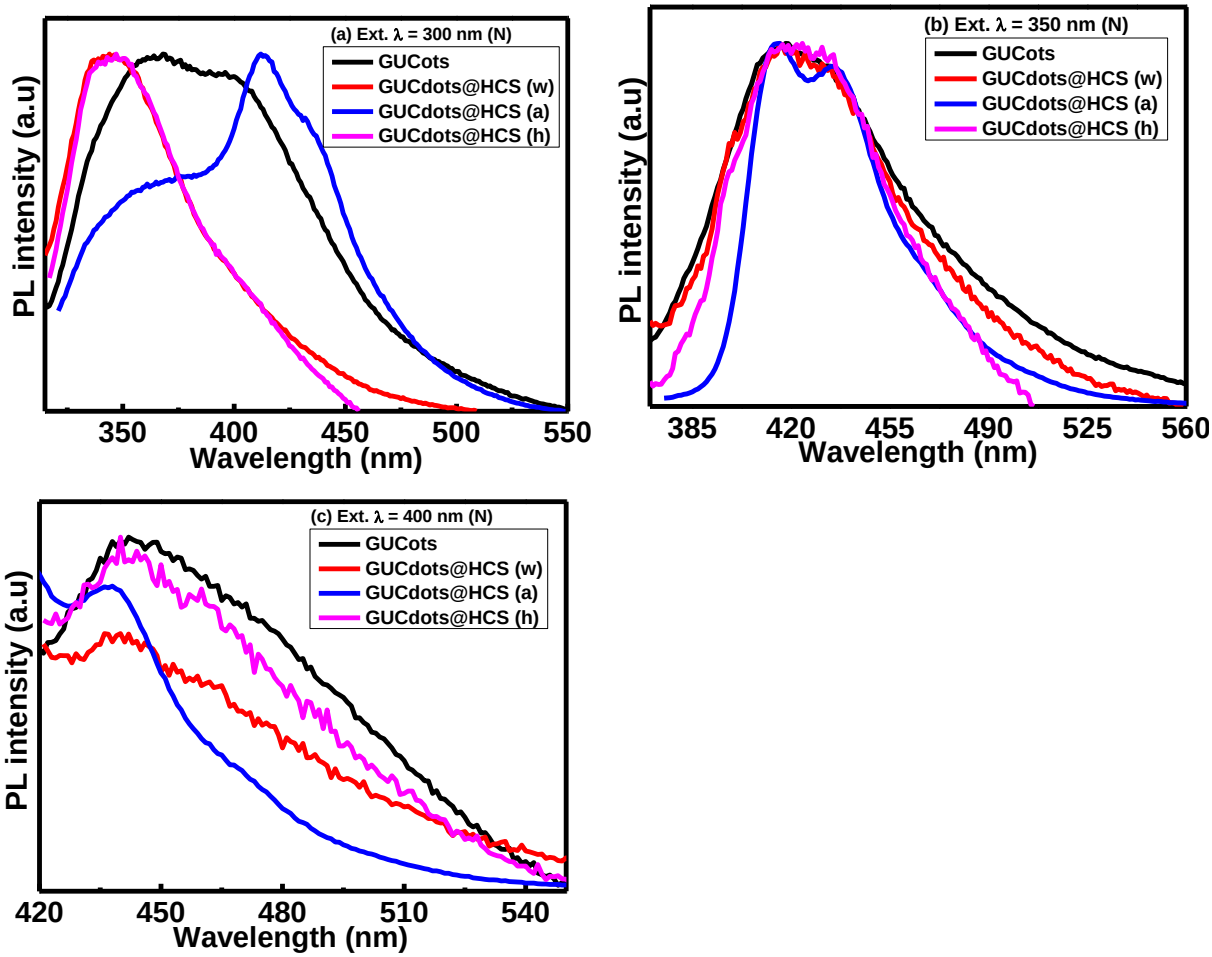

Figure 4.6 Normalized PL spectrum of GUCdots and GUCdots@HCSs composite excited with (a) 300 nm, (b) 350 nm, and 400 nm wavelength and dispersed in water, acetone and hexane. *note, w = water, a = acetone and h = hexane solvents.

4.3.3.3 Time-resolved PL spectroscopy

The lifetime of the as-synthesized bare Cdots and the Cdots@HCSs composites was investigated using time-resolved photoluminescence spectroscopy. The lifetime of the fluorophore species was measured using "deconvolution of the reference method" and the experimental decay profile of a reference emitter in place of the instrument response function was obtained with a reference solution of LUDOX colloidal silica. The transition of an excited state to the ground state in any molecule can be expressed using the equation (4.1) below:

$$I(t) = I_0\, e^{(-t/\tau)} \quad \ldots\ldots (4.1)$$

Where I (t) and I_0 are the intensity at a time (t) and intensity upon excitation at time zero, τ is the lifetime between excited decay to ground state. τ or lifetime can be defined as the time it

takes for intensity to decrease to about 37 %. For a multi-exponential decay system, equation (4.2) below can be used:

$$I(t) = \sum_i a_i e^{(-t/\tau_i)} \ldots\ldots (4.2)$$

Where a_i is a pre-exponential factor for the i^{th} term of the lifetime component. The lifetime can be expressed using equation (4.3) below: where K_r is K_{nr} are radiative and nonradiative rates.

$$\tau = \frac{1}{K_r - K_{nr}} \ldots\ldots (4.3)$$

Figure 4.7 shows the intensity decay spectrum for (a) bare GCdots and GUCdots, (b) GCdots@HCSs and GUCdots@HCSs composites, respectively, IRF is the instrument response function. The PL decay has been observed to be multi-exponential and was best fitted to tri-exponential decay (R = 0.99n, where n can be any integer between 5 and 9.5). The triple decay lifetime for GCdots was 3.02, 0.55 and 0.53 ns and for GUCdots was 3.95, 0.53 and 0.53 nm. These tri-lifetime decay components suggest the existence of heterogeneous emissive sites within the Cdots.[204] Interestingly, the measured lifetime for GCdots@HCSs and GUCdots@HCSs composites were 0.34/0.34/4.90 ns and 0.34/0.34/5.12 ns, respectively. The change in lifetime decay for bare Cdots and their respective composites is likely to be caused by HCSs support which acts as a trapping site for excited states.

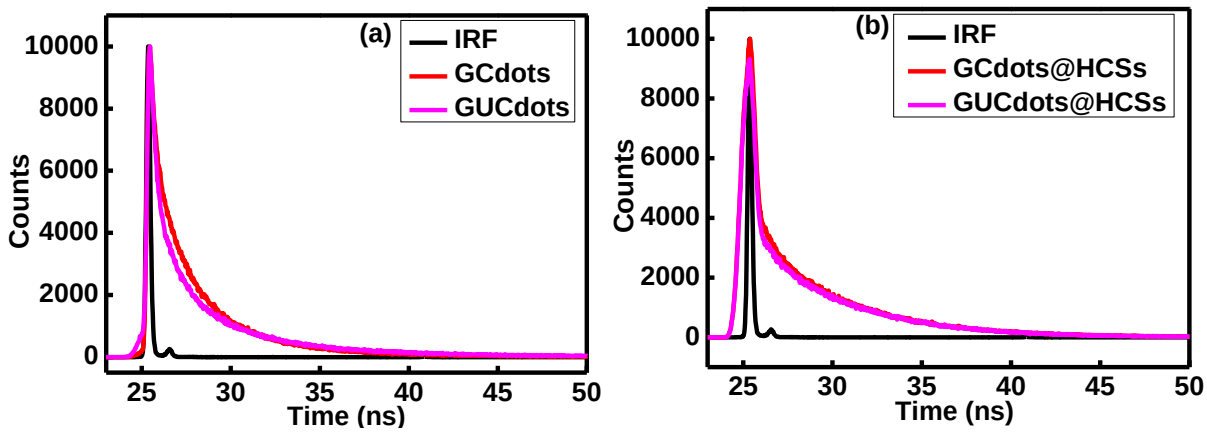

Figure 4.7 Shows the intensity decay trace of (a) GCdots, and GUCdots, (b) GCdots@HCSs, and GUCdots@HCSs in an aqueous medium and excitation of 377 nm. IRF is the instrument response function (377 nm nano-LED laser source) and Ludox colloidal silica was used as reference.

4.3.3.4 Real-time emissions

The luminescence was observed under normal light and UV illumination. For illumination, a 365 nm UV lamp was used and the samples were dispersed in water, hexane, and acetone. Figure 4.8 shows the bare Cdots under (a) normal light, and UV illumination in (b) water, (c) hexane, and (d) acetone solvents, respectively. The image set is ordered from left to right as, GCdots and GUCdots. As shown in figure 4.8 (a), under normal light, GCdots were light yellow while GUCdots were yellow. As shown in figure 4.8 (b), under UV illumination and dispersion in water, the GCdots and GUCdots showed a light pastel purple emission. Interestingly, dispersion of the samples in hexane and acetone resulted in strong emission having a light blue color for all Cdots, figure 4.8 (c) and (d).

Figure 4.9 shows the composite images taken under normal light and UV illumination at 365 nm. The image sets are GCdots@HCSs and GUCdots@HCSs from left to right. Under normal light, the composites were black while under UV illumination and dispersion in the water a blue light emission was observed. Interestingly, under the same UV illumination and dispersion in hexane and acetone a strong emission of light blue color was observed, see figure 4.9 (c) and (d), respectively.

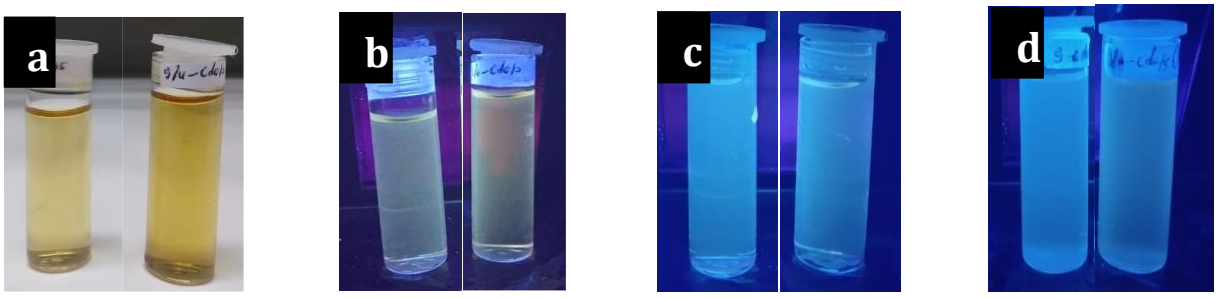

Figure 4.8 Figure 6. Images of bare GCdots (left) and GUCdots (right) taken under (a) normal light, and UV illumination at 365 nm, dispersed in (b) water, (c) hexane, and (d) acetone.

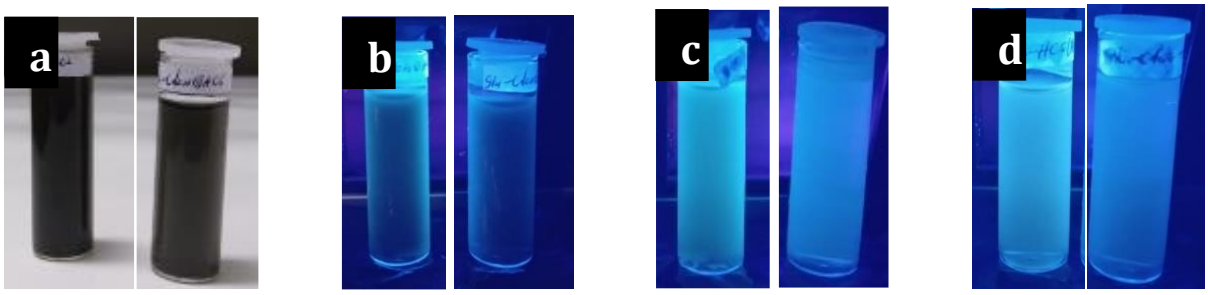

Figure 4.9 Images of GCdots@HCSs (left) and GUCdots@HCSs (right) composites taken under (a) normal light, and UV illumination at 365 nm and dispersed in (b) water, (c) hexane, and (d) acetone.

It was observed that changing dispersion solvent influenced the emission characteristics of the materials under UV illumination. Dispersing of the samples in acetone and hexane enhanced the emission/glow. These observations of solvent-dependant emissions can be attributed to different interactions such as hydrogen bonding and/or dipole-dipole that exist between the composites and solvent.

4.4. Conclusion

The study demonstrated a facile strategy for the encapsulation of Cdots made from glycerol and urea inside hollow carbon spheres cavities using the microwave-assisted method. The Cdots encapsulated inside the hollow carbon spheres cavity had various functional groups (N, O). The solid-state composites exhibited PL emissions upon excitation with various wavelengths and gave different glow under UV lamp illuminations at 365 nm. The solvatochromism investigation using water, acetone, and hexane as solvents suggested that surface states or surface functional groups in Cdots were the main components responsible for PL emissions. This was attributed to a solvent-dependent PL emission nature of the composites which resulted in bathochromic shift and was associated with hydrogen bonding, dipole-dipole interactions and solvent polarity. Dispersion of the composites in acetone resulted in induced multi-PL emission and higher bathochromic shift when compared to water and hexane. The treatment of composites with different solvents can be used as a post-modification method and acetone is recommended for the understanding of optical centers responsible for emissions. The time-resolved investigations of the bare Cdots and the composites revealed a multi-decay step and were best fitted to tri-exponential decay. The triple lifetime (ns) decay of the composites was greatly influenced by the HCSs support.

4.5. Supporting information: Appendix B

Chapter 5

One-pot carbonization of chitosan into N-doped carbon-dots/chitosan composites for the adsorption of methyl orange from aqueous solutions

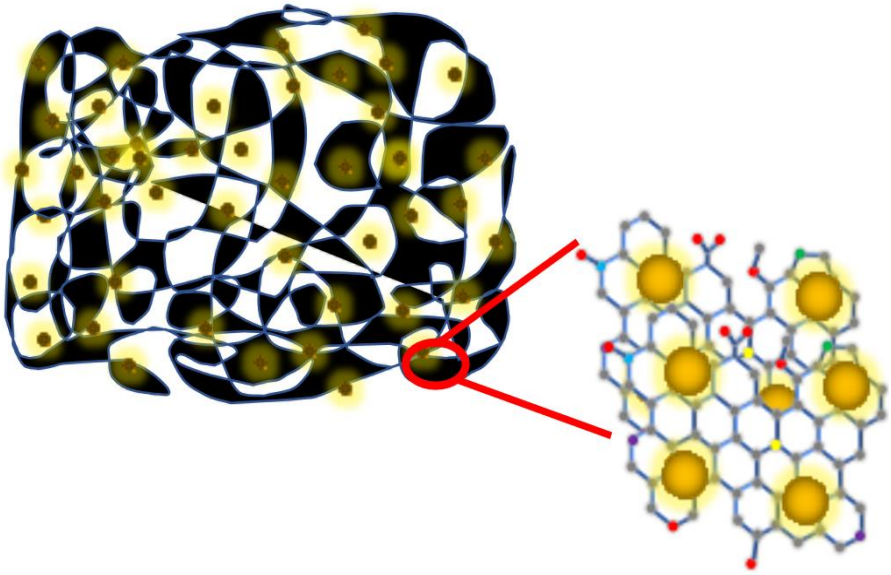

Abstract

Hydrothermal carbonization (HTC) of carbon-rich materials using an autoclave reactor vessel give a hydrochar mixture consisting of small carbonaceous materials (i.e. carbon dots) and other carbonized carbon products. In most studies, centrifugation, microfiltration and dialysis are employed to extract carbon dots (Cdots) for use in applications such as imaging and sensing. In this study, pristine chitosan (CHIT) was hydrothermally carbonized in an autoclave reactor for 1 h and 3 h to form carbonized chitosan adsorbents (CHIT-1h and CHIT-3h) and NCdots/CHIT (NCdots/CHIT-1h and NCdots/CHIT-3h) composites. The properties of all the new carbons were characterized using TEM, SEM, PL, XRD, Raman, FTIR, and TGA, CHNS and BET techniques. HTC resulted in the formation of well-structured carbon materials with higher N and C content, having well-defined graphitic (I_G) and defect (I_D) ratio and an increased surface area of 8.4 m^2/g from 0.06 m^2/g for pristine CHIT. The transformation of pristine CHIT occurred via deoxygenation and dehydration reactions whereby neighboring CHIT moieties undergo crosslinking with each other. The HTC treated materials exhibited higher methyl orange (MO) removal efficiency as compared to pristine CHIT. With partially carbonized NCdots/CHIT-1h composite exhibiting highest adsorption capacity reaching up to 370 mg/g at pH = 4 ([dosage] = 10 mg, [MO] =40 mg/L, and 100 mL dye solution). The equilibrium adsorption capacity (q_e) increased with an increase in initial dye concentration. The experimental kinetics and isotherm data were well correlated with a pseudo-second-order kinetic model and a Langmuir equilibrium model. The reusability test for the NCdots/CHIT-1h composite was conducted and the adsorption decreased from 91.2 to 83.8 % after three cycles.

5.1. Introduction

Chitosan (CHIT) is one of the highly available biopolymers that is abundant and occurs naturally in the shells of arthropods such as crabs, shrimps, and lobsters are cheap and environmentally friendly.[226,141] Due to its high content of functional groups such as amino (-NH_2) and hydroxyl (-OH), it possesses a high adsorption capacity for metal ions and organics.[227] Structurally, CHIT is formed by alkaline deacetylation of chitin and it is a linear copolymer of D-glucosamine and N-acetyl-D-glucosamine.[228] Although CHIT has shown potential for metal ions and dye removal from wastewater, in its pure form, the activity of CHIT for metal and dye removals is problematic due to the formation of a gel in aqueous media and its ability to readily agglomerate which makes it lose its adsorption capacity. Furthermore, CHIT is less stable under harsh conditions and is soluble at low pH, especially in organic acids thus limiting its

applicability as an adsorbent.[140,141] Processes such as crosslinking, grafting of new functionalities, and acetylation have been used to chemically modify chitosan and to improve its absorption activity.[229] Furthermore, chitosan composites such as chitosan-intercalated-montmorillonite,[230] chitosan/bentonite,[231] chitosan/MgO[232], chitosan-lutaraldehyde[226], and chitosan/alumina[227] have been used to enhance its dye removal efficiency in wastewater. However, most of these methods make use of harsh and complex processes for the modification of the CHIT. Also, crosslinkers react with the functional groups (such as -NH_2 and -OH) of CHIT which reduces the active sites and their adsorption activity.[233]

Hydrothermal carbonization (HTC) of low cost and natural abundant resources such as biomass has been investigated for use in the adsorption of pollutants from water. The HTC method is very useful in converting low-value naturally occurring carbon materials into carbon-rich, energy-dense, and value-added hydrochar materials with improved adsorption properties.[234,235] This strategic method can improve the stability of the adsorbent and create a surface with abundant functional groups without making use of harsh solvents.[236,237] Ganesh et al. used the HTC method (at 250 °C) to convert urban food waste to a high-value-added hydrochar which showed improved removal efficiency of acridine orange and rhodamine from wastewater.[234] Another study by Shen et al. also demonstrated how the HTC method improved chitosan-derived hydrochar for removal of Cr(VI) from aqueous solution.[237] After HTC the hydrochar is usually washed in which small carbon materials such as carbon dots (Cdots) are easily washed away as filtrate owing to their small size (≤ 10 nm). Due to their small size, abundant functional groups and good dispersion they can be useful in overcoming the shortcomings faced by CHIT in the adsorption of dyes at various environmental conditions.[125]

Hence, a simple hydrothermal carbonization method (HTC) was used to enhance the adsorption efficiency of CHIT toward methyl orange (MO) removal from wastewater. The HTC was carried out in an autoclave reactor at 180 ℃ for 1h and 3 h. The obtained hydrochar contained a mixture of carbonized CHIT residuals and NCdots which can be separated by centrifugation and washing.[237] In this study the carbonized CHIT and NCdots were not washed or centrifuged but (i) stabilized by refluxing in a mixture of ethanol and water to obtain a NCdots/ CHIT-xh composite or (ii), washed and centrifuged to produce carbonized CHIT. The pristine CHIT, carbonized CHIT and NCdots/CHIT-*x*h composites were used for methyl orange (MO) removal, and the effect of the initial dye concentration, pH, and contact time were investigated. The adsorption kinetics, equilibrium isotherms, and reusability tests on modified CHIT materials were demonstrated.

5.2. Methodology

5.2.1 Materials

Chitosan $(C_6H_{11}NO_4)_n$ with low molecular weight (50,000 Da) was purchased from Sigma Aldrich (75 - 85% deacetylated). Deionized H_2O (resistivity > 18.2 MΩ cm $^{-1}$) was used as a solvent. Methyl orange (ACS reagent, dye content 85 %, Sigma Aldrich) was used as a model dye. Ethanol, (EtOH, 96%, Merck) was used for washing the adsorbent. The pH of the dye solution was adjusted using a 0.1 M HCl or 0.1 M NaOH (Sigma Aldrich) solution. All chemicals were of reagent grade and were used as received without further purification.

5.2.2 Carbonization of chitosan

Typically, CHIT (1 g) was added to 50 mL of deionized H_2O inside a Teflon cup and the solution was sonicated for 30 minutes at room temperature. The solution inside the Teflon cup was placed inside an autoclave reactor with ~60 mL capacity. This was followed by hydrothermal carbonization (HTC) of the mixture at 180 ^oC in an oven for 1 h and 3h.[56,235] After the reaction was complete, the samples were allowed to cool to room temperature. The portion of the hydrochar sample (1 h and 3 h carbonization) was filtered, washed several times, and centrifuged for 15 minutes at 18 000 rpm 3 times to remove all small carbonaceous residuals. The remaining hydrochar portion from both samples was not washed, filtered, or centrifuged but refluxed in 10 % ethanol solution and thereafter solvent was removed in a rotary evaporator at 65 °C to remove water and ethanol. The obtained materials were labeled as CHIT, CHIT-1h, CHIT-3h, NCdots/CHIT-1h, and NCdots/CHIT-3h. All samples were further dried at 80 ℃ for 24 h before use in the adsorption studies.

5.2.3. Batch adsorption experiments

The batch method was used for the adsorption of MO using pristine CHIT, CHIT-1h, NCdots/CHIT-1h composite, CHIT-3h, and NCdots/CHIT-3h composite as adsorbents. In a typical experiment, the adsorption was conducted by mixing 0.05 g of an adsorbent with 100 mL of MO solution at an initial dye concentration of 10 to 40 mg/L. The effects of initial dye concentration, pH, and contact time was investigated. The pH of the MO solutions was adjusted by using 0.1 M of HCl and 0.1 M of NaOH. The desired initial concentration of MO was prepared from a 1000 mg/L stock solution. The MO solution and adsorbent were shaken in an

Orbishaker at 200 rpm, while aliquots were collected every 5 minutes and were filtered using a 0.22 µm PDVF membrane to remove all adsorbant. After filtration, the samples were analyzed immediately using a UV-vis spectrophotometer at a wavelength of 464 nm to determine the concentration of the MO. The adsorption capacity (q_t) in (mg/g) was determined using equation (5.1) below:[238,239]

$$q_t = \frac{(C_o - C_e)V}{m} \qquad (5.1)$$

where C_o and C_e are the initial and the equilibrium liquid-phase concentrations (g/L) of MO, respectively, q_t is the absorption capacity, V and m are the volumes of the MO solution and mass of the adsorbate used for batch adsorption studies, respectively.[227]

The percentage (%) MO removal or removal efficiency was calculated using equation (5.2) below:[240]

$$\%\ Removal = \frac{C_O - C_t}{C_O} \times 100 \qquad (5.2)$$

where C_o and C_t are the initial dye concentration and concentration of the dye at a particular time (t), respectively. The calculated parameters from equations (5.1) and (5.2) were used to plot curves of q_t versus t (min) and % removal versus t (min), respectively.[241,242]

5.2.4. Characterization techniques

Characterization techniques used in this chapter are listed in chapter 3, section 2.7. The concentration of MO at a wavelength of 464 nm, a typical absorption wavelength of MO.[243]

5.3. Results and discussion

5.3.1 TEM and SEM images

The morphologies of the pristine CHIT, CHIT-*x*h and NCdots/CHIT-*x*h composites were determined from TEM and SEM images, (*x* can be 1h or 3h). Figure 5.1 shows the TEM images of (a) pristine CHIT, (b) CHIT-*x*h and (c) NCdots/CHIT-*x*h composites, respectively. As shown in Figures 5.1 (a) and (b), the pristine CHIT and CHIT-*x*h are observed to consist of aggregated lumps of interconnected carbon structures that are stacked on top of each other with no definite morphology.[235] The pristine CHIT had bigger lumps while CHIT-*x*h had smaller lumps of carbon aggregates. Figure 5.1 (c) shows the NCdots/CHIT-*x*h composite which can be seen to consist of some smaller carbon structures (i.e. NCdots) supported on the larger carbon structure of CHIT-*x*h. It is worth noting that the morphology of the 1 h and 3 h carbonized CHIT were

similar. The filtration, washing, and centrifugation steps of the CHIT hyrdochar led to the removal of NCdots while rotary evaporation generated the formation of the NCdots/CHIT-*x*h composite. A TEM image of the extracted NCdots is shown in the supplementary section (Figure S5.1; particle size 5.2 nm); The NCdots were not used for the adsorption study due to their small size as they cannot be separated from a MO dye solution by filtration through a 0.22 µm PDVF membrane.

The SEM images of the pristine CHIT, CHIT-*x*h and NCdots/CHIT-*x*h composites are shown in figure 5.1 (d-f). The pristine CHIT consists of a lump of amorphous carbon with a smooth surface while the CHIT-xh comprises a connected carbon network having a rough surface with macropores.[244,245] Figure 5.1 (f) shows the NCdots/CHIT-*x*h composite which can be seen to be comprised of smaller carbon aggregated that are connected to form a big lump of network carbon with a rough surface.

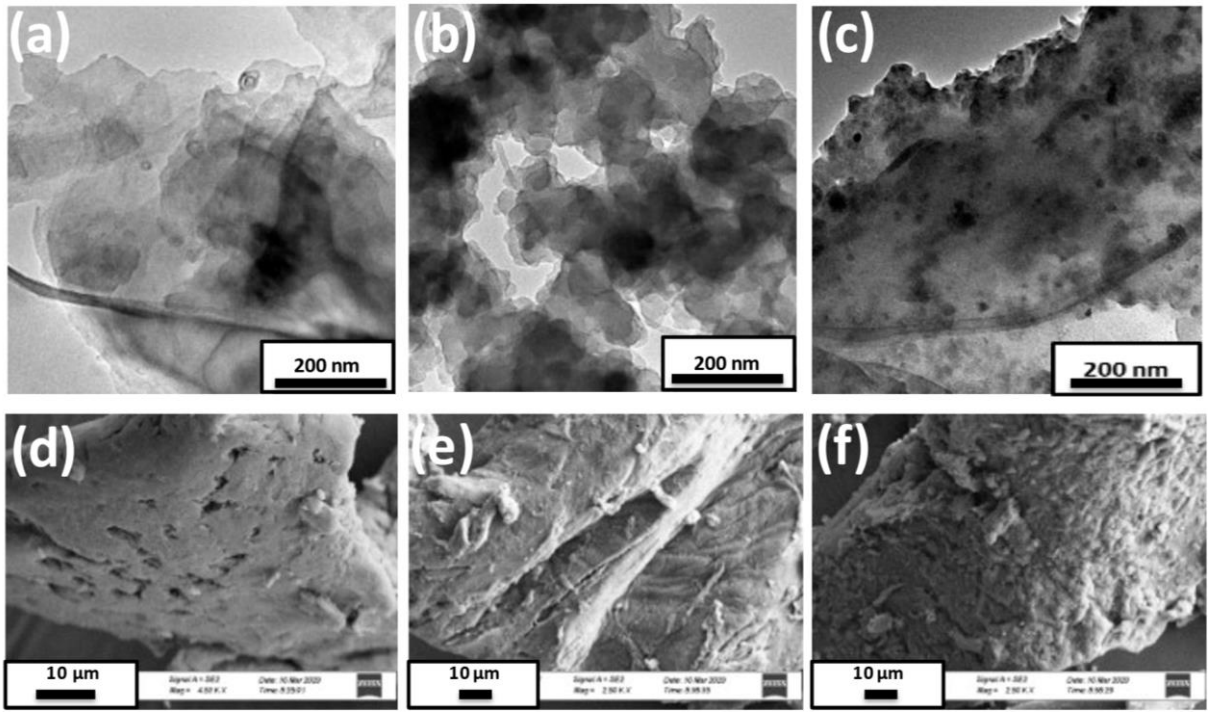

Figure 5.1 TEM images of (a) pristine CHIT, (b) CHIT-*x*h (c) NCdots/CHIT-*x*h composite. SEM images are shown in (d) pristine CHIT, (e) CHIT-*x*h (f) NCdots/CHIT-*x*h composite.

5.3.2 PL, XRD, Raman, and FTIR spectroscopy

The PL spectrum for the extracted NCdots and the NCdots/CHIT-*x*h nanocomposites are shown in figure 5.2 (a). The extracted NCdots were found to have a strong emission at 452 nm when an excitation wavelength of 380 nm was used, see figure S5.1. As shown in figure 5.2 (a), the NCdots/CHIT-1h and Cdots/CHIT-3h composites had PL emission peaks at 458 nm and 452 nm when the same excitation wavelength was used, respectively. The NCdots/CHIT-1h showed a more intense emission peak than the NCdots/CHIT-3h composite likely due to the higher content of fluorescent NCdots on the surface of the CHIT-*x*h. Interestingly, insignificant PL emissions were observed when CHIT-*x*h materials were analyzed. This might suggests that NCdots were lost as filtrate during the washing steps, and the PL emissions originate from NCdots as seen by insignificant PL emission on CHIT-*x*h samples.

The nature (amorphous or crystallinity) of pristine CHIT, CHIT-1h, NCdots/CHIT-1h composite, CHIT-3h, and NCdots/CHIT-3h composite was investigated using XRD. As shown in figure 5.2 (b), the pristine CHIT has reflection peaks at 9.5 °, 19.8 ° and a shoulder peak at ca. 27.5 ° which are attributed to the amorphous, crystalline carbon framework, and amorphous carbon network of CHIT, respectively.[104,244] After carbonization, the CHIT-1h had a new peak at 15.5 ° which can be attributed to the formation of a new anhydrous polymorph or partially carbonized CHIT. All CHIT-*x*h and NCdots/CHIT-*x*h composites peaks at 9.5 ° and 19.8 ° were observed to reduce and broadened toward higher angles, respectively. In addition, it was observed that the shoulder peak between 22 – 29.5 ° was enhanced and broadened as a result of HTC treatment. The broadening of the peak at ca. 19.8 ° is be attributed to the presence of highly amorphous carbonaceous materials formed during HTC, which further indicates that pristine CHIT was carbonized. While the reduction of the peak at 9.5 ° which is accompanied by prominant shoulder peak between 22 – 29.5 ° suggest that the former phase of CHIT is unstable at HTC temperature used, which resulted in the formation of later form of CHIT or amophouus CHIT which is stable and favourable at HTC conditions used.[246,247] These observations suggest that HTC treatment favors different forms of CHIT.

Raman: To further understand the structural changes of the materials formed during hydrothermal carbonization, Raman spectroscopy was employed to elucidate the types of vibrational modes present within the materials. Figure 5.2 (c) shows the CHIT, CHIT-1h, NCdots/CHIT-1h composite, CHIT-3h and NCdots/CHIT-3h composite. The pristine CHIT did not display any significant Raman vibrations which suggest that the sp^2 and sp^3 carbon network do not have a long-range order. After HTC treatment, the CHIT-1h sample had a broad and prominent G peak at 1543 cm^{-1} which was attributed to being a vibrational mode originating

from ordered sp^2 hybridized carbon.[248] The peak broadening and absence of sp^3 peak suggest that the amorphous form of CHIT was present, while its peak position can be attributed to the presence of a different form of CHIT (peak at 15.5 ° in XRD). The NCdots/CHIT-1h composite, CHIT-3h, and NCdots/CHIT-3h composite had two peaks observed at 1358 cm^{-1} and at 1578 cm^{-1} which originate from amorphous sp^3 and ordered sp^2 carbon network, respectively.[249] Interestingly, as the carbonization time was increased from 1 h to 3 h the intensity of these peaks was enhanced. The enhancement of the peak at 1358 cm^{-1} suggests that as the carbonization time was increased more defects (amorphous carbon) were formed. The I_D/I_G ratio was 0.67 for samples that were carbonized for 3 h implying that the graphitic carbon structures were more dominant than the amorphous carbon network. In addition, the I_G peaks were sharper than I_D peaks which imply that the graphitic carbons were more ordered than the amorphous peaks. However, their full width at half maximum (FWHM) were 202 cm^{-1} and 104 cm^{-1} for D and G peaks for CHIT-3h and was 184 cm^{-1} and 103 cm^{-1} for NCdots/CHIT-3h, respectively. The difference in the FWHM can be attributed to the presence of NCdots in the NCdots/CHIT-3h composite. These observations further suggest that HTC treatment results in the formation of different and ordered forms of CHIT.

FTIR spectroscopy was also used to elucidate the functional groups present within the materials. As shown in figure 5.2 (d), several peaks were observed at different vibrational frequencies. For all adsorbents, a broad stretching vibration from 3536 cm^{-1} to 3060 cm^{-1} (centered at 3290 cm^{-1}) was designated as the O-H/N-H stretching vibrations that overlap with each other.[250] The two small peaks at 2924/2870 cm^{-1} correspond to the symmetric and antisymmetric stretching vibrations of CH_2 and CH_3 groups.[251] The peaks at 1640/1557 cm^{-1}, 1418 cm^{-1}, 1365 $cm^{-}1$, 1313 cm^{-1} are assigned to stretching vibrations of carbonyl groups, C-H, C-O and N-H bending vibrations. The sharp and intense peaks at 1065/1025 cm^{-1} and a peak at 889 cm^{-1} are assigned to the C-C/C-O-C and C-N vibrational modes, respectively.[250,252] The carbonization of CHIT retains all the functional groups and their vibrational positions regardless of the carbonization time. However, after HTC treatment the peak due to C-O/C-O-C vibrational modes at 1065/1025 cm^{-1} was drastically reduced, this peak was reduced by approximately 64 % for NCdots/CHIT-*x*h composites and approximately 84 % for CHIT-*x*h samples. Which suggest that the C-O functional groups are involved in deoxygenation reactions that allow crosslinking of neighboring CHIT moieties, and/or some of the C-O functional groups are concentrated on small (NCdots) carbonaceous materials formed during HTC treatment as seen by a slight decrease in the C-O peaks as compared to drastically decrease for samples without NCdots.[235] In addition, the N-H/O-H peaks for NCdots/CHIT-*x*h composites were more intense than CHIT-

*x*h which suggest that during HTC treatment more functional groups are concentrated at NCdots particles.[104]

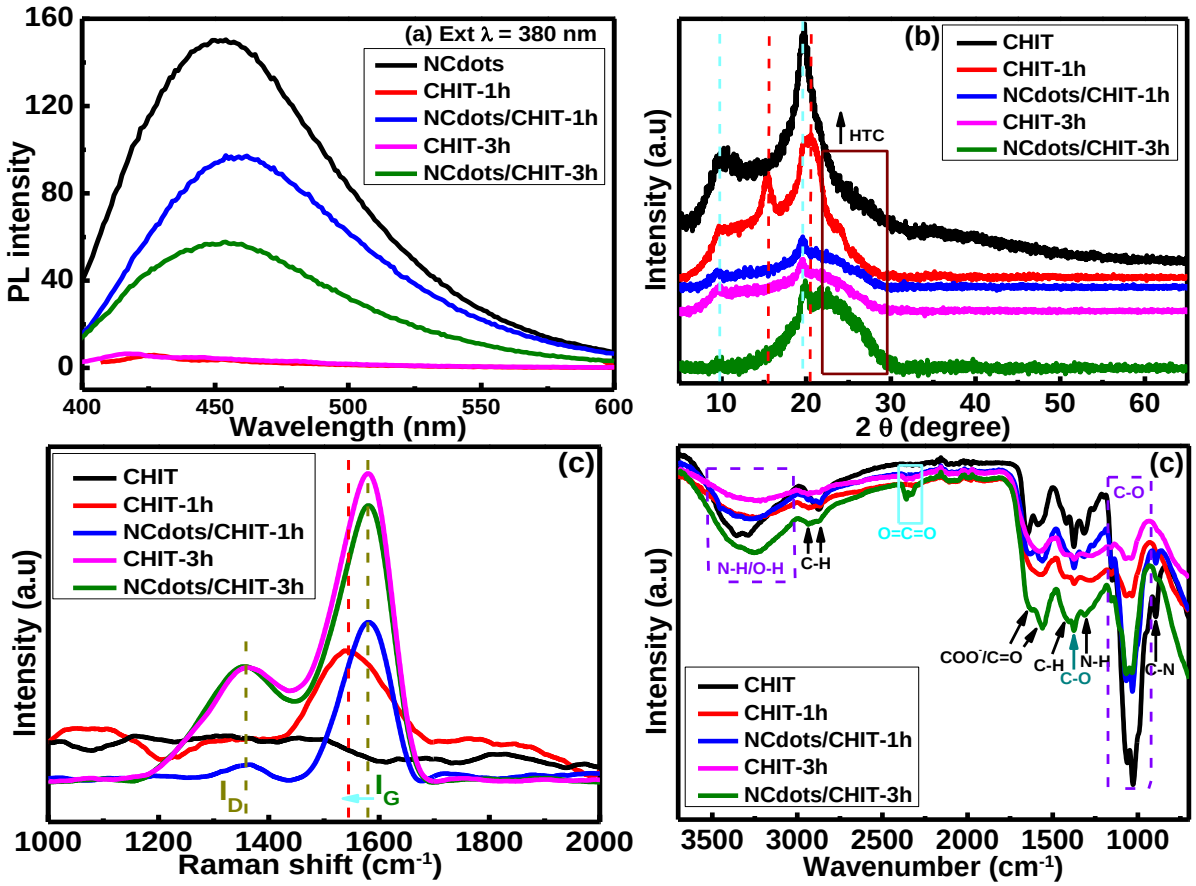

Figure 5.2 Shows the (a) PL spectra, (b) XRD patterns, (c) Raman spectra and (d) FTIR spectra of pristine CHIT, CHIT-1h, NCdots/CHIT-1h composite, CHIT-3h and NCdots/CHIT-3h composite.

5.3.3 Thermal analysis

The thermal stability for all samples was investigated using thermal gravimetric analysis. Figure 5.3 (a) shows the TGA curves of all the samples, the initial weight loss of about 10 % for all adsorbents is associated with the loss of physio-adsorbed moisture on the surface of the adsorbents desorbing up to 100 °C.[253] The functional groups such as amine, carbonyl, carbon dioxide, hydroxyl, carboxylic acids were lost between 215 °C to 380 °C for all adsorbents. The functional group weight losses are attributed to depolymerization, decomposition of pyranose rings through dehydration, deamination, and ring-opening.[125] The peaks due to the functional group's decomposition increased or were prolonged toward higher temperature as the carbonization time was increased. This suggests that some functional groups are likely to be incorporated into the core carbon network or within the pores of the adsorbents.[251] This was

also observed by DTA thermograms in which a slight increase in functional groups decomposition was observed after carbonization of Ch. The decomposition peaks were centered at 293 °C, 297 °C, 302 °C for CHIT, CHIT-1h, NCdots/CHIT-1h and at and 324 °C for CHIT-3h and NCdots/CHIT-3h, respectively.

The final decomposition of the core carbon structure was observed between 400 °C and 650 °C for all samples. Interestingly, the decomposition of the carbon structure for CHIT and CHIT-1h was observed to have two peaks at 535/615 °C and 535/597 °C suggesting the existence of two different carbon structures or the presence of partially carbonized CHIT within the CHIT-1h, this can be substantiated by the XRD peak at 15.5 ° for CHIT-1h. The decompositions peaks of the NCdots/CHIT-1h, CHIT-3h, and NCdots/CHIT-3h observed by DTA were centered at 557 °C, 515 °C, 535 °C suggesting a slight decrease in thermal stability as the carbonization time was increased from 1 h to 3 h. In addition, as the carbonization time is increased from 1 h to 3 h the peaks responsible for functional groups decrease while the peaks for core carbon broadened suggesting the incorporation of more functionalities within core carbon structure or loss of functional groups (mainly C-O, deoxygenation reactions) during CHIT crosslinking.

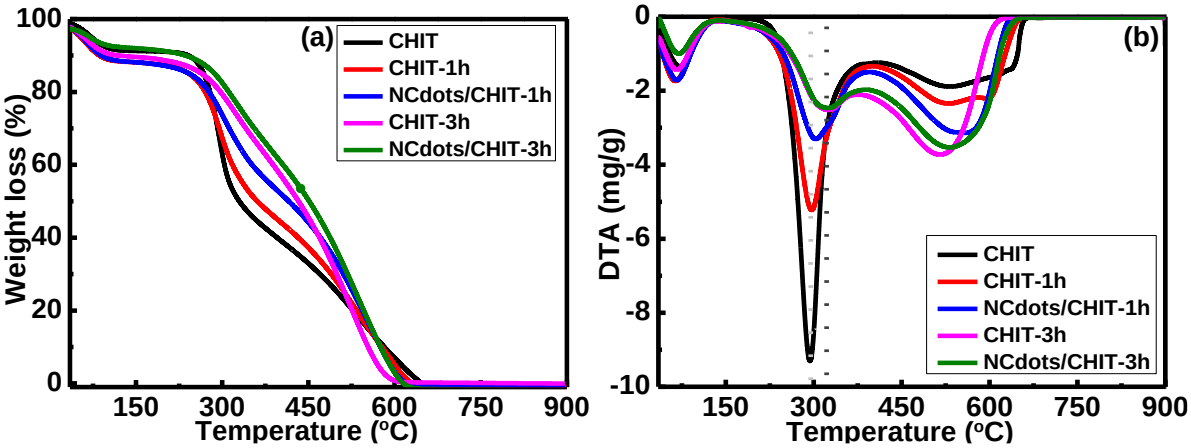

Figure 5.3 Present the (a) TGA curves and (b) DTA thermograms for pristine CHIT, CHIT-1h, NCdots/CHIT-1h composite, CHIT-3h and NCdots/CHIT-3h composite.

The increase in carbonization degree coupled with the reduction in the C-O/C-O-C peak intensities at 1065/1025 cm^{-1} (FTIR, figure 5.2 d) suggests that chitosan carbonization occurs via deoxygenation reactions.[235] The deoxygenation reactions result in the crosslinking between CHIT moieties which form ordered carbonized carbon structures with defined and continuous

sp^2 (I_G peaks) and sp^3 (I_D) as observed by the Raman spectrum.[237] In addition, the TGA peaks assigned to functional groups decomposition were reduced as the carbonization time was increased suggesting crosslinking of the CHIT moieties and substantiating the deoxygenation reaction taking place. Hence, a consistent picture has emerged about the structure of new materials produced during HTC treatment, and proposed structures of the materials formed during HTC treatment are presented in figure 5.4.

Due to the small size of NCdots (≤ 10 mn) they can be easily washed away as filtrate during filtration. As shown in figure 5.4, the obtained hydrochar was refluxed in ethanol solution and a rotary evaporator was used to obtain solid NCdots/Ch-*x*h composites. Other porting of the obtained hydrochar was filtered, washed and then centrifuged to remove all Cdots and other small carbonaceous materials to obtain a CHIT-*x*h. Due to the presence of NCdots in the composite, it is expected to have a higher adsorption capacity than carbonized CHIT. This is due to the hydrophilic nature of NCdots which will result in good dispersion, no/fewer agglomerations, and provide more active sites for adsorption of MO.[254]

As illustrated in figure 5.4, during HTC at higher temperature and pressure the neighboring interwoven CHIT polymeric moieties undergoes crosslinking via deoxygenation and dehydration reactions. This results in the formation of various carbon structures (hydrochar) such as carbonized CHIT and NCdots. As compared to pristine CHIT with an insignificant surface area of 0.06 m^2/g and cavities having a pore diameter of 147 nm. The carbon structures obtained after HTC (i.e. NCdots/CHIT-1h composite) have an increased surface area of 8.44 m^2/g and pore diameter of 10 nm, see figure S5.2 for BET isotherms. These observations suggest that during HTC the cross-linkage between CHIT molecules produces well-defined carbon structures with well-defined pores that lead to an increase in surface area.[235,255]

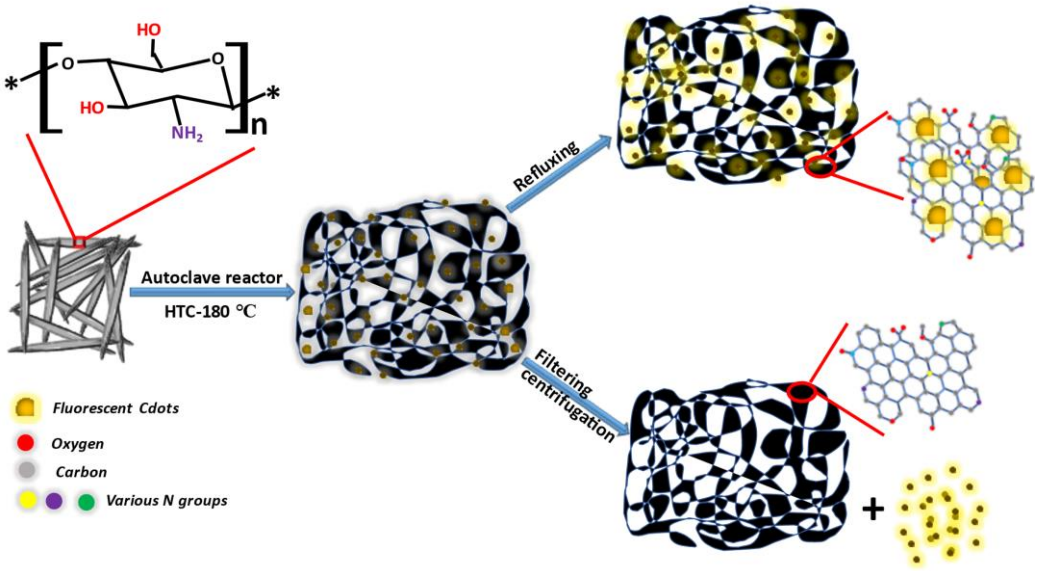

Figure 5. 4 Proposed schematic illustration of the conversion of chitosan during HTC treatment in an autoclave reactor.

5.4. Batch adsorption studies

5.4.1 Effect of pH

The effect of pH for MO adsorption was conducted in the range pH 2 – 10, initial dye concentration of 10 mg/L and 50 mg of adsorbent dosage to establish the optimum pH condition for the MO removal. As shown in figure 5.5, at pH 4 all the adsorbents showed better MO removal and reached a removal capacity of up to 67 %, 95 %, and 97 % for pristine CHIT, CHIT-1h&3h, and NCdots/CHIT-1h&3h composites within 40 min, respectively. The higher MO removal at pH 4 can be attributed to the higher number of protons present in the solution which interacted with the amine and hydroxyl groups to form protonated functional groups which resulted in the formation of a positively charged adsorbent. The positively charged groups on the adsorbents readily interact with the anionic MO dye molecules through strong electrostatic interactions.[256,141] At the higher pH of 6-10 the MO removal efficiency is reduced drastically due to deprotonation of the adsorbent functional groups which led to electronic repulsions between the MO and the adsorbent. At pH 2, the adsorbent is likely to form a gel, aggregate and/or dissolve in the acidic medium which resulted in a slight decrease in the adsorption capacity of the adsorbent.[190,79]

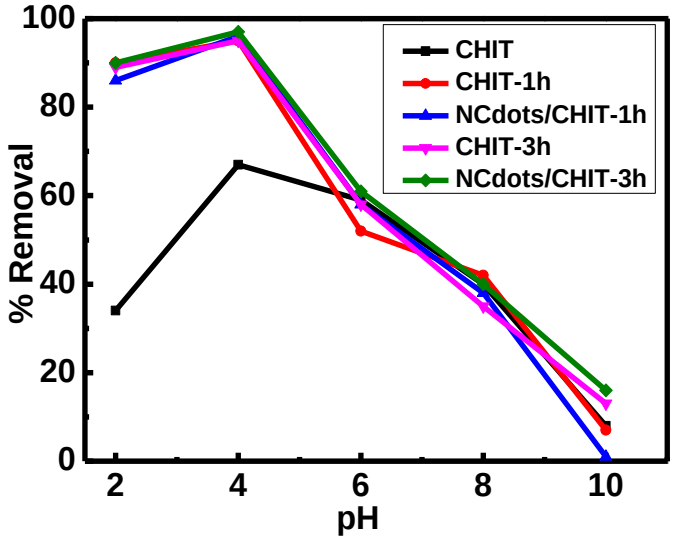

Figure 5.5 Effect of pH (2-10) on MO adsorption at room temperature, initial dye concentration of 10 mg/L, 50 mg adsorbent, 100 mL dye solution, 200 rpm agitation speed for 40 min.

5.4.2 Effect of initial dye concentration

The initial dye concentration was varied from 10 mg/L to 40 mg/L using 50 mg of the adsorbent, 100 mL of the dye solution, at pH 4 (optimum pH) for a contact time of 120 min. Figure 5.6 shows the percentage (%) removal efficiency of MO using pristine CHIT, CHIT-1h, NCdots/CHIT-1h composite, CHIT-3h, and NCdots/CHIT-3h composite. The percentage of MO removal was found to vary between 61 - 76 % at all initial dye concentrations when pristine CHIT was used. The HTC treated adsorbents showed improved MO removal efficiency (%) as compared to pristine CHIT, with CHIT-1h having a removal efficiency of 90 - 95 % while the NCdots/CHIT-1h composite maintained a 94 - 98 % at all initial dye concentrations. Similar adsorption capacities were observed with an adsorbent that was carbonized for 3h, with trend viz. CHIT-3h (84 % - 90 %) < NCdots/CHIT-3h (90 - 94 %). The NCdots/CHIT-*x*h composites showed higher MO removal efficiency than the CHIT-*x*h adsorbents. With the NCdots/CHIT-1h composite having the highest MO removal at all initial dye concentrations. The higher MO removal efficiency can be attributed to the presence NCdots on the surface of CHIT-*x*h which facilitates good dispersion of the adsorbent, and increase adsorption sites as seen by intense C-O and O-H/N-H peaks on FTIR, figure 5.2 (d).[134,257] These observations coincide with PL and XRD. The partially carbonized composite (NCdots/CHIT-1h) was selected for further studies due to its higher MO removal efficiency.

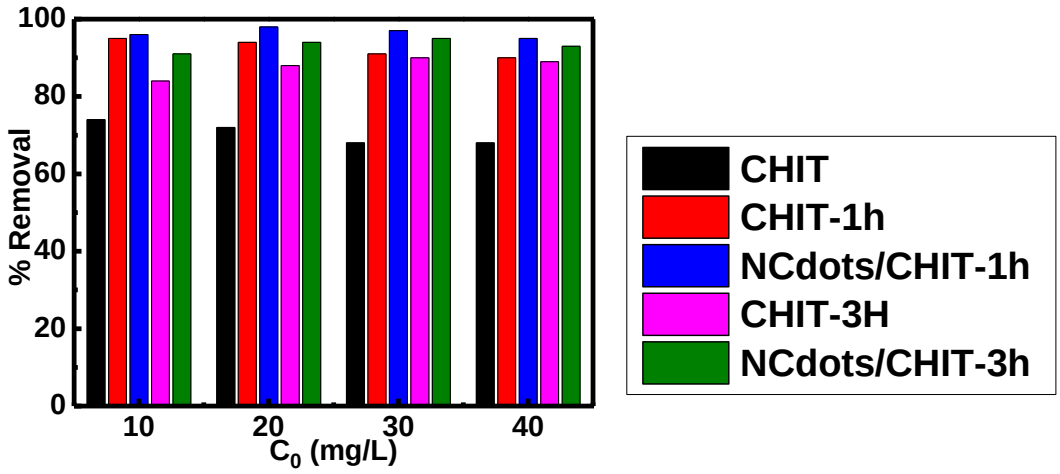

Figure 5.6 The effect of initial dye concentration (10 to 40 mg/L). Conducted using adsorbent/dye-solution of 50 mg / 100 mL, at pH 4 and 200 rpm agitation speed, for 120 min.

5.4.3 Effect of adsorbent dosage and contact time.

The effect of adsorbent dosage was conducted on the NCdots/CHIT-1h composite using 10, 25 and 50 mg at an initial dye concentration of 10 mg/L to 40 mg/L, 100 mL dye solution for 120 min. As shown in figure 5.7 (a), the removal efficiency was dependent on adsorbent dosage and it increased with an increase in the adsorbent dosage. At adsorbent dosages of 50, 25 and 10 mg, the removal efficiency were maintained between 94.5 - 97.6 %, 89 - 96 % and 87.5 - 96 % at initial dye concentration of 10 mg/L to 40 mg/L. As expected, the removal efficiency decreased with an increase in initial dye concentration, which is attributed to excess MO molecules available than the adsorption sites on the adsorbent.

Figure 5.7 (b) – (d) shows the effect of contact time on the MO adsorption conducted for 120 min at an adsorbent dosage of 10, 25 and 50 mg, respectively. The adsorption capacity (q_t) in (mg/g) increased with an increase in initial dye concentration and a decrease in adsorbent dosage. The NCdots/CHIT-1h composite showed a rapid increase in the MO removal within the first 15 minutes at all adsorbent dosages. However, after 15 minutes the MO removal decreased which is attributed to available active sites on the surface of the adsorbent being occupied by MO molecules.[232] This was followed by the diffusion of MO molecules into the bulk of the adsorbents which increased MO adsorptions.[258] After 40 minutes the adsorbate-adsorbent reached equilibrium and insignificant adsorption occurred thereafter. The adsorbent to adsorbates curves are smooth and continuous which suggest good interaction between the adsorption active sites and dye molucules.[259]

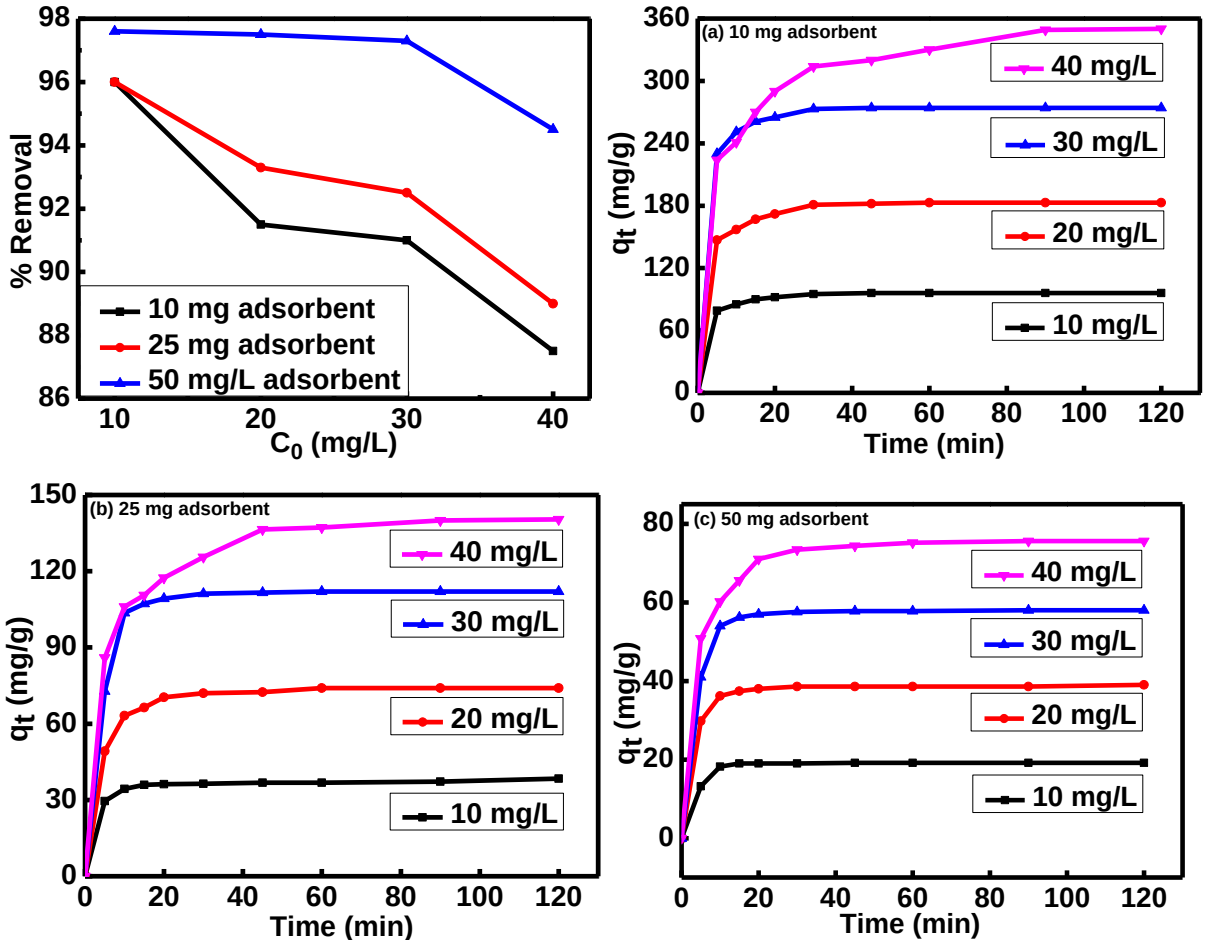

Figure 5.7 The (a) effect of adsorbent dosage and (b) - (d) adsorption capacity (q_t) in (mg/g) over contact time of 120 min, at initial dye concentration of 10 to 40 mg/L, adsorbent dosage of 10, 25 and 50 mg, per 100 mL of dye solution at pH 4 and 200 rpm agitation speed.

5.4.4 Adsorption kinetics study

A mechanistic insight of the adsorption process was elucidated using two models; the pseudo-first-order (PFO) and pseudo-second-order (PSO) models. The suitability of the kinetic models was determined by linearizing the obtained data in the coordinates of their integral equations. A pseudo-first-order model for the solid-liquid system was used (equation (5.3)):[239]

$$In(q_e - q_t) = Inq_e - k_1 t \qquad (5.3)$$

where k_1 represents the rate constant for pseudo-first-order adsorption, q_e and q_t both in ($mg.g^{-1}$) represent the amount of dye adsorbed at equilibrium and at time = t. [,259,260] Plots of In (q_e - q_t) against time (t) in minutes give a straight line with k_1 as the slope and Inq_e as intercept. The adsorption capacity at equilibrium q_e (mg/g) was calculated after the adsorbate-adsorbent equilibrium was reached.

The pseudo-second-order method (equation (5.4)) was also used:

$$\left(\frac{t}{qt}\right) = \frac{1}{k_2 q_e^2} + \frac{1}{qe}\,(t) \qquad (5.4)$$

where k_2 is the rate constant for pseudo-second-order adsorption, q_e and q_t both in ($mg.g^{-1}$) represents the amount of dye adsorbed at equilibrium and time (t), respectively. The values of q_e and k_2 were obtained from plotting t/q_t against t.[261]

Figure 5.8 and 5.9 shows the linear plots for the pseudo-first-order kinetic model [log (q_e-q_t) versus t (min)] and pseudo-second-order kinetic model [t/q_t versus t (t)] plots, respectively. It is observed that the linearity plots for the pseudo-second-order kinetic model was best suited to describe the kinetics of dye and adsorbents adsorption as compared to the linearity plots of a pseudo-first-order kinetic model. The experimental adsorption capacity ($q_{e,exp}$) and theoretical adsorption capacity ($q_{e,\ cal}$) for pseudo-second-order kinetics are comparable and mostly increase with an increase in the initial dye concentration, (table S5.4 to S5.6). The pseudo-first-order experimental and theoretical adoption capacities showed a poor relationship, (see table S5.1 – S5.3). The experimental adsorption capacity and theoretical adsorption capacity (at 40 mg/L dye concentration) at equilibrium and adsorbent dosage of 10, 25 and 50 mg was found to be 350 mg/g and 357.14 mg/g, 142 mg/g and 144.72 mg/g, 75.6 mg/g and 88.89 mg/g, respectively. These adsorption capacities are very comparable when using the PSO kinetic model. The adsorption capacity at other initial dye concentrations and adsorbent dosage can be found in the supplementary section (table S5.4 - S5.6)

The pseudo-second-order adsorption capacity for the theoretical and experimental data suggests that the adsorption of MO on the adsorbent depends on both the MO molecules and the adsorbent, and the overall adsorption kinetics involves chemical bonding between MO molecules and adsorbent adsorption sites.[238] In addition, to validate the kinetic models that best describe the interaction mechanism between dye molecules and adsorbents, the correlation coefficient (R^2) was calculated and the data are shown in the supplementary section (table S5.1 to S5.6). The correlation coefficient for the pseudo-first-order kinetic model was lower while the correlation coefficient for the pseudo-second-order kinetics ware almost 1 (0.99n, where n can be any integer). Hence, the pseudo-second-order best describes the kinetics and is a suitable model to describe the adsorption of dye molecules into the adsorbent at all initial dye concentrations and adsorbent dosage.

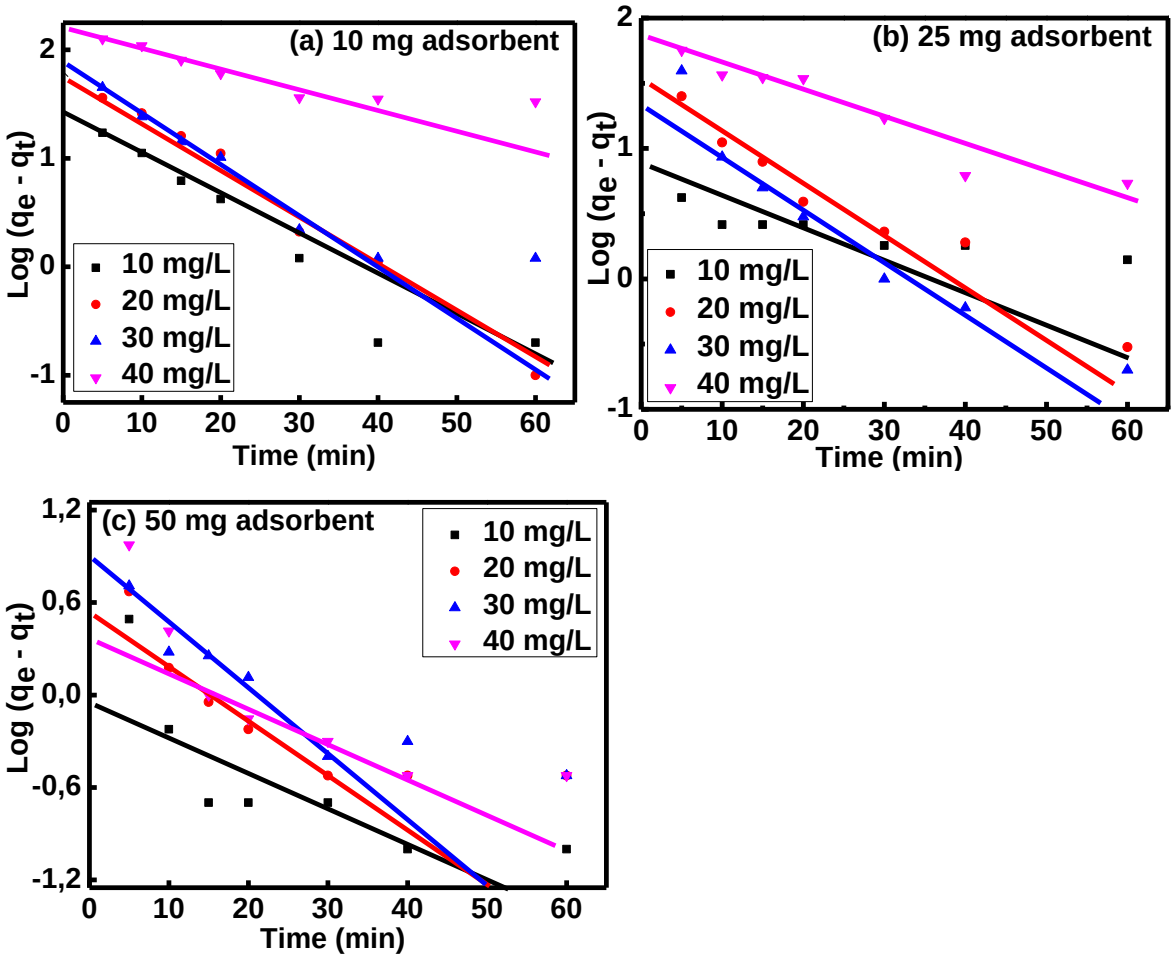

Figure 5.8 Shows the linear fitting of pseudo-first-order plots obtained from varying adsorbent dosage (10 mg, 25 mg and 50 mg) at an initial dye concentration of 10 to 40 mg/L with adsorbent/dye-solution (50 mg/100 mL) for 120 minutes at pH 4 and 200 rpm agitation speed.

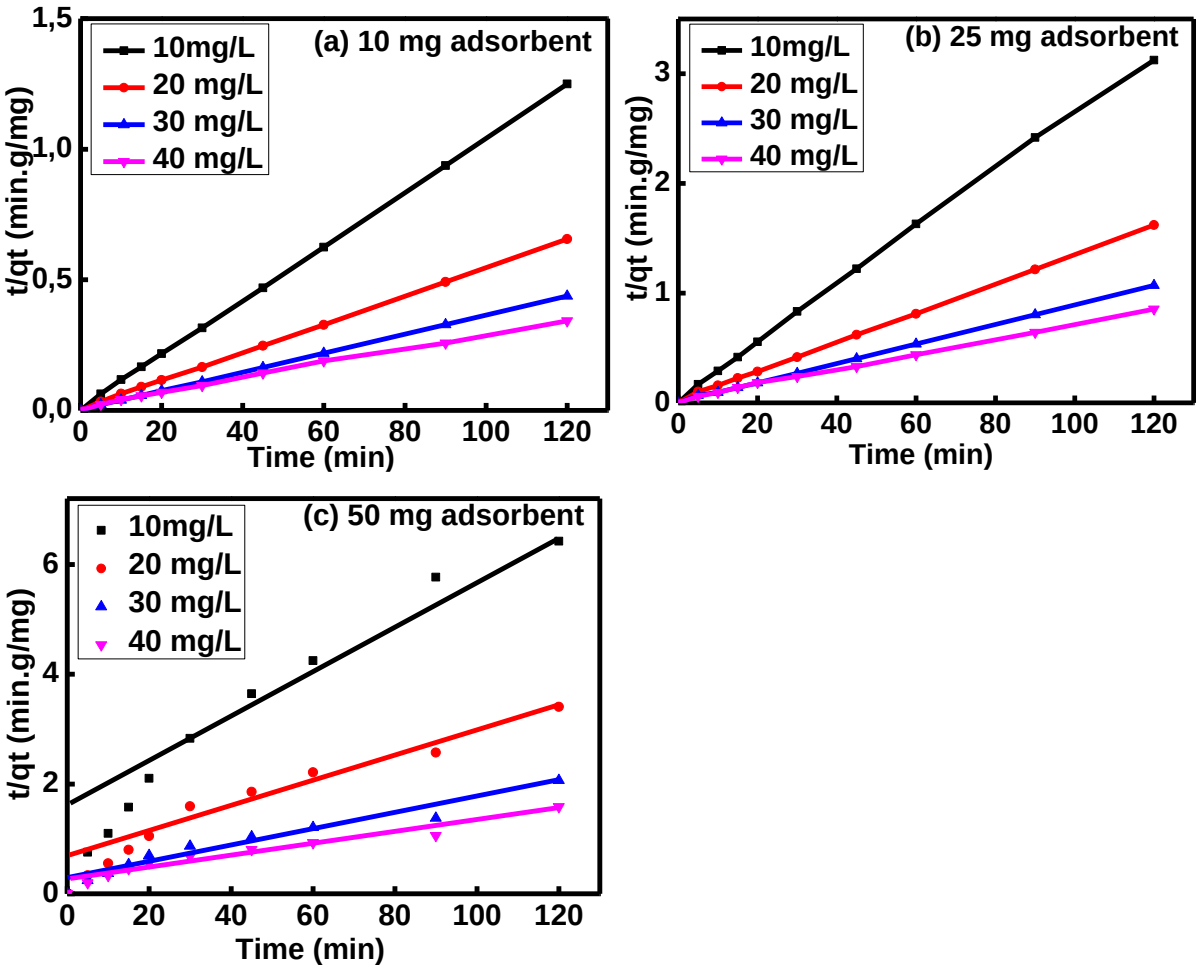

Figure 5.9 Pseudo-second-order plots for MO adsorption varied at initial dye concentration from 10 to 40 mg/L with adsorbent/dye-solution (50 mg/100 mL) for 40 minutes at pH 4 and 200 rpm agitation speed.

5.4.5 Comparison of the adsorption capacity

Table 5.1 shows the results of other studies that used different adsorbents and modified chitosan composites for MO adsorption in an aqueous medium. Pristine chitosan was modified using various strategies and reagents to improve its adsorption properties and remove dyes and toxic metals from wastewaters. Most studies use complicated methods and unfriendly reagents to modify pristine CHIT. Contrary, this study has demonstrated a friendly and simpler method for modifying pristine CHIT. The as-synthesized composite had improved adsorption capacity and show potential for application in adsorption studies.

Table 5. 1 Comparison of NCdots/CHIT-1h nanocomposite adsorbents with other modified chitosan adsorbents for methyl orange removal.

Adsorbent	*pH*	*Isotherm*	*Q_{max} (mg/g)*	*Reference*
NCdots/CHIT-1h	4	Langmuir	370	This study
chitosan/polyvinyl Alcohol/zeolite	4	Langmuir	153	[140]
Chitosan microspheres	3.1	Langmuir	207	[262]
Waste-cellulose-derived porous carbon	2.6	Langmuir	337.8	[263]
protonated crosslinked chitosan	4.5	Langmuir	89.29	[264]
Fe3O4/Al2O3/chitosan composite	6	Langmuir	416	[265]
activated carbon	4	Langmuir	217.39	[266]
chitosan-coated Fe3O4 nanocomposites	8	Langmuir	758	[267]
hollow molybdenum disulfide	3	Langmuir	41.52	[268]
Porous-flowers-like magnesium oxide	5	Langmuir	1715	[269]
chitosan-coated sodium zeolites composites films	8	Langmuir	287	[270]

5.4.6 Isotherms

The Langmuir and Freundlich isotherm was used to evaluate the adsorption process (see Supp for equations) and results are presented in Table 5.2 and 5.3.[271,272] The coefficient value (R^2) from Freundlich plots are lower than those from the Langmuir plots suggesting that the surfaces of the adsorbents are homogeneous with monolayer surface coverage by the dye molecules with ~~is~~ no possibility of interaction between neighboring dye molecules.[140] In addition, the Q_{max} from Langmuir shows a better correlation and the data are closer to the experimental Q_{max}. The R_L separation factors at all concentrations were less than 1 implying that the adsorption of the adsorbates onto the adsorbent active sites was favorable. The highest Langmuir adsorption capacity (Q_{max}) was 370 mg/g at pH 4 (initial concentration of 40 mg/L and 10 mg adsorbent

dosage). At these conditions, the NCdots/CHIT-1h composite performed much better than the pristine CHIT which had a Q_{max} of 118 mg/g.

Table 5. 2 Langmuir constants.

NCdots/CHIT-1h	K_L	R_L	$Q_{max,L}$	R^2
10 mg	0.87	0.028	370	0.964
25 mg	0.73	0.033	168	0.976
50 mg	0.67	0.036	89	0.989

Table 5. 3 Freundlich constants.

NCdots/CHIT-1h	*n*	K_F *[(mg/g)/(L(mg)^n]*	R^2
10 mg	1.90	153.0	0.946
25 mg	1.77	64.88	0.945
50 mg	1.46	50.96	0.623

CHNS analysis was used to compare the elemental composition between pristine CHIT and NCdots/CHIT-1h composite. The nitrogen and carbon content increased from 7.14 % to 8.11 % and 40.53% to 49.66 % during HTC CHIT into the NCdots/CHIT-1h composite. While the hydrogen composition was reduced from 8.04 % to 7.04 % under the same conditions, table S5.9. The textural properties analyzed using BET revealed an increase in surface area from 0.06 m^2/g (pore diameter = 147 nm ; pore volume 0.12 cm^3/g) to 8.44 m^2/g (pore diameter = 10 nm; pore volume of 0.11 cm^3/g) for Ch and NCdots/CHIT-1h, respectively, (see figure S5.2). These observations substantiate the proposed conversion of pristine CHIT using HTC, figure 5.4. The increase in N and C content and a decrease in H content is attributed to the transformation of pristine CHIT via deoxygenation and dehydration reactions which favored crosslinking of neighboring CHIT moieties to form well-defined structured materials as proposed in figure 5.4. The crosslinking of CHIT moieties results in the formation of secondary pores as observed by a decrease in pristine CHIT cavities from 174 nm to 10 nm. The formation of secondary pores

and an increase in nitrogen content resulted in the formation of well-structured carbon materials having higher surface area. Hence, the NCdots/CHIT-1h composite exhibited higher adsorption capacity for MO removal due to abundant available active sites

5.4.7 Reusability test

The reusability of the adsorbent was tested using NCdots/CHIT-1h (50 mg) composite using 20 mg/L initial dye concentration for 120 min. The adsorbent was washed using a modified method established elsewhere.[243] Typically, the MO saturated adsorbent was separated from the solution using filtration and was transferred to a solution containing 50 mL of 0.1 M NaOH solution. This was followed by shaking at 200 rpm for 6 h. Thereafter the adsorbent was filtered and washed several times with ethanol and water before drying at 80 °C for 3 h. These desorption steps were followed after each cycle. As shown in figure 5.10, the MO adsorption capacity reduced from was 91.2 % to 83.8 % after 3 cycles. The easy recovery, generation and reuse of NCdots/CHIT-*x*h composite make it a potential adsorbent for use in adsorption applications.

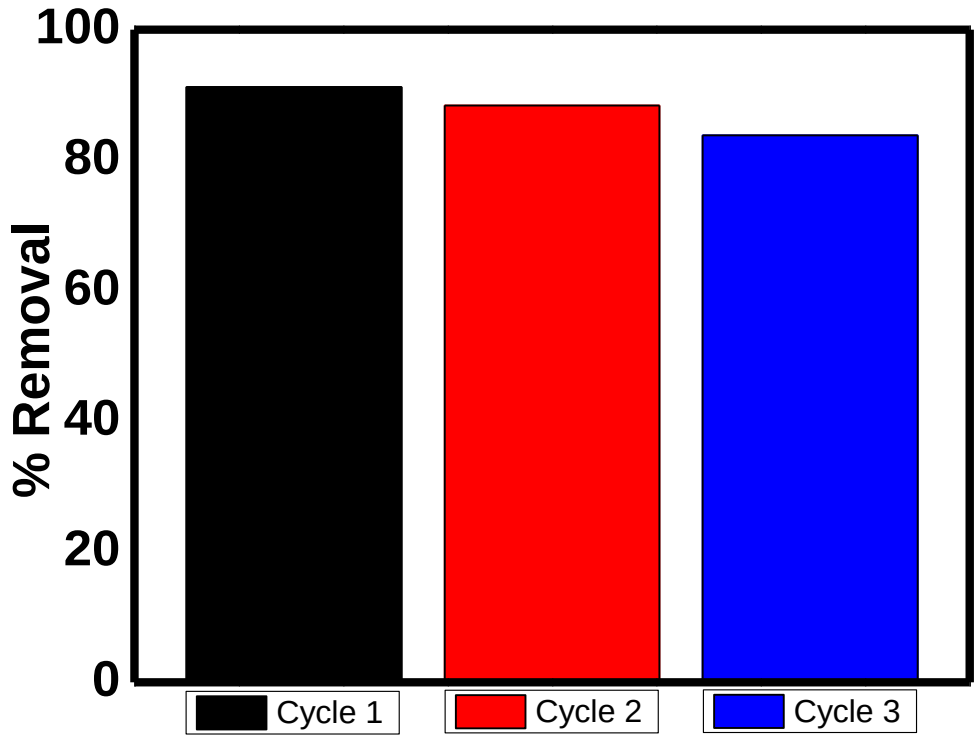

Figure 5.10 Reusability test using NCdots/CHIT-1h adsorbent over 3 cycles at the initial MO concentration of 20 mg/L using 50 mg of adsorbent and 100 mL dye.

5.5. Conclusion

Pristine chitosan was hydrothermally carbonized using an autoclave reactor into a NCdots/Ch-*x*h hydrochar. Hydrothermal carbonization of chitosan resulted in the formation of well-structured carbon materials (NCdots and CHIT-*x*h) with higher surface area and nitrogen content. The conversion of pristine chitosan into NCdots/Chit-*x*h composites occurs through deoxygenation and dehydration reaction whereby the neighboring chitosan moieties undergo crosslinking. The NCdots/CHIT-1h composite exhibited higher methyl orange adsorption reaching up to 370 mg/g adsorption capacity. The adsorption kinetics and isotherms of MO on NCdots/CHIT-1h composite were better fit to pseudo-second-order kinetic and related to Langmuir isotherm, suggesting monolayer adsorption of dye molecules on the surface of adsorbent occurring through electrostatic attraction. The optimum condition for methyl orange removal was (pH = 4, [dosage] = 10 mg, [MO] =40 mg/L, and 100 mL dye solution). The reusability test was maintained at 83.8 % after three cycles.

Supporting information: Appendix C

Chapter 6

N-doped carbon dots decorated on the surface of TiO_2 for photocatalytic degradation of methyl orange from aqueous solution

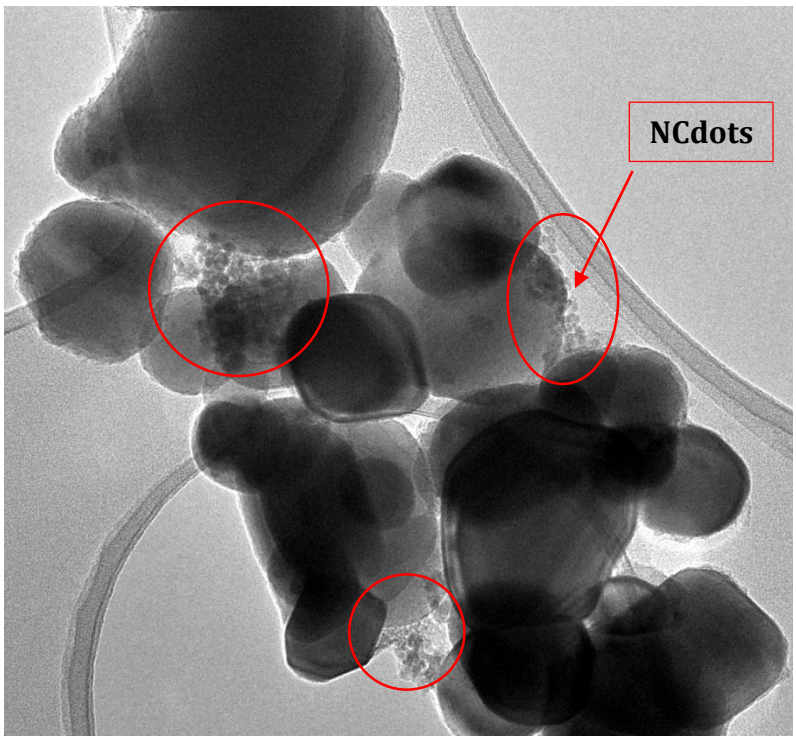

Abstract

Heterogeneous semiconductor photocatalysis using TiO_2 as a catalyst has received considerable attention. However, its major limitation in a photocatalytic application is faster recombination of photogenerated electron-hole pairs and its utilization of only 5 % (UV region) of the solar spectrum. Carbon dots with outstanding optical and electronic properties can be employed in improving the photocatalytic activity of TiO_2 by reducing recombination, enhancing photosensitization, and facilitating electron transfer in the composite matrix. Herein, a microwave-assisted method was used for the synthesis of N-doped carbon dots (NCdots) derived from chitosan. The NCdots (5 – 30 wt. % loading) were incorporated onto the surface of anatase TiO_2 and its physicochemical properties were characterized using TEM, FTIR, XRD, TGA, Raman, CHNS and PL. The NCdots/TiO_2 nanocomposites were used for photocatalytic degradation of methyl orange (MO), and they exhibited enhanced photocatalytic degradation compared to TiO_2 particles. A 10%-NCdot/TiO_2 exhibited higher methyl orange degradation which was ascribed to due to a synergistic effect between NCdots and TiO_2 nanoparticles. The degradation of methyl orange was dependent on the initial pH of the solution, with acidic pH 4 being optimum and reaching a 100 % decolorization within 80 min. At pH 7 and 10 the MO decolorization reached 40 % and 20 % after 80 min, respectively.

6.1 Introduction

The direct or indirect disposal of waste from textile, pharmaceutical and personal care product from industries pose a negative impact on the ecosystem.[273] Over the past years, the breaking down of organic pollutants from wastewater using heterogeneous photocatalysis has received considerable attention.[28] TiO_2 as a photocatalyst has received huge attention for use in wastewater to break down water contaminants such as dyes.[274] This is due to its low-cost TiO_2, low toxicity, good chemical and physical stability, optical and electronic properties (photostability), good surface area, tunable properties and suitable bandgap. This allows TiO_2 to have outstanding properties over the classical photocatalysts such as zinc oxides, metal sulfides and carbon nitrides.[42,71]

Although anatase TiO_2 with a bandgap of 3.2 eV has exhibited an outstanding performance toward the degradation of a wide range of dyes. Shortcomings such as fast recombination generated electron-hole pairs, lower interfacial charge-transfer rates of photogenerated carriers limit its potential application. This includes its inability to utilize a wide range of solar energy since can only utilize about 3-5 % (UV region) of the incoming solar energy.[25,275] These have

led to many studies working on the strategies to mitigate TiO_2 shortcomings, with a focus on enhancing its solar energy utilization, prolonging the recombination of the electron-hole pair, and increasing its photocatalytic activity.[52] These drawbacks can be mitigated by varying synthetic strategies, starting materials, doping of TiO_2 with hetero-atoms, and the use of supported TiO_2 materials.[137] For example, non-metal dopants such as C, N, and S can improve the photocatalytic activity of TiO_2, i.e., N is known to increase the catalyst activity toward visible light, changes hardness, refractive index, elastic modulus, and electronic conductivity. Carbon as a dopant can narrow bandgap, increase surface area, and introduce new states (C 2p) close to VB of TiO_2 (O 2p). In addition, operating parameters such as the pH of the dye solution, oxidizing agents, catalyst calcination temperature, dopant content, and catalyst loading have all been found to be effective in enhancing the photocatalytic degradation processes of dyes in wastewater.[72]

The addition of a carbon-based co-sorbent has been found to improve the photocatalytic efficiency of TiO_2. To date, various carbon materials such as carbon nanotubes, graphene and other carbon derivatives have been used for stimulating TiO_2 sensitivity toward visible light capturing, reducing electron-hole recombination, and for narrowing its bandgap.[55] Carbon nanotubes/TiO_2 (CNTs/TiO_2) composite has been proven to induce photocatalytic efficiency toward MO degradation which was related to higher surface area and good electronic properties of CNT that reduces electronic accumulation and decreased electron-hole pairs recombinations.[273] Multi-walled carbon nanotubes (MWCNTs) were also found to prolong photogenerated electron-hole pairs due to delocalized π-structure that facilitates the transfer of photoinduced electrons and can perform as an excellent electron acceptor leading to electron-hole separation on TiO_2.[52] In addition, TiO_2-coated activated carbon (TiO_2/AC) composite has also been reported to have a synergistic effect that inhibits recombination of electrons-holes pairs and provided active sites for adsorption of MO, resulting in higher photooxidation and improved photocatalytic activity.[276] Among other carbon materials, the discovery of carbon dots (Cdots) as new carbon-based nanomaterials has gained significant attention for use in inducing the photocatalytic activity of TiO_2.[204]

Carbon dots (Cdots) have demonstrated outstanding properties which led to their exploration for use as carbon co-sorbent in TiO_2 composites. The conjugated π-structure in Cdots has been reported to facilitate adsorption of organic dyes and makes the composite to be more stable with efficient charge transfer, leading to improved photocatalytic activity.[57,277] In addition, Cdots have been confirmed to have multiple photon-absorption which can facilitate the upconversion

photoluminescence properties, in which low energy light is converted to high energy light that is utilizable by TiO_2 particles.[278] Studies by Tian and Xuejiao have demonstrated a simple method for fabricating carbon quantum dots (CQDs) and various TiO_2 morphologies for use in photocatalytic degradation of MO and rhodamine B. One of their findings was the up-conversion of low energy photons by CQD into high energy photons that can be utilized by TiO_2, resulting in increasing its photocatalytic activity.[279,280]

Herein, a naturally occurring and highly available polysaccharide known as chitosan (Ch) was used as both a nitrogen and carbon source for the synthesis of NCdots. NCdots derived from chitosan can be useful when incorporated on the surface of TiO_2 due to abundant hydroxyl and amino groups, fluorescent emissions and conjugated π-structure that can facilitate dye adsorption, higher electron transfer, photosensitization and synergetic effect, which will enhance photocatalytic activity.[55,204] The NCdots were synthesized using a microwave-assisted method and then incorporated on the surface of TiO_2 using a systematic method established in our previous study.[125] Therefore, the NCdots/TiO_2 composites were used in the photocatalytic degradation of MO under visible light illumination. In addition, parameters such as the effect of pH, initial dye concentration and catalyst dosage were investigated.

6.2. Experimental section

6.2.1 Materials

Chitosan was used as both a carbon and nitrogen source for the synthesis of N-doped Cdots (NCdots). Titanium tetrabutoxide ($Ti(oBu)_4$, 97% Aldrich), deionized H_2O (resistivity > 18.2 MU cm $^{-1}$), ethanol, (EtOH, 96%, Merck), ammonium hydroxide, (NH_4OH, 25%, Fluka from Merck), and methyl orange dye was used without further purification.

6.2.2 Synthesis of NCdots

NCdots were synthesized using a microwave-assisted method using chitosan (1g) as the starting reagent. The chitosan was dispersed in 100 mL of water and sonicated for 30 minutes at room temperature. Thereafter, the mixture was transferred equally into four microwave tubes and synthesis of NCdots was done using a microwave reactor set at the power of 700 W for approximately 15 minutes. The synthesis temperature inside the microwave tubes was between 180 °C to 190 °C, thereafter it was allowed to cool to ambient conditions. The microwave tubes were then filled with a mixture of water/ethanol to disperse the hydrochar mixture. The hydrochar mixture was filtered using filtration and the filtrates containing NCdots were centrifuged at 18 000 rpm for 20 minutes to further remove the insoluble black particles. This

was followed by filtering using a 0.22 μm PDVF membrane. A gel-like NCdots was obtained after rotary evaporation at 60 °C and dying in an oven at 80 °C for 7 days, (54 % yield, the Cdots % yield was determined concerning to the initial mass of chitosan used in the reaction).

6.2.3 Synthesis of TiO_2 nanoparticles

TiO_2 nanoparticles were synthesized by dissolving 4 mL of $Ti(oBu)_4$ precursor in 100 mL ethanol and 0.1 M nitric acid (5 mL) in a round bottom flask placed in an ice bath while stirring. This was followed by the addition of 50 mL of H_2O (dropwise) under vigorous stirring for 30 minutes. Thereafter, the solution mixture of ethanol, $Ti(oBu)_4$ and water was refluxed at 80 °C for 6 h. To neutralize the solution mixture, 0.1 M of NaOH was added dropwise until a pH 7 and further refluxed for another 3 h. The obtained sol-gel was allowed to cool naturally, followed by washing with a mixture of water and ethanol. Thereafter it was dried at 100 °C for 6 hours. The obtained white powder was calcined at 500 °C in air for 4 h to obtain crystalline anatase TiO_2 (78 % yield).

6.2.4 Synthesis of NCdots/TiO_2 composites

The last step was to incorporate 5, 10, 15, and 30 wt. %-NCdots on the surface of the as-prepared TiO_2 powder. To achieve this, two solutions were prepared in a beaker and round bottom flask. In a beaker, a desired amount of NCdots was dispersed in a mixture of 10 mL of H_2O and 5 mL of ethanol under sonication for 15 min. The round bottom flask contained 100 mg of TiO_2 powder dispersed in a mixture of NH_4OH (2.5 mL), H_2O (100 mL), ethanol (50 mL) under sonication. The two mixtures were mixed and refluxed at 80 °C for 4 h. The product was washed using water and thereafter dried at 100 °C for 3 h in an oven, 84 % yield.

6.2.5 Instrumentation

See chapter 3, section 2.7 for characterization techniques. A Newport model 69911 solar simulator was used as a sunlight simulator for photocatalytic experiments.

6.2.6 Methyl orange degradation

Typically, the photocatalytic experiments took place in a 250 mL beaker containing either 25 mg, 50 and 75 mg of the catalyst dosage (NCdots, TiO_2 and NCdots/TiO_2 composite), dispersed in 100 mL of 20 mg/L MO solution, at pH 4, 7 and 10 for 80 min. All MO solutions were prepared using a 1000 mg/L stock solution and the pH was adjusted using 0.1 M of NaOH and HCl. Before each experiment, the mixture was sonicated for 5 minutes and then stirred in the dark for 1 h to homogenize the solution. After 1 h, 2 mL of the solution was taken before

illumination with a solar simulator. Thereafter, a solar simulator fitted with a 300 W Xe short arc lamp was used as a source of light for illuminating the solution. The aliquots were drawn at various time intervals using a plastic disposable syringe fitted with a 0.22 µm PVDF membrane filter. A set of standards was used to calibrate the UV-vis spectrometer for the analysis of the collected aliquots.

6.3. Results and discussions

6.3.1 TEM images

The TEM image of TiO_2 and 10%-NCdots/TiO_2 composite is shown in figure 6.1. As shown in figure 6.1 (a) the TiO_2 particles consist of different shapes and sizes having a particle size range between 40 to 220 nm, with an average size of 106 ± 34 nm, see figure 6.1 (c) for particle size distribution. The TiO_2 particles were heterogeneously distributed (truncated tetragonal bipyramid and tetragonal cuboid) with semi-spherical morphologies being dominant.[281,282] As shown in figure 6.1 (b), the TiO_2 particles maintained their shape and size after the incorporation of 10% NCdots on the surface. The NCdots (pointed by red arrows) were unevenly distributed and agglomerated around the TiO_2 particles, see figure S6.1. The TEM image of NCdots particles on the surface of TiO2 confirms the formation of NCdots/TiO_2 composite.

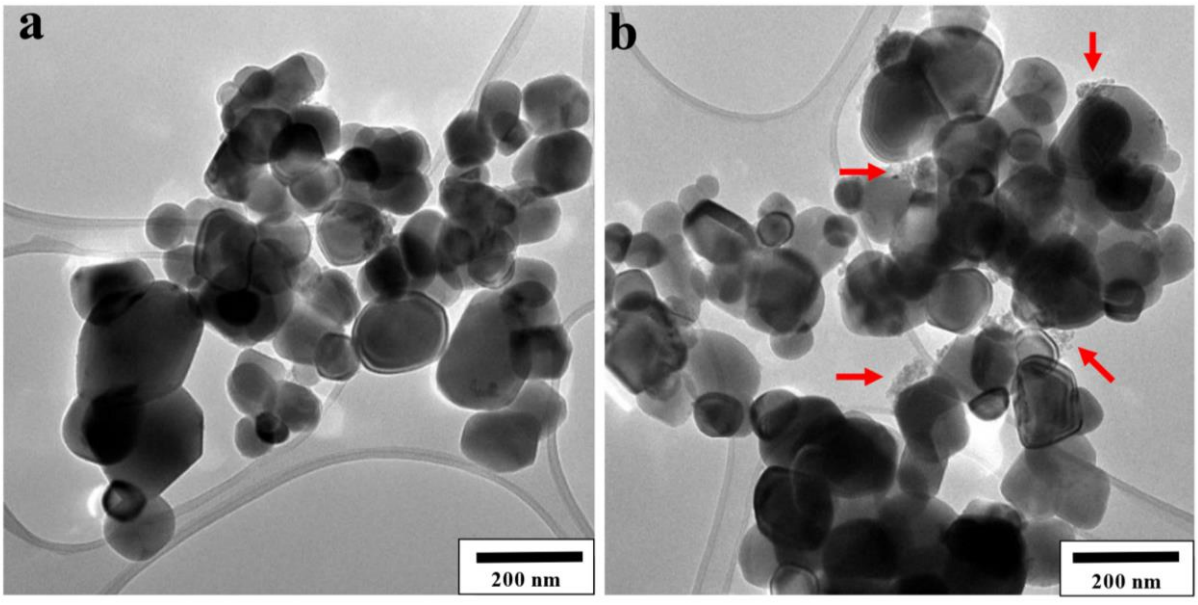

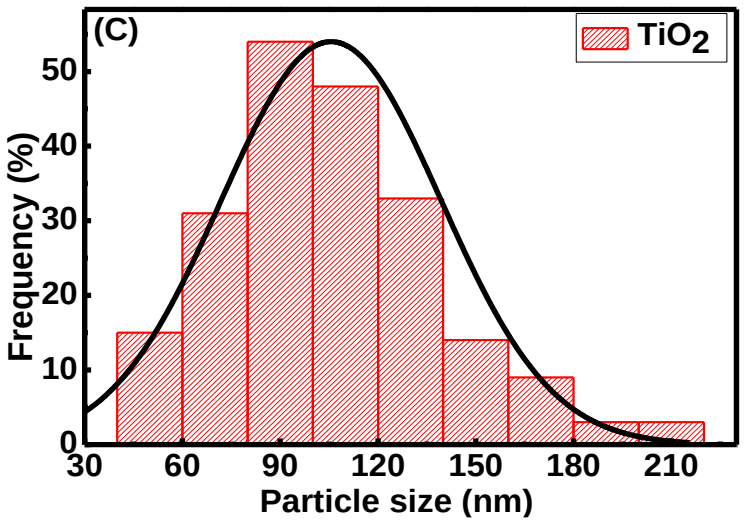

Figure 6.1 TEM images of (a) TiO_2, (b) 10%-NCdots/TiO_2 composite and (c) particle size distribution of TiO_2.

6.2 FTIR spectroscopy

NCdots derived from chitosan are known to contain various functional groups such as hydroxyl, nitrogenated, carbonyl and carboxyl. Herein, the NCdots derived from chitosan were incorporated on the surface of anatase TiO_2. Figure 6.2 (a) and (b) shows the FTIR spectrum of anatase TiO_2 and NCdots/TiO_2 composites, respectively. The annealed TiO_2 had peaks at 3440 cm^{-1}, 1650 cm^{-1} and 1133 cm^{-1} corresponding to the surface water present within the sample and Ti-O-Ti vibrational modes, respectively.[283] Upon incorporation of NCdots on the surface of TiO_2, new functional groups were observed at various vibrational frequencies. Interestingly, the broad peaks observed from 2978 cm^{-1} to 3710 cm^{-1} (and centered at 3340 cm^{-1}) due to OH/NH, increased with an increase in NCdots loading. This peak at 3340 cm^{-1} has also been reported to originate from a superposition of the OH symmetric and antisymmetric vibrational modes of water molecules that interact with each other and coordinate with Ti^{4+} cations.[283] Typical peaks originating from the C-H symmetric and antisymmetric stretching vibrational bands of the CH_2 and CH_3 groups were observed at 2855 cm^{-1} and 2930 cm^{-1}, respectively. The vibrational modes of all NCdots/TiO_2 composites were observed at 1665 cm^{-1}, 1625 cm^{-1}, 1495 cm^{-1}, 1412 cm^{-1}, 1121 cm^{-1}, 1046 cm^{-1}, 1021 cm^{-1} and 924 cm^{-1} and were ascribed to C=O, C=C, C-O, C-C, Ti-O-C and Ti-O-Ti stretching and bending vibrations.[137,284] These new vibrational bands indicated that NCdots were successfully incorporated on the surface of TiO_2. The incorporation of the NCdots has introduced functional groups such as amines, carbonyl, carboxyl, and hydroxy which can facilitate the adsorption of MO molecules closer to TiO_2, resulting in enhanced photocatalytic activity.

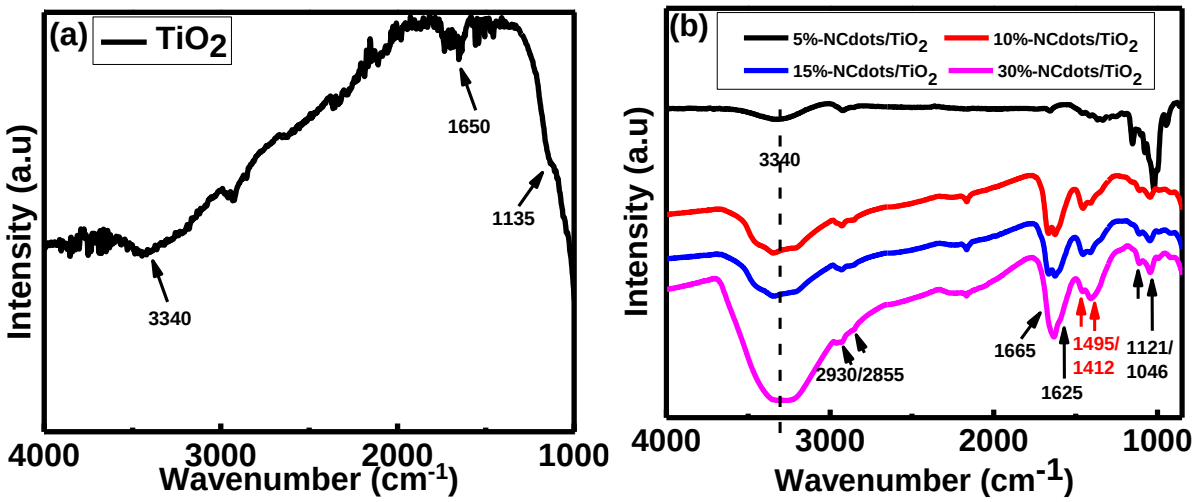

Figure 6.2 (a) FTIR spectra of TiO_2 and (b) 5%-NCdots/TiO_2, 10%-NCdots/TiO_2, 15%-NCdots/TiO_2, 30%-NCdots/TiO_2.

6.3 XRD and Raman spectra

The TiO_2 powder was calcined at 500 ℃ for 4 h and then analyzed using XRD to determine the phases within the sample. As shown in figure 6.3 (a) and (b), the diffraction patterns of the calcined TiO_2 powder consisted of dominant reflections matched to card # 00-001-0562 for TiO_2 Anatase. The reflections at 2 theta values of 23.4, 39.8, 48.1, 53.9, 55.2, 62.8, 68.8, 70.3, 75.1 and 82.6 ° can be indexed to the (101), (004), (200), (105), (211), (204), (116), (220), (215) and (224) crystal phases of the anatase TiO_2, respectively.[285] In addition, smaller reflections of rutile TiO_2 were observed at 2 theta values of 23, 27.4, 39.9 °.[49,286] Upon addition of NCdots on the surface of the TiO_2 minor shifts in the reflections were observed, however, no reflections were observed from the Cdots. This is likely due to the highly amorphous nature of the NCdots and the strong reflection of anatase TiO_2 at 25.4 ° which overlaps with the NCdots.[164]

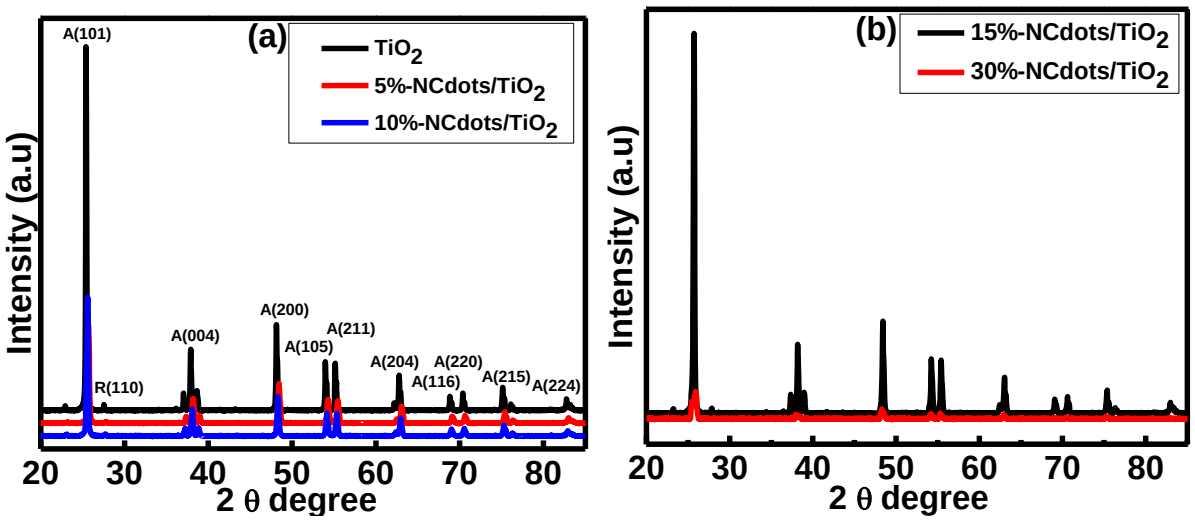

Figure 6.3 XRD reflections of (a) TiO_2, 5%-NCdots/TiO_2 and 10%-NCdots/TiO_2, and (b) 15%-NCdots/TiO_2 and 30%-NCdots/TiO_2.

The physiochemical properties of the anatase TiO_2 were also investigated using Raman spectroscopy. As shown in figure 6.4, the Raman shifts at 141, 393, 511, 636 cm^{-1} are ascribed to $E_{g(1)}$, $B_{1(g)}$, $A_{1g} + B_{1g(2)}$, and $E_{g(2)}$ modes of the anatase TiO_2. $E_{g(1)}$ and $E_{g(2)}$ have been reported to originate from Ti^{4+}-O vibrational bonds.[287] In addition, the Raman peak at 193 cm^{-1} was ascribed to a Ti-O vibrational mode of the rutile phase TiO_2 present within the sample.[50] Incorporation of NCdots on the surface of TiO_2 did not have any influence on the peak position. However, a spectral glide was observed as the NCdots were incorporated on the surface of TiO_2. At 30 % loading, only a small peak at 141 cm^{-1} was observed while other peaks disappeared. The spectral glide and the disappearance of the peaks can be attributed to fluorescence interference originating from NCdots and the instrument laser. The XRD and Raman analysis coincides with the TEM images which suggest that incorporation of NCdots does not affect the physiochemical structure of anatase TiO_2.

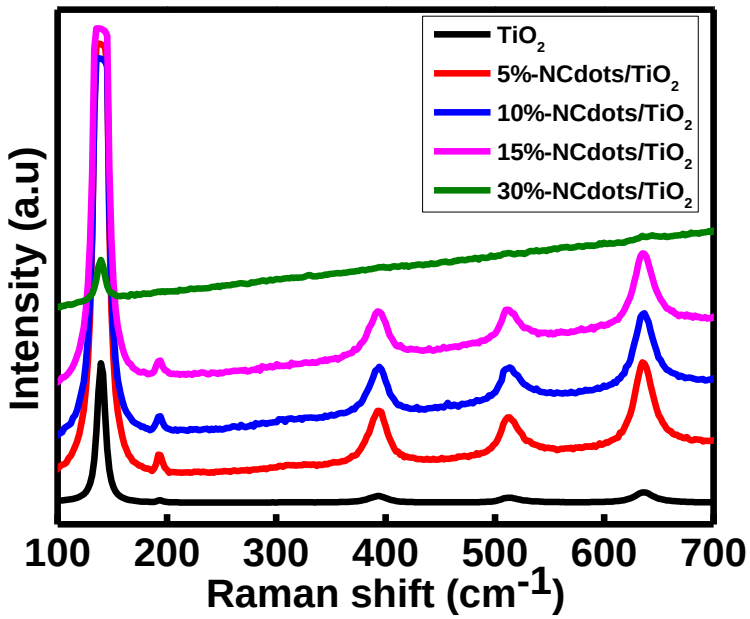

Figure 6.4 Raman spectra of 5%-NCdots/TiO_2, 10%-NCdots/TiO_2, 15%-NCdots/TiO_2, 30%-NCdots/TiO_2.

6.4 TGA and DTA thermograms

The stability of the samples was investigated using TGA analysis. As shown in figure 6.5 (a), thermal treatment of anatase TiO_2 from room temperature to 900 ℃ using TGA resulted in a 1.5 % weight change which was attributed to losing moisture, indicating a very stable TiO_2 particle.[288] Upon incorporation of NCdots on the surface of TiO_2 new decomposition peaks were observed. The peak up to 100 ℃ with weight loss of 1 % for 5%-NCdots/TiO_2, 10%-NCdots/TiO_2, 15%-NCdots/TiO_2 was assigned to the loss of moisture from the Cdots. This peak up to 100 ℃ had a 4 % weight loss for 30%-Cdots/TiO_2. The decomposition of surface functional groups such as hydroxyl, carbonyl, carboxyl, and amines for 5-30%-NCdots/TiO_2 composites was observed from 140 ℃ to 205 ℃ having weight losses of 4, 4.5, 5.5, and 13 % respectively. Their corresponding DTA peaks showed a slight increase in decomposition temperature as the NCdots loading was increased, for 5%, 10%, 15% and 30%-NCdots/TiO_2 composites with DTA peaks centered at 175, 182, 187 and 202 ℃, respectively. The increase in decomposition temperature can be attributed to stronger interactions between NCdots functional groups with TiO_2 particles.

Additional weight loss of core functional groups was observed between 235 to 350 ℃ for the 5-30%-NCdots/TiO_2 composites having a 2, 3, 4 and 4.5% weight loss, respectively. All composites have a shoulder peak between 350 - 400 ℃ presumed to be from functional groups (Ti-O-C and carboxylic groups) that are strongly interacting with TiO_2. The corresponding

weight losses were 0.5, 1.5, 2 and 4 % for the 5-30%-NCdots/TiO_2 composites, respectively. The final decomposition temperature of the core carbon was observed between 450 to 570 ℃ having a 0.5, 0.8, 1 and 2 % weight loss for 5-30%-NCdots/TiO_2 composites, respectively. The total mass loss from the functional groups, core carbon and TiO_2 structural rearrangement was 9, 12.5, 14.8 and 29 % for the 5-30%-NCdots/TiO_2 composites, respectively. The five decomposition peaks due to surface moisture, surface functional groups, core functionalities, functionalities interacting with TiO_2 and core carbons were centered at approximately 60, 190, 310, 365 and 512 ℃ as shown in the DTA profile, figure 6.3 (b).

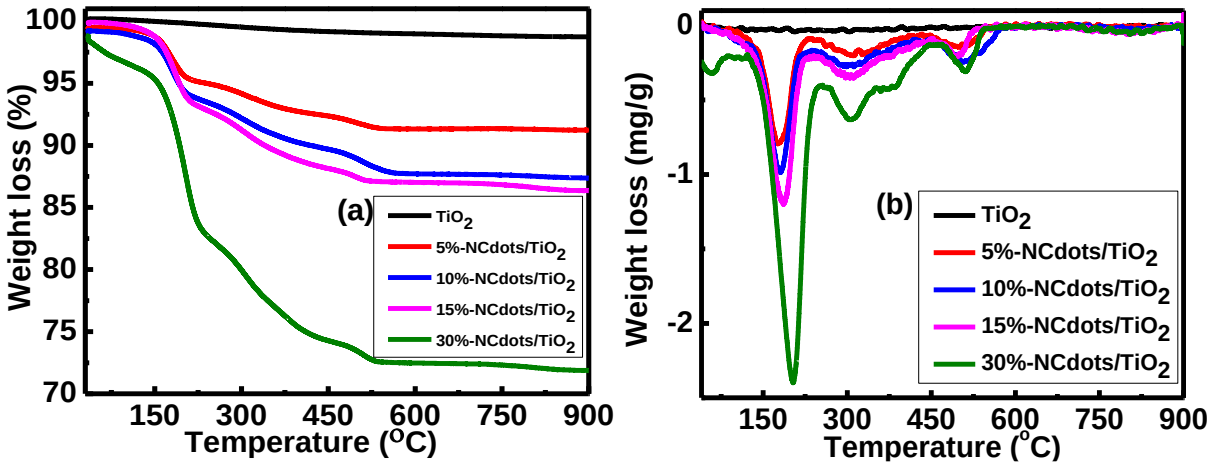

Figure 6.5 (a) TGA thermogram and (b) DTA of 5%-NCdots/TiO_2, 10%-NCdots/TiO_2, 15%-NCdots/TiO_2 and 30%-NCdots/TiO_2.

In addition to the TGA and FTIR data, elemental compositions were probed using CHNS analysis. As expected, the amount of nitrogen, carbon and hydrogen increased with an increase in NCdots loading on the surface of TiO_2. As shown in Table 6.1, the nitrogen content was 1.15, 1.17, 1.70 and 2.45 % for the 5-30%-Cdots/TiO_2 composites, respectively.

Table 6. 1 CHNS elemental composition of the NCdots/TiO_2 composites.

Composites	*C*	*H*	*N*
5%-NCdots/TiO_2	4.91	0.72	1.15
10%-NCdots/TiO_2	4.85	0.70	1.17
15%-NCdots/TiO_2	10.42	2.11	1.70
30%-NCdots/TiO_2	23.76	3.044	2.45

6.5. UV vis analysis

The optical properties of pristine TiO_2 and the NCdots/TiO_2 composites were investigated using UV-vis. As shown in figure 6.6 (a), the pristine TiO_2 and the composites had a broad absorption band that extended up to 800 nm. This peak was centered at 425 nm for pristine TiO_2. Notable, this absorption peak shifted toward a longer wavelength (redshift) and was centered at 460 nm when 5, 10 and 15 %-NCdots were loaded on the surface of TiO_2. This suggests that the presence of NCdots enhanced the visible light absorption of the composites which will, in turn, enhance the photocatalytic activity of TiO_2. In addition, this could suggest the suppression of electrons and holes recombinations, formation of Ti^{3+} ions and existence of Ti-C-O between TiO_2 and NCdots of the composites.[289,139] However, when the loading was increased to 30 %-NCdots loading, the peak was centered at 405 nm which can suggest that higher NCdots is likely to result in higher sites for electron and holes recombinations.[289]

The UV-vis spectrum was further used to determine the bandgap of pristine TiO_2 and the composites. The bandgap energy (Eg) of the synthesized TiO_2 particles was obtained using the equation, Eg = 1240/λ eV. Where Eg is the bandgap in electron volt (eV) and λ is the wavelength of the absorption edges in nanometer (nm). The Tauc plots are shown in figure 6.6 (a) and the calculated band gaps were 3.17, 3.25, 3.34, 3.38, and 3.11 eV for pristine TiO_2, 5, 10,15, and 30%-NCdots/TiO_2 composites, respectively. Increasing NCdots loading from 5-15 % loading can be attributed to an increase in defect sites.[290] The increase in defect sites or functional groups will facilitate more adsorption sites for dye molecules and bring them closer to TiO_2 which will result in enhanced photodegradation.

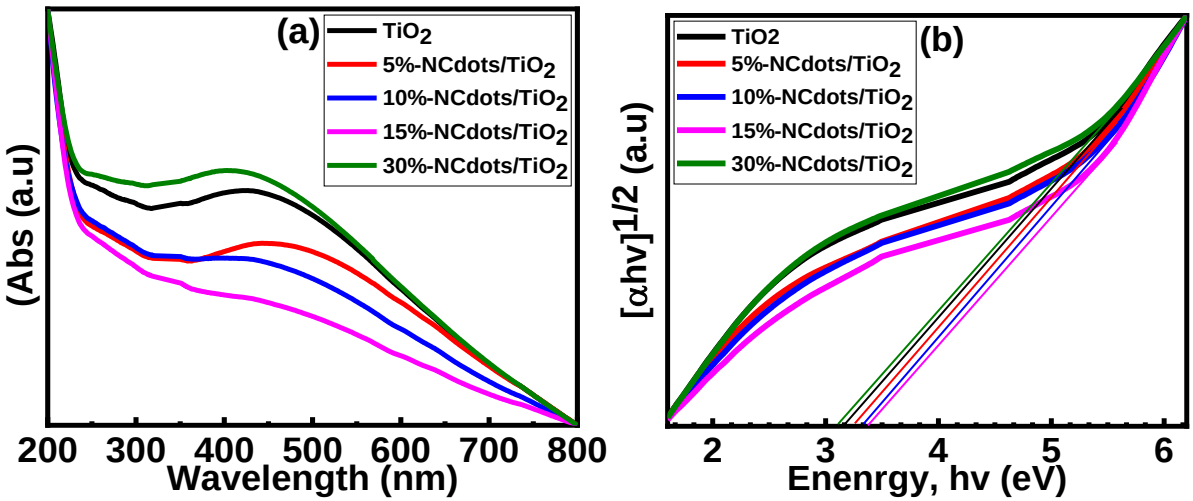

Figure 6.6 (a) UV-Vis spectrum and (b) Tauc plots of pristine TiO_2, and 5-30%-NCdots/TiO_2 composites.

6.6 PL spectroscopy

The optical properties of the NCdots and the NCdots/TiO_2 composites were investigated using PL spectroscopy. It has been reported that the emission peak intensity of PL studies is directly proportional to electron-hole recombination and inversely proportional to photocatalytic efficiency. Since PL records the emitted energy upon recombination of electrons and holes, a high-intensity peak implies a high rate of recombination (short of lifespan, low photocatalytic efficiency) while low-intensity peaks imply a lower rate of recombination (longer lifespan, high photocatalytic efficiency).[206]

The PL emission of bare NCdots, TiO_2 and NCdots/TiO_2 composites was carried at an excitation wavelength of 400 nm. The excitation wavelength of 400 nm was selected since the bare NCdots showed the highest PL emission. This implies that at 400 nm the NCdots have a higher rate of electrons and holes recombination. As shown in figure 6.7, the bare NCdots had a maximum PL emission at 485 nm while a bare TiO_2 showed multi photon emissions observed between 425 nm to 560 nm when an excitation wavelength of 400 nm was used. These several emission peaks from TiO_2 suggest the existence of heterostructure nature due to the presence of anatase and rutile phases of TiO_2 which results in the complex PL emissions.[278] Upon incorporation of the NCdots on the surface of TiO_2, no emissions from NCdots were observed which suggest that the electrons and holes recombination is suppressed by TiO_2. Implying that the excited electrons from NCdots do not go to the ground state but are likely to be transferred to the TiO_2 conduction band.[291] This in turn induced the PL emissions of the NCdots/TiO_2 composites due to photoinduced electron transfer from NCdots to TiO_2 and will be beneficial for enhancing the photocatalytic efficiency of the TiO_2.

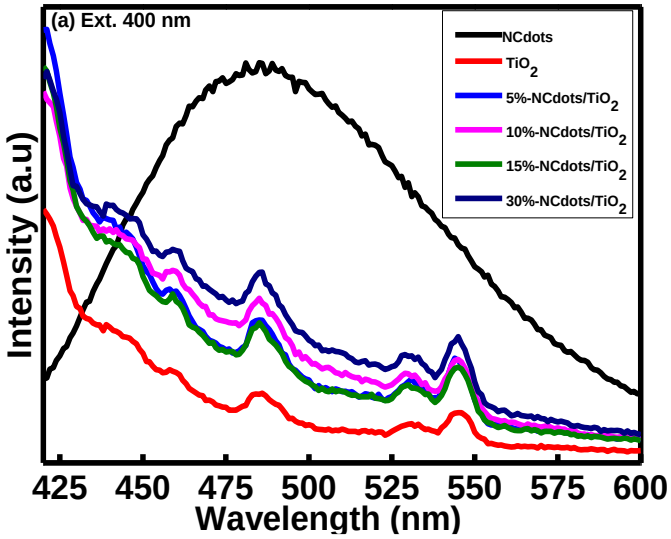

Figure 6.7 PL emissions spectrum of NCdots, anatase TiO_2 and 5-30%-NCdots/TiO_2 composites excited at 400 nm.

6.7 Photocatalytic degradation of methyl orange

The photodegradation of methyl orange was done by varying parameters such as solution pH, initial dye concentration and catalyst dosage. Initially, photodegradation experiments were conducted using all the composites to establish the optimum NCdots loading with efficient catalytic activity towards MO. The study was conducted using 10 mg catalyst dosage, at pH 4 and 10 mg/L (100 mL) initial dye concentration for 30 min. As shown in Figure 6.8, the 10%-Cdots/TiO_2 composite showed better methyl orange degradation as compared to other catalysts. Within 30 min of photocatalytic experiments, the bare TiO_2 and 5, 10, 15 and 30 wt. %-NCdots/Cdots composites reached removal efficiency of 44 %, 42 %, 50 %, 47 % and 41 %, respectively. For further studies, bare TiO_2 and 10%-Ncdots/TiO_2 nanocomposite were used.

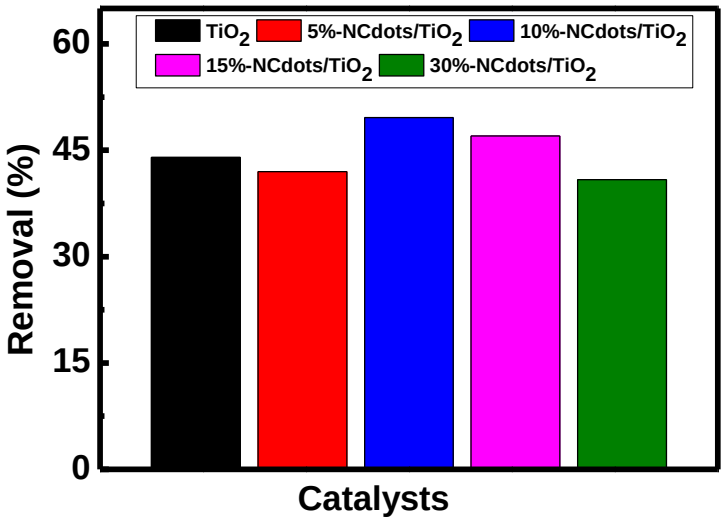

Figure 6.8 Photodegradation efficiency of MO using TiO_2 and 5-30%-NCdots/TiO_2 composites. Conditions: 5 mg catalyst dosage, at pH 4 and 10 mg/L (100 mL) initial MO concentration conducted for 30 min.

6.7.1 Effect of pH

The pH is the influencing factor on photocatalytic degradation processes. The initial MO solution was prepared from the stock solution and the pH was adjusted using 0.1 M NaOH and HCl. The photocatalytic degradation of MO was conducted for 80 min using 25 mg of catalyst dosage, 100 mL of 20 mg/L initial dye concentration at pH 4, 7, and 10. The initial pH of the dye solution affected UV-vis absorptions of MO, at pH 7 and 10 the MO absorbance occurred at its typical wavelength of 464 nm, while at an acidic pH 4 its absorbance was at 508 nm (see MO absorption spectra on of figure S6.3).

The effect of pH on the photodegradation efficiency of MO using 10%-NCdots/TiO_2 composite and TiO_2 particles is shown in Figures 6.9 (a) and (b). As shown in figure 6.9 (a) and (b), at pH 4 the MO degradation occurred rapidly within the first 20 min when 10%-NCdots/TiO_2 composite was used. The degradation efficiency (%) reached up to 96.5 % and 43 % within the first 40 min when 10%-NCdots/TiO_2 composite and TiO_2 were used, respectively. After 80 min, no MO absorption band was observed which suggests that a 100 % MO decolorization was achieved when 10%-NCdots/TiO_2 composite was used, while 87 % MO decolorization was reached when TiO_2 was used.

When the pH was 7 and 10, the degradation efficiency (%) was below 40 % and 20 % after 80 min for of 10%-NCdots/TiO_2 composite and TiO_2, respectively. The change in the initial pH of the dye solution can alter the overall charge of the dye and the catalyst, which can affect the rate of adsorption of dye molecules on the catalyst.[292] At the acidic pH 4, the surface of the composite and TiO_2 is positively charged, this allows easy adsorption of anionic MO molecules through electrostatic attraction. The adsorption of MO molecules on the surface of the catalyst allows for photo-oxidation to take place which induces a photocatalytic degradation process. While at the basic media, the surface of the catalysts and MO molecules are negatively charged and an electrostatic repulsion is favored, this results in a decrease in degradation efficiency.[292,52]

These observations when varying the initial pH of the dye solution can be summarized using equations 6.1 and 6.2 below. As it has been previously reported that the photodegradation efficiency of most organic compounds increases with decreasing the pH value due to sufficient generation of hydroxyl radicals on the surface of aqueous TiO_2. However, this is mainly due to

electrostatic attraction between the charged MO molecules and the charged surface of TiO_2 nanoparticles.[293] With the point of zero charges (PZC) of TiO_2 been reported to be at 6.8, and the MO dye consisting of negatively and positively charges species, and when the pH is decreased its color changes from yellow to light red (and also changes its absorption character, figure S6.3). The color change results in a change in MO ionic character, which destabilizes it and favors its photodegradation efficiency. As shown in equation 6.1, at pH lower than PZC the surface of TiO_2 starts to gain protons and it becomes positively charged. In addition, according to equation 6.2 at a lower pH value, H_2O molecules are absorbed into the TiO_2 surface and react with a valence band hole to generate a sufficient number of hydroxyl radicals. These exhibit higher transfer of photogenerated electrons to the surface of TiO_2 and react with adsorption oxygen. Thus, at acidic conditions, the photocatalytic efficiency toward MO is enhanced due to the higher generation of radicals and stronger electrostatic attraction between TiO_2 and dye molecules.[293,294]

$$TiOH + H^+ \rightarrow TiOH_2^+ \ldots\ldots\ldots\ldots (6.1)$$

$$H_2O + h_{vb}^+ \rightarrow \bullet OH + H^+ \ldots\ldots\ldots (6.2)$$

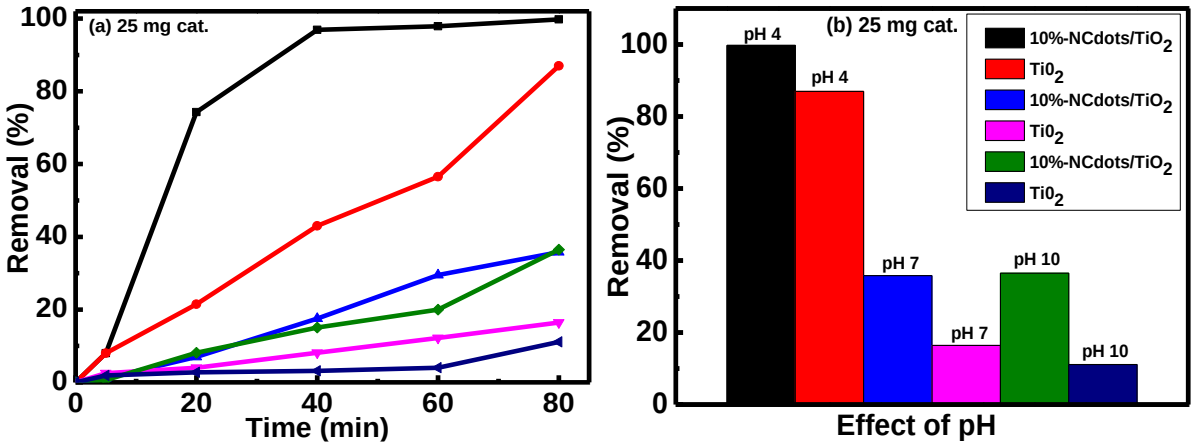

Figure 6.9 The effect of pH 4, 7, and 10 on MO degradation. Conditions: 25 mg catalyst dosage, 100 mL of 20 mg/L MO concentration conducted for 80 min.

6.7.2 Effect of catalyst dosage

The effect of dosage was carried out using 25 mg, 50 mg, and 75 mg of 10%-NCdots/TiO_2 and TiO_2 catalysts at pH 4. As shown in figure 6.10, the catalyst dosage influenced the degradation rate of MO. At 5 and 20 min, the removal (%) efficiency when using 25 mg (see figure 6.10 (a)), 50 mg and 75 mg catalyst dosage was 8 % and 74.5 %, 22 % and 87.3 %, 54 % and 88.8 %, respectively. Hence, increasing the catalyst dosage increased degradation efficiency which

can be attributed to the availability of active sites for degradation to occur as the catalyst dosage was increased.

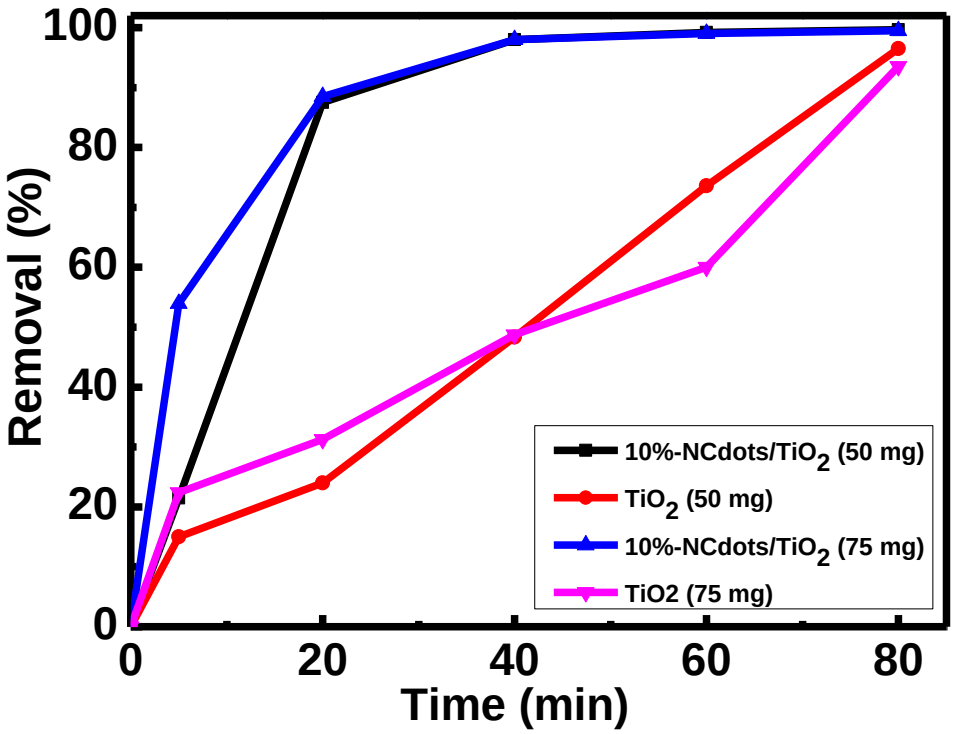

Figure 6.10 The effect of dosage with 50 and 75 mg on MO degradation. Conditions: 25 mg catalyst dosage, 100 mL of 20 mg/L MO concentration conducted for 80 min.

The 10%-NCdots/TiO_2 composite performed better than TiO_2, implying that the presence of NCdots played a major role in increasing the degradation efficiency of TiO_2 under visible light irradiation. The NCdots did not show any upconversion characteristics when excited using 400 nm, while its PL emission was suppressed when incorporated on the surface of TiO_2. This suggests that the recombination of photogenerated electrons and holes in the excited NCdots is suppressed implying that photo-induced electron transferred was exhibited. Hence, NCdots act as a photosensitizer of TiO_2 and induce the reduction efficiency of TiO_2. In addition, the N-doping can lower the work function of carbon which favored the increased generation of excited electrons in NCdots that in turn are injected into TiO_2.[55]

6.7.3 Perceived breakdown of MO using 10 wt. %-NCdots/TiO_2 composite

The UV-vis analysis of MO aliquots was recorded from 0 to 80 minutes after exposure to solar simulated light, see Figures S6.2 and S6.3 for UV-vis spectra. The UV-vis intensity of MO was decreased as the exposure time was increased, and no MO peak was observed after 80 minutes of solar exposure when 10 wt %NCdots/TiO_2 composite was used. This suggests that the MO

was degraded to smaller organics resulting in its decolorization. The orange color of the MO solution became colorless due to the change in the chromophore of MO molecules.[295]

6.7.4 Proposed mechanism of 10 wt. %-NCdots/TiO_2 composite

The photocatalytic activity of TiO_2 is known to be suppressed by the faster recombinations of photogenerated electrons and holes. Under UV irradiation, the electrons from the valence band get excited to the conduction band, creating holes in the valence band. Due to faster recombinations, these charge carries quickly recombine and only a fraction participate in a photocatalytic reaction resulting in the poor activity of TiO_2.[24]

In our case, illumination of TiO_2 with a solar simulator results in the lower generation of electrons and holes because TiO_2 can only utilize UV radiation which is ≤ 5 % from the light source.[296] This drawback coupled with faster recombination processes in TiO_2 results in low photocatalytic activity. However, it was observed that the incorporation of NCdots on the surface of TiO_2 exhibited higher photocatalytic activity for MO degradation. As shown in figure 6.11, the NCdots did not show any upconversion character while its PL emission was suppressed when incorporated on the surface of TiO_2. Hence, it can be depicted that under visible light irradiation the NCdots utilize more visible light and enhances the light harvesting, charge separation and transfer properties of the composite.[297] In addition, the presence of NCdots on the surface of TiO_2 induces the adsorption of MO molecules closer to the surface of TiO_2 and photocatalytic reactions take place faster and effectively.[137,298]

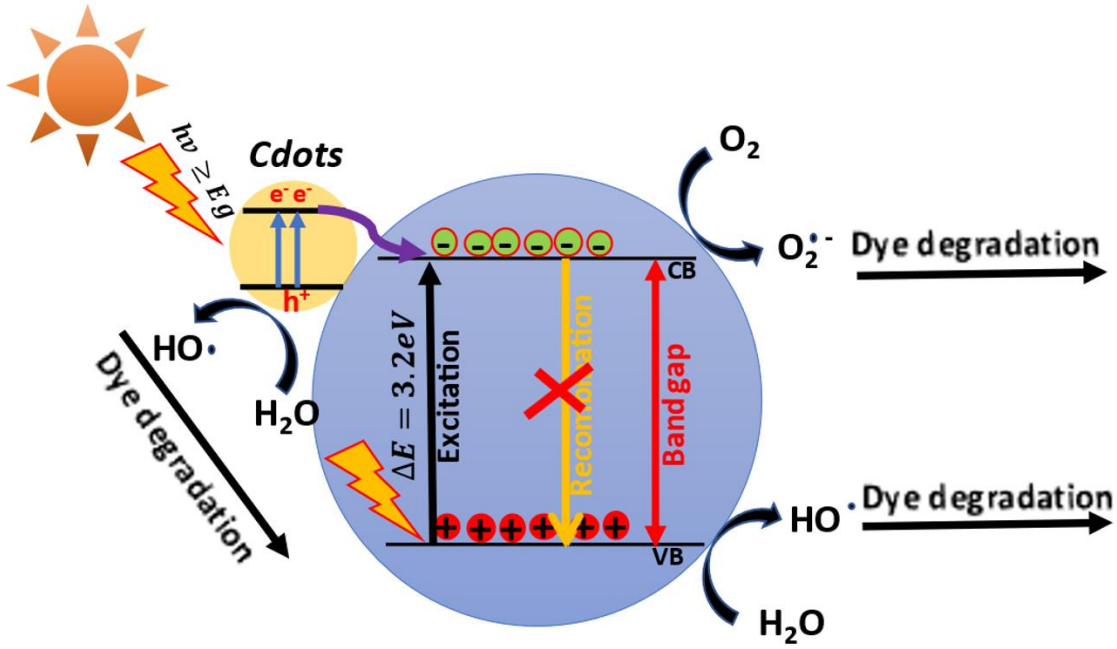

Figure 6.11 Proposed mechanism for photosensitization and degradation of MO using 10%-NCdots/TiO_2 composite.

6.8. Conclusion

In conclusion, N-doped carbon dots with abundant functional groups and quasi-spherical in shape were synthesized using the microwave-assisted method. The anatase TiO_2 particles consisting of various morphologies such as cuboid, truncated tetragonal, and semi-spherical were obtained via the refluxing at 80 °C. The successful formation of NCdots/TiO_2 composites was revealed by agglomerated Cdots, abundant functional groups, decomposition curves and elemental composition. The anatase TiO_2 maintained its pure phase after the incorporation of NCdots which were inhomogeneously distributed on the surface. The incorporation of 10 % NCdots was found to be an optimum concentration of NCdots on the TiO_2, and it exhibited higher photocatalytic activity toward methyl orange degradation. The photocatalytic activity of the TiO_2 and 10%-NCdots/TiO_2 composite was influenced by the initial pH of the dye solution and catalyst dosage. The higher photocatalytic activity of the 10%-NCdots/Cdots composite was attributed to photosensitization (photo-induced electron transfer) and synergetic effect between TiO_2 by NCdots.

Supporting information: Appendix D

Chapter 7

Conclusions

This project has demonstrated two ‘‘bottom-up’’ strategic approaches for the synthesis of nitrogen-doped carbon dots (NCdots) using three different starting reagents and water as a solvent. The synthesis was carried out using an autoclave reactor and a microwave-assisted approach using chitosan, glycerol, and urea as carbon and nitrogen sources. The typical spherically shaped NCdots with a particle size of ≤ 10 nm were obtained using the above-mentioned methods and reagents. The obtained NCdots were systematically incorporated on the surface of hollow and solid carbon spheres, silica spheres and TiO_2 particles. The NCdots were well dispersed on ethanol, water and ammonia solution mixture, and they maintained their original shape and size after incorporation on the surface of the solid supports. In addition, a one-pot hydrothermal method was used for the synthesis of NCdots/chitosan composites.

The optical properties of the NCdots and NCdots/support composites were investigated using PL spectroscopy. All the materials showed a typical excitation wavelength dependency (redshift) nature when excited at different wavelengths. It was observed that the incorporation of the NCdots on the surface of the supports altered the PL emission properties of the supported Cdots. This resulted in the composites emitting at different wavelengths as compared to unsupported NCdots. Due to different interactions between NCdots and the supports, the intensities of their PL emissions were greatly dependent on the support. Hence, the photoluminescent quantum yield (PLQY) varied with the support used, with NCdots supported on a silica matrix exhibiting a higher PLQY. Furthermore, under UV illumination at 365 nm the bare NCdots and the supported NCdots exhibited glowing emissions giving rise to different colors depending on the support. The realization of PL emissions from the solid-state NCdots/support composites is promising for potential applications in photonics, optoelectronic devices, and photochemistry.

The NCdots/CHIT-1h and NCdots/TiO_2 composites were used for methyl orange removal from wastewater via adsorption and photodegradation processes, respectively. These composites were robust in the removal of methyl orange, with the NCdots/CHIT-1h composite reaching a maximum adsorption capacity of up to 370 mg/g, at pH 4 (40 mg/L;100 mL initial dye concentration) via batch adsorption experiments. On the other hand, the NCdots/TiO_2 composite exhibited higher photocatalytic degradation of methyl orange due to a photo-induced electron transfer (photosensitization) reaction from NCdots to the TiO_2 VB. The synergistic

effect of the composite prolonged the electrons and holes recombination. The adsorption and photodegradation of methyl orange using NCdots/CHIT-1h and NCdots/TiO_2 reached above 96 % removal efficiency after 40 min, and the catalysts were greatly dependent on the initial pH of the dye solution with pH 4 being optimum. Factors such as catalyst dosage and initial dye concentration were observed to influence the adsorption and photodegradation efficiency of methyl orange. These composites showed potential for use in the adsorption and photodegradation of methyl orange.

Outlook

This study has shown a systematic approach for the incorporation of NCdots on the surface of hollow and solid carbon spheres, silica spheres, and TiO_2 particles. The supports were observed to influence the optical properties of the NCdots owing to the nature and interaction between the support and NCdots. The study further demonstrated the use of NCdots/support composites in wastewater treatment via adsorption and photocatalytic means.

Safety and experimental issues

(i) When using autoclave reactor and microwave-assisted methods it is important to be considerate of the solvent used, to minimize temperature fluctuations, and to have well-functioning pressure release valves. Lack of caution on these issues can result in explosions and instrument malfunctioning.

(ii) Temperature and pressure are important factors to consider during the synthesis of Cdots using either autoclave or microwave methods. In addition, the purification steps that are used to separate Cdots from other residual hydrochar should be followed carefully.

Future perspective

This research has highlighted some of the Cdots endeavors which can be used shortly. This includes but is not limited to (i) facile synthesis of Cdots and the formation of its composites, (ii) exploration of fluorescent properties of bare Cdots and its composite materials, including solvatochromism and (iii) potential applications of Cdots composite materials in MO removal using adsorption and photocatalytic processes.

However:

- A fundamental step-by-step investigation to probe the fluorescent/chromophores

centers responsible for fluorescent emission in Cdots is still needed.

- Establishment of a mechanism that leads to different fluorescent emissions when Cdots solution and solid-state needs further investigation.
- Exploration of various porous solid support matrix should be accelerated for the potential design, manufacture and commercialization in photonics, optoelectronics, sensing devices, and photochemical applications.

Closing remark: A new fluorescent Cdots/support (solid-state material) composite device based on this study is to be investigated for possible commercialization.

Chapter 3. Supplementary information

(Appendix A)

A comparison of fluorescent N-doped carbon dots supported on the surface of hollow and solid carbon spheres, and solid silica spheres

S3.1. Contents

S3.1.1 XPS of bare Cdots

X-ray photoelectron spectroscopy (XPS) was carried out to investigate the presence of functional groups and bonding environments within the Cdots structure. Data are similar to those reported by others.[104,175] With similar functionalities such as C=N/C=O, C-O, C-N, C-C/C=C. N-H as that from IR (figure S3.2). The chemical composition of the NCdots was found to comprise 67.7 atomic % of C1s, 23.9 atomic % of O1s, and 6.1 atomic % of N1s. The nitrogen atomic % composition is comparable to that obtained from CHNS elemental analysis which was 6.95 % of nitrogen, (table S3.3). This would imply that the N is evenly distributed throughout the NCdots structure and not only found on the surface. This can further imply that the as-synthesized NCdots constitute multistate sites (from defects or various functional groups and NCdots size) which will contribute to their optical properties.

S3.1.2 Quantum yield calculations

The relative quantum yield of the NCdots, NCdots/SSs, NCdots/HCSs were calculated by using the PL intensities with quinine sulfate (QS) as the reference. The procedure for calculating quantum yield followed previous literature reports.[143,166] The equation used for calculating quantum yield was as follows:

$$Q_s = Q_r \left(\frac{I_s}{I_r}\right)\left(\frac{A_r}{A_s}\right) \dots\dots\dots\dots\dots\dots S3.1$$

Where Q_s the quantum yield of the sample, I_s and I_r are the measured intensities of fluorescent emissions for sample and the quinine sulphate reference, respectively. The A_r and A_s are the measured absorbance of the reference and sample, respectively. The measured absorbance for NCdots, NCdots/SSs, NCdots/HCSs and QS are in table S3.5 and the refractive index was assumed to be 1 since the same solvent was used. The percentage quantum yield (% QY) was derived from equation S3.2.

$$\% \, QY = \frac{Experimental \, QY}{Ref. Theoretical \, QY} \times 100 \, \% \ldots\ldots S3.2$$

S3.1.3 Supplementary figures

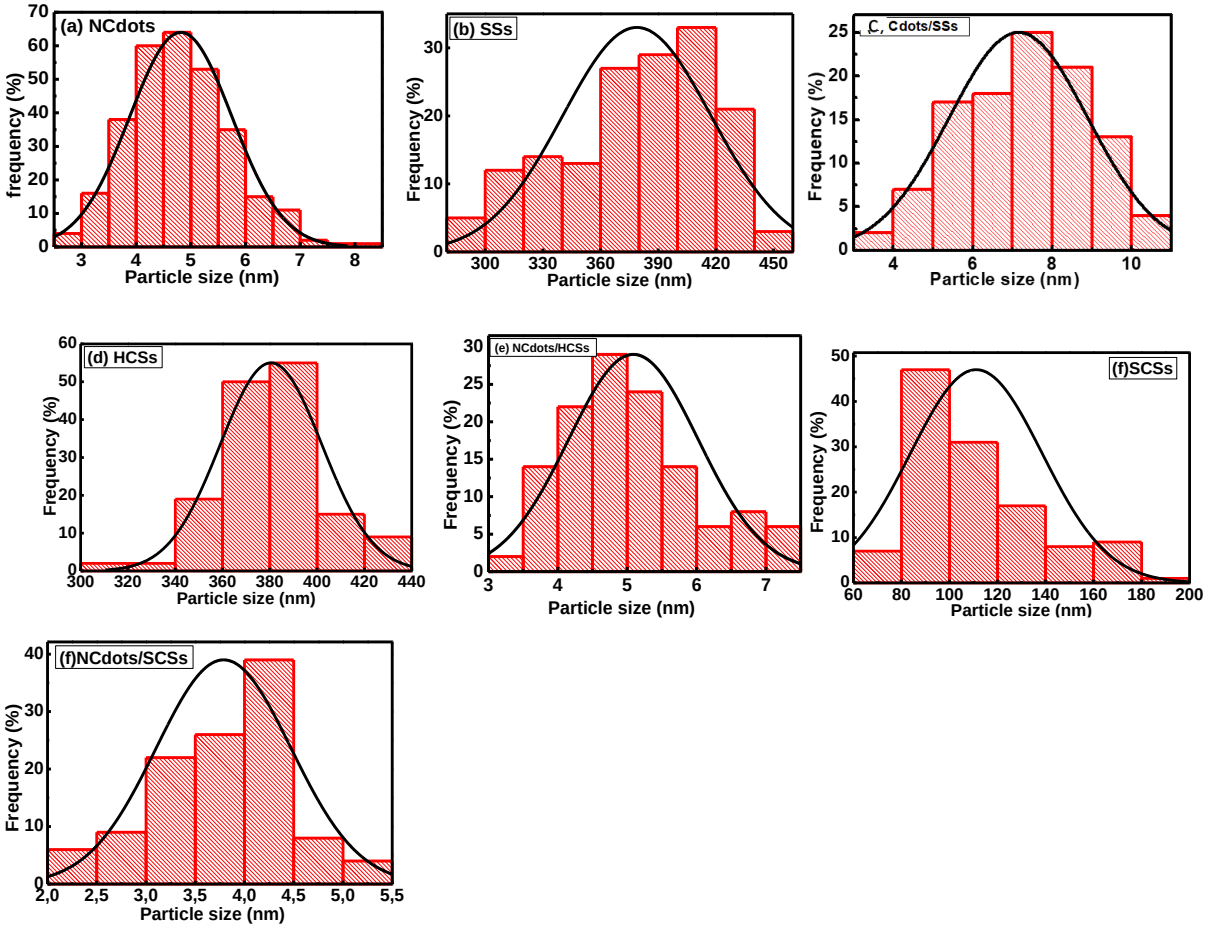

Figure S3.1 Particle size distribution of (a) NCdots, (b) SSs, (c) NCdots/SSs, (d) HCSs (e) NCdots/HCSs, (f) SCSs and (g) NCdots/SCSs calculated using ImageJ 1.52 v software.

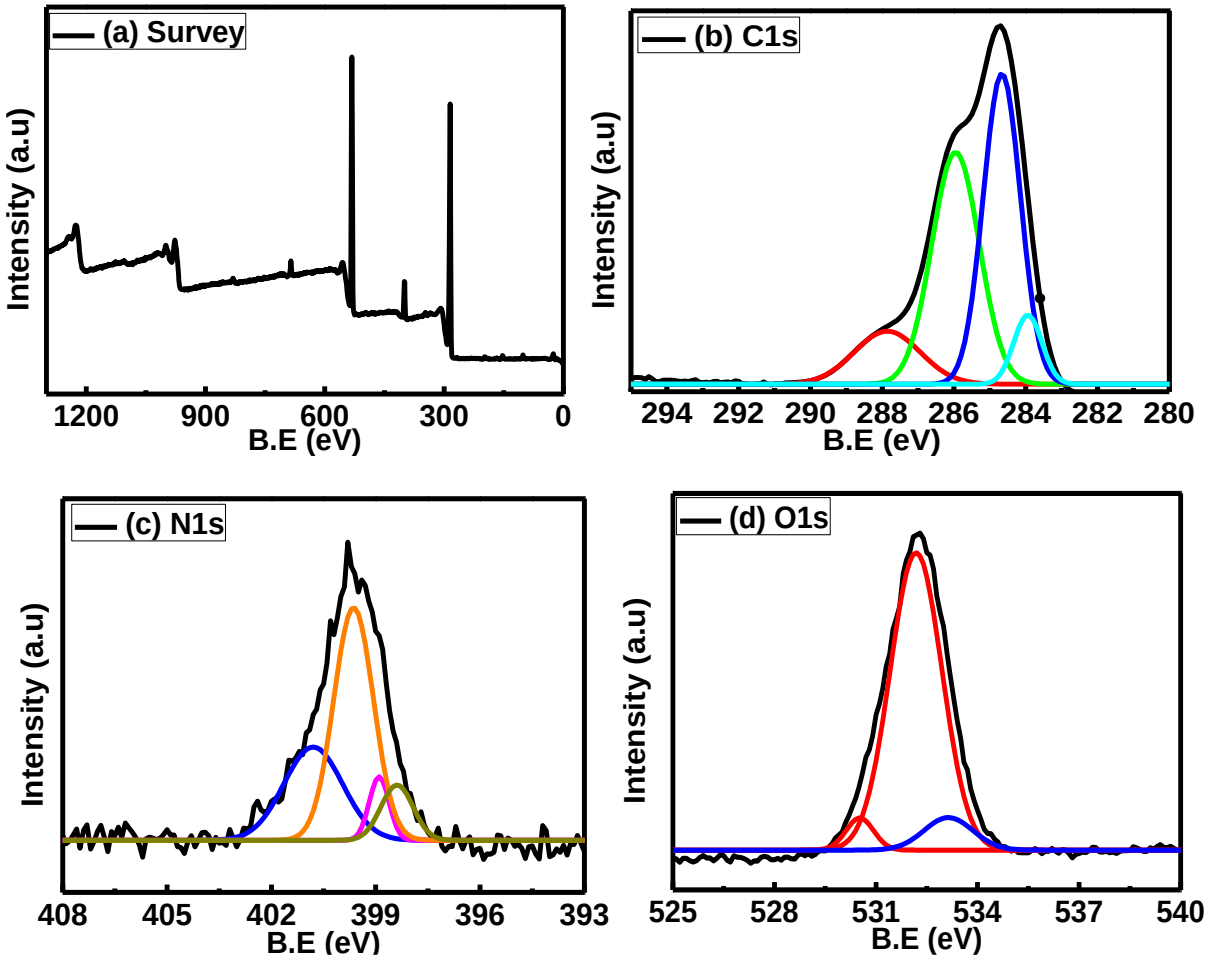

Figure S3.2 XPS spectrum of bare (a) NCdots, higher resolution of (b) C1s, (c) N1s and (d) O1s, respectively.

1.4. Tables

Table S3. 1 Various solid materials used to support NCdots.

Support	**Cdots size (loading)**	**PLQY**	**Application or finding**	**Ref**
Silica	≤ 10 nm (19.2 wt %)	41 %	Fabricated on white LED prototypes	[156]
MOFs	≤ 10 nm	—	Optical bio-imaging	[165]
SiO_2-PEG	5.5 nm	32 %	Drug delivery	[119]
TiO_2	4.6 nm	—	Photocatalytic hydrogen evolution	[57]

MWCNT's	≤10 nm	__	Bacterial removal from water	[136]
HCSs	3 nm	__	Inkjet printing and sensitized solar cells	[166]
Cdots/porous carbon spheres	2-3 nm	__	Good for energy storage	[167]
Starch/g-CDs composite	≤10 nm	~50%	Enhanced PLQY	[168]
Cdots/Au or Ag	0.6 nm to 8.7 nm	__	Findings: Enhanced PL emissions	[169]
CD/polymer films	2.6 nm	~34%	Strong fluorescence emissions	[115]
Polymer-dots@Carbon core shell	~ 4 nm, polymer Cdots	8.6 %	Cu^{2+} adsorption	[158]
SSs	≤ 10 nm (~ 20 %)	35 %	Finding: Enhanced PLQY	This work
HCSs	≤ 10 nm (~ 20 %)	13 %	Finding: Lowered PLQY	This work
SCSs	≤ 10 nm (~ 20 %)	7.5 %	Finding: Lowered PLQY	This work

Table S3.2 IR vibrational modes for bare NCdots and 20 % NCdots loaded on SSs, HCSs and SCSs.

Vibrations	**OH/ NH**	**C-H stretch**	**C-H bending**	**COOH**	**C=C**	**N-H bending**	**C-C/ C-O-C**	**Si-O-Si stretch**	**Si-O-Si bending**

NCdots	3305 cm^{-1}	2935/ 2880 cm^{-1}	918/850 cm^{-1}	1651/ 1583 cm^{-1}	1408 cm^{-1}	1325 cm^{-1}	1035 cm^{-1}	___	___
SSs	___	___	___	___	___	___	___	1069 cm^{-1}	946/782 cm^{-1}
20%Cdots /SSs	3328 cm^{-1}	2943/ 2879 cm^{-1}	950 cm^{-1}	1646/ 1579 cm^{-1}	1416 cm^{-1}	___	1050 cm^{-1}	1050 cm^{-1}	798 cm^{-1}
HCSs	___	2903/ 2840 cm^{-1}	796 cm^{-1}	___	1585 cm^{-1}	___	1065 cm^{-1}	___	___
20%NCdots/ HCSs	___	2903/ 2840 cm^{-1}	796 cm^{-1}	___	1586 cm^{-1}	1219 cm^{-1}	1039 cm^{-1}	___	___
SCSs	___	___	1047/ 887 cm^{-1}	___	___	___	1110/ 1195 cm^{-1}	___	___
20%NCdots/ SCSs	___	2911 cm^{-1}	1047/ 887 cm^{-1}	___	1455 cm^{-1}	___	1195 cm^{-1}	___	___

Table S3.3 CHNS of NCdots and the NCdots/support composites.

	CHN results (%)		
Sample name	**C**	**H**	**N**
NCdots	45.75	5.52	6.95
NCdots/SSs	8.26	2.26	0.58
NCdots/HCSs	52.14	4.35	1.62
NCdots/SCSs	55.18	6.79	0.62

Table S3.4 PL emissions at an excitation wavelength of 350 nm.

Sample/PL emissions	HCSs	SCSs	SSs
NCdots (emmision = 424 nm)	-	-	-
5%NCdots	416 nm	403 nm	417 nm
10%NCdots	415 nm	403 nm	419 nm
15%NCdots	415 nm	415 nm	415 nm
20%NCdots	416 nm	417 nm	420 nm

Table S3.5 Quantum yield calculations

Sample	Integrated Emission Intensity	Abs@350 nm (A)	% Quantum Yield (Q)
QS ref	1407494	0,1585	0.54 (known)
NCdots	149696	0,0918	0,1836
5%NCdots/HCSs	48003	0,1955	0,0277
10%NCdots/HCSs	96657	0,338	0,0322
15%NCdots/HCSs	48003	0,1299	0,0416
20%NCdots/HCSs	114767	0,184	0,0702
5%NCdots/SCSs	11463	0,1397	0,0832
10%NCdots/SCSs	13992	0,096	0,2282
15%NCdots/SCSs	25786	0,1172	0,1819
20%NCdots/SCSs	33161	0,0918	0,1920
5%NCdots/SSs	31758,99	0,043	0,0093

10%NCdots/SSs	51262,12	0,0253	0,0164
15%NCdots/SSs	64440,15	0,0399	0,0248
20%NCdots/SSs	50966,775	0,0299	0,0407

Chapter 4: Supplementary information

(Appendix B)

Encapsulation of carbon dots prepared from glycerol and urea inside hollow carbon spheres

S4.1 Contents

S4.1.1 Supplementary figures.

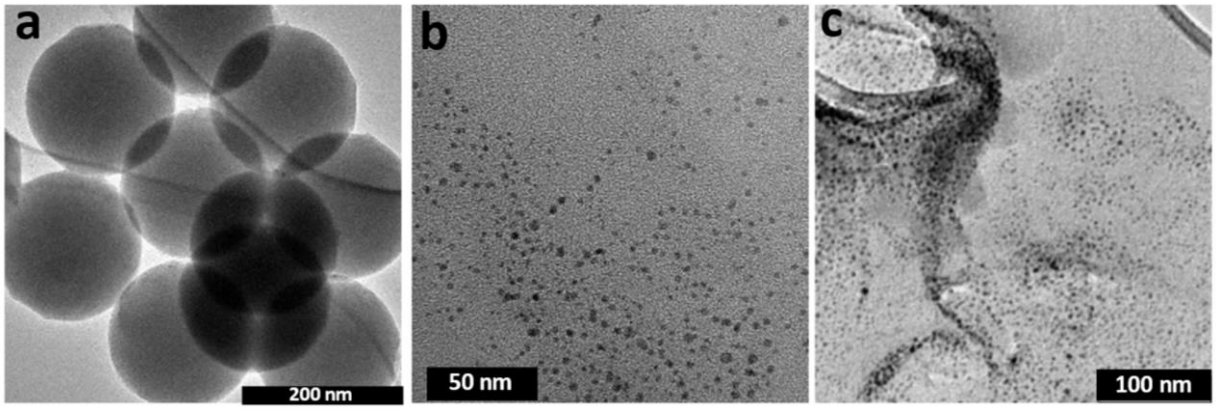

Figure S4.1 (a) SSs and (b) GCdots and GUCdots extracted from the supernatant matrix.

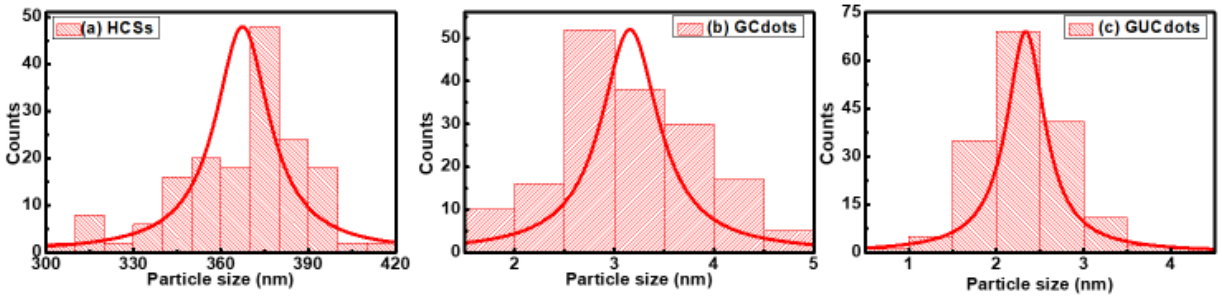

Figure S4.2 Particle size distribution for (a) HCSs, supernatant (b) GCdots and (c) GUCdots calculated using ImageJ.

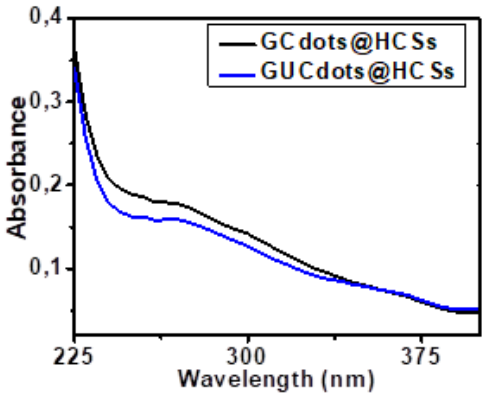

Figure S4.3 Normalized UV-vis spectrum of GCdots@HCSs and GUCdots@HCSs composites.

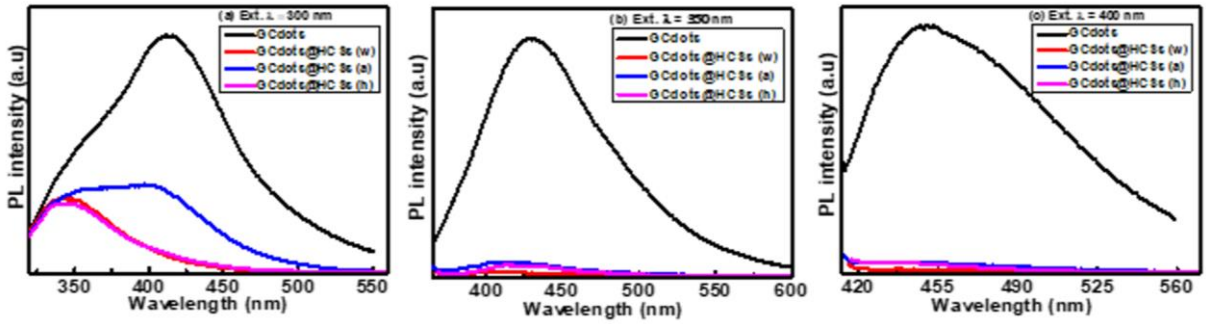

Figure S4.4 PL emission spectrum of GCdots and GCdots@HCSs dispersed in water, acetone, and hexane, and λ_{ext} at (a) 300 nm, (b) 350 nm and (c) 400 nm.

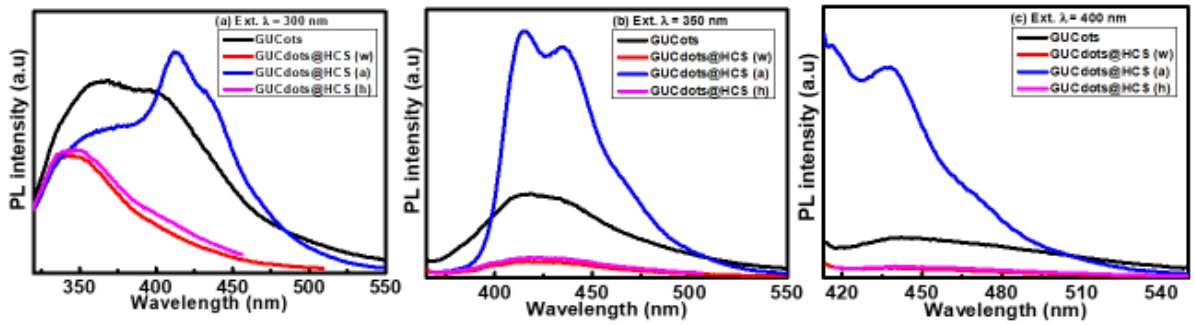

Figure S4.5 PL emission spectrum of GUCdots and GUCdots@HCSs dispersed in water, acetone, and hexane, and λ_{ext} at (a) 300 nm, (b) 350 nm and (c) 400 nm.

4.1.2. Supplementary tables

*(s) for shoulder peak

* (h) for hump-like peak

Table S4.1 Raman parameters of HCSs, GCdots@HCSs, and GUCdots@HCSs.

Sample name	I_G *(area)*	I_D *(area)*	I_D/I_G *(ratio)*	I_G *(peak position)*	I_D *(peak position)*	I_G *(FWHM)*	I_D *(FWHM)*
HCSs	210302	383411	1.82	1590	1357	86	244
GCdots@HCSs	100746	288648	2.87	1589	1339	100	296
GUCdots@HCSs	83422	233094	2.79	1587	1339	96	291

Table S4.2 PL emission peaks of GCdots and GCdots@HCSs dispersed in water, acetone, and hexane. PL λ_{ext} at (a) 300 nm, (b) 350 nm and (c) 400 nm.

Sample name	λ_{ext} *= 300 nm*	λ_{ext} *= 350 nm)*	λ_{ext} *= 400 nm*
GCdots	384 (s) & 412 nm	430 nm	450
GCdots@HCSs (w)	344 nm	411 nm	436
GCdots@HCSs (a)	362 & 398 nm	410 nm	438 nm
GCdots@HCSs (h)	344 nm	415 nm	436 nm

Table S4.3 PL emission peaks of GUCdots and GUCdots@HCSs dispersed in water, acetone, and hexane. PL λ_{ext} at (a) 300 nm, (b) 350 nm and (c) 400 nm.

Sample name	λ_{ext} *= 300 nm*	λ_{ext} *= 350 nm)*	λ_{ext} *= 400 nm*
GUCdots	365 & 395 nm	422 nm	442 nm
GUCdots@HCSs (w)	344 nm	422 nm	440 nm
GUCdots@HCSs (a)	362 (h), 412 & 432 (s)	416 & 434 nm	416 & 437 nm
GUCdots@HCSs (h)	344 nm	422 nm	442 nm

Chapter 5. Supplementary information

(Appendix C)

One-pot carbonization of chitosan into N-doped carbon-dots/chitosan nanocomposites for the adsorption of methyl orange from aqueous solutions

S5.1 Contents

S5.1.1 Supplementary figures

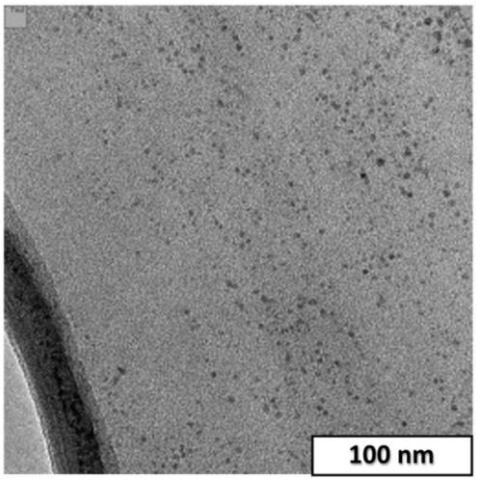

Figure S5.1 TEM image of NCdots.

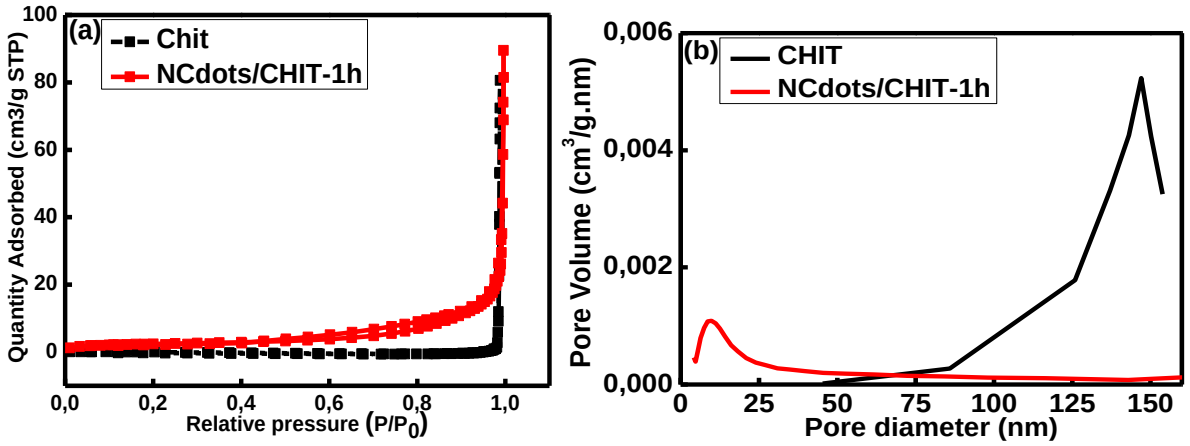

Figure S5.2 (a) N_2 adsorption-desorption isotherm and (b) corresponding pore size distribution curves of pristine CHIT and NCdots/CHIT-1h nanocomposite.

S5.1.2 Supplementary tables

Table S5.1 Pseudo-first (PFO) kinetic parameters for 10 mg adsorbent.

Concentration	R^2 *(linear)*	K_1	$q_{e,exp}$	$q_{e,cal}$
10 (mg/L)	0.8896	0.00395	96	22.96
20 (mg/L)	0.9895	0.00238	183	75.80
30 (mg/L)	0.8290	0.00103	275	40.80
40 (mg/L)	0.7642	0.00028	350	117.5

Table S5.2 Pseudo-first (PFO) kinetic parameters for 25 mg adsorbent.

Concentration	R^2 *(linear)*	K_1	$q_{e,exp}$	$q_{e,cal}$
10 (mg/L)	0.8068	0.0074	38.4	3.56
20 (mg/L)	0.9555	0.0016	74	25.03
30 (mg/L)	0.8971	0.0013	112	24.14
40 (mg/L)	0.8984	0.0005	142	66.40

Table S5.3 Pseudo-first (PFO) kinetic parameters for 50 mg adsorbent.

Concentration	R^2 *(linear)*	K_1	$q_{e,exp}$	$q_{e,cal}$

10 (mg/L)	0.5105	0.0021	18.2	1.62
20 (mg/L)	0.6058	0.0001	34.8	2.45
30 (mg/L)	0.7868	0.0001	56.2	4.15
40 (mg/L)	0.6364	0.0001	75.6	8.53

Table S5.4 Pseudo second order kinetic parameters for 10 mg adsorbent.

Concentration	R^2 *(linear)*	K_2	$q_{e,exp}$	$q_{e,cal}$
10 (mg/L)	0.9999	8,77E-07	96	96.81
20 (mg/L)	0.9998	1,67E-07	183	184.84
30 (mg/L)	0.9999	2,89E-08	275	275.48
40 (mg/L)	0.9967	8,69E-08	350	357.14

Table S5.5 Pseudo second order kinetic parameters for 25 mg adsorbent.

Concentration	R^2 *(linear)*	K_2	$q_{e,exp}$	$q_{e,cal}$
10 (mg/L)	0.9994	2,3E-05	38.4	38.26
20 (mg/L)	0.9997	3,46E-06	74	75.08
30 (mg/L)	0.9996	6,35E-07	112	113.12
40 (mg/L)	0.9998	1,19E-06	142	144.72

Table S5.6 Pseudo second order kinetic parameters for 50 mg adsorbent.

Concentration	R^2 *(linear)*	K_2	$q_{e,exp}$	$q_{e,cal}$
10 (mg/L)	0.9492	0,002113	18.2	18.89
20 (mg/L)	0.9384	0,000275	34.8	37.64
30 (mg/L)	0.9366	5,61E-05	56.2	66.71

40 (mg/L)	0.9256	2,75E-05	75.6	88.89

Table S5.7 Langmuir constants.

Pristine CHIT	K_L	R_L	$Q_{max, L}$	R^2
10 mg dosage	0.17	0.166	118	0.944
25 mg dosage	0.13	0.198	98	0.943
50 mg dosage	0.10	0.205	53	0.954

Table S5.8 Freundlich constants

Pristine CHIT	*n*	K_F *[(mg/g)/(L(mg)^n]*	R^2
10 mg dosage	1.80	22.78	0.886
25 mg dosage	1.63	15.65	0.925
50 mg dosage	1.45	7.34	0.945

Table S5.9 Elemental composition of pristine CHIT and NCdots/CHIT-1h composite.

Adsorbent	*C*	*H*	*N*
CHIT	40.53 %	8.04 %	7.24 %
NCdots/CHIT-1h	49.66 %	7.04 %	8.11 %

Table S5.10 BET textural properties of pristine CS and Cdots/CS-1h nanocomposite.

Adsorbent	*SA (m^2/g)*	*PD (nm)*	*PV (cm^3/g)*
CHIT	0.06	147	0.12
NCdots/CHIT-1h	8.44	10	0.11

S5.1.1 Supplementary equations

Langmuir

The Langmuir isotherm is based on monolayer adsorption and is best described by the equation (S5.1) below.[271]

$$q_e = \frac{q_{\max} \times K_L \times C_e}{1 + K_L \times C_e} \qquad (S5.1)$$

and this can be linearized to equation S5.2 below:

$$\frac{C_e}{q_e} = \frac{1}{K_L \times q_{max}} + \frac{1}{q_{max}} \quad (S5.2)$$

where K_L is the Langmuir constant and q_{max} is the maximum amount of adsorption of the complete coverage on the surface, C_e and q_e are are the dye concentration at equilibrium (mg/L) and adsorption capacity at equilibrium (mg/g), respectively.

The R_L which is a constant separation of the solid-liquid adsorption system was calculated using equation S5.3 below. Where C_o is the initial adsorbate concentration.[299]

$$R_L = \frac{1}{1 + K_L C_O} \quad (S5.3)$$

Freundlich isotherm

The Freundlich isotherm assumption is based on multilayer coverage of the adsorbent surface by adsorbate. The Freundlich model is given by equation (S5.3) below:[140]

$$q_{e=} k_f C_e^{1/n} \qquad (S5.4)$$

And a linear form of the Freundlich model is as following:[271]

$$\log q_e = \log K_f + \frac{1}{n} \log C_e \quad (S5.5)$$

Where K_f (mg/g) is a constant that relates to the adsorption capacity and 1/n is an empirical parameter relating to the adsorption intensity, depending on the heterogeneity of the adsorbent.[272,262]

Chapter 6. Supplementary information

(Appendix D)

N-doped carbon dots decorated on the surface of TiO_2 for photocatalytic degradation of methyl orange from aqueous solution.

Contents S6.1

S6.1.1. Supplementary figures

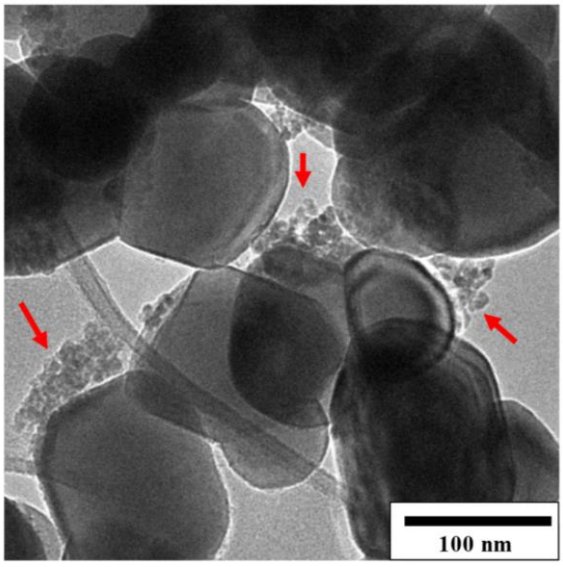

Figure S6.1 TEM image of 10 wt. %-NCdots/TiO_2 composite.

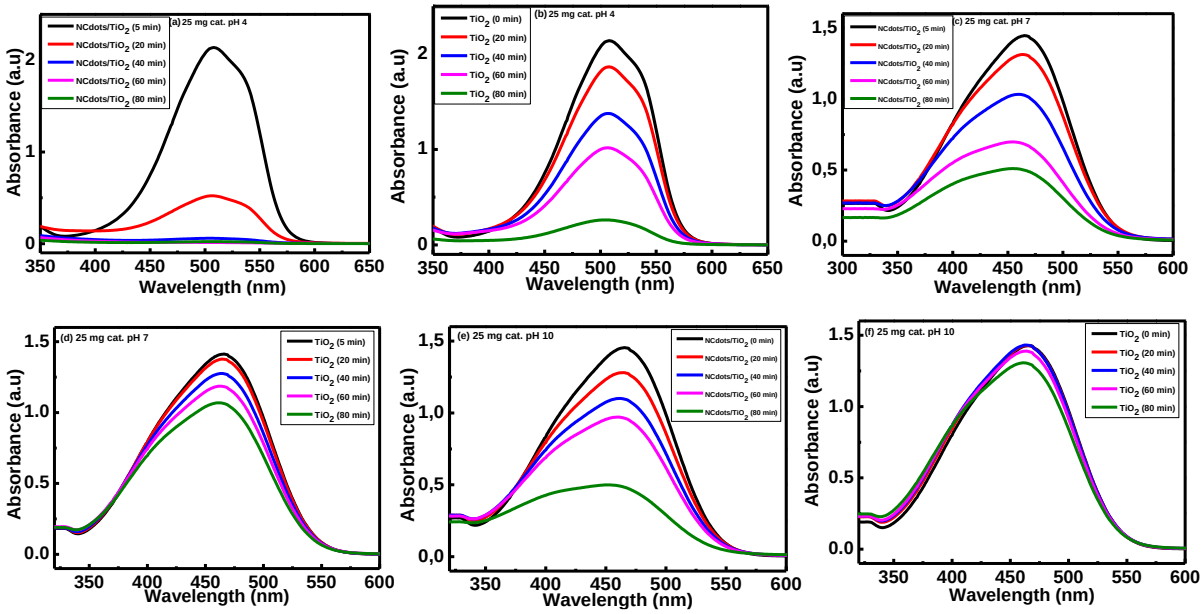

Figure S6.2 Absorption spectra of MO degradation at (a) - (b) pH 4, (c) - (d) pH 7, and (e) - (f) pH 10 over 10%-NCdots/TiO_2 and TiO_2 catalysts. Condition: 25 mg catalyst dosage, 100 mL of 20 mg/L dye solution, for 80 minutes.

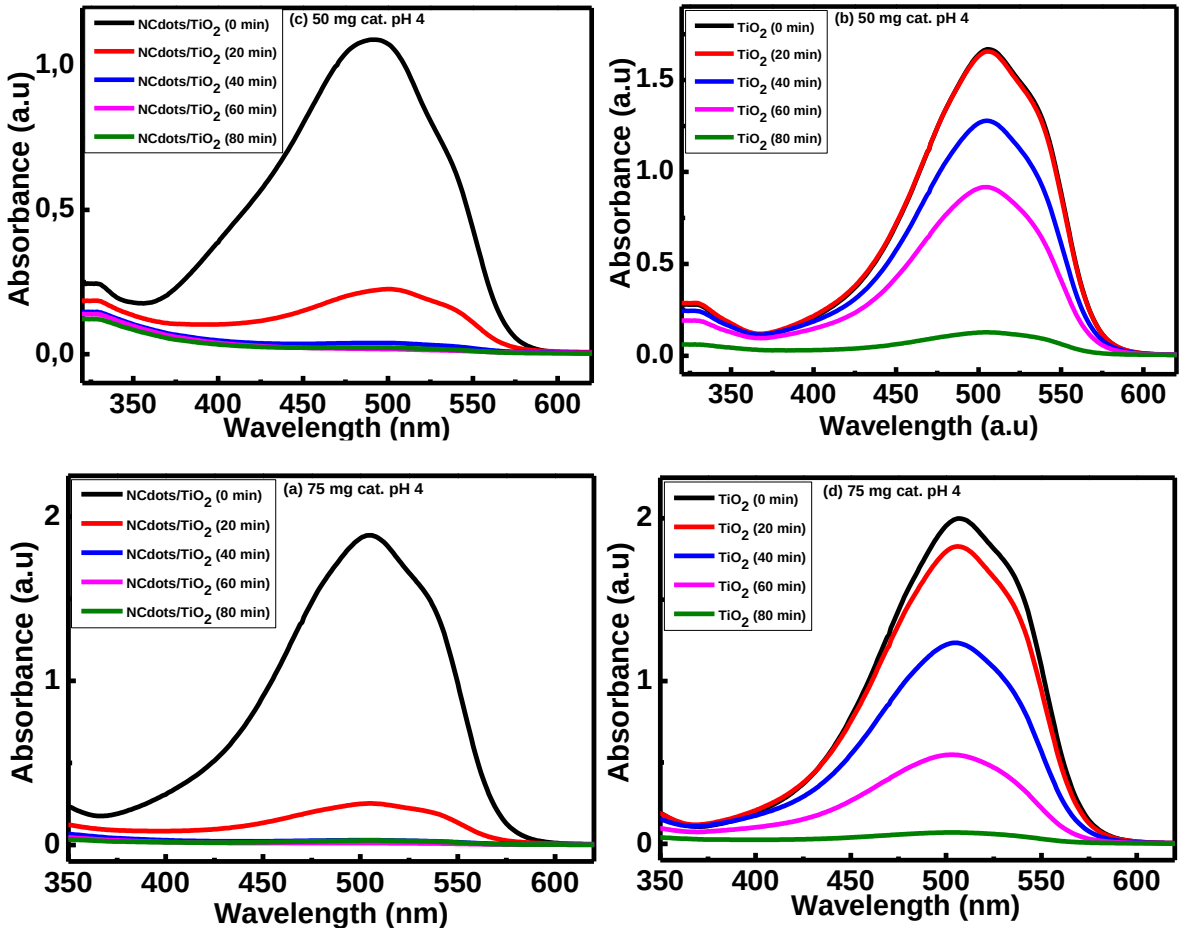

Figure S6.3 Absorption spectra of MO degradation at (a) - (b) 50 mg, (c) - (d) 75 mg cataylts dosage at pH 4, 25 mg catalyst dosage (10%-NCdots/TiO_2 and TiO_2), 100 mL of 20 mg/L dye solution, for 80 minutes.

S6.1.2 Supplementary Equations

The percentage degradation of MO was calculated using equation (S6.1). Where C_0 and C_t are initial MO concentration and its concentration at a particular time (t), respectively.[278]

$$\% \, Deg = \frac{C_0 - C_t}{C_0} \times 100 \, \% \ldots\ldots\ldots (S6.1)$$

References

1. Https://www.theguardian.com/environment/gallery/2012/dec/06/toxic-threads-greenpeace-fashion-pollution-in-pictures. No Title.

2. Https://www.carmenbusquets.com/journal/post/fashion-dye-pollution. No Title.

3. Jo, W. K. & Tayade, R. J. Recent developments in photocatalytic dye degradation upon irradiation with energy-efficient light emitting diodes. *Cuihua Xuebao/Chinese J. Catal.* **35,** 1781–1792 (2014).

4. Rajabi, M., Mahanpoor, K. & Moradi, O. Removal of dye molecules from aqueous solution by carbon nanotubes and carbon nanotube functional groups: Critical review. *RSC Adv.* **7,** 47083–47090 (2017).

5. Https://br.pinterest.com/pin/471681760970490009/?amp_client_id=CLIENT_ID(_)&mweb_unauth_id={{default.session}}&simplified=true. No Title.

6. Cruzat, D. & Jerez-Hanckes, C. Electrostatic fog water collection. *J. Electrostat.* **96,** 128–133 (2018).

7. Pinheiro, R. A., Silva, A. A., Trava-Airoldi, V. J. & Corat, E. J. Water vapor condensation and collection by super-hydrophilic and super-hydrophobic VACNTs. *Diam. Relat. Mater.* **87,** 43–49 (2018).

8. Qin, K., Liu, J., Yan, L. & Huang, H. Integrating ecosystem services flows into water security simulations in water scarce areas: Present and future. *Sci. Total Environ.* **670,** 1037–1048 (2019).

9. Holmes, R., Rivera, J. de D. & de la Jara, E. Large fog collectors: New strategies for collection efficiency and structural response to wind pressure. *Atmos. Res.* **151,** 236–249 (2015).

10. Sharma, V., Sharma, M., Kumar, S. & Krishnan, V. Investigations on the fog harvesting mechanism of Bermuda grass (Cynodon dactylon). *Flora* **224,** 59–65 (2016).

11. Mellor, J. E., Smith, J. A., Learmonth, G. P., Netshandama, V. O. & Dillingham, R. A. Modeling the complexities of water, hygiene, and health in Limpopo Province, South Africa. *Environ. Sci. Technol.* **46,** 13512–13520 (2012).

12. Nastar, M. & Ramasar, V. Transition in south african water governance: Insights from a perspective on power. *Environ. Innov. Soc. Transitions* **4,** 7–24 (2012).

13. Olivier, J. & De Rautenbach, C. J. The implementation of fog water collection systems in South

Africa. *Atmos. Res.* **64,** 227–238 (2002).

14. Ersel, M. Water and sanitation standards in humanitarian action. *Turkish J. Emerg. Med.* **15,** 27–33 (2015).

15. Dungumaro, E. W. Socioeconomic differentials and availability of domestic water in South Africa. *Phys. Chem. Earth* **32,** 1141–1147 (2007).

16. Fessehaye, M. *et al.* Fog-water collection for community use. *Renew. Sustain. Energy Rev.* **29,** 52–62 (2014).

17. Carneiro, P. A., Umbuzeiro, G. A., Oliveira, D. P. & Zanoni, M. V. B. Assessment of water contamination caused by a mutagenic textile effluent/dyehouse effluent bearing disperse dyes. *J. Hazard. Mater.* **174,** 694–699 (2010).

18. Ramalingam, S. & Jonnalagadda, R. R. Tailoring Nanostructured Dyes for Auxiliary Free Sustainable Leather Dyeing Application. *ACS Sustain. Chem. Eng.* **5,** 5537–5549 (2017).

19. Karimi, L., Zohoori, S. & Yazdanshenas, M. E. Photocatalytic degradation of azo dyes in aqueous solutions under UV irradiation using nano-strontium titanate as the nanophotocatalyst. *J. Saudi Chem. Soc.* **18,** 581–588 (2014).

20. Khataee, A. R. & Kasiri, M. B. Photocatalytic degradation of organic dyes in the presence of nanostructured titanium dioxide: Influence of the chemical structure of dyes. *J. Mol. Catal. A Chem.* **328,** 8–26 (2010).

21. Brüschweiler, B. J. & Merlot, C. Azo dyes in clothing textiles can be cleaved into a series of mutagenic aromatic amines which are not regulated yet. *Regul. Toxicol. Pharmacol.* **88,** 214–226 (2017).

22. Vacchi, F. I. *et al.* Occurrence and risk assessment of an azo dye - The case of Disperse Red 1. *Chemosphere* **156,** 95–100 (2016).

23. Fernando, E., Keshavarz, T. & Kyazze, G. Simultaneous co-metabolic decolourisation of azo dye mixtures and bio-electricity generation under thermophillic (50°C) and saline conditions by an adapted anaerobic mixed culture in microbial fuel cells. *Bioresour. Technol.* **127,** 1–8 (2013).

24. Rauf, M. A., Meetani, M. A. & Hisaindee, S. An overview on the photocatalytic degradation of azo dyes in the presence of TiO2 doped with selective transition metals. *Desalination* **276,** 13–27 (2011).

25. Teh, C. M. & Mohamed, A. R. Roles of titanium dioxide and ion-doped titanium dioxide on photocatalytic degradation of organic pollutants (phenolic compounds and dyes) in aqueous solutions: A review. *J. Alloys Compd.* **509,** 1648–1660 (2011).

26. Chequer, F. M. D. *et al.* Analyses of the genotoxic and mutagenic potential of the products formed after the biotransformation of the azo dye Disperse Red 1. *Toxicol. Vitr.* **25,** 2054–2063 (2011).

27. Vacchi, F. I., Vendemiatti, J. A. de S., da Silva, B. F., Zanoni, M. V. B. & Umbuzeiro, G. de A. Quantifying the contribution of dyes to the mutagenicity of waters under the influence of textile activities. *Sci. Total Environ.* **601-602,** 230–236 (2017).

28. Pathania, D. *et al.* Photocatalytic degradation of highly toxic dyes using chitosan-g-poly(acrylamide)/ZnS in presence of solar irradiation. *J. Photochem. Photobiol. A Chem.* **329,** 61–68 (2016).

29. Yu, L. *et al.* The degradation mechanism of methyl orange under photo-catalysis of TiO 2. *Phys. Chem. Chem. Phys.* **14,** 3589–3595 (2012).

30. Guo, J. *et al.* Adsorption of dye from wastewater using chitosan-CTAB modified bentonites. *J. Colloid Interface Sci.* **382,** 61–66 (2012).

31. Pillai, I. M. S., Gupta, A. K. & Tiwari, M. K. Multivariate optimization for electrochemical oxidation of methyl orange: Pathway identification and toxicity analysis. *J. Environ. Sci. Heal. - Part A Toxic/Hazardous Subst. Environ. Eng.* **50,** 301–310 (2015).

32. Xu, J. *et al.* A review of functionalized carbon nanotubes and graphene for heavy metal adsorption from water: Preparation, application, and mechanism. *Chemosphere* **195,** 351–364 (2018).

33. Nguyen, T. A. H. *et al.* Applicability of agricultural waste and by-products for adsorptive removal of heavy metals from wastewater. *Bioresour. Technol.* **148,** 574–585 (2013).

34. Liu, Z. *et al.* Synthesis of multi-walled carbon nanotube – hydroxyapatite composites and its application in the sorption of Co (II) from aqueous solutions. *J. Mol. Liq.* **179,** 46–53 (2013).

35. Ihsanullah *et al.* Heavy metal removal from aqueous solution by advanced carbon nanotubes: Critical review of adsorption applications. *Sep. Purif. Technol.* **157,** 141–161 (2016).

36. Xin, X. *et al.* Highly efficient removal of heavy metal ions by amine-functionalized mesoporous Fe 3O 4 nanoparticles. *Chem. Eng. J.* **184,** 132–140 (2012).

37. Grassi, M., Kaykioglu, G., Belgiorno, V. & Lofrano, G. *SpringerBriefs in Molecular Science - Green Chemistry for Sustainability: Ultrasound Technology in Green Chemistry*. *Emerg. Compd. Remov. from Wastewater* (2012). at <http://link.springer.com/10.1007/978-94-007-2409-9>

38. Byrne, C., Subramanian, G. & Pillai, S. C. Recent advances in photocatalysis for environmental

applications. *J. Environ. Chem. Eng.* 0–1 (2017). doi:10.1016/j.jece.2017.07.080

39. Shayegan, Z., Lee, C. S. & Haghighat, F. TiO2 photocatalyst for removal of volatile organic compounds in gas phase – A review. *Chem. Eng. J.* **334,** 2408–2439 (2018).

40. Luo, B. *et al.* Characterization and photocatalytic activity of Bi3TaO7 prepared by hydrothermal method. *J. Solid State Chem.* **256,** 203–212 (2017).

41. Akbar, A., Fakhari, M., Hamidinezhad, H. & Haddadi, H. TiO 2 nanoparticles immobilized on carbon nanotubes for enhanced visible-light photo-induced activity. *Integr. Med. Res.* **4,** 126–132 (2014).

42. Chatterjee, D. & Dasgupta, S. Visible light induced photocatalytic degradation of organic pollutants. *J. Photochem. Photobiol. C Photochem. Rev.* **6,** 186–205 (2005).

43. Ling, L., Wang, C., Ni, M. & Shang, C. Enhanced photocatalytic activity of TiO2/single-walled carbon nanotube (SWCNT) composites under UV-A irradiation. *Sep. Purif. Technol.* **169,** 273–278 (2016).

44. Pelaez, M. *et al.* A review on the visible light active titanium dioxide photocatalysts for environmental applications. *Appl. Catal. B Environ.* **125,** 331–349 (2012).

45. Shayegan, Z., Lee, C. & Haghighat, F. TiO 2 photocatalyst for removal of volatile organic compounds in gas phase – A review. *Chem. Eng. J.* **334,** 2408–2439 (2018).

46. Jiang, T. *et al.* Particuology Carbon nanotubes / TiO 2 nanotubes composite photocatalysts for efficient degradation of methyl orange dye. *Particuology* **11,** 737–742 (2013).

47. Sivakumar, T., Yeob, J., Bajaj, H. C., Jo, W. & Tayade, R. J. Synthesis of multiwall carbon nanotubes / TiO 2 nanotube composites with enhanced photocatalytic decomposition efficiency. *Catal. Today* **282,** 13–23 (2017).

48. Ling, L., Wang, C., Ni, M. & Shang, C. Enhanced photocatalytic activity of TiO 2 / single-walled carbon nanotube (SWCNT) composites under UV-A irradiation. *Sep. Purif. Technol.* **169,** 273–278 (2016).

49. Zhang, Y., Tang, Z.-R., Fu, X. & Xu, Y.-J. TiO_2 −Graphene Nanocomposites for Gas-Phase Photocatalytic Degradation of Volatile Aromatic Pollutant: Is TiO_2 −Graphene Truly Different from Other TiO_2 −Carbon Composite Materials? *ACS Nano* **4,** 7303–7314 (2010).

50. Koo, Y. *et al.* Synthesis and characterization of Ag-TiO2-CNT nanoparticle composites with high photocatalytic activity under artificial light. *Compos. Part B Eng.* **57,** 105–111 (2014).

51. Gu, L., Chen, Z., Sun, C., Wei, B. & Yu, X. Photocatalytic degradation of 2, 4-dichlorophenol using granular activated carbon supported TiO2. *Desalination* **263,** 107–112 (2010).

52. Saleh, T. A. & Gupta, V. K. Photo-catalyzed degradation of hazardous dye methyl orange by use of a composite catalyst consisting of multi-walled carbon nanotubes and titanium dioxide. *J. Colloid Interface Sci.* **371,** 101–106 (2012).

53. Jelinek, R. *Carbon Quantum Dots*. (2017). doi:10.1007/978-3-319-43911-2

54. Hola, K. *et al.* Photoluminescence effects of graphitic core size and surface functional groups in carbon dots: COO- induced red-shift emission. *Carbon N. Y.* **70,** 279–286 (2014).

55. Zhang, Y. Q., Ma, D. K., Zhang, Y. G., Chen, W. & Huang, S. M. N-doped carbon quantum dots for TiO2-based photocatalysts and dye-sensitized solar cells. *Nano Energy* **2,** 545–552 (2013).

56. Wang, Y. & Hu, A. Carbon quantum dots: synthesis, properties and applications. *J. Mater. Chem. C* **2,** 6921 (2014).

57. Yu, H. *et al.* Carbon quantum dots/TiO2 composites for efficient photocatalytic hydrogen evolution. *J. Mater. Chem. A* **2,** 3344–3351 (2014).

58. Essner, J. B., Kist, J. A., Polo-Parada, L. & Baker, G. A. Artifacts and Errors Associated with the Ubiquitous Presence of Fluorescent Impurities in Carbon Nanodots. *Chem. Mater.* acs.chemmater.7b04446 (2018). doi:10.1021/acs.chemmater.7b04446

59. Zhang, M., Yao, Q., Guan, W., Lu, C. & Lin, J. Layered Double Hydroxide-Supported Carbon Dots as an E ffi cient Heterogeneous Fenton-Like Catalyst for Generation of Hydroxyl Radicals. (2014). doi:10.1021/jp5012268

60. Li, Y., Yang, T., Chen, M. & Wang, J. Talanta Supported carbon dots serve as high-performance adsorbent for the retention of trace cadmium. *Talanta* **180,** 18–24 (2018).

61. Liu, C. *et al.* Controllable Synthesis of Functional Hollow Carbon Nanostructures with Dopamine As Precursor for Supercapacitors. *ACS Appl. Mater. Interfaces* **7,** 18609–18617 (2015).

62. Chen, Y. *et al.* A Self-Quenching-Resistant Carbon-Dot Powder with Tunable Solid-State Fluorescence and Construction of Dual-Fluorescence Morphologies for White Light-Emission. *Adv. Mater.* **28,** 312–318 (2016).

63. Li, X. *et al.* Hollow Carbon Spheres with Abundant Micropores for Enhanced CO2 Adsorption. *Langmuir* **33,** 1248–1255 (2017).

64. Qi, J. *et al.* Nitrogen doped porous hollow carbon spheres for enhanced benzene removal. *Sep. Purif. Technol.* **188,** 112–118 (2017).

65. Li, S., Pasc, A., Fierro, V. & Celzard, A. Hollow carbon spheres, synthesis and applications – a review. *J. Mater. Chem. A* **4,** 12686–12713 (2016).

66. Bao, Y., Shi, C., Wang, T., Li, X. & Ma, J. Microporous and Mesoporous Materials Recent progress in hollow silica : Template synthesis , morphologies and applications. *Microporous Mesoporous Mater.* **227,** 121–136 (2016).

67. Https://ewn.co.za/2020/04/17/covid-19-ximausa-residents-in-limpopo-left-to-dig-in-dry-riverbed-for-water. No Title.

68. ximausi.pdf.

69. Brusseau, M. L., Walker, D. B. & Fitzsimmons, K. Physical-Chemical Characteristics of Water. in Environmental and Pollution Science 23–45 (Elsevier, 2019). doi:10.1016/b978-0-12-814719-1.00003-3. No Title.

70. Gaya, U. I. & Abdullah, A. H. Heterogeneous photocatalytic degradation of organic contaminants over titanium dioxide: A review of fundamentals, progress and problems. *J. Photochem. Photobiol. C Photochem. Rev.* **9,** 1–12 (2008).

71. Rajeshwar, K., Zanoni, M. V. B., Kajitvichyanukul, P. & Krishnan-Ayer, R. Heterogeneous photocatalytic treatment of organic dyes in air and aqueous media. *J. Photochem. Photobiol. C Photochem. Rev.* **9,** 171–192 (2008).

72. Akpan, U. G. & Hameed, B. H. Parameters affecting the photocatalytic degradation of dyes using TiO2-based photocatalysts: A review. *J. Hazard. Mater.* **170,** 520–529 (2009).

73. Al-Tohamy, R. *et al.* A critical review on the treatment of dye-containing wastewater: Ecotoxicological and health concerns of textile dyes and possible remediation approaches for environmental safety. *Ecotoxicol. Environ. Saf.* **231,** 113160 (2022).

74. Masheane, M. L., Nthunya, L. N., Malinga, S. P., Nxumalo, E. N. & Mhlanga, S. D. Chitosan-based nanocomposites for de-nitrification of water. *Phys. Chem. Earth* **100,** 212–224 (2017).

75. Jayasantha Kumari, H., Krishnamoorthy, P., Arumugam, T. K., Radhakrishnan, S. & Vasudevan, D. An efficient removal of crystal violet dye from waste water by adsorption onto TLAC/Chitosan composite: A novel low cost adsorbent. *Int. J. Biol. Macromol.* **96,** 324–333 (2017).

76. Mu, B. & Wang, A. Adsorption of dyes onto palygorskite and its composites: A review. *J. Environ. Chem. Eng.* **4,** 1274–1294 (2016).

77. Zhang, L., Zeng, Y. & Cheng, Z. Removal of heavy metal ions using chitosan and modified chitosan: A review. *J. Mol. Liq.* **214,** 175–191 (2016).

78. Wan Ngah, W. S., Teong, L. C. & Hanafiah, M. A. K. M. Adsorption of dyes and heavy metal ions by chitosan composites: A review. *Carbohydr. Polym.* **83,** 1446–1456 (2011).

79. Crini, G. & Badot, P. M. Application of chitosan, a natural aminopolysaccharide, for dye removal from aqueous solutions by adsorption processes using batch studies: A review of recent literature. *Prog. Polym. Sci.* **33,** 399–447 (2008).

80. Coville, N. J., Mhlanga, S. D., Nxumalo, E. N. & Shaikjee, A. A review of shaped carbon nanomaterials. *S. Afr. J. Sci.* **107,** 1–15 (2011).

81. Kaushik, B. K. & Majumder, M. K. Carbon Nanotube Based VLSI Interconnects. (2015). doi:10.1007/978-81-322-2047-3

82. Saha, D. *et al.* A study on the cytotoxicity of carbon-based materials. *Mater. Sci. Eng. C* **68,** 101–108 (2016).

83. Uo, M., Akasaka, T., Watari, F., Sato, Y. & Tohji, K. Toxicity evaluations of various carbon nanomaterials. **1,** (2011).

84. Shaikjee, A. & Coville, N. J. The synthesis , properties and uses of carbon materials with helical morphology. *J. Adv. Res.* **3,** 195–223 (2012).

85. Nasir, S. Carbon-Based Nanomaterials / Allotropes : A Glimpse of Their Synthesis , Properties and Some Applications. 1–24 (2018). doi:10.3390/ma11020295

86. Polytechnic, S. S. A Critical Review of Glucose Biosensors Based on Carbon Nanomaterials: Carbon Nanotubes and Graphene. 5996–6022 (2012). doi:10.3390/s120505996

87. Liew, K. M., Lei, Z. X. & Zhang, L. W. Mechanical analysis of functionally graded carbon nanotube reinforced composites : A review. *Compos. Struct.* **120,** 90–97 (2015).

88. Xia, D., Otyepka, M., Li, X., Liu, W. & Zheng, Q. Carbon-based materials at nanoscale. *J. Nanomater.* **2015,** 2–4 (2015).

89. Yamada, Y. *et al.* Carbon materials with controlled edge structures. *Carbon N. Y.* **122,** 694–701 (2017).

90. Mansur, H. S. Quantum dots and nanocomposites. 113–129 (2010). doi:10.1002/wnan.78

91. Zhang, B. *et al.* Communications Polymer Dots in Liposomes Very Important Paper Polymer Dots Compartmentalized in Liposomes as a Photocatalyst for In Situ Hydrogen Therapy Angewandte. **518055,** 2744–2748 (2019).

92. Yan, Y. *et al.* van der Waals Heterojunction between a Bottom-Up Grown Doped Graphene Quantum Dot and Graphene for Photoelectrochemical Water Splitting. *ACS Nano* **14,** 1185–1195 (2020).

93. Himaja, A. L., Karthik, P. S. & Prakash, S. Carbon Dots : The Newest Member of the Carbon

Nanomaterials Family. 595–615 (2015). doi:10.1002/tcr.201402090

94. Yu, H. *et al.* Smart Utilization of Carbon Dots in Semiconductor Photocatalysis. 9454–9477 (2016). doi:10.1002/adma.201602581

95. Namdari, P., Negahdari, B. & Eatemadi, A. Synthesis, properties and biomedical applications of carbon-based quantum dots: An updated review. *Biomed. Pharmacother.* **87,** 209–222 (2017).

96. Yuan, F. *et al.* Shining carbon dots: Synthesis and biomedical and optoelectronic applications. *Nano Today* **11,** 565–586 (2016).

97. Cao, L., Meziani, M. J., Sahu, S. & Sun, Y.-P. Photoluminescence Properties of Graphene versus Other Carbon Nanomaterials. *Acc. Chem. Res.* **46,** 171–180 (2013).

98. Tuerhong, M., XU, Y. & YIN, X.-B. Review on Carbon Dots and Their Applications. *Chinese J. Anal. Chem.* **45,** 139–150 (2017).

99. Jia, X., Li, J. & Wang, E. One-pot green synthesis of optically pH-sensitive carbon dots with upconversion luminescence. *Nanoscale* **4,** 5572 (2012).

100. Zhao, P. & Zhu, L. and / or organic solvents. 5401–5406 (2018). doi:10.1039/c8cc02279h

101. Kurian, M. & Paul, A. Recent trends in the use of green sources for carbon dot synthesis – A short review. *Carbon Trends* **3,** 100032 (2021).

102. Liang, Q., Ma, W., Shi, Y., Li, Z. & Yang, X. Easy synthesis of highly fluorescent carbon quantum dots from gelatin and their luminescent properties and applications. *Carbon N. Y.* **60,** 421–428 (2013).

103. Baptista, F. R., Belhout, S. A., Giordani, S. & Quinn, S. J. Recent developments in carbon nanomaterial sensors. *Chem. Soc. Rev.* **44,** 4433–4453 (2015).

104. Liu, X., Pang, J., Xu, F. & Zhang, X. Simple Approach to Synthesize Amino-Functionalized Carbon Dots by Carbonization of Chitosan. *Sci. Rep.* **6,** 1–8 (2016).

105. Sachdev, A. & Gopinath, P. Green synthesis of multifunctional carbon dots from coriander leaves and their potential application as antioxidants, sensors and bioimaging agents. *Analyst* **140,** 4260–4269 (2015).

106. Tajik, S. *et al.* Carbon and graphene quantum dots: A review on syntheses, characterization, biological and sensing applications for neurotransmitter determination. *RSC Adv.* **10,** 15406–15429 (2020).

107. Mehta, V. N., Jha, S., Basu, H., Singhal, R. K. & Kailasa, S. K. One-step hydrothermal approach to fabricate carbon dots from apple juice for imaging of mycobacterium and fungal cells. *Sensors*

Actuators, B Chem. **213,** 434–443 (2015).

108. Guo, Z., Zhu, Z., Zhang, X. & Chen, Y. Facile synthesis of blue-emitting carbon dots @ mesoporous silica composite spheres. *Solid State Sci.* **76,** 100–104 (2018).

109. Moon, B. J. *et al.* Facile and Purification-Free Synthesis of Nitrogenated Amphiphilic Graphitic Carbon Dots. *Chem. Mater.* **28,** 1481–1488 (2016).

110. Online, V. A., De, B. & Karak, N. RSC Advances A green and facile approach for the synthesis of water. 8286–8290 (2013). doi:10.1039/c3ra00088e

111. Yang, X. *et al.* Novel and green synthesis of high-fluorescent carbon dots originated from honey for sensing and imaging. *Biosens. Bioelectron.* **60,** 292–298 (2014).

112. Huang, Q. *et al.* A sensitive and reliable dopamine biosensor was developed based on the Au@carbon dots-chitosan composite film. *Biosens. Bioelectron.* **52,** 277–280 (2014).

113. Article, E. & Ledendecker, M. Chemical Science urea reaction †. 8256–8266 (2020). doi:10.1039/d0sc01605e

114. Hill, M. C., Nguyen, M. K., Jeon, O. & Alsberg, E. Supporting Information. 31–42 (2014). doi:10.1107/S1600536809047072

115. Zuo, P., Lu, X., Sun, Z., Guo, Y. & He, H. A review on syntheses, properties, characterization and bioanalytical applications of fluorescent carbon dots. *Microchim. Acta* **183,** 519–542 (2016).

116. Reyes, D. *et al.* Laser Ablated Carbon Nanodots for Light Emission. *Nanoscale Res. Lett.* (2016). doi:10.1186/s11671-016-1638-8

117. Chu, K., Lee, S. L., Chang, C. & Liu, L. Recent Progress of Carbon Dot Precursors and Photocatalysis Applications. (2019).

118. Thongpool, V., Asanithi, P. & Limsuwan, P. Synthesis of carbon particles using laser ablation in ethanol. *Procedia Eng.* **32,** 1054–1060 (2012).

119. Chem, J. M. gram scale production of carbon dots / mSiO 2 for cell imaging and drug. 14403–14409 (2012). doi:10.1039/c2jm32206d

120. Massad-Ivanir, N., Bhunia, S. K., Raz, N., Segal, E. & Jelinek, R. Synthesis and characterization of a nanostructured porous silicon/carbon dot-hybrid for orthogonal molecular detection. *NPG Asia Mater.* **10,** e463 (2018).

121. Pandey, S., Mewada, A., Thakur, M. & Pillai, S. RSC Advances. 1174–1179 (2014). doi:10.1039/c3ra45227a

122. Zhao, A. *et al.* Recent advances in bioapplications of C-dots. *Carbon N. Y.* **85,** 309–327 (2015).

123. Zheng, X. T., Ananthanarayanan, A., Luo, K. Q. & Chen, P. Glowing graphene quantum dots and carbon dots: Properties, syntheses, and biological applications. *Small* **11,** 1620–1636 (2015).

124. Moniruzzaman, M. & Kim, J. N-doped carbon dots with tunable emission for multifaceted application: solvatochromism, moisture sensing, pH sensing, and solid state multicolor lighting. *Sensors Actuators, B Chem.* **295,** 12–21 (2019).

125. Mkhari, O., Ntuli, T. D., Coville, N. J., Nxumalo, E. N. & Maubane-nkadimeng, M. S. Diamond & Related Materials A comparison of fluorescent N-doped carbon dots supported on the surface of hollow and solid carbon spheres , and solid silica spheres. *Diam. Relat. Mater.* **118,** 108500 (2021).

126. Shen, L.-M. & Liu, J. New development in carbon quantum dots technical applications. *Talanta* **156-157,** 245–256 (2016).

127. Roy, P., Chen, P. C., Periasamy, A. P., Chen, Y. N. & Chang, H. T. Photoluminescent carbon nanodots: Synthesis, physicochemical properties and analytical applications. *Mater. Today* **18,** 447–458 (2015).

128. Dong, Y. *et al.* Natural carbon-based dots from humic substances. *Sci. Rep.* **5,** 1–8 (2015).

129. Siddique, A. B., Pramanick, A. K., Chatterjee, S. & Ray, M. Amorphous Carbon Dots and their Remarkable Ability to Detect. 1–10 (2018). doi:10.1038/s41598-018-28021-9

130. Li, X., Zhang, S., Kulinich, S. A., Liu, Y. & Zeng, H. Engineering surface states of carbon dots to achieve controllable luminescence for solid-luminescent composites and sensitive Be2+ detection. *Sci. Rep.* **4,** 1–8 (2014).

131. Chen, J., Liu, J., Li, J., Xu, L. & Qiao, Y. One-pot synthesis of nitrogen and sulfur co-doped carbon dots and its application for sensor and multicolor cellular imaging. *J. Colloid Interface Sci.* **485,** 167–174 (2017).

132. Fong, J. F. Y., Ng, Y. H. & Ng, S. M. *Carbon dots as a new class of light emitters for biomedical diagnostics and therapeutic applications. Fullerenes, Graphenes Nanotub. A Pharm. Approach* (Elsevier Inc., 2018). doi:10.1016/B978-0-12-813691-1.00007-5

133. Zhang, Y.-Q. *et al.* One-pot synthesis of N-doped carbon dots with tunable luminescence properties. *J. Mater. Chem.* **22,** 16714 (2012).

134. Rani, U. A., Ng, L. Y., Ng, C. Y. & Mahmoudi, E. A review of carbon quantum dots and their applications in wastewater treatment. *Adv. Colloid Interface Sci.* **278,** 102124 (2020).

135. Liu, Y., Zhao, Y. & Zhang, Y. One-step green synthesized fluorescent carbon nanodots from bamboo leaves for copper(II) ion detection. *Sensors Actuators, B Chem.* **196,** 647–652 (2014).

136. Dong, X., Al Awak, M., Wang, P., Sun, Y. P. & Yang, L. Carbon dot incorporated multi-walled carbon nanotube coated filters for bacterial removal and inactivation. *RSC Adv.* **8,** 8292–8301 (2018).

137. Zhang, J., Zhang, X., Dong, S., Zhou, X. & Dong, S. N-doped carbon quantum dots/TiO2 hybrid composites with enhanced visible light driven photocatalytic activity toward dye wastewater degradation and mechanism insight. *J. Photochem. Photobiol. A Chem.* **325,** 104–110 (2016).

138. Li, H. *et al.* Water-soluble fluorescent carbon quantum dots and photocatalyst design. *Angew. Chemie - Int. Ed.* **49,** 4430–4434 (2010).

139. Luo, H. *et al.* Nitrogen-Doped Carbon Dots/TiO2 Nanoparticle Composites for Photoelectrochemical Water Oxidation. *ACS Appl. Nano Mater.* **3,** 3371–3381 (2020).

140. Habiba, U. *et al.* Adsorption study of methyl orange by chitosan/polyvinyl alcohol/zeolite electrospun composite nanofibrous membrane. *Carbohydr. Polym.* **191,** 79–85 (2018).

141. Yoshida, H., Okamoto, A. & Kataoka, T. Adsorption of acid dye on cross-linked chitosan fibers: Equilibria. *Chem. Eng. Sci.* **48,** 2267–2272 (1993).

142. Jiang, Y. *et al.* Cross-linked chitosan/β-cyclodextrin composite for selective removal of methyl orange: Adsorption performance and mechanism. *Carbohydr. Polym.* **182,** 106–114 (2018).

143. Tyagi, A., Tripathi, K. M., Singh, N., Choudhary, S. & Gupta, R. K. RSC Advances Green synthesis of carbon quantum dots from lemon peel waste : applications in sensing and. 72423–72432 (2016). doi:10.1039/c6ra10488f

144. Deng, Y., Sik, Y., Mohan, D., Pittman, C. U. & Dou, X. Carbamazepine removal from water by carbon dot-modified magnetic carbon nanotubes. *Environ. Res.* **169,** 434–444 (2019).

145. Chen, J. *et al.* Structural design of carbon dots/porous materials composites and their applications. *Chem. Eng. J.* **421,** 127743 (2021).

146. Jiang, K. *et al.* Red, green, and blue luminescence by carbon dots: Full-color emission tuning and multicolor cellular imaging. *Angew. Chemie - Int. Ed.* **54,** 5360–5363 (2015).

147. Mokoloko, L. L. *et al.* Evolution of large-area reduced graphene oxide nanosheets from carbon dots via thermal treatment. *Carbon Trends* **4,** 100074 (2021).

148. Lim, S. Y., Shen, W. & Gao, Z. Carbon quantum dots and their applications. *Chem. Soc. Rev.* **44,** 362–381 (2015).

149. Liu, R. *et al.* An Aqueous Route to Multicolor Photoluminescent Carbon Dots Using Silica Spheres as Carriers **. 4598–4601 (2009). doi:10.1002/anie.200900652

150. Fong, J. F. Y., Ng, Y. H. & Ng, S. M. *Carbon dots as a new class of light emitters for biomedical diagnostics and therapeutic applications. Fullerenes, Graphenes Nanotub. A Pharm. Approach* (Elsevier Inc., 2018). doi:10.1016/B978-0-12-813691-1.00007-5

151. Ma, Z., Ming, H., Huang, H., Liu, Y. & Kang, Z. One-step ultrasonic synthesis of fluorescent N-doped carbon dots from glucose and their visible-light sensitive photocatalytic ability w. **1,** 861–864 (2012).

152. Xu, P., Nan, Z., Zhu, A. & Gu, Z. A facile method for preparation of hollow mesoporous silica sphere and its application. *Mater. Lett.* **205,** 20–23 (2017).

153. Zhang, H. *et al.* Preparation and characterization of carbon dot-decorated silica stationary phase in deep eutectic solvents for hydrophilic interaction chromatography. *Anal. Bioanal. Chem.* **409,** 2401–2410 (2017).

154. He, L. *et al.* Spectrochimica Acta Part A : Molecular and Biomolecular Spectroscopy Carbon-dot-based dual-emission silica nanoparticles as a ratiometric fl uorescent probe for vanadium (V) detection in mineral water samples. *Spectrochim. Acta Part A Mol. Biomol. Spectrosc.* **189,** 51–56 (2018).

155. Rao, H. *et al.* Silica-coated carbon dots conjugated to CdTe quantum dots: a ratiometric fluorescent probe for copper(II). *Microchim. Acta* **183,** 581–588 (2016).

156. Zhou, D. *et al.* Conquering Aggregation-Induced Solid-State Luminescence Quenching of Carbon Dots through a Carbon Dots-Triggered Silica Gelation Process. (2017). doi:10.1021/acs.chemmater.6b05375

157. Gogoi, S. & Karak, N. Solar-Driven Hydrogen Peroxide Production Using Polymer- Supported Carbon Dots as Heterogeneous Catalyst. *Nano-Micro Lett.* **9,** 1–11 (2017).

158. Qiao, Z. A. *et al.* A 'ship-in-a-bottle' approach to synthesis of polymer dots@silica or polymer dots@carbon core-shell nanospheres. *Adv. Mater.* **24,** 6017–6021 (2012).

159. Su, F., Zhao, X. S., Wang, Y., Wang, L. & Lee, J. Y. Hollow carbon spheres with a controllable shell structure. *J. Mater. Chem.* **16,** 4413 (2006).

160. Schliebe, C., Graske, T., Gemming, T. & Lang, H. Metal nanoparticle-loaded porous carbon hollow spheres by twin polymerization. *J. Mater. Sci.* **52,** 12653–12662 (2017).

161. Dai, X. Y., Zhang, X., Meng, Y. F. & Shen, P. K. Preparation of hollow carbon spheres by carbonization of polystyrene/polyaniline core-shell polymer particles. *Xinxing Tan Cailiao/New Carbon Mater.* **26,** 389–395 (2011).

162. Zhang, Y., Ma, D., Zhang, Y. & Chen, W. N-doped carbon quantum dots for TiO 2 -based

photocatalysts and dye-sensitized solar cells. *Nano Energy* **2,** 545–552 (2013).

163. Zhang, B., Yang, Q., Li, Z. & Hao, J. Colloids and Surfaces A : Physicochemical and Engineering Aspects Green synthesis of luminescent carbon dots and carbon-coated metal particles : Two birds with one stone. *Colloids Surfaces A Physicochem. Eng. Asp.* **485,** 34–41 (2015).

164. Yang, Y. *et al.* Carbon dots supported upon N-doped TiO2 nanorods applied into sodium and lithium ion batteries. *J. Mater. Chem. A* **3,** 5648–5655 (2015).

165. Chowdhuri, A. R., Singh, T., Ghosh, S. K. & Sahu, S. K. Carbon Dots Embedded Magnetic Nanoparticles @Chitosan @Metal Organic Framework as a Nanoprobe for pH Sensitive Targeted Anticancer Drug Delivery. *ACS Appl. Mater. Interfaces* **8,** 16573–16583 (2016).

166. Chen, Q. L., Ji, W. Q. & Chen, S. Direct Synthesis of Multicolor Fluorescent Hollow Carbon Spheres Encapsulating Enriched Carbon Dots. *Sci. Rep.* **6,** 1–8 (2016).

167. Deng, Y., Ji, Y., Chen, F., Ren, F. & Tan, S. Superior performance of flexible solid-state supercapacitors enabled by ultrafine graphene quantum dot-decorated porous carbon spheres. *New J. Chem.* **44,** 13591–13597 (2020).

168. Sun, M. *et al.* Towards efficient solid-state photoluminescence based on carbon-nanodots and starch composites. *Nanoscale* **6,** 13076–13081 (2014).

169. Chowdhury, D., Gogoi, N. & Majumdar, G. Fluorescent carbon dots obtained from chitosan gel. *RSC Adv.* **2,** 12156–12159 (2012).

170. Georgakilas, V., Perman, J. A., Tucek, J. & Zboril, R. Broad Family of Carbon Nanoallotropes: Classification, Chemistry, and Applications of Fullerenes, Carbon Dots, Nanotubes, Graphene, Nanodiamonds, and Combined Superstructures. *Chem. Rev.* **115,** 4744–4822 (2015).

171. Cui, X. *et al.* A fluorescent biosensor based on carbon dots-labeled oligodeoxyribonucleotide and graphene oxide for mercury (II) detection. *Biosens. Bioelectron.* **63,** 506–512 (2015).

172. Hutton, G. A. M., Martindale, B. C. M. & Reisner, E. Chem Soc Rev solar-driven catalysis. *Chem. Soc. Rev.* **46,** 6111–6123 (2017).

173. Wang, L. *et al.* Common Origin of Green Luminescence in Carbon Nanodots and Graphene Quantum Dots. 2541–2547 (2014). doi:10.1021/nn500368m

174. Soler-carracedo, K., Afonso, M. M., Palenzuela, J. A. & Martín, I. R. Carbon dots as temperature nanosensors in the physiological range. *J. Lumin.* **196,** 313–315 (2018).

175. Mohan, R., Drbohlavova, J. & Hubalek, J. Dual band emission in carbon dots. *Chem. Phys. Lett.* **692,** 196–201 (2018).

176. Schneider, J. *et al.* Molecular Fluorescence in Citric Acid-Based Carbon Dots. (2017). doi:10.1021/acs.jpcc.6b12519

177. Hola, K. *et al.* Carbon dots —– Emerging light emitters for bioimaging , cancer therapy and optoelectronics. *Nano Today* **9,** 590–603 (2014).

178. Himaja, A. L., Karthik, P. S. & Sreedhar, B. Synthesis of Carbon Dots from Kitchen Waste : Conversion of Waste to Value Added Product. 1767–1773 (2014). doi:10.1007/s10895-014-1465-1

179. Sendão, R. M. S. *et al.* Insight into the hybrid luminescence showed by carbon dots and molecular fluorophores in solution. *Phys. Chem. Chem. Phys.* **21,** 20919–20926 (2019).

180. Reckmeier, C. J. *et al.* Aggregated Molecular Fluorophores in the Ammonothermal Synthesis of Carbon Dots. (2017). doi:10.1021/acs.chemmater.7b03344

181. Innocenzi, P., Malfatti, L. & Carboni, D. Graphene and carbon nanodots in mesoporous materials: an interactive platform for functional applications. *Nanoscale* **7,** 12759–12772 (2015).

182. Stober, W. E. R. N. E. R. Controlled Growth of Monodisperse Silica Spheres in the Micron Size Range 1. **69,** 62–69 (1968).

183. Hümmelgen, I. A. & Coville, N. J. Hollow carbon spheres and a hollow carbon sphere/polyvinylpyrrolidone composite as ammonia sensors. **5,** (2017).

184. Mutuma, B. K. *et al.* Generation of radical species in CVD grown pristine and N-doped solid carbon spheres using H2 and Ar as carrier gases. *RSC Adv.* **7,** 21187–21195 (2017).

185. Ibrahim, I. a. M., Zikry, a. a. F. & Sharaf, M. a. Preparation of spherical silica nanoparticles: Stober silica. *J. Am. Sci.* **6,** 985–989 (2010).

186. Eurov, D. A. *et al.* Luminescent Properties of Carbon Nanodots Bound to the Surface of Spherical Microresonator. *Phys. Solid State* **62,** 1898–1904 (2020).

187. Chen, A. *et al.* Thin-walled, mesoporous and nitrogen-doped hollow carbon spheres using ionic liquids as precursors. *J. Mater. Chem. A* **1,** 1045–1047 (2013).

188. Panickar, R., Sobhan, C. B. & Chakravorti, S. Chemical vapor deposition synthesis of carbon spheres: Effects of temperature and hydrogen. *Vacuum* **172,** 109108 (2020).

189. Chen, X. *et al.* CVD generated mesoporous hollow carbon spheres as supercapacitors. *Colloids Surfaces A Physicochem. Eng. Asp.* **396,** 246–250 (2012).

190. Konwar, A., Gogoi, N., Majumdar, G. & Chowdhury, D. Green chitosan-carbon dots nanocomposite hydrogel film with superior properties. *Carbohydr. Polym.* **115,** 238–245 (2015).

191. Liu, R. & Wang, C. Synthesis of hollow mesoporous silica spheres with radially aligned mesochannels and tunable textural properties. *Ceram. Int.* **41,** 1101–1106 (2015).

192. Wang, F.-L. *et al.* Simple synthesis of hollow carbon spheres from glucose. *Mater. Lett.* **63,** 2564–2566 (2009).

193. Wang, H. *et al.* Biocompatible PEG-Chitosan@Carbon Dots Hybrid Nanogels for Two-Photon Fluorescence Imaging, Near-Infrared Light/pH Dual-Responsive Drug Carrier, and Synergistic Therapy. *Adv. Funct. Mater.* **25,** 5537–5547 (2015).

194. Sharma, A. *et al.* Origin of Excitation Dependent Fluorescence in Carbon Nanodots. *J. Phys. Chem. Lett.* **7,** 3695–3702 (2016).

195. Kurdyukov, D. A. *et al.* Controllable spherical aggregation of monodisperse carbon nanodots. *Nanoscale* **10,** 13223–13235 (2018).

196. Gong, X. *et al.* Analytica Chimica Acta Facile synthesis of nitrogen-doped carbon dots for Fe 3 + sensing and cellular imaging. *Anal. Chim. Acta* **861,** 74–84 (2015).

197. Xiao, D., Yuan, D. & Lu, J. Microwave-assisted one-step green synthesis of amino-functionalized fl uorescent carbon nitride dots from chitosan. 612–615 (2013). doi:10.1002/bio.2486

198. Wang, C. *et al.* Tunable Carbon-Dot-Based Dual-Emission Fluorescent Nanohybrids for Ratiometric Optical Thermometry in Living Cells. (2016). doi:10.1021/acsami.5b11317

199. Zhou, L., Li, Z., Liu, Z., Ren, J. & Qu, X. Luminescent Carbon Dot-Gated Nanovehicles for pH-Triggered Intracellular Controlled Release and Imaging. (2013).

200. Liu, Y., Liu, C. Y., Zhang, Z. Y., Yang, W. D. & Nie, S. D. Plasmon-enhanced photoluminescence of carbon dots-silica hybrid mesoporous spheres. *J. Mater. Chem. C* **3,** 2881–2885 (2015).

201. Wang, F., Xie, Z., Zhang, H., Liu, C. & Zhang, Y. Highly Luminescent Organosilane-Functionalized Carbon Dots. 1027–1031 (2011). doi:10.1002/adfm.201002279

202. Stepanidenko, E. A. *et al.* Strongly luminescent composites based on carbon dots embedded in a nanoporous silicate glass. *Nanomaterials* **10,** (2020).

203. Pawar, S., Togiti, U. K., Bhattacharya, A. & Nag, A. Functionalized Chitosan-Carbon Dots: A Fluorescent Probe for Detecting Trace Amount of Water in Organic Solvents. *ACS Omega* **4,** 11301–11311 (2019).

204. Wang, X. *et al.* Photoinduced electron transfers with carbon dots. *Chem. Commun.* 3774–3776 (2009). doi:10.1039/b906252a

205. Mosconi, D. *et al.* Synthesis and photochemical applications of processable polymers enclosing photoluminescent carbon quantum dots. *ACS Nano* **9,** 4156–4164 (2015).

206. Luo, L., Ma, J., Zhu, H. & Tang, J. Embedded carbon in a carbon nitride hollow sphere for enhanced charge separation and photocatalytic water splitting. *Nanoscale* **12,** 7339–7346 (2020).

207. Zhu, X. *et al.* Green emitting N , S-co-doped carbon dots for sensitive fluorometric determination of Fe (III) and Ag (I) ions , and as a solvatochromic probe. (2018).

208. Wang, Q. *et al.* Hollow luminescent carbon dots for drug delivery. *Carbon N. Y.* **59,** 192–199 (2013).

209. Zhang, B. T., Wang, Q., Zhang, Y., Teng, Y. & Fan, M. Degradation of ibuprofen in the carbon dots/Fe3O4@carbon sphere pomegranate-like composites activated persulfate system. *Sep. Purif. Technol.* **242,** 116820 (2020).

210. Zhang, G. *et al.* Facile ‘ Spot-Heating ’ Synthesis of Carbon Dots / Carbon Nitride for Solar Hydrogen Evolution Synchronously with Contaminant Decomposition. **1706462,** 1–8 (2018).

211. Guo, W. *et al.* A novel molecularly imprinted electrochemical sensor modified with carbon dots, chitosan, gold nanoparticles for the determination of patulin. *Biosens. Bioelectron.* **98,** 299–304 (2017).

212. Esmaeilzadeh, M., Sadjadi, S. & Salehi, Z. Pd immobilized on hybrid of magnetic graphene quantum dots and cyclodextrin decorated chitosan: An efficient hydrogenation catalyst. *Int. J. Biol. Macromol.* **150,** 441–448 (2020).

213. Zhao, X. *et al.* Enhancing photoluminescence of carbon quantum dots doped PVA films with randomly dispersed silica microspheres. *Sci. Rep.* **10,** 1–10 (2020).

214. Uriarte, D., Domini, C. & Garrido, M. New carbon dots based on glycerol and urea and its application in the determination of tetracycline in urine samples. *Talanta* **201,** 143–148 (2019).

215. Uriarte, D., Domini, C. & Garrido, M. Talanta New carbon dots based on glycerol and urea and its application in the determination of tetracycline in urine samples. *Talanta* **201,** 143–148 (2019).

216. Qi, J. *et al.* Porous carbon spheres for simultaneous removal of benzene and H 2 S. *Chem. Eng. J.* **339,** 499–508 (2018).

217. Wen, S., Ng, L., Yilmaz, G., Li, W. & Wei, G. Applied Catalysis B : Environmental One-step activation towards spontaneous etching of hollow and hierarchical porous carbon nanospheres for enhanced pollutant adsorption and energy storage. *Appl. Catal. B Environ.* **220,** 533–541 (2018).

218. Milan, P., Pal, H. & Dutta, S. Spectrochimica Acta Part A : Molecular and Biomolecular Spectroscopy Photophysics and luminescence quenching of carbon dots derived from lemon juice and glycerol. *Spectrochim. Acta Part A Mol. Biomol. Spectrosc.* **209,** 14–21 (2019).

219. Kasprzyk, W. *et al.* Luminescence phenomena of carbon dots derived from citric acid and urea-a molecular insight. *Nanoscale* **10,** 13889–13894 (2018).

220. Kundu, A. *et al.* Multicolor emissive carbon dot with solvatochromic behavior across the entire visible spectrum. *Carbon N. Y.* **156,** 110–118 (2020).

221. Jones, S. S., Sahatiya, P. & Badhulika, S. One step , high yield synthesis of amphiphilic carbon quantum dots derived from chia seeds : a solvatochromic study †. 13130–13139 (2017). doi:10.1039/c7nj03513f

222. Lai, C. W., Hsiao, Y. H., Peng, Y. K. & Chou, P. T. Facile synthesis of highly emissive carbon dots from pyrolysis of glycerol; Gram scale production of carbon dots/mSiO 2 for cell imaging and drug release. *J. Mater. Chem.* **22,** 14403–14409 (2012).

223. Wei, X. *et al.* Surface States Induced Photoluminescence Enhancement of Nitrogen-Doped Carbon Dots Via Post-Treatments. *Nanoscale Res. Lett.* **14,** (2019).

224. Wei, X. *et al.* Surface States Induced Photoluminescence Enhancement of Nitrogen-Doped Carbon Dots Via Post-Treatments. (2019).

225. Kim, J. Sensors and Actuators B : Chemical N-doped carbon dots with tunable emission for multifaceted application : solvatochromism , moisture sensing , pH sensing , and solid state multicolor lighting. *Sensors Actuators B. Chem.* **295,** 12–21 (2019).

226. Azari, A. *et al.* Experimental design, modeling and mechanism of cationic dyes biosorption on to magnetic chitosan-lutaraldehyde composite. *Int. J. Biol. Macromol.* **131,** 633–645 (2019).

227. Zhang, J., Zhou, Q. & Ou, L. Kinetic, isotherm, and thermodynamic studies of the adsorption of methyl orange from aqueous solution by chitosan/alumina composite. *J. Chem. Eng. Data* **57,** 412–419 (2012).

228. Xing, J. *et al.* Preparation of micro-nano fi brous chitosan sponges with ternary solvents for dye adsorption. *Carbohydr. Polym.* **198,** 69–75 (2018).

229. Ngah, W. S. W. & Fatinathan, S. Adsorption of Cu (II) ions in aqueous solution using chitosan beads , chitosan – GLA beads and chitosan – alginate beads. **143,** 62–72 (2008).

230. Li, J. *et al.* Adsorption of reactive red 136 onto chitosan/montmorillonite intercalated composite from aqueous solution. *Appl. Clay Sci.* **167,** 9–22 (2019).

231. Liu, Q., Yang, B., Zhang, L. & Huang, R. Adsorption of an anionic azo dye by cross-linked

chitosan/bentonite composite. *Int. J. Biol. Macromol.* **72,** 1129–1135 (2015).

232. Haldorai, Y. & Shim, J. J. An efficient removal of methyl orange dye from aqueous solution by adsorption onto chitosan/MgO composite: A novel reusable adsorbent. *Appl. Surf. Sci.* **292,** 447–453 (2014).

233. Wang, J. & Zhuang, S. Removal of various pollutants from water and wastewater by modified chitosan adsorbents. *Crit. Rev. Environ. Sci. Technol.* **47,** 2331–2386 (2017).

234. Parshetti, G. K., Chowdhury, S. & Balasubramanian, R. Hydrothermal conversion of urban food waste to chars for removal of textile dyes from contaminated waters. *Bioresour. Technol.* **161,** 310–319 (2014).

235. Simsir, H., Eltugral, N. & Karagoz, S. Hydrothermal carbonization for the preparation of hydrochars from glucose, cellulose, chitin, chitosan and wood chips via low-temperature and their characterization. *Bioresour. Technol.* **246,** 82–87 (2017).

236. He, C. *et al.* Waste shrimp shell-derived hydrochar as an emergent material for methyl orange removal in aqueous solutions. *Environ. Int.* **134,** (2020).

237. Shen, F., Su, J., Zhang, X., Zhang, K. & Qi, X. Chitosan-derived carbonaceous material for highly efficient adsorption of chromium (VI) from aqueous solution. *Int. J. Biol. Macromol.* **91,** 443–449 (2016).

238. Kim, U. J., Kimura, S. & Wada, M. Highly enhanced adsorption of Congo red onto dialdehyde cellulose-crosslinked cellulose-chitosan foam. *Carbohydr. Polym.* **214,** 294–302 (2019).

239. Lipatova, I. M., Makarova, L. I. & Yusova, A. A. Adsorption removal of anionic dyes from aqueous solutions by chitosan nanoparticles deposited on the fibrous carrier. *Chemosphere* **212,** 1155–1162 (2018).

240. Xing, J. *et al.* Preparation of micro-nanofibrous chitosan sponges with ternary solvents for dye adsorption. *Carbohydr. Polym.* **198,** 69–75 (2018).

241. Ma, H. *et al.* Ultrahigh adsorption capacities for anionic and cationic dyes from wastewater using only chitosan. *J. Clean. Prod.* **214,** 89–94 (2019).

242. Sharma, A., Syed, Z., Brighu, U., Gupta, A. B. & Ram, C. Adsorption of textile wastewater on alkali-activated sand. *J. Clean. Prod.* **220,** 23–32 (2019).

243. Subbaiah, M. V. & Kim, D. S. Adsorption of methyl orange from aqueous solution by aminated pumpkin seed powder: Kinetics, isotherms, and thermodynamic studies. *Ecotoxicol. Environ. Saf.* **128,** 109–117 (2016).

244. Yen, M. T., Yang, J. H. & Mau, J. L. Physicochemical characterization of chitin and chitosan

from crab shells. *Carbohydr. Polym.* **75,** 15–21 (2009).

245. Uzun, I. Kinetics of the adsorption of reactive dyes by chitosan. *Dye. Pigment.* **70,** 76–83 (2006).

246. Belamie, E., Domard, A. & Giraud-Guille, M. M. Study of the solid-state hydrolysis of chitosan in presence of HCl. *J. Polym. Sci. Part A Polym. Chem.* **35,** 3181–3191 (1997).

247. Jaworska, M., Sakurai, K., Gaudon, P. & Guibal, E. Influence of chitosan characteristics on polymer properties. I: Crystallographic properties. *Polym. Int.* **52,** 198–205 (2003).

248. Primo, A., Atienzar, P., Sanchez, E., Delgado, J. M. & García, H. From biomass wastes to large-area, high-quality, N-doped graphene: Catalyst-free carbonization of chitosan coatings on arbitrary substrates. *Chem. Commun.* **48,** 9254–9256 (2012).

249. Tong, X. *et al.* Tailoring the physicochemical properties of chitosan-derived N-doped carbon by controlling hydrothermal carbonization time for high-performance supercapacitor application. *Carbohydr. Polym.* **207,** 764–774 (2019).

250. Mahmoodi, N. M., Salehi, R., Arami, M. & Bahrami, H. Dye removal from colored textile wastewater using chitosan in binary systems. *Desalination* **267,** 64–72 (2011).

251. Zawadzki, J. & Kaczmarek, H. Thermal treatment of chitosan in various conditions. *Carbohydr. Polym.* **80,** 394–400 (2010).

252. Varma, R. & Vasudevan, S. Extraction, Characterization, and Antimicrobial Activity of Chitosan from Horse Mussel Modiolus modiolus. 0–6 (2020). doi:10.1021/acsomega.0c01903

253. Pawlak, A. & Mucha, M. Thermogravimetric and FTIR studies of chitosan blends. *Thermochim. Acta* **396,** 153–166 (2003).

254. Wang, Y. *et al.* Electrodeposition of a carbon dots/chitosan composite produced by a simple in situ method and electrically controlled release of carbon dots. *J. Mater. Chem. B* **3,** 7511–7517 (2015).

255. Tiwary, A. K. & Rana, V. Cross-linked chitosan films: Effect of cross-linking density on swelling parameters. *Pak. J. Pharm. Sci.* **23,** 443–448 (2010).

256. Annadurai, G., Ling, L. Y. & Lee, J. F. Adsorption of reactive dye from an aqueous solution by chitosan: isotherm, kinetic and thermodynamic analysis. *J. Hazard. Mater.* **152,** 337–346 (2008).

257. Lu, S., Yuan, G., Zhu, Y. & Yu, S. Carbon dots crosslinked chitosan/cellulose sponge capture of methyl blue by an adsorption process. *Luminescence* 1–10 (2021). doi:10.1002/bio.4089

258. Tanhaei, B., Ayati, A., Lahtinen, M. & Sillanpää, M. Preparation and characterization of a novel chitosan/Al2O3/magnetite nanoparticles composite adsorbent for kinetic, thermodynamic and

isotherm studies of Methyl Orange adsorption. *Chem. Eng. J.* **259,** 1–10 (2015).

259. Mane, V. S., Mall, I. D. & Srivastava, V. C. Use of bagasse fly ash as an adsorbent for the removal of brilliant green dye from aqueous solution. *Dye. Pigment.* **73,** 269–278 (2007).

260. Momenzadeh, H., Tehrani-Bagha, A. R., Khosravi, A., Gharanjig, K. & Holmberg, K. Reactive dye removal from wastewater using a chitosan nanodispersion. *Desalination* **271,** 225–230 (2011).

261. Simonin, J. P. On the comparison of pseudo-first order and pseudo-second order rate laws in the modeling of adsorption kinetics. *Chem. Eng. J.* **300,** 254–263 (2016).

262. Zhai, L., Bai, Z., Zhu, Y., Wang, B. & Luo, W. Fabrication of chitosan microspheres for efficient adsorption of methyl orange. *Chinese J. Chem. Eng.* **26,** 657–666 (2018).

263. Sun, B. *et al.* Waste-cellulose-derived porous carbon adsorbents for methyl orange removal. *Chem. Eng. J.* **371,** 55–63 (2019).

264. Huang, R., Liu, Q., Huo, J. & Yang, B. Adsorption of methyl orange onto protonated cross-linked chitosan. *Arab. J. Chem.* **10,** 24–32 (2017).

265. Tanhaei, B., Ayati, A., Lahtinen, M. & Sillanpää, M. Preparation and characterization of a novel chitosan/Al2O3/magnetite nanoparticles composite adsorbent for kinetic, thermodynamic and isotherm studies of Methyl Orange adsorption. *Chem. Eng. J.* **259,** 1–10 (2015).

266. Chen, S. *et al.* Equilibrium and kinetic studies of methyl orange and methyl violet adsorption on activated carbon derived from Phragmites australis. *Desalination* **252,** 149–156 (2010).

267. Yang, D., Qiu, L. & Yang, Y. Efficient Adsorption of Methyl Orange Using a Modified Chitosan Magnetic Composite Adsorbent. *J. Chem. Eng. Data* **61,** 3933–3940 (2016).

268. Wu, Y. *et al.* Superior adsorption of methyl orange by h-MoS2 microspheres: Isotherm, kinetics, and thermodynamic studies. *Dye. Pigment.* **170,** 1–8 (2019).

269. Ahmed, S. *et al.* Solvent assisted synthesis of hierarchical magnesium oxide flowers for adsorption of phosphate and methyl orange: Kinetic, isotherm, thermodynamic and removal mechanism. *Surfaces and Interfaces* **23,** 100953 (2021).

270. Hussain, S. *et al.* Adsorption, kinetics and thermodynamics studies of methyl orange dye sequestration through chitosan composites films. *Int. J. Biol. Macromol.* **168,** 383–394 (2021).

271. Ayawei, N., Ebelegi, A. N. & Wankasi, D. Modelling and Interpretation of Adsorption Isotherms. *J. Chem.* **2017,** (2017).

272. Saha, T. K. Adsorption of Methyl Orange onto Chitosan from Aqueous Solution. *J. Water*

Resour. Prot. **02,** 898–906 (2010).

273. Jiang, T. *et al.* Carbon nanotubes/TiO2 nanotubes composite photocatalysts for efficient degradation of methyl orange dye. *Particuology* **11,** 737–742 (2013).

274. Bhatkhande, D. S., Pangarkar, V. G. & Beenackers, A. A. C. M. Photocatalytic degradation for environmental applications - A review. *J. Chem. Technol. Biotechnol.* **77,** 102–116 (2002).

275. Ge, L., Han, C. & Liu, J. Novel visible light-induced g-C3N4/Bi2WO6 composite photocatalysts for efficient degradation of methyl orange. *Appl. Catal. B Environ.* **108-109,** 100–107 (2011).

276. Li, Y., Li, X., Li, J. & Yin, J. Photocatalytic degradation of methyl orange in a sparged tube reactor with TiO2-coated activated carbon composites. *Catal. Commun.* **6,** 650–655 (2005).

277. Sun, M. *et al.* A nanocomposite of carbon quantum dots and TiO2 nanotube arrays: Enhancing photoelectrochemical and photocatalytic properties. *RSC Adv.* **4,** 1120–1127 (2014).

278. Hu, Y. *et al.* Visible-Light Upconversion Carbon Quantum Dots Decorated TiO 2 for the Photodegradation of Flowing Gaseous Acetaldehyde. *Appl. Surf. Sci.* **440,** 266–274 (2018).

279. Tian, J. *et al.* Carbon quantum dots/hydrogenated TiO2 nanobelt heterostructures and their broad spectrum photocatalytic properties under UV, visible, and near-infrared irradiation. *Nano Energy* **11,** 419–427 (2015).

280. Yu, X., Liu, J., Yu, Y., Zuo, S. & Li, B. Preparation and visible light photocatalytic activity of carbon quantum dots/TiO2 nanosheet composites. *Carbon N. Y.* **68,** 718–724 (2014).

281. Niu, X. *et al.* Hydrothermal synthesis and formation mechanism of the anatase nanocrystals with co-exposed high-energy {001}, {010} and [111]-facets for enhanced photocatalytic performance. *RSC Adv.* **7,** 24616–24627 (2017).

282. Roy, N., Park, Y., Sohn, Y. & Pradhan, D. Controlled synthesis and facets-dependent photocatalysis of TiO2 nanocrystals. *Semicond. Sci. Technol.* **30,** 44005 (2015).

283. Amin, M., Sadatlu, A. & Mozaffari, N. ScienceDirect Synthesis of mesoporous TiO 2 structures through P123 copolymer as the structural directing agent and assessment of their performance in dye-sensitized solar cells. *Sol. Energy* **133,** 24–34 (2016).

284. Li, F. *et al.* One-step synthesis of nanohybrid carbon dots and TiO2 composites with enhanced ultraviolet light active photocatalysis. *RSC Adv.* **5,** 8389–8396 (2015).

285. Djellabi, R., Yang, B., Wang, Y., Cui, X. & Zhao, X. Carbonaceous biomass-titania composites with Ti–O–C bonding bridge for efficient photocatalytic reduction of Cr(VI) under narrow visible light. *Chem. Eng. J.* **366,** 172–180 (2019).

286. Ashkarran, A. A., Fakhari, M., Hamidinezhad, H., Haddadi, H. & Nourani, M. R. TiO2 nanoparticles immobilized on carbon nanotubes for enhanced visible-light photo-induced activity. *J. Mater. Res. Technol.* **4,** 126–132 (2015).

287. Peng, Z., Tang, H. & Yao, K. Recyclable TiO2/carbon nanotube sponge nanocomposites: Controllable synthesis, characterization and enhanced visible light photocatalytic property. *Ceram. Int.* **41,** 363–368 (2015).

288. Zhao, J., Li, Y. & Na, P. Facile Construction of Carbon Dots Layer and Oxygen Vacancies Simultaneously onto TiO2 to Enhance Photoreduction Activity. *Chinese J. Chem.* **39,** 1310–1318 (2021).

289. Etacheri, V. *et al.* Journal of Photochemistry and Photobiology C : Photochemistry Reviews Visible-light activation of TiO 2 photocatalysts : Advances in theory and experiments. *J. Photochem. Photobiol. C Photochem. Rev.* **25,** 11–29 (2015).

290. Pang, Y. L. & Abdullah, A. Z. Effect of carbon and nitrogen co-doping on characteristics and sonocatalytic activity of TiO2 nanotubes catalyst for degradation of Rhodamine B in water. *Chem. Eng. J.* **214,** 129–138 (2013).

291. Wang, W., Ni, Y. & Xu, Z. One-step uniformly hybrid carbon quantum dots with high-reactive TiO2 for photocatalytic application. *J. Alloys Compd.* **622,** 303–308 (2015).

292. Zhang, Z. *et al.* Microwave degradation of methyl orange dye in aqueous solution in the presence of nano-TiO 2-supported activated carbon (supported-TiO 2/AC/MW). *J. Hazard. Mater.* **209-210,** 271–277 (2012).

293. Yang, H. *et al.* Sol-gel synthesis of TiO2 nanoparticles and photocatalytic degradation of methyl orange in aqueous TiO2 suspensions. *J. Alloys Compd.* **413,** 302–306 (2006).

294. Al-mamun, R. *et al.* Synthesis, characterization, and photocatalytic performance of methyl orange in aqueous TiO2 suspension under UV and solar light irradiation. *South African J. Chem. Eng.* 0–44 (2022). doi:10.1016/j.sajce.2022.02.002

295. Glow, C., Electrolysis, D., Jianying, G. & Weimin, C. The decolourisation of Methyl Orange and textile effluent under UV using commercial and The decolourisation of Methyl Orange and textile effluent under UV using commercial and synthesized nano-TiO 2. (2018).

296. Hazarika, D. & Karak, N. Photocatalytic degradation of organic contaminants under solar light using carbon dot/titanium dioxide nanohybrid, obtained through a facile approach. *Appl. Surf. Sci.* **376,** 276–285 (2016).

297. Zhou, J. *et al.* Role of carbon quantum dots in titania based photoelectrodes: Upconversion or

others? *J. Colloid Interface Sci.* **529,** 396–403 (2018).

298. Liu, J., Zhu, W., Yu, S. & Yan, X. Three dimensional carbogenic dots/TiO2 nanoheterojunctions with enhanced visible light-driven photocatalytic activity. *Carbon N. Y.* **79,** 369–379 (2014).

299. Tran, H. N., You, S. J., Hosseini-Bandegharaei, A. & Chao, H. P. Mistakes and inconsistencies regarding adsorption of contaminants from aqueous solutions: A critical review. *Water Res.* **120,** 88–116 (2017).

Swi hetisekile